國　立　中　央　大　學

物理所

博　士　論　文

在 CERN COMPASS 實驗組量測 190-GeV π 介子束流所產生 Drell-Yan 過程反應截面

研 究 生：謝佳諭

指導教授：林宗泰

共同指導：章文箴

中 華 民 國　　110 年　　6 月

National Central University

Physics Department

Doctoral Thesis

Measurement of the differential Drell–Yan cross sections with 190-GeV pion beams in the COMPASS Experiment at CERN

Student：Chia-Yu Hsieh

Advisor : Willis T. Lin

Co-adviser : Wen-Chen Chang

June, 2021

國　立　中　央　大　學

物理所

博　士　論　文

在 CERN COMPASS 實驗組量測 190-GeV π 介子束流所產生 Drell-Yan 過程反應截面

研 究 生：謝佳諭

指導教授：林宗泰

共同指導：章文箴

中 華 民 國　　110 年　　6 月

National Central University

Physics Department

Doctoral Thesis

Measurement of the differential Drell–Yan cross sections with 190-GeV pion beams in the COMPASS Experiment at CERN

Student：Chia-Yu Hsieh

Advisor : Willis T. Lin

Co-adviser : Wen-Chen Chang

June, 2021

國立中央大學圖書館學位論文授權書

填單日期：2021/08/10　　2019.9 版

授權人姓名	謝佳諭	學 號	101282005
系所名稱	物理所	學位類別	□碩士　☑博士
論文名稱	在 CERN COMPASS 實驗組量測 190-GeV π 介子束流所產生 Drell-Yan 過程反應截面	指導教授	林宗泰 章文箴

學位論文網路公開授權

授權本人撰寫之學位論文全文電子檔：

・在「**國立中央大學圖書館博碩士論文系統**」.

(✓)同意立即網路公開

(　)同意 於西元＿＿＿年＿＿＿月＿＿＿日網路公開

(　)不同意網路公開，原因是：＿＿＿＿＿＿＿＿＿＿

・在**國家圖書館「臺灣博碩士論文知識加值系統」**

(✓)同意立即網路公開

(　)同意 於西元＿＿＿年＿＿＿月＿＿＿日網路公開

(　)不同意網路公開，原因是：＿＿＿＿＿＿＿＿＿＿

依著作權法規定，非專屬、無償授權國立中央大學、台灣聯合大學系統與國家圖書館，不限地域、時間與次數，以文件、錄影帶、錄音帶、光碟、微縮、數位化或其他方式將上列授權標的基於非營利目的進行重製。

學位論文紙本延後公開申請 (紙本學位論文**立即公開者此欄免填**)

本人撰寫之學位論文紙本因以下原因將延後公開

・**延後原因**

(　)已申請專利並檢附證明，專利申請案號：

(　)準備以上列論文投稿期刊

(　)涉國家機密

(　)依法不得提供，請說明：＿＿＿＿＿＿＿＿

・**公開日期**：西元＿＿＿＿年＿＿＿＿月＿＿＿＿日

※繳交教務處註冊組之紙本論文(送繳國家圖書館)若不立即公開，請加填「國家圖書館學位論文延後公開申請書」

研究生簽名：謝佳諭　　指導教授簽名：林宗泰

*本授權書請完整填寫並親筆簽名後，裝訂於論文**封面之次頁**。

National Central University Library
Authorization for Thesis/ Dissertation

Application Date：2021/08/10 The latest version since Sep. 2019

Applicant Name	Chia-Yu Hsieh	Student Number	101282005
Schools / Departments	Physics Department	Graduate Degree	☐Master ☑ Doctor
Thesis/Dissertation Title	Measurement of the differential Drell–Yan cross sections with 190-GeV pion beams in the COMPASS Experiment at CERN	Advisor Name	Willis T. Lin Wen-Chen Chang

Authorization for Internet Access of Thesis/ Dissertation

This license authorizes my complete electronic thesis to be archived and read in the

- National Central University Library Electronic Theses & Dissertations System .
  - (✓) Released for Internet access immediately
  - ( ) Released for Internet access starting from: _____/_____/_____ (YYYY / MM / DD)
  - ( ) Disagree, because:_____
- NDLTD(National Digital Library of Theses and Dissertations in Taiwan).
  - (✓) Released for Internet access immediately
  - ( ) Released for Internet access starting from: _____/_____/_____ (YYYY / MM / DD)
  - ( ) Disagree, because:_____

I hereby agree to authorize the electronic versions of my thesis/dissertation and work to National Central University, University System of Taiwan(UST) and National Central Library(National Digital Library of Theses and Dissertations in Taiwan), in a non-exclusive way and without reimbursement, in accordance with the Copyright Act. The fore-mentioned authorized items can be reproduced by the authorized institution in the form of text, video tape, audio tape, disc and microfilm, or converted into other digital formats, without the limitation of time, places, and frequency for non-commercial uses.

Delayed Public Release for Paper Copy of Thesis/Dissertation

(You do not need to fill out this section if you make the paper copy of your thesis/dissertation available to the public immediately.)

- Reasons for the delayed release (choose one)
  - ( ) Filing for patent registration. Registration number: _____
  - ( ) Submission for publication
  - ( ) Your research contains information pertaining to national non-disclosure agreements.
  - ( ) Contents withheld according to the law. Please specify_____
- Delayed Until：_____/_____/_____ (YYYY / MM / DD)

You should submit another paper copy to National Central Library (NCL) through the NCU Division of Registrar. If you would like to delay the release of this paper copy in NCL, please fill out the "Application for Embargo of thesis/dissertation" of NCL.

Signature of the Applicant：Chia Yu Hsieh Signature of the Advisor：

*Please attach this form after the thesis/dissertation cover when submitting your thesis/dissertation.

國立中央大學博士班研究生

論文指導教授推薦書

物理學系/研究所 謝佳諭 研究生所提之論文

“在 CERN COMPASS 實驗組量測 190-GeV π 介子束流所產生 Drell-Yan 過程反應截面”係由本人指導撰述，同意提付審查。

指導教授 林宗泰 (簽章)

2021 年 7 月 15 日

104.07.24

National Central University

Advisor's Recommendation for Doctoral Students

This thesis titled "Measurement of the differential Drell–Yan cross sections with 190-GeV pion beams in the COMPASS Experiment at CERN" is written by Chia-Yu Hsieh (謝佳諭) from the graduate program in High-energy and gravitation under my supervision. I hereby recommend it for examination.

Advisor 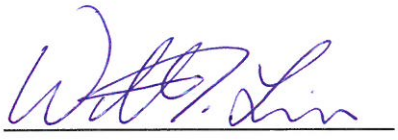

07, 15, 2021

1080618

國立中央大學博士班研究生
論 文 口 試 委 員 審 定 書

物理學系博士班 學系/研究所 謝佳諭 研究生

所提之論文 在 CERN COMPASS實驗組量測190-GeVπ介子束流所產生Drell-Yan過程反應截面

經由委員會審議，認定符合博士資格標準。

學位考試委員會召集人 _____

委　　員 林宗泰

_____

_____

_____

中　華　民　國　110　年　8　月　3　日

1100726

國立中央大學博士班研究生
論 文 口 試 委 員 審 定 書

物理學系博士班 學系/研究所 謝佳諭 研究生

所提之論文 在 CERN COMPASS實驗組量測190-GeVπ介子束流所產生Drell-Yan過程反應截面

經由委員會審議，認定符合博士資格標準。

學位考試委員會召集人 郭家銘

委　　員

中　華　民　國　110　年　8　月　3　日

1100726

國立中央大學博士班研究生
論 文 口 試 委 員 審 定 書

物理學系博士班 學系/研究所 謝佳諭 研究生

所提之論文 在 CERN COMPASS實驗組量測190-GeVπ介子束流所產生Drell-Yan過程反應截面

經由委員會審議，認定符合博士資格標準。

學位考試委員會召集人 _____

委　　員 _____

_____

_____

_____

_____

中　華　民　國　110　年　08　月　03　日

1100726

國立中央大學博士班研究生
論文口試委員審定書

物理學系博士班 學系/研究所 謝佳諭 研究生

所提之論文 在 CERN COMPASS實驗組量測190-GeVπ介子束流所產生Drell-Yan過程反應截面

經由委員會審議，認定符合博士資格標準。

學位考試委員會召集人 _____

委　　員 高崇文

_____

_____

_____

中　華　民　國　110　年　8　月　3　日

1100726

國立中央大學博士班研究生
論 文 口 試 委 員 審 定 書

物理學系博士班 學系/研究所 謝佳諭 研究生

所提之論文 在 CERN COMPASS實驗組量測190-GeVπ介子束流所產生Drell-Yan過程反應截面

經由委員會審議，認定符合博士資格標準。

學位考試委員會召集人 _____

委　　員 章文沃

_____

_____

_____

中　華　民　國　　年　　月　　日

1100726

國立中央大學博士班研究生
論文口試委員審定書

Jiunn-Wei Chen

物理學系博士班 學系/研究所 謝佳諭 研究生

所提之論文 在 CERN COMPASS實驗組量測190-GeVπ介子束流所產生Drell-Yan過程反應截面

經由委員會審議，認定符合博士資格標準。

學位考試委員會召集人 _____

委　　員 _____

Jiunn-Wei Chen 陳俊瑋

_____

_____

_____

中　華　民　國　　年　　月　　日

1100726

在CERN COMPASS實驗組量測190-GeV π介子束流所產生Drell-Yan過程反應截面

摘要

位於歐洲核子研究中心的COMPASS實驗組, 在2015年與2018年利用190十億電子伏特的π介子束碰撞三種物質極化鞍靶,鋁靶,以及鎢靶, 進行Drell-Yan過程的碰撞截面積量測。選取不變質量爲4.3GV-8.5GeV的雙渺子事件，本論文報告多維度的Drell-Yan碰撞截面積的分析方法和結果，事件分佈在費米變量從-0.1到0.9以及橫向動量0.0到3.6 GeV/c範圍。此量測結果將有助於決定π介子的部分子動量分布。COMPASS的實驗量測反應截面和量子色動力學的理論計算有很好的吻合度。在橫向動量平均分布方面的量測,COMPASS的實驗組的量測結果也與過去的實驗量測結果有一致性，可以用於決定π介子的內部節構。

Measurement of the differential Drell–Yan cross sections with 190-GeV pion beams in the COMPASS Experiment at CERN

Abstract

The COMPASS experiment at CERN performed measurements of Drell-Yan process using a 190-GeV negative pion beam scattering off a NH3 target and nuclear alumina and tungsten targets in 2015 and 2018. We present the results of differential cross sections of the dimuon events with the invariant mass between 4.5 and 8.5 GeV in the kinematic regions of x-Feynman from -0.1 to 0.9 and transverse momentum up to 3.6 GeV/c. Our results are valuable input for constraining the parton distribution functions (PDFs) of the pion. The measured differential cross sections are compared with the next-to-leading order QCD calculations with pion PDFs provided by JAM and xFitter groups and a reasonable agreement is observed. The result of the mean square of the transverse momentum versus the center-of-mass energy from COMPASS agrees with the measurements of the other pion-induced Drell-Yan experiments and constrains the intrinsic transverse momentum of pions.

Acknowledgments

It is a long journey of my phD study and finally it almost comes to the end. I am grateful to my family, especially my mother and my older brother. This journey could not reach to the end without their unconditional supports. I also would like to especially thanks to my advisors, Dr. Wen-Chen Chang and Dr. Willis T. Lin. They gave me a great assistance and a large degree of freedom so that I was able to enjoy the scientific research over the past years. I would like to express thanks to my colleagues, Dr. Yu-Shiang Lian and Dr. Vincent Andrieux for the huge help and many meaningful discussions in both the hardware and the analysis.

In the beginning of my research, I started with the development of the drift chamber, DC05. I received a significant assistance and gained new knowledge from the engineers, the professors and the students in Academia Sinica and COMPASS, Dr. Ming-Lee Chu, Dr. Chih-Hsun Kin, Dr. Ping-Kun Teng, Mr. Yu-Sheng Teng, Mr. Fuxiong Chang, Mr. Tobias Grussenmeyer, Mr. Didier Gerard Cotte, Dr. Alain Magnon, Dr. Robert Heitz, Dr. Yakov Petrovich Kulinich, Dr. IhnJea Choi, Dr. Caroline Riedl, Mr. Benjamin Moritz Veit, Dr. Igor Konorov, Dr. Johannes Bernhard, Dr. Matthias Grosse-Perdekamp, Dr. Yann Bedfer, Ms. April Michelle Townsend, and Mr. Gregory Mattson. Many thanks to them for the participation and helps. This project would not have been possible without the contributions of them.

In my research concerning the data analysis, I also cooperated with many kind and experienced COMPASS colleagues. I would like to acknowledge the aids from Dr. Catarina Quintans, Dr. Marcia Quaresma, Dr. Takahiro Sawada, Dr. Stephane Platchkov, Dr. Marco Meyer, Dr. Charles-Joseph Naim, Mr. Evgenii Mitrofanov.

There are good time and hard time during the past few years in my phD journey. I would like to thanks to the companies of my friends in climbing, hiking, and traveling activities we had enjoyed together, so that the pressure of the work could be released. Many thanks to Ms. Brendy Shih, Ms. Ping-Fang Wang, Ms. Yi-Hsuan Lee, Dr. Yi-Ting Duh, Dr. Lucien Lo, Dr. Doan Hien, Dr. Ting-Wei Liao, Mr. Jason Ling, and Dr. Greg Chen, and Mr. Dominik Steffen.

Thanks for my defense committees, Dr. A Chen, Dr. Chung-Wen Kao, Dr. Kao Chung-Wen, Dr. Jiunn-Wei Chen, Dr. Chia-Ming Kuo. The work was enhanced and fined tuned in the end by the valuable comments given by them.

Contents

List of Figures

List of Tables

List of Symbols

Variable	Description
P_π, P_N	4-momenta of the π^-, and of the target nucleon
P_{μ^+}, P_{μ^-}	4-momenta of the μ^+, and of the μ^-
$P = P_\pi + P_N$	4-momenta of hadronic system
$q = P_{\mu^+} + P_{\mu^-}$	4-momenta of virtual photon/dimuon system/partonic system
$s = P^2$	Center-of-mass energy of hadronic system
$Q^2 = q^2$	Energy square of virtual photon/dimuon system/partonic system
$M_{\mu\mu} \sim \sqrt{Q}$	Invariant mass of the dimuon
$\tau = M^2_{\mu\mu}/P^2 = x_\pi x_N$	Fraction of energy between hadronic system and dimuon
p_T	Transverse momentum of the virtual photon/dimuon system/parton system (with respect to the beam direction)
p_L	Longitudinal momentum of the virtual photon/dimuon system/parton system (with respect to the beam direction)
$x_\pi = [\ x_F + \sqrt{x_F^2 + 4\tau}]/2$	Momentum fraction of parton inside π^- (often refereed as x_1)
$x_N = [-x_F + \sqrt{x_F^2 + 4\tau}]/2$	Momentum fraction of parton inside nucleon target (often refereed as x_2)
$x_F = p_L/(\sqrt{s}/2) = x_\pi - x_N$	Feynman-x of the virtual photon/dimuon/quarkonium

Overview

Pion, as the lightest quantum charmodynamics(QCD) bound state was proposed by Hideki Yukawa in 1935. An important concept was suggested that π meson is the carrier responsible for the long-range nucleon-nucleon interaction. Besides, pion is also the Goldston boson of dynamical chiral symmetry break. It is important to understand the internal feature of pion. The internal parton distribution of pion - pion parton distribution, has been studied since 1980s, however the understand of it is still poorly know after 30 years. There are two popular processes are often applied in the extraction of pion parton distribution : Drell-Yan process sensitive to valence quark distribution and J/ψ process sensitive to gluon distribution. In this thesis, these two topics will be discussed:

1) The measurement of the cross-section of Drell-Yan process was performed in COMPASS experiment at CERN 10 2015 and 2018 with 190GeV pion beam and various targets, polarized ammonia targets, aluminum target, and tugstum target in COMPASS experiments. The pion-induced Drell-Yan data has not been updated for 20 years therefore COMPASS data will bring a new input to constrain the valence distribution of pion parton distribution function (PDF).

2) The global fit of long-distance parameterizations of the J/ψ production mechanism under non-relativity QCD framework is performed with fixed-target data from both pion and proton beams. The past studies were only done with the proton data either collision or fixed-target, however, the pion data is first included in this analysis. Furthermore, we investigate the sensitivity of gluon distribution of pion PDF with the new long-distance parameterizations of J/Ψ production mechanism.

Additionally, a certain amount of the phD program of mine was dedicated to the hardware service. One of the major detector in COMPASS, Drift-Chamber Number 5 (DC05), was built to replace an old straw tube chamber. It was a joint project participated by University of Illinois in US responsible for the construction of the chamber, and Acadamia Sinica in Taiwan built the electronics. This project started in 2012 and finished in 2016. DC05 serves in COMPASS from 2016 till now. The work of the development, construction, and the performance of DC05 will be described in this thesis.

The arrangement of the chapters in this thesis is as outlined below :

- Sec. 1 : The first part is the theoretical descriptions. The basic physics knowledge including standard model, QCD, and parton model are briefly introduced. The state-of-the-art of the study of Drell-Yan process, J/ψ process, and pion PDFs are illustrated next.

- Sec. 2 : The experimental setup of COMPASS experiment is introduced including the types of beam, target system, trigger system, and the spectrometer. The work of the hardware service of DC05 is discussed in this section.

- Sec. 3 : The measurement of pion-induced Drell-Yan cross-section with 2018 COMPASS data is presented in this section including the Monte-Carol simulation, the selection of data, the analysis method, finally the results compared with the passed measurements and the perturbative QCD calculation.

- Sec. 4 : The phenomenology study of J/ψ mechanism under NRQCD framework is given with the fixed-target of proton and pion beam. On top of that, the sensitivity of gluon distribution inside pion is explored with the new long-distance parameterizations of J/ψ production mechanism.

- Sec. 4.3 : The conclusion of this thesis and the outlook of the future work is summarized in the end.

Chapter 1

Theory

Drell-Yan process and J/ψ process are served as tools to constrain the the pion PDF. In order to understand them, the basic theoretical framework of Standard Model and QCD are first introduced. After that, the pion PDF is introduced. Finally, the production mechanism, the past experiments results, and the unsolved mysteries of Drell-Yan process and J/ψ process are stated at the end.

1.1 Quantum chromodynamics

Standard Model(SM) describes the fundamental forces carriers and classifies the elementary particles in the particle and nuclear physics. The elementary particles and force bosons are characterized by their Spin, Charge, Color, and the mass. The force carriers is called Bosons (spin integral) including gluon, photon, W boson and Z boson. Additionally, Higgs boson is a scalar Boson responsible for the the masses of all the other Bososns and elementary particles except for gluon and photon. The elementary particles are Fermions (spin half) including the quarks, electrons, muons, and neutrinos.

The quantum filed theory(QFT) provides the mathematical framework for Standard Model. The dynamics and kinematics of the QFT are derived from the Lagrangian with the assumption of the symmetries of the system. The groups SU(3)×SU(2)×U(1) gauge symmetries define the standard model. The three groups is roughly corresponding to the three fundamental interactions : SU(3) group provides the symmetries of the quantum chromodynamics(QCD), SU(2) group is related to the week interaction, U(1) group describes the quantum electromagnetic theory (QED). The number of gauge Bosons corresponds to the dimensions of the gauge group N^2-1 for SU(N) : 8 gauge Bosons (8 type of colors of gluon) for strong interaction SU(3), 3 gauge Bosons (W^+, W^-, and Z^0) for the week interaction SU(2), 1 gauge Bosons(γ) for electromagnetic interaction.

QED describes the interactions the between all the particles carry electric charges. Charged particles interact by the exchange of photons carrier the electromagnetic force. QCD describes the interactions between all the particles carries colors. Color particles interact by exchanges gluons carries the strong force. Quarks are of three possible colors : red, blue, green; the anti-quark are of the three anti-colors : anti-red, anti-blue, anti-green.

Quarks and anti-quarks compose hadrons in two categories : Byron and Meson. The stable hadrons must be colorless or called color white because of the color confinement feature of QCD discussed in the next section. For example, a stable Meson composed by one quark and one anti-quark($q\bar{q}$), like pion(π^-=$\bar{u}d$) and kaon($K^- = s\bar{u}$), is a possible color state of $r\bar{r}$, $b\bar{b}$, or $g\bar{g}$. A stable Byron composed by three quarks, like proton(uud)

and neutron(udd), is the color state of rbg.

Gluon also carries colors. The color states of gluon are described in Gell-Mann matrices which are the generators of SU(3) group :

$$g_i = \lambda_i \begin{pmatrix} r\bar{r} & r\bar{b} & r\bar{g} \\ b\bar{r} & b\bar{b} & b\bar{g} \\ g\bar{r} & g\bar{b} & g\bar{g} \end{pmatrix}, i = 1, 2, ..., 8$$

There are 9 possible combinations of the color states of gluons, which can be further categorized into color-singlet and color-octet states. Color-singlet state is called as colorless or color white state, which is mathematically analogous to a spin-singlet state expressed as :

$$(r\bar{r} + b\bar{b} + g\bar{g})/\sqrt{3}$$

However gluon in the color-singlet state is forbidden because of the confinement feature of QCD. The other eight color states are also known as color-octet state.

$$\begin{aligned} (r\bar{b} + b\bar{r})/\sqrt{2} \qquad & -i(r\bar{b} - b\bar{r})/\sqrt{2} \\ (r\bar{g} + g\bar{r})/\sqrt{2} \qquad & -i(r\bar{g} - g\bar{r})/\sqrt{2} \\ (b\bar{g} + g\bar{b})/\sqrt{2} \qquad & -i(b\bar{g} - g\bar{b})/\sqrt{2} \\ (r\bar{r} - b\bar{b})/\sqrt{2} \qquad & (r\bar{r} + b\bar{b} - 2g\bar{g})/\sqrt{3} \end{aligned}$$

Those 8 states are linear independent : as a results, the combination of any of those states won't reproduce another. The concept of color-singlet and color-octet also applies for the the quantum states of J/ψ meson ($c\bar{c}$) to be discussed in Sec.1.4.

Gluons carry colors therefore they interact with each other and quarks. This feature makes the strong interaction significantly complicated than electromagnetic interaction where photons have no charge so they do not interact with each other. The strong force grows stronger when the quarks and gluons within a bound state move away from each others so called confinement; in contrast, the strong interaction is weaker when they are approaching to each other, as said as asymptotic freedom.

The interaction potential of QCD is described as follows :

$$V_{QCD} = -\frac{4}{3}\frac{\alpha_s}{r} + kr$$

where r is the interaction distance, α_s is the coupling constant of QCD, k is the factor of string tension around $1GeV/fm$. QCD potential has two components. one is the short range potential in Coulomb-like term $-\frac{4}{3}\frac{\alpha_s}{r}$; the other is the long-range potential in linear-like term $+kr$.

The coupling constant in physics is a number to determines the strength of the force in an interaction. Event though 'constant' is in its name, it varies with the mass of the exchanged Boson in QCD. The coupling constant varies with the energy of the interaction, so called the running coupling constant as defined below :

$$\alpha_S(Q^2) = \frac{\alpha(\mu^2)}{1 + \beta_0\alpha(\mu^2)\log(\frac{Q^2}{\mu^2})} \ , \ \beta_0 = \frac{11N_c - 2N_f}{12\pi}$$

where μ is the normalization scale, N_f is the number fermion, N_c is number of color. To find the turning point where α_s becomes large than 1, and μ=Λ_{QCD} is chosen. The coupling constant α_s is described as follows :

$$\alpha_S(Q^2) = \frac{1}{\beta_0 \log \frac{Q^2}{\Lambda^2_{QCD}}}$$

- **Asymptotic freedom** : The potential of the strong interaction reduces while the color objects are getting closer. As a results α_S is small, the QCD processes are calculable. The perturbative QCD theory is built under large energy scale $Q > 0.2GeV$ and short distance$r < 1fm$. The dimension of hadrons is smaller than the QCD scale, therefore the quarks inside the hadrons can be seen as the free particle due to the very small interaction between them.

- **Color confinement** : The potential of the strong interaction grows while the color objects are separating. The energy generated during the separation turns into quark-antiquark pairs, then further turning into jets, then in the end the forming the colorless hadrons. This process is known as fragmentation. As the fragmentation occurs when α_s is large, therefore the calculation in higher order involved with many gluons are not converged. The fragmentation can not be calculated by perturbative QCD. The parameterization of it has to be done through the experimental measurement.

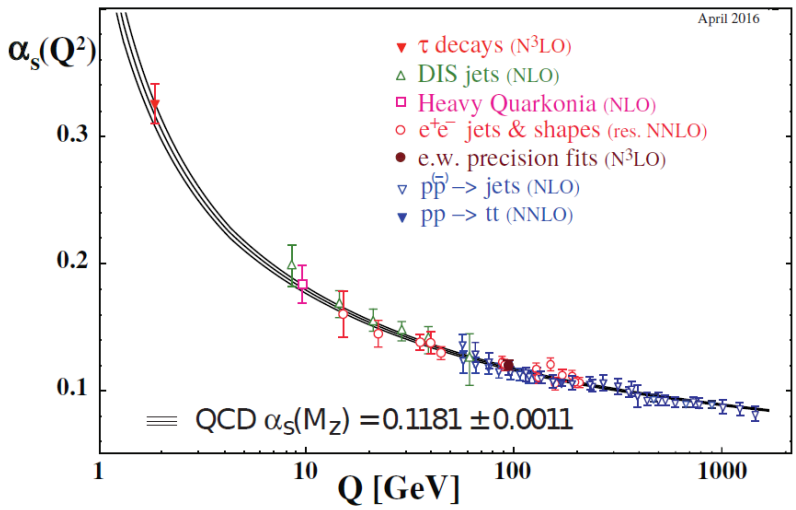

Figure 1.1: *The measurements of α_S as function of the energy scale Q from different measurements summarized by PDG [1].*

1.2 Parton distribution function

1.2.1 Parton model

Parton model was proposed by Richard Feynman in 1968. A hadron is considered as a composition of a number of point-like constituents, so called "partons". Partons are referred today as quarks and gluons. A quantity "Bjorken-x" is proposed by Bjorken to define the momentum fraction of partons inside hadron. Bjorken-x is defined in the infinity momentum frame, along with longitudinal momentum of hadron. The transverse momentum of hadron is ignored under the infinity momentum frame. Bjorken-x, as a dimensionless variable, is formulated as below :

$$x = \frac{P_q}{P_h}$$

where x is Bjorken-x, P_q is the parton momentum and P_h is the hadron momentum in the infinity momentum frame.

The idea of parton model is used to describe the inner structure of hadrons. The probability finding the valance quark, gluon, and sea quark as function of their Bjorken-x inside hadron are called the parton distribution function (PDF). Among all the hadrons, proton PDF is the one studied the most because of the high statistics from both fixed-target data worldwide using proton target(nucleus) and collider data e.g from LHC experiments using proton beam. As for pion PDF, it is still not well understood due to the limited data sets. The difficulty of performing the experiments using pion is that there is no stable pion target unlike proton target, only pion beam available. The fixed-target experiment with pion beam and nucleus is the main tool to probe the pion PDF. There are not many experimental facilities available. In the next two sections, the proton PDF is described first, afterwards the pion PDF is explicitly discussed in more details.

1.2.2 Parton distribution function of proton

Deep Inelastic Scattering(DIS) is traditionally applied to study the inner structure of proton. In Fig. 1.2, it shows the Feynman diagram of DIS process where a lepton scatters on a hadron with the exchange of a virtual photon $\gamma*$. A parton is struck out of the hadron through DIS, also the rest part of hadron breaks into the secondary hadrons. The cross-section of DIS is formulated below based on the parton model and QED :

$$\frac{d^2\sigma}{dxdQ^2} = \frac{4\pi\alpha_{em}}{Q^4}[(1-y)\frac{F_2(x,Q^2)}{x} + y^2F_1(x,Q^2)]$$

where Q^2 is the 4-momentum square of virtual photon, x is the the momentum fraction of parton inside the hadron, α_{em} is the coupling constant of electromagnetic force $\sim 1/137$, y is the rapidity, $F_1(x,Q^2)$ and $F_2(x,Q^2)$ are the structure functions of hadron as function of Bjorken-x and Q^2.

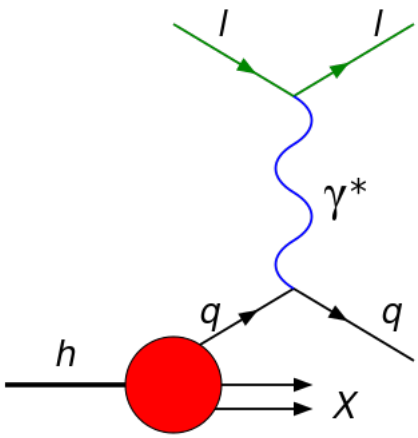

Figure 1.2: *Deep Inelastic Scattering(DIS) demonstrates a lepton (l) scatters on a hadron (h). A virtual photon ($\gamma*$) knocks a quark (q) out of the hadron. And the rest part of hadron breaks into the secondary hadrons (X).*

$F_1(x, Q^2)$ and $F_1(x, Q^2)$ were first measured in SLAC with 20GeV electron beam collides with proton target (nucleus). The results shows that $F_1(x, Q^2)$ and $F_1(x, Q^2)$ do not vary with an increase of the probing energy of photon Q. This phenomena is so called scaling. The observation of the scaling in the structure function suggests the point-like components inside the proton. Actually the parton model proposed by Feynman came after the energy scaling observation of DIS experiments. Also, if the proton is formed by the spin-1/2 quarks, the relation of $F_2(x) = 2xF_1(x)$ was validated in DIS measurements.

However, when the probing energy of lepton was beyond 20 GeV as the time passed by, the violation of energy scaling effect started to show with the increase of the probing energy of lepton. In Fig. 1.3 shows the DIS cross section at DESY, Germany using electron beam scattered with proton target [2]. When the probing energy Q in the range of 10 to 100 GeV and Bjorken-x in the range of 0.4 to 0.032 (shown in the black-square dots), the scaling effect is observed. Nevertheless, the violation of energy scaling starts to show when the measured kinematic range beyond the probing energy Q and Bjorken-x just mentioned. Later people realized the reason is that the higher probing energy means higher resolution of the proton structure. Proton structure can't be simply explained by the composition of three-free-valance quarks but even finer and more dynamic structure including gluon and sea quark activities involved.

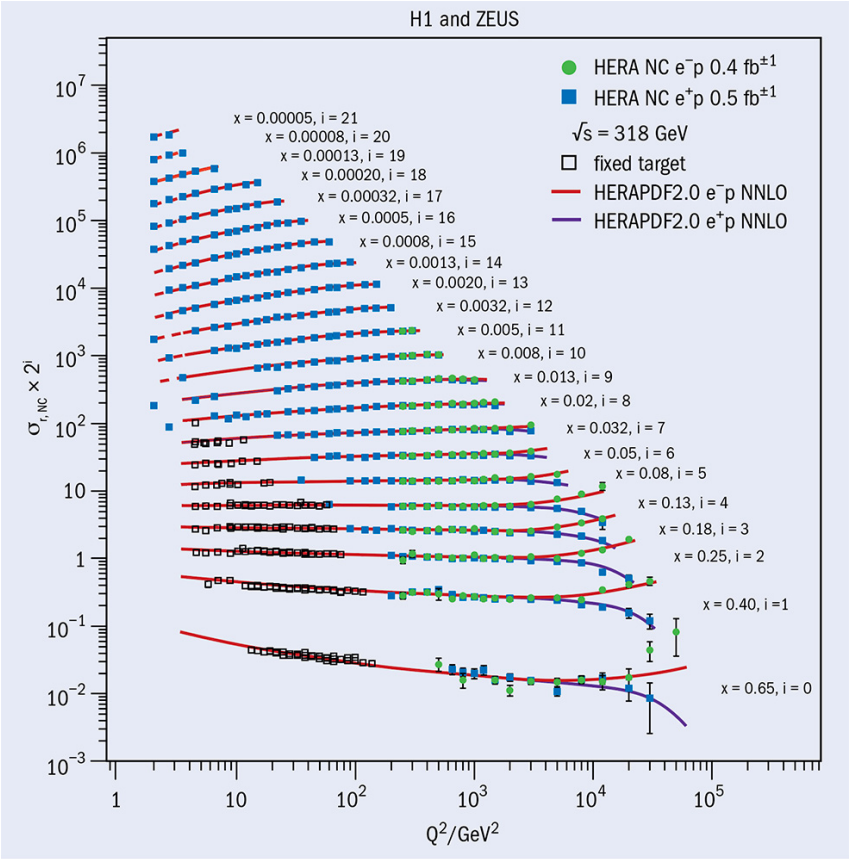

Figure 1.3: *The ep DIS corss-section results obtained from HERA [2] as function of the probing energy Q and Bjorken-x.*

Proton parton distribution of proton, the probability finding valance quark, gluon, and sea quark as function of the interaction energy Q and Bjorken-x, nowadays is decided through the global fits on numerous cross section data from different physics processes in a wide coverage of interaction energy Q^2 and Bjorken-x. Except for DIS process, data of the pp collision , the pN collision, etc, are all used. The common procedure to extract proton PDF from the global data is as follows : (1) Parameterising the parton distribution of valance quark, gluon and sea quarks on Bjorken-x at low Q^2 around 10 GeV based on QCD framework below which the incalculable terms of non-pQCD are negligible, (2) Evolving the parameterising proton PDFs with Q^2 through Dokshitzer–Gribov–Lipatov–Altarelli–Parisi(DGLAP) equation to have Q-evaluated PDFs, (3) The proton PDFs and the factorization theories combined allow one to predict the cross-section and determine the the parameters as fit variables. There are many different groups perform the global fits, such as CT14 [3] and NNPDF [4], etc. Different groups have their own choice of the data sets and parameterization of the PDFs. Fig. 1.4 [4] shows the proton PDF extracted by NNPDF group at $Q^2 = 10\ GeV^2$ and $Q^2 = 10^4\ GeV^2$. In the low energy, $Q^2 = 10\ GeV^2$, the momentum of hadron is mainly carried by valance quarks, the momentum fraction of u quark and d quark are around 0.6 and 0.3 of proton, respectively. With the increase of the probing energy $Q^2 = 10^4\ GeV^2$, the contribution from gluon and sea quarks increase.

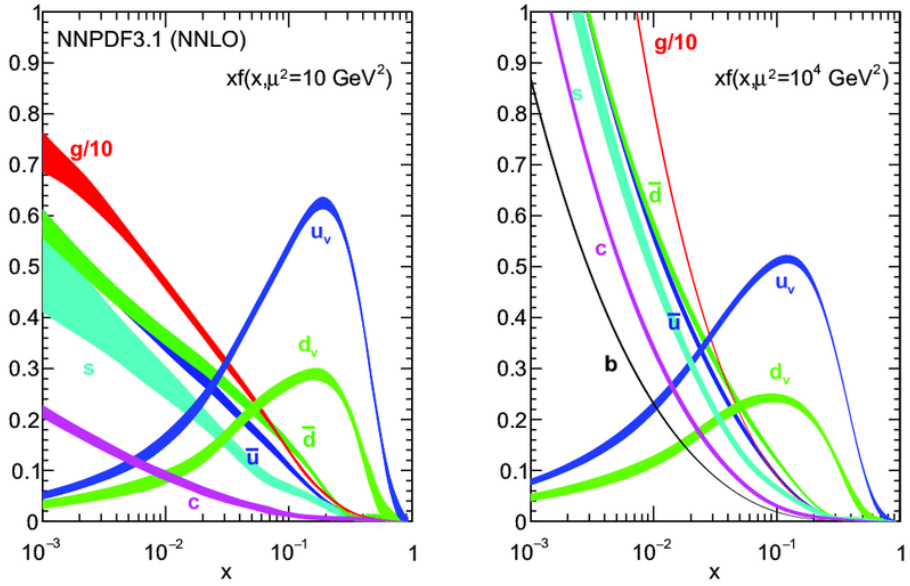

Figure 1.4: *The proton PDFs at (left) Q^2=10GeV^2 (Q labeled as μ is the figures) and (right) 10^4 GeV^2 from NNLO QCD fits of the global data from NNPDF group [4]. (left) At low probing energy $Q^2 = 10$ GeV^2 , the averaged momentum carries by u quark is around 0.6 and d quark around 0.3; (right) At high probing energy $Q^2 = 10^4$ GeV^2, the contribution from sea quark and gluon increases so the momentum for u quark and d quark reduce.*

1.2.3 Parton distribution function of pion

Pion is the lightest QCD bound state consists, and has three states : $\pi^+(u\bar{d})$, $\pi^-(\bar{u}d)$, $\pi^0(u\bar{u}$ *or* $d\bar{d})$. In 1935, Hideki Yukawa proposed that π meson is the carrier responsible for the long-range nucleon-nucleon interaction. Besides, pion is also the Goldston boson of dynamical chiral symmetry break. It is important to understand the internal feature of pion. Furthermore, the contrast of the partonic structures between protons and pions [6] in terms of the gluon density distribution is importance in understanding the phenomenon of hadronic mass [7].

There are good progress of the theoretical developments on the calculation of the pion structure in the recent years including Nambu-Jona-Lasinio model [8], Dyson-Schwinger equations (DSE) [9], etc. The most interesting breakthrough is the first-principle calculations of partonic structures of hadrons in lattice QCD [10].

The pion PDFs are extracted from the processes generated with pion beam collides with rest nucleus target, such as Drell-Yan production, J/ψ production, Prompt-γ production. Recently, the Leading Neutron Deep Inelastic Scattering (LN-DIS) data from ep scattering of HERA experiment was first used in the global analysis of pion PDFs.

Table. 1.1 shows a list of pion PDF sets from the global fit and their features. Before 2000, the global analysis of the pion PDF were mostly from QCD analyses of Drell-Yan, J/ψ, and prompt photon production data including pion PDF sets, such as Owens(OW) [11], Aurenche–Baier– Fontannaz–Kienzle-Focacci–Werlen(ABFKW) [12], Sutton- Martin-Roberts-Stirling(SMRS) [15], Gluck-Reya-Vogt(GRV) [13], Gluck-Reya-Schienbein(GRS) [14]. OW and ABFKW are the two oldest pion PDFs proposed in 1984 and 1989, respectively. SMRS and GRV are the ones used often proposed both in 1992. GRS is the extended study with respect to GRV published in 1999. Pion PDFs were not

updated for nearly 20 years and the reason is that there is no updated of pion-induced data since after E615 data published in 1989. Jefferson lab Angular Momentum (JAM) [16] collaboration used the LN-DIS *ep* scattering data from HERA [17] to extract a new Pion PDF set. For the first time, the data sets other than the pion-induced data apply to the global analysis of the pion PDFs. Since then, the interest of pion PDF is raised again. New PDF set, xFitter [18] use, was published only last year in 2020. xFitter uses same data set as GRV, GRS and SMRS, but with different approach. Most of the PDFs are analyzed under the frameworks of pQCD calculation in NLO and QCD-evolution based on DGLAP equation except for OW. OW is obtained in the LO of pQCD calculation.

Table 1.1: *Pion PDF sets available before 2021. Most of the PDFs are analyzed under the frameworks of perturbation QCD(pQCD) calculation in NLO and Q-evolution except for OW was in LO of pQCD calculation and there is no Q-evalution of it.*

PDF	Year	pQCD Cal.	QCD-evl.	Ref.
OW	1984	LO	Yes	[11]
ABFKW	1989	NLO	Yes	[12]
SMRS	1992	NLO	Yes	[15]
GRV/GRS	1992/1999	NLO	Yes	[13]/ [14]
JAM	2018	NLO	Yes	[16]
xFitter	2020	NLO	Yes	[18]

PDF	Data Useed			
	Pion-induced Drell-Yan	Pion-induced J/ψ	Pion-induced prompt-γ	LN-DIS
OW	NA3, WA39	NA3, E537	-	-
ABFKW	NA3, NA10, E537, E615	NA3, E537	WA70, NA24	-
SMRS	NA10, E615	-	WA70	-
GRV/GRS	NA10, E615	-	WA70	-
JAM	NA10, E615	-	-	HERA
xFitter	NA10, E615	-	WA70	-

There are four kinds of data used in the global fits of pion PDFs : Drell-Yan process from $\pi^- N$ scattering(N represent nucleus target), J/ψ from from $\pi^- N$ scattering, prompt-γ from from $\pi^- N$ scattering, and LN-DIS from *ep* scattering. The general descriptions of these four processed are given below :

- **Pion-induced Drell-Yan process** ($\pi^{\pm} p \to \mu^+ \mu^- X$) : The Feynman diagram of Drell-Yan process at leading order(LO) is drawn in Fig. 1.5 : $q\bar{q} \to \gamma^* \to l\bar{l}$. It was proposed by Sidney D. Drell and Tung-Mow Yan in 1970 [19]. Drell-Yan process is the production of lepton–antilepton pairs via a virtual photon or Z boson when a quark(/anti-quark) of pion and an antiquark(/quark) of a nuclear target annihilate.

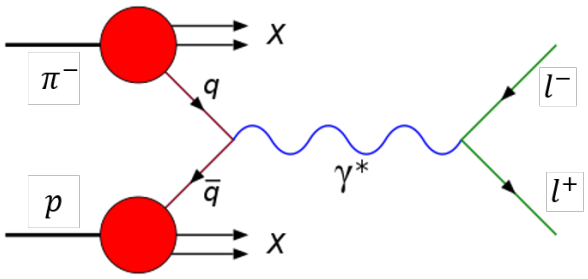

Figure 1.5: *Feynman diagram of Drell-Yan process in LO from $\pi^{\pm}p$ scattering : $q\bar{q} \rightarrow \gamma^* \rightarrow l^+l^-$.*

The leading-order Drell-Yan process shows that pion-induced Drell-Yan cross section is sensitive to the valance quark content in pion. There were many experiments performing the measurements of pion-induced Drell-Yan measurements 20 years ago, but no new data available afterwards. COMPASS experiment performed pion-induced Drell-Yan measurements in 2015 and 2018. One of the main topic of this thesis is to present the results of the Drell-Yan cross section with COMPASS 2018 data. It will provide a new input to the analysis of pion PDFs. More theoretical studies concerning Drell-Yan mechanism are described in Sec. 1.3. The data analysis of Drell-Yan cross-section measurement with COMPASS 2018 data is described in Sec. 3.

- J/ψ **process** ($\pi^{\pm}p \rightarrow J/\psi\ X$) : J/ψ resonance was discovered is 1974. The two experimental groups lead by Burton Richter and Samuel Ting were awarded the 1976 Nobel Prize in Physics due to this work. This important discovery is well-known as "November Resolution" because it was the first discovery of quark-antiquark bound state predicted by quark models proposed by Glashow, Iliopoulos and Maiani (GIM). Since then, a series of particles predicted by quark model were discovered and improved our understanding of the strong interaction. J/ψ is composed by one charm and one anticharm quark in the quark model. In Fig. 1.6, the LO contributions of J/ψ cross section are shown. There are two processes, one is the quark-antiquark annihilation $q\bar{q} \rightarrow c\bar{c} \rightarrow J/\psi\ X$, and another one is the gluon fusion $gg \rightarrow c\bar{c} \rightarrow J/\psi\ X$. J/ψ production at LO is sensitive to gluon distribution inside pion. Pion PDF sets in the early stages, OW and ABFKW, used pion-induced J/ψ data to extract gluon PDF. The advantage of using pion-induced J/ψ data for pion PDF global analysis is that the production cross-section is high. However, the J/ψ production mechanism (charmonium production) still remaining unclear even though it is discovered over 3 decades, therefore the gluon constraining using J/ψ data is associated with uncertainty. In this thesis, the charmonium-production will be further elaborated in Sec. 1.4 and the phenomenology study of the charmonium-production is performed and shown in Sec. 4.

- **Prompt-γ process** ($\pi^{\pm}p \rightarrow \gamma X$) : The Feynman diagram of prompt-γ production in LO from πp scattering is shown in Fig. 1.7. There are two processes : one is the quark-gluon Compton scattering $qg \rightarrow \gamma q$ and another one is the quark-antiquark annihilation $q\bar{q} \rightarrow \gamma g$. The prompt-$\gamma$ data is sensitive to both gluon PDF of pion. Most of pion PDF sets, ABFKW, SMRS, GRV, GRS, xFitter, are using prompt-γ data from WA70 to constrain the gluon distribution inside pion. However, the

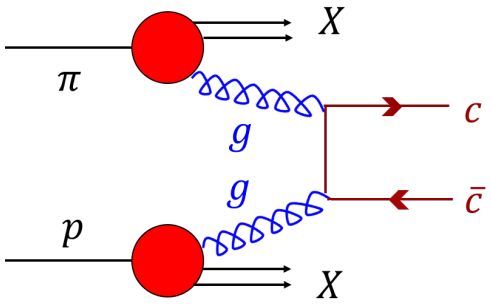

Figure 1.6: *The Feynman diagrams of J/ψ production at LO from $\pi^{\pm}p$ scattering.*

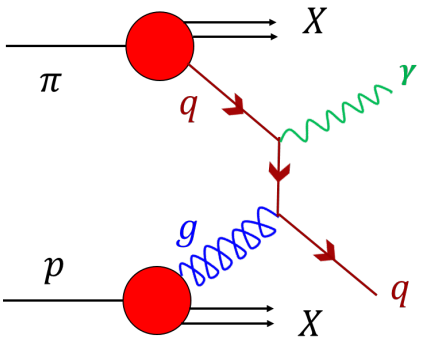

Figure 1.7: *The Feynman diagrams of prompt-γ at LO from $\pi^{\pm}p$ scattering.*

difficulty of the pion-induced prompt-γ experiment is that the background γ signals from the secondary π^0 decay is hard to be distinguished from the direct photon production [18].

- **Leading Neutron Deep Inelastic Scattering (LN-DIS)** $(ep \to nX)$: JAM collaboration was the first group to include LN-DIS data in the global analysis of pion PDF. Fig. 1.8 shows the Feynman diagram of LN-DIS process. It is a DIS experiment with ep scattering. Electron scatters with the pion cloud of the proton thus a neuron is knocked out of the proton. The idea of considering pion cloud in the pion PDF analysis is fresh and give also a better resolution of pion PDFs in low Feymann x region, $x_\pi < 0.2$ which are lack of in the pion-induced Drell-Yan data. The improved resolution of valance quark of pion PDFs in the low-x region also helps to better constrain the gluon and sea distributions. The reason is explained as follow.

  The common approach in the global fit of pion PDFs is to first constrain valance distribution with Drell-Yan data, then the gluon distribution with J/ψ and prompt-γ data, and in the end constrain sea distribution by the momentum sum rule. The general issue from the past global analysis is that the statistics of Drell-Yan data is low in $x_\pi < 0.2$. This bring large impact to the constrain of gluon and sea distributions because they are mainly dominated in the low x_π region. Furthermore, the two processes to constrain the gluon distribution, pion-induced J/ψ production suffers from the model-dependent theorem in charmonion production. The gluon PDF of pion is not as well constrained as valance PDF. The uncertainty of sea distribution and gluon distributions are still large till nowadays. To overcome this problem, the new idea from JAM group uses LN-DIS data from HERA to gain the constrain power in low x region down to 10^{-3} with high statistics.

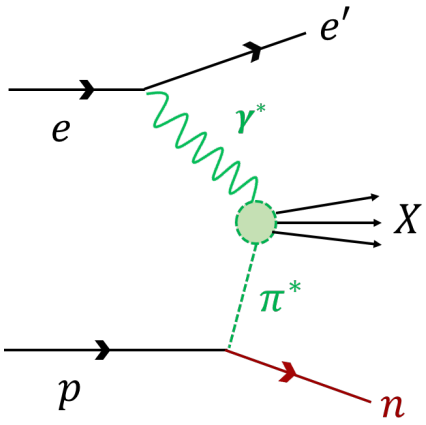

Figure 1.8: *The Feynman graphs for LN-DIS from ep scattering. Electron scatters with the pion cloud of the proton thus a neuron is knocked out of the proton.*

In Ref. [20], it gives the the valance distribution, sea distribution, and gluon distribution inside pion from all the pion PDF sets at Q^2 =9.6 GeV^2 shown in Fig.1.10. The left-hand-sided plot shows the pion PDFs (the probabilities of finding valance, gluon and sea along Bjorken-x) and the right-handed-side plot shows their distributions compared to GRV PDF. The first thing to notice is that only the new PDF Sets, JAM and xFitter, provides the uncertainty band. Second, the valance distribution is dominated in middle x_π region around 0.5. The gluon distribution is dominated in low x_π region. The contribution from sea is low compared to valance quark and gluon. The discussions on valance PDF, gluon PDF, and sea PDF are given below :

- **Valance distributions** : Fig.1.10(a), it shows the valance distributions of all the pion PDF sets on the left and its comparison to GRV on the right. From observation of the ratios to GRV, one notice that SMRS, JAM, and xFitter have similar distributions and higher magnitude in valance compared to the GRV and OW distribution up to 20%–30%. Considering the uncertainty band given by JAM and xFitter, three PDF sets, SMRS, JAM, xFitter are consistent. OW gives a slower fall-down shape in high x_π region compare to the others. The shape of valance distribution in high x_π region has been discussed heavily in the recent years. The parameterization of the valance distribution of pion in pQCD NLO level is formulated as follows :

$$v_{\pi^-}(x_{\pi^-}) = A^v x^\alpha (1-x)^\beta (1+\gamma x^\delta) \tag{1.1}$$

The behavior of valance PDF in high x_π region ($x_\pi \to 1$) is controlled by the parameter, β. E615 collaboration [21], NA10 collaboration [22], NA3 collaboration [23], GRV [13], SMRS [15], and Nambu-Jona-Lasinio models [24] all favor $(1-x_\pi)^1$. While Dyson-Schwinger equations(DSE) [25] and NLL [26] obtain $(1-x_\pi)^2$ because they consider the soft-gluon resummation in high x_π. Fig. 1.9 [25] shows the comparison of valance distribution predicted by GRV, SMRS, DSE, and NLL. In this figure, "fit 3" and [8] are the results from NLL and DSE, and they got the same trend in high x_π, $(1-x_\pi)^2$; while, GRV and SMRS gave the trend $(1-x_\pi)^1$.

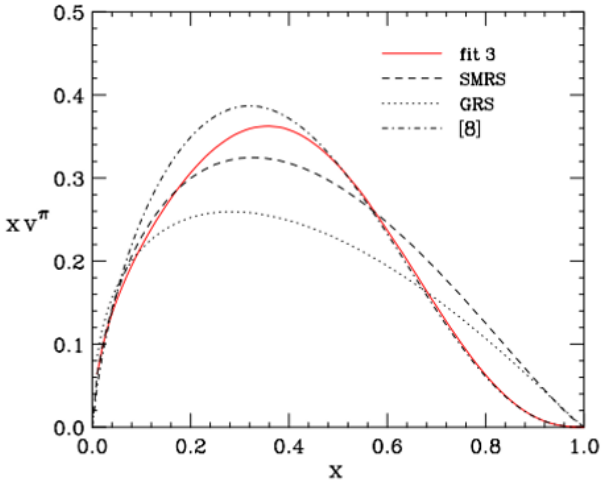

Figure 1.9: *The comparison of valance distribution of Pion predicted from different groups. "fit 3" and [8] are the results from NLL and DSE. GRV and SMRS have the trend* $(1-x_\pi)^1$ *in* $x \to 1$ *while DSE and NLL favor in* $(1-x_\pi)^2$ *[25].*

In the paper of xFitter [18], the comments of $(1-x_\pi)^\beta$ behavior was made. They conclude that there are still some ambiguities to compare valance distribution in $x_\pi \to 1$ from different fits and different models. The reasons are as follows :

- The measurement of cross section in x_π region experimentally is difficult because the statistics rapidly decrease toward high x_π. The reliability of the measurements in high x_π region is vulnerable.
- Theoretically, the uncertainty of pQCD calculation in NLO increased when $x_\pi \to 1$. However, except for JAM and xFitter, the rest of the extractions and predictions do not give uncertainty.
- Valance distribution is not an experimental observable. The extracted results are schemes dependent.

Due to all these reasons, it is too early to judge the goodness between $\beta \sim 1$ and $\beta \sim 2$.

- **Sea distributions** : In Fig.1.10(b), it shows the sea distributions of all the pion PDF sets on the left and its comparison to GRV on the right. The contamination of sea quark in pion drop fast and close to zero at x_π=0.6. This is the reason why the experimental data in low x_π is important to constrain sea quark. On average, sea quarks carry the smallest momentum inside pion. Among all the PDF sets, GRV and xFitter gave different shape compared to the others : GRV is lower than the others and xFitter is higher than the others. The uncertainty band JAM and xFitter are large. It also shows that the sea distribution inside pion is far from certain. There is a suggestion of performing the Drell-Yan measurement with π^+ and π^- beams on the iscoscalar deuterium to better constrain the sea distribution [27].

- **Gluon distributions** : In Fig.1.10(c), it shows the gluon distributions of all the pion PDF sets on the left and their ratios to GRV on the right. OW, ABFKW, SMRS, and GRV have relatively large gluon contamination in the range of $x_{pi} >$ 0.1 compared to the recent pion PDFs, xFitter and JAM PDFs. Considering the

uncertainty band, the distribution of JAM and xFitter are consistent. On average, the gluon composition inside pion is higher for OW, ABFKW, SMRS, and GRV compare to JAM and xFitter. In Ref. [20], the authors use J/ψ data from pion-induced pion and proton experiments combine with the color evaporation model (one of the model for charmonium production) to study the current pion PDFs. They concludes the current J/ψ data from pion-induced pion and proton experiments favors SMRS, and GRV sets other than JAM and xFitter.

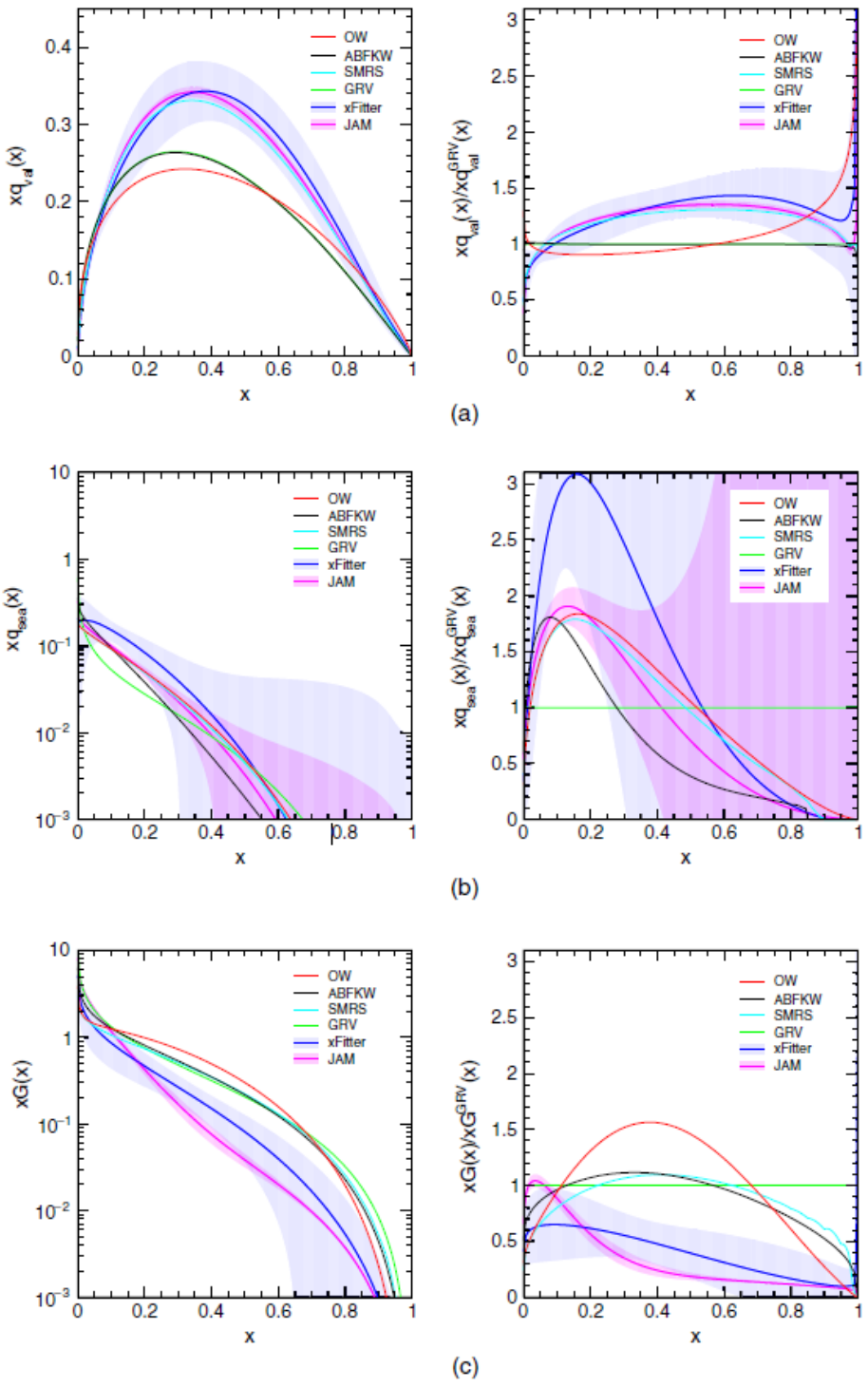

Figure 1.10: *(Right) The pion PDFs of OW, ABFKW, SMRS, GRV, JAM, and xFitter at the scale of J/ψ mass (Q^2 =9.6 GeV^2) : (a) valence quark distributions, (b) sea quarks distributions, and (c) gluon distributions. (Left) The absolute value. (Left) The distributions of various pion PDFs compares to GRV [20].*

There are still many unsolved problems for pion PDFs. The Drell-Yan cross-section measured by COMPASS could helps to resolve them.

1.3 Drell-Yan process

1.3.1 Introduction

Drell-Yan process was first discovered in Brookhaven National Laboratory(BNL) by Columbia-Fermilab-Stony Brook(CFS) collaboration leaded by L. Lederman measured the μ^+ $\mu-$ pairs produced by 28.5GeV proton beam collided with uranium target in 1970s. The differential cross section as a function of the invariant mass of dimuon reported is shown in Fig. 1.11 [28]. The structure of the distribution is composed by two parts : (1) a rapid fall of production cross-section with a increase of dimuon mass. (2) a shoulder founded around mass at 3 GeV. At that time, this mass spectrum was puzzled, but later it was understood. The rapid fall part is the Drell-Yan process and the shoulder part is the famous J/ψ particle. These two process are both important tools to probe hadron PDFs and provide the fundamental test of QCD. In this section, the Drell-Yan process will be introduced and the J/ψ production will be discussed in the next section, Sec. 1.4.

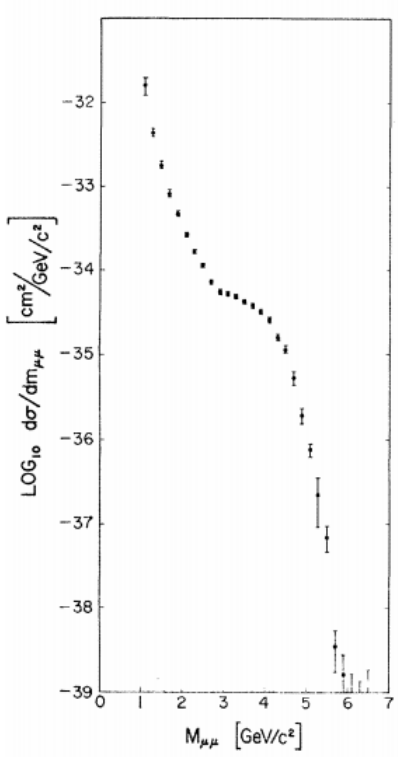

Figure 1.11: *The differential cross section as function of the invariant mass of dimuon pair reported by the group L. Lederman leaded. A rapid-fall cross section as function of mass was later discovered as the Drell-Yan process. The shoulder around 3 GeV was discovered as J/ψ, the most common bound state of charmonium production [28].*

1.3.2 Mechanism of naïve Drell-Yan model

The mechanism of the rapid-falling distribution was proposed and named after Sidney D. Drell and Tung-Mow Yan, so called Drell-Yan process [19]. The Feynman diagram of this process is drawn in Fig. 1.12 : $h_A + h_B \rightarrow \mu^+ + \mu^- + X$. Based on the parton model and QED theorem, they describe the production of lepton–antilepton pairs via a virtual photon or Z boson when a quark and an antiquark from two hadrons annihilate.

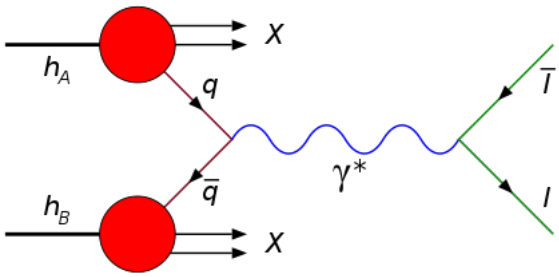

Figure 1.12: *Feynman diagram of Drell-Yan process at LO: $q\bar{q} \rightarrow \gamma^* \rightarrow l^+l^-$. It describes the production of lepton–antilepton pairs via a virtual photon or Z boson when a quark and an antiquark annihilate.*

Based on the theory proposed by Bjorken, the 4-momentum of the quark and antiquark are fraction of the 4-momentum of the the hadrons:

$$P_q = x_A P_{h_A} \tag{1.2}$$

$$P_{\bar{q}} = x_B P_{h_B} \tag{1.3}$$

The 4-momentum of the virtual photon $q*$ with a large energy is defined as follows :

$$q* = P_q + P_{\bar{q}} = P_l + P_{l'} \tag{1.4}$$

The charge, momentum, energy, angular momentum are conserved between the quark system(quark-antiquark), the virtual photon, and the dilepton system. The detection of dimuon pair properties can be used to study the physics of quark system.

The invariant mass of dimuon pair is the same as the energy of virtual photon :

$$q*^2 = Q^2 = M^2_{ll'} = (P_l + P_{l'})^2 \tag{1.5}$$

A variable, τ, is defined as the fraction of energy transferred from the incoming hadron system and the outgoing dilepton system :

$$\tau = \frac{M^2_{ll'}}{s} \ , \quad and \quad s = (P_{h_A} + P_{\bar{h_B}})^2 \tag{1.6}$$

τ is a dimensionless variable and it is also often used as an normalized variable when comparing the results from the experiments with different probing energy.

In center-of-mass(CM) frame of hadron system, the momentum of two colliding hadrons are $\frac{\sqrt{s}}{2}$ and $-\frac{\sqrt{s}}{2}$. The 4-momentum ($\vec{p}$, E) of hadrons and quarks are defined as :

$$P_{hA} = \frac{\sqrt{s}}{2}(1,1), \quad P_{hB} = \frac{\sqrt{s}}{2}(-1,1) \tag{1.7}$$

$$P_q = x_A\frac{\sqrt{s}}{2}(1,1), \quad P_{\bar{q}} = x_B\frac{\sqrt{s}}{2}(-1,1) \tag{1.8}$$

Note that in the naïve Drell-Yan model, the transverse momentum is neglected, therefore only the momentum along the momentum of hadron system is shown.

The 4-momentum of quark system (or dimuon system, or virtual photon)is given as follows :

$$(p_l, E) = P_q + P_{\bar{q}} = P_l + P_{l'} \tag{1.9}$$

$$p_l = (x_A - x_B)\frac{\sqrt{s}}{2} \tag{1.10}$$

$$E = (x_A + x_B)\frac{\sqrt{s}}{2} \tag{1.11}$$

The dilepton mass square and the dimensionless energy-scaling factor τ can be expressed in Bjorken variables :

$$M^2_{ll'} = E^2 - p_l^2 = s\ x_A x_B \tag{1.12}$$

$$\tau = \frac{M^2_{ll'}}{s} = x_A x_B \tag{1.13}$$

The Feynman variable x_F is defined as the longitudinal momentum of dimuon pair divided by the maximum possible longitudinal momentum which is hadron momentum $(\sqrt{s}/2)$:

$$x_F = \frac{2p_l}{\sqrt{s}} = x_A - x_B \tag{1.14}$$

In the fixed-target experiment, x_F is used to quantify the fraction of longitudinal momentum of dimuon pair from the beam. There is another variable, rapidity y, plays a similar role, which is often used in collider experiment. The definition of rapidity is defined as follow.

$$y = \frac{1}{2} ln \frac{E + p_l}{E - p_l} \tag{1.15}$$

If the longitudinal momentum of dilepton is the same as the energy of the hadron system($E \sim p_l$), it leads to $y \to \infty$. On the other hand, the rapidity is close to zero when the longitudinal momentum of dilepton is zero($p_l = 0$).

The Bjorken variables can be expressed by x_F and τ as follows:

$$x_A = \frac{1}{2}[\sqrt{x_F^2 + 4\tau} + x_F] \tag{1.16}$$

$$x_B = \frac{1}{2}[\sqrt{x_F^2 + 4\tau} - x_F] \tag{1.17}$$

x_A and x_B are not experimental observables. This formulation gives the way to access x_A and x_B from the two measurable variables, x_F and τ.

1.3.3 Experimental overview of Drell-Yan measurements

It is usually a proton-proton collision or a hadron beam (π, K, proton, antiproton) collides with a fixed nucleus target. Following by the target, a thick and heavy material is set to absorb all the secondary hadrons(X). Due to the heavy absorbor, only leptons are left in the end of detection.

Table 1.2: *Table of the Drell-Yan experiments. This table is compiled based on the information collected by these two very nice papers [29] [30].*

Exp.	E_{beam} (GeV)	$\sqrt{s}$ (GeV)	target	$M_{ll'}$ (GeV)	x_F
$p\ p \rightarrow e^+\ e^-\ X$					(pp collision)
CERN-R108(1979) [31]	-	62.4	-	>6.5	-0.2 - 0.2
CERN-R808(1980) [32]	-	53, 63	-	4.5 - 18.	-0.2 - 0.2
$\bar{p}$ *nucleus* $\rightarrow e^+\ e^-\ X$					(pp collision)
CERN-UA2(1992) [33]	-	630	-	10 - 70	-
$p\ p \rightarrow \mu^+\ \mu^-\ X$					(pp collision)
CERN-R209(1981) [34]	-	44, 62	-	5.0 - 20	-0.1 - 0.5
$\bar{p}$ *nucleus* $\rightarrow \mu^+\ \mu^-\ X$					(fixed-target)
FNAL-E537(1988) [35]	125	15.3	W	4.0 - 9.0	0.0 - 1.0
$K^{\pm}$ *nucleus* $\rightarrow \mu^+\ \mu^-\ X$					(fixed-target)
CERN-NA3(1985) [23]	400	27.4	Pt	4.0 - 8.5	0.0 - 1.0
CERN-WA39(1980) [36]	39.5	8.6	W	2.0 - 6.0	-0.4 - 1.0
p *nucleus* $\rightarrow \mu^+\ \mu^-\ X$					(fixed-target)
FNAL-E288(1981) [37]	200, 300, 400	19.4, 23.7, 27.4	Pt, Cu	4.0 - 18.0	-0.1 - 0.4
FNAL-E325(1979) [38]	200, 300, 400	19.4, 23.7, 27.4	Cu	7.0 - 11.0	∼0
FNAL-E444(1979) [39]	225	20.5	C, Cu, W	2.0 - 8.5	0.0 - 1.0
FNAL-E439(1981) [40]	400	27.4	W	1.5 - 15.0	-0.2 - 1.0
CERN-NA3 (1985) [23]	400	27.4	Pt	4.0 - 8.5	0.0 - 1.0
FNAL-E605(1991) [41]	800	38.7	Cu	7.0 - 18.0	-0.3 - 0.3
FNAL-E772(1990) [42]	800	38.7	H_2, C, Ca, Fe, W	2.0 - 15.0	-0.1 - 0.8
FNAL-E866(1999) [43]	800	38.7	Be, Fe, W	4.0 - 8.4	0.13 - 0.93
π^- *nucleus* $\rightarrow \mu^+\ \mu^-\ X$					(fixed-target)
CERN-WA11(1979) [45]	150, 175	16.8, 18.1	Be	3.8 - 8.5	-0.2 - 0.8
CERN-WA39(1980) [36]	39.5	8.6	W, H_2	2.0 - 6.0	-0.4 - 1.0
CERN-NA3 (1985) [23]	150, 200, 280	16.8, 19.4, 22.9	Pt, H_2	4.0 - 8.5	0.0 - 1.0
CERN-NA10(1985) [22]	140, 194, 286	16.2, 19.1, 23.2	W, D_2	4.0 - 8.5	-0.3 - 1.0
FNAL-E326(1985) [44]	225	20.5	W	>11	-0.4 - 0.6
FNAL-E444(1979) [39]	225	20.5	C, Cu, W	2.0 - 8.5	0.0 - 1.0
FNAL-E537(1988) [35]	125	15.3	W	4.0 - 9.0	0.0 - 1.0
FNAL-E615(1989) [21]	252	21.7	W	>4.05	0.0 - 1.0
π^+ *nucleus* $\rightarrow \mu^+\ \mu^-\ X$					(fixed-target)
CERN-WA39(1980) [36]	39.5	8.6	W, H_2	2.0 - 6.0	-0.4 - 1.0
CERN-NA3 (1985) [23]	150, 200, 280	16.8, 19.4, 22.9	Pt, H_2	4.0 - 8.5	0.0 - 1.0
FNAL-E444(1979) [39]	225	20.5	C, Cu, W	2.0 - 8.5	0.0 - 1.0

Table. 1.2 lists the information of the past Drell-Yan experiments summarized in Ref. [30]. The physics programs of Drell-Yan process include pp collision and hN scattering, where h could be $\pi^{\pm}, K^{\pm}, p, \bar{p}$ and N is nucleus. Since COMPASS is an $\pi^- N$ experiment, the comparison of our data is mainly done with the other $\pi^- N$ experiments, such as NA3, NA10, E615. There are some general comments for the Drell-Yan experiments based on Table. 1.2 listed below :

- **Detection of dimuon or di-electron :** The detection of the muons is preferable compared to electrons by the reason that the detection of electron requires good special and energy resolution detectors which are expensive and difficult to be built. On the other hand, the detection of muon requires just heavy material with the scintillator counter, a much simpler system.

- **Collision or fixed-target experiment :** There are two kinds of experimental setup, collision and the fixed-target experiment. The energy scale of pp collision is usually higher than the fixed-target experiment so the dilepton mass is larger and cleaner. However, Drell-Yan process with collision is not interested for the people who studies the non-perturbative QCD effect and the nuclear effect. The fixed-target experiment is preferred instead.

- **Hadron beams :** The choices of hadron beam could be $\pi^+(u\bar{d})$, $\pi^-(\bar{u}d)$, $K^+(u\bar{s})$, $K^+(\bar{u}s)$, $p(uud)$, and $\bar{p}(\bar{u}\bar{u}\bar{d})$. Among them, π^- and p beam are the common choices because of their long lifetime. Compare to proton beam, π^- beam gives larger Drell-Yan cross section owing to the antiquark composition. The data of Drell-Yan cross section from $\bar{p}$, π^+ and $K^\pm$ are very little since it is difficult to produce the $\bar{p}$ and $K^\pm$ beams with high purity due to the the technical issue. The data from the Drell-Yan measurement with π^+ and π^- beams on the iscoscalar deuterium would be interesting to constrain sea distribution [27] of pion as long as the technical issue of π^+ beam could be resolved.

- **Nucleus targets :** The choice of nucleus targets are varied in a wide range, ex. hydrogen (H_1, 1 proton), deuterium (H_2, 1 proton and 1 neutron), helium (H_4, 2 protons and 2 neutrons), carbon (C, 6 protons and 6 neutrons), copper(Cu, 19 protons and 34 neutrons), platinum (Pt, 78 protons and 78 neutrons), tungsten (74 proton and 110 neutron). The heavy ones, like tungsten, are commonly used as target by the reason that the larger Drell-Yan cross section to have good statistics. In the study of the nuclear effect, various nucleus are used, from the light ones to heavy ones. The light deuterium target provides a baseline in the study of nuclear effect since there is only one proton contained.

  When doing the nuclear effect study, one must consider the isoscaler effect. Proton(uud) and neutron(udd) have different Drell-Yan cross section because of the quark composition. For example, the $\pi^-(\bar{u}d)$-$p(uud)$ collision has two times larger cross section than the $\pi^-(\bar{u}d)$-$n(udd)$ thanks to two times u quark composition in proton compared to neutron. The Drell-Yan cross-section is usually demonstrated in the unit of cm per nucleon. The heavy targets usually contents higher neutron components so that they give lower Drell-Yan cross section per nucleon compared to the proton target. This is so called the isospin effect which one must consider when doing the nuclear effect study.

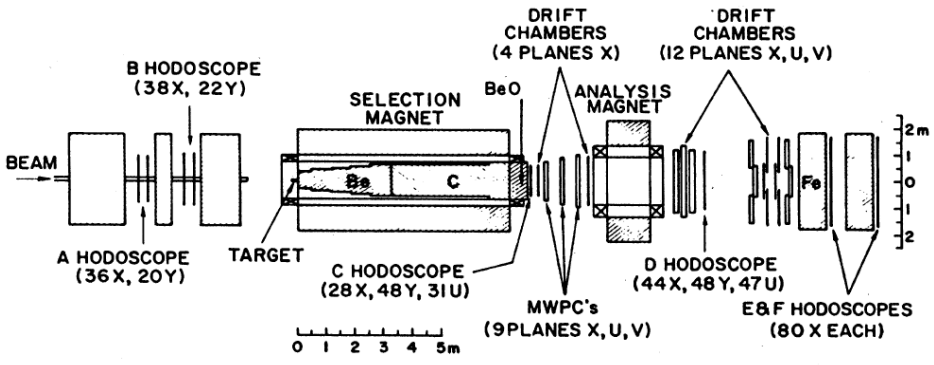

Figure 1.13: *The experimental setup of E615 experiment. It demonstrates the setup of typical Drell-Yan measurement in fixed-target experiment [21].*

Fig. 1.13 [21] shows the experimental setup of the fixed-target experiment using π^- beam, E615 experiment at Fermilab. In general, all the fixed-target experiments have very similar arrangement contains of Hadron beam, nucleus target, and an absorbor made by heavy material. A hadron beam shots into a fixed nucleus target, and right after the target, a thick and heavy material is placed in order to absorb the scattered secondary hadrons. The thick material is called absorbor. Only the leptons are the detective signals.

However, one must notice that a large background decays directly from the π^- beam. The beam-decay-muon background is usually distributed in the low mass region and has very large momentum inherited from beam. It is a difficult task keep a good balance in between the detection of Drell-Yan events and the veto of beam-decay muons in both the design of the experimental trigger and the analysis. Fig. 1.14 shows the mass spectrum of COMPASS experiment performed in 2015. The low mass region ($M_{ll'} < 4.0\ GeV/c^2$) contents high contamination of the beam-decay background (labeled as Comb. background in the black dash line). The mass region chosen is usually larger than $4GeV/c^2$ to avoid the background.

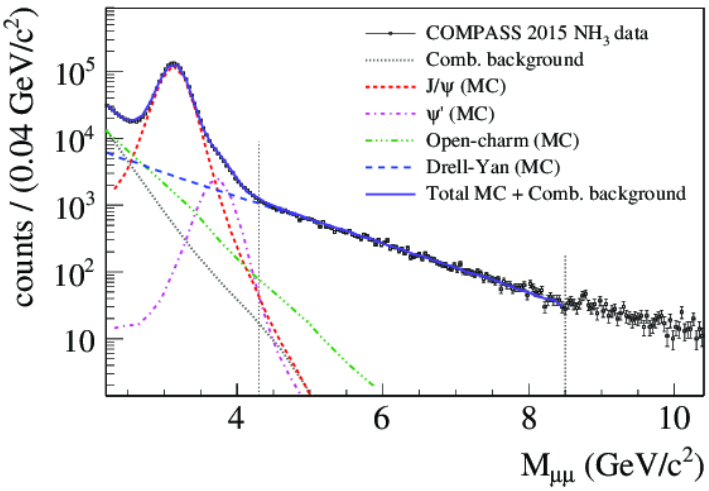

Figure 1.14: *Dimuon mass spectrum of COMPASS experiment performed in 2015 [46]. COMPASS data is black dots. The combinatorial background is in the black dash line. The Monte-Carol(MC) simulation of J/ψ, $\psi^{'}$, open-charm, and Drell-Yan processes are in the red, magenta, green dash lines, respectively. COMPASS data has nice agreement with the sum of the MC simulations and the backgrounds.*

Except for the issue of beam-decay muon, another problem of the fixed-target experimental setup is the multiple scattering of muons passing through heavy absorbor. The mass, momentum, and the vertex resolutions are typically poor for Drell-Yan fixed-target experiment compared to the collider experiments.

1.3.4 Predictions from naïve Drell-Yan model

The naïve Drell-Yan model proposed by D. Drell and Tung-Mow Yan successfully made a list of predictions to characteristics Drell-Yan process. The details are described in this paragraph.

- **Rapid fall of cross-section with the increased dilepton mass**

  The naïve Drell-Yan cross-section is based on the simple parton model and QED. To derive the Drell-Yan cross section in the naïve model, the two scattering partons are

treated as two point-like particles, so that the Drell-Yan cross-section production is easily mirrored to the electron-positron annihilation. The cross section is written as below :

$$\sigma = \frac{4\pi\alpha^2 Q_e^2}{3M_{ll'}^2} \tag{1.18}$$

where α_{em} is the electromagnetic coupling constant, Q_e is the charge of electron, and $M_{ll'}$ is the invariant mass of dimuon pair.

Next, the hadrons are considered as the composition of quarks based on the parton model. The total cross section is the sum of the annihilation of all the possible quark-antiquark pairs considering their flavor.

$$\frac{d^2\sigma}{dx_A dx_B} = \frac{4\pi\alpha^2}{9M_{ll'}^2} \sum Q_q^2 [q(x_A)\bar{q}(x_B) + q(x_A)\bar{q}(x_B)] \tag{1.19}$$

where x_A is the 4-momentum fraction of parton inside hadron h_A, x_B is the 4-momentum fraction of parton inside hadron h_B, $q(x_A)$ is the pion PDF of h_A, $q(x_B)$ is the pion PDF of h_B, $q(x_A)dx_A$ is the probability of finding quark inside hadron h_A, $\bar{q}(x_B)dx_B$ is the probability of finding quark inside hadron h_B, and Q_q is the charge of quark.

The expression of Drell-Yan cross section could be reformed in the Feynman-x and τ with Eq. 1.16 and Eq. 1.17 :

$$\frac{d^2\sigma}{dM_{ll'}dx_F} = \frac{2\pi\alpha^2}{9M_{ll'}^3}\left(\frac{x_A x_B}{x_A + x_B}\right) \sum Q_q^2 [q(x_A)\bar{q}(x_B) + q(x_A)\bar{q}(x_B)] \tag{1.20}$$

Eq. 1.20 shows the rapid fall of cross section with the increase of dilepton mass $M_{ll'}$ in the order of 3. The naïve Drell-Yan model predicts a rapid fall of cross-section with the increased dilepton mass.

- **Energy scaling**

  Eq. 1.20 is rearranged as follows assuming that the dilepton system has zero longitudinal momentum :

$$x_F = 0 = x_A - x_B \ , \ assuming \ x_A = x_B = \sqrt{\tau} \tag{1.21}$$

$$M_{ll'}^3 \frac{d^2\sigma}{dM_{ll'}dx_F}\Big|_{x_F=0} = \frac{2\pi\alpha^2\sqrt{\tau}}{9} \sum Q_q^2 [q(x_A)\bar{q}(x_B) + q(x_A)\bar{q}(x_B)] = F(\sqrt{\tau}) \tag{1.22}$$

Drell-Yan cross-section, $M_{ll'}^3 \frac{d^2\sigma}{dM_{ll'}dx_F}\Big|_{x_F=0}$, is only related to the dimensionless value $\sqrt{\tau} = \frac{M_{\mu\mu}}{s}$ and regardless of the incident energy s of hadron system. One can replace x_F with rapidity y and find the same behavior.

$$M_{ll'}^3 \frac{d^2\sigma}{dM_{ll'}dy}\Big|_{y=0} = F(\sqrt{\tau}) \tag{1.23}$$

Fig. 1.15 shows measured Drell-Yan cross section with scale of $M^s_{ll'}$ in rapidity $y = 0$ given by R808 experiment is independent of the center-of-mass energy $\sqrt{s}$ but linear-correlated with $\sqrt{\tau}$ which is a dimension less variable gives the ratio of dilepton mass with respect to $\sqrt{s}$, $\sqrt{\tau} = \frac{M_{ll'}}{\sqrt{s}}$. When comparing the Drell-Yan cross-section from different experiments with different beam energy, one must compare them in the variable of $\sqrt{\tau}$.

The energy scaling behavior is also shown at various Feynman-x x_F and rapidity y regions. Fig. 1.16 shows the the differential cross section of proton-nucleus collisions, $m^3 \frac{d^2\sigma}{dmdx_F} = F(x_F, \sqrt{\tau})$, independent of the beam energy $\sqrt{s}$.

$$M^3_{ll'} \frac{d^2\sigma}{dM_{ll'}dx_F} = F(\sqrt{\tau}, x_F) \tag{1.24}$$

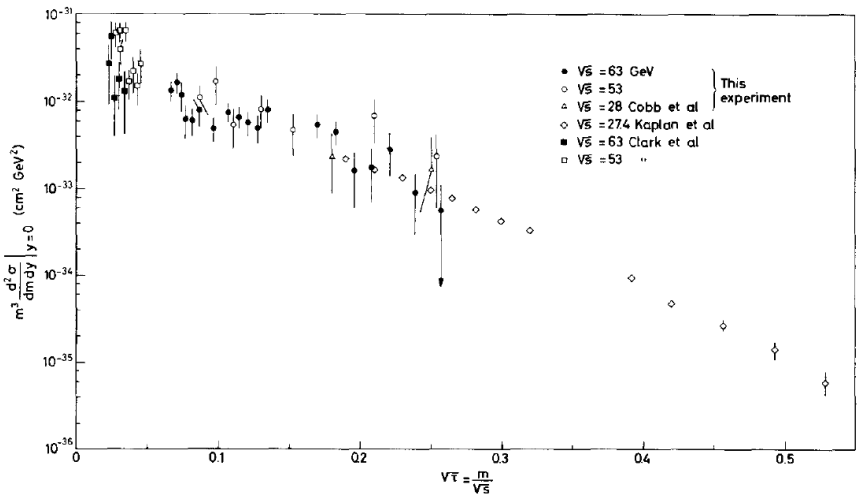

Figure 1.15: *R808 experiment [32] shows a plot of* $M^3_{ll'} \frac{d^2\sigma}{dM_{ll'}dy}\Big|_{y=0}$ *for the Drell-Yan electron pair continuum with different energy of pp collision* $\sqrt{s}$*. The energy scaling effect is demonstrated.*

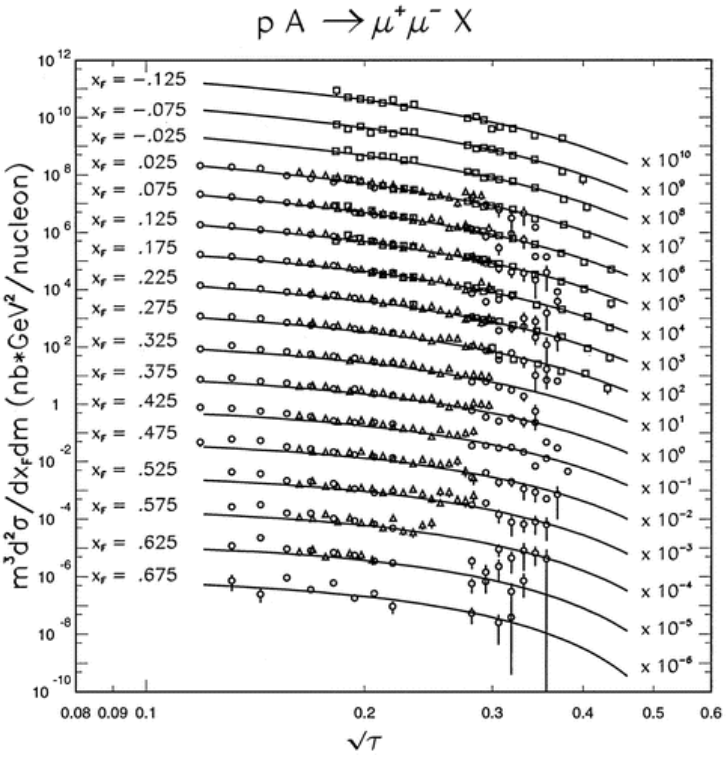

Figure 1.16: *Drell-Yan cross section from proton-nucleus collisions : △ for NA3 has proton beam energy at 400 GeV/c, □ for E605 has proton beam energy at 800 GeV/c, and ◯ for E772 has proton beam energy at 800 GeV/c. The lines are the next-to-leading(LO) order calculations using the CTEQ4M proton PDF. The scaling effect is observed in various Feynman-x x_F and rapidity y regions. [47].*

- **Angular distribution of the dilepton pair fits** $1 + cos^2\theta$.

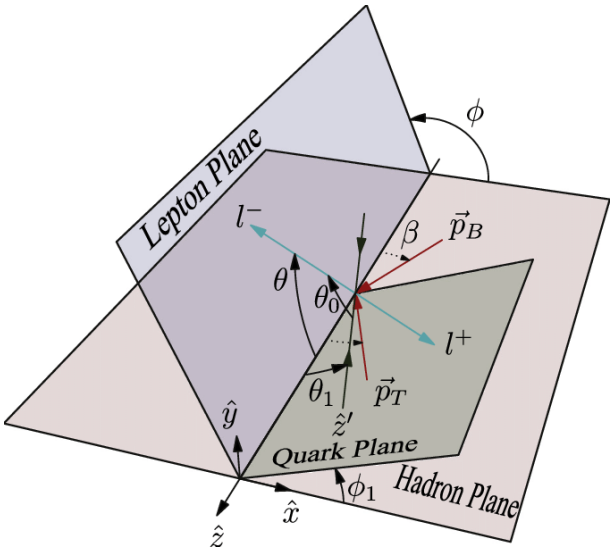

Figure 1.17: *Sketch of Collins-Soper(CS) frame [48].*

Fig. 1.17 shows the sketch of Collins-Soper(CS) frame called also dilepton-rest frame [48] which is usually used in describing the angular description of dilepton pair. There are three planes defined, lepton plane, quark plane, and hadron plane, which

are defined by the 4-momentum of lepton system(lepton l, antilepton l'), quark system, and hadron system(beam p_B, target p_T), respectively. The z-axis is the bisects of the beam and target momenta. Both z-axis and x-axis are lied on the hadron plane. The angles θ and ϕ are defined as the polar and azimuthal angles of negative lepton $l^-(e^-$ or $\mu^-)$. Under CS frame, the Drell-Yan cross section is written as follows :

$$\frac{1}{\sigma_0}\frac{d\sigma}{d\Omega} = \frac{3}{4\pi}\frac{1}{\lambda+3}(1+\lambda\cos^2\theta+\mu\sin 2\theta\cos\phi+\frac{\nu}{2}\sin^2\theta\cos 2\phi) \tag{1.25}$$

In naïve Drell-Yan modle, the coefficients λ, μ, and ν are predicted to be $\lambda = 1$ and $\mu = \nu = 0$ since the co-linear partons lead to a transversely polarized virtual photon, as results of that the Drell-Yan cross section is proportional to $1 + cos^2\theta$.

$$\lambda = 1 \; and \; \mu = \nu = 0 \; , \; \frac{d\sigma}{d\Omega} \propto (1+\cos^2\theta)$$

Fig. 1.18 shows the Drell-Yan angular distribution from E772 experiment. The data shows a consistent result as predicted from the naïve Drell-Yan model, $\lambda = 0.96 \pm 0.04 \pm 0.06$.

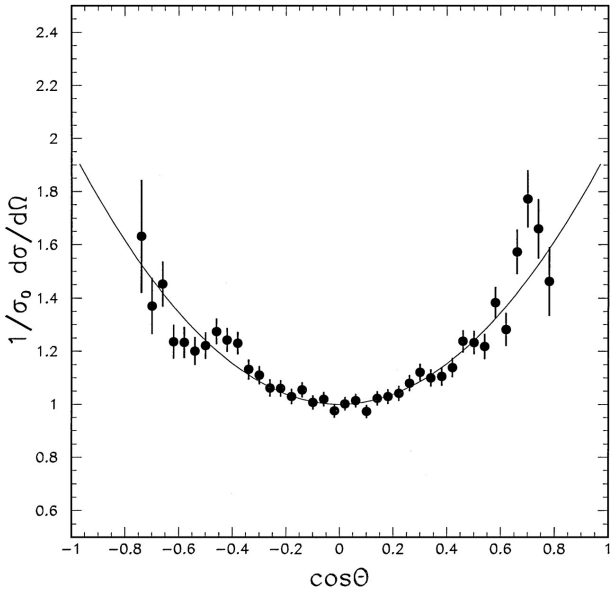

Figure 1.18: *The Drell-Yan angular distribution published by E772 experiment with 800 GeV proton beam collides Cu target. Data is fitted with* $1+\lambda\cos^2\theta$*, where* $\lambda = 0.96 \pm 0.04 \pm 0.06$ *[47].*

- **Mass number of the nucleus target is nearly linear dependence of the cross section**

  The Drell-Yan cross section is the sum over the cross section of all the possible annihilations from quark and antiquark pairs, as shown in Eq. 1.20. Consequently, the Drell-Yan cross section is proportional to the mass number A, without considering the nuclear effect. The formulation of the linear dependence with the mass number of the nucleus target is written as below :

$$\sigma_A = A^\alpha \sigma_0 \tag{1.26}$$

where σ_A is the cross section of nucleus target with mass number A, σ_0 is the cross section of nucleon, and α is close to the unity 1.

In Eq. 1.26, σ_0 refers to the cross section of nucleon which could be neutron or proton. However, the cross section of $\pi^- p$ scattering and $\pi^- n$ scattering are different because of its quark composition as explained previously in Sec. 1.3.3. Ideally, if one use isoscaler nucleus targets (equal number of neutron and proton, ex. H_2, C, Be, Pt) to study nuclear effect with Drell-Yan measurements, thus one do not have to consider the pn-mixture effect. On the other hand, the fixed-target Drell-Yan experiments with heavy nucleus targets (number of neutron more than proton) are often used to increase the production cross section. Considering the isospin effect, Eq. 1.26 is reformed as follows:

$$\sigma(Z, A) = A^{\alpha'} \sigma_0(Z, A) \tag{1.27}$$

where $\sigma_0(Z, A)$ represents a cross section corrected for departure from an isoscalar target.

Fig. 1.19 [49] shows the Drell-Yan cross section ratio of C/H_2, Ca/H_2, Fe/H_2, and W/H_2 from E772 experiment with pN collision fits Eq. 1.27. It shows that the nearly linear dependence of cross section on mass number of the target nucleus, $\alpha' \sim 1$.

Table. 1.3 lists the α or α' measured by NA3 [50] and NA10 [51]. α' after the isospin-correction is closer to unity than α as predicted by the naïve Drell-Yan model including the consideration of isospin correction.

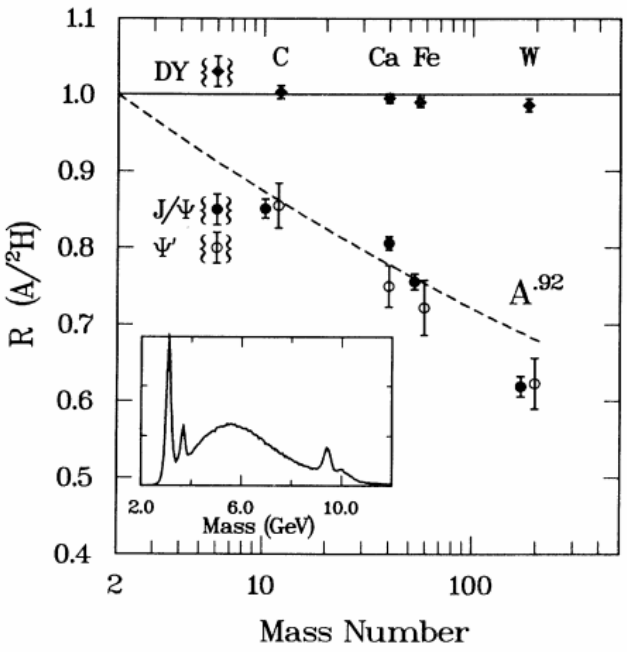

Figure 1.19: *The ratios of the cross-section of the nucleus target compares to the deuterium for the J/ψ, ψ', and Drell-Yan process from E772 experiment with 800 GeV proton beam scattered to C, Ca, Fe, and W targets. The solid curve is a fit of Eq.1.27 to the Drell-Yan data. α' of Drell-Yan measurement is close to 1 [49](solid line). $J/$ and ψ' data give $\alpha' = 0.92$, far below 1, but the discussion of the results of J/ψ is out of the scope of this paragraph.*

Table 1.3: *α and α' from Eq. 1.26 and Eq. 1.27 measured by NA10 and NA3 experiments. α' is close to unity as predicted in Drell-Yan model.*

Exp.	beam	E_{beam} (GeV)	target	$M_{ll'}$ (GeV)	α	α'
NA3 [50]	π^-	200	H_2, Pt	4-9	1.35 ± 0.13	1.02 ± 0.03
	π^+	200	H_2, Pt	4-9	1.13 ± 0.19	0.95 ± 0.04
	π^-	150	H_2, Pt	4-9	1.00 ± 0.10	1.00 ± 0.02
	π^-	280	H_2, Pt	4-9	1.40 ± 0.07	1.00 ± 0.02
NA10 [51]	π^-	280	C, Cu, W	4-8.4	0.94 ± 0.02	0.97 ± 0.02

1.3.5 QCD improved Drell-Yan model

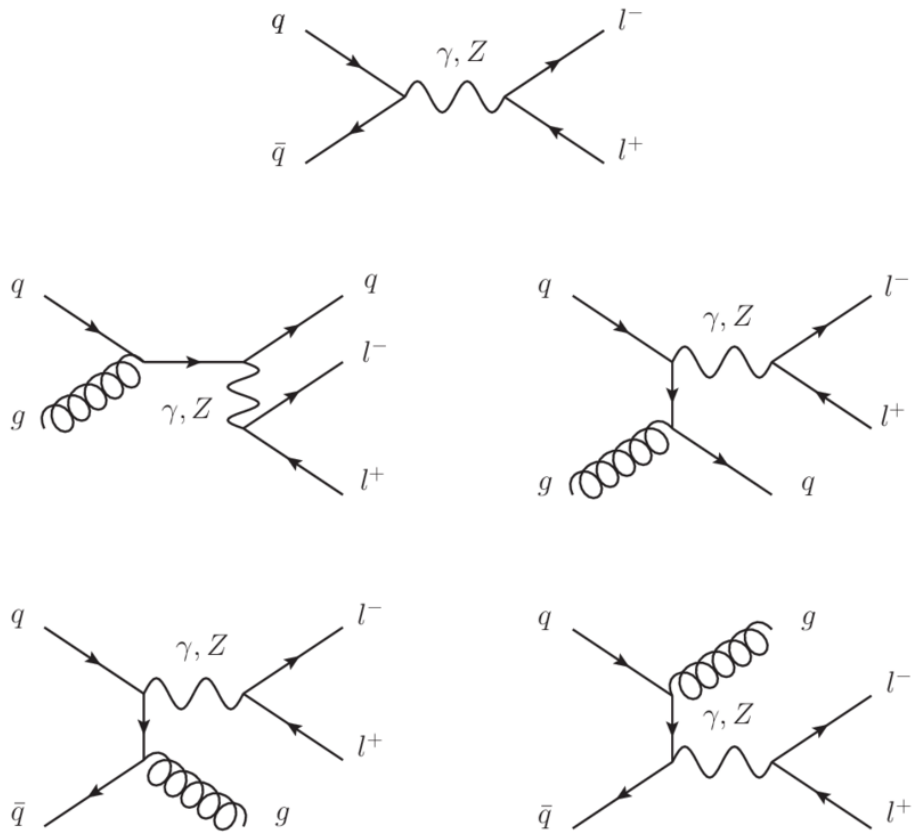

Figure 1.20: *The Feynman graphs for Drell-Yan pair production at LO and NLO. [52].*

Despite of a huge success of the naïve Drell-Yan model proposed by Sidney D. Drell and Tung-Mow Yan based on QED and the parton model, it failed in explaining some of the experimental results. The failures of the model need the extra corrections from QCD. The QCD-improved Drell-Yan model considers additionally the gluon activities includeing the quark-gluon scattering, antiquark-gluon scattering, and gluon emission, etc. Fig. 1.20 shows the Feynman diagrams of Drell-Yan process in LO with only QED effect and NLO including one gluon participation. In the following paragraphs, the experimental results were failed to be explained by the naïve QCD and are discussed as follows :

- **The measured cross-section in around 2 times larger than naïve Drell-Yan**

model predicted : The absolute value of the measured cross-section in around 2 times larger than theoretical prediction of naïve Drell-Yan model. Due to the non-perturbative feature in QCD, the calculation of Drell-Yan cross section including the gluon interaction needs the special treatment to prevent the divergence in the calculations. The idea was proposed by Sachrajda in 1987, so-called leading-log approximation (LLA). (The details of LLA method won't be discussed here.) Based on Qe. 1.24, the QCD-improved Drell-Yan process cross section in LLA is written as :

$$M_{ll'}^3 \frac{d^2\sigma_{QCD}}{dM_{ll'}dx_F} = F(\sqrt{\tau}, x_F, ln(M_{ll'}^2/\Lambda_{QCD})) \tag{1.28}$$

where Λ is the QCD scale $\sim 0.2GeV$(or $1fm$ in space). In LLA, the Drell-Yan cross section is not only x_F and $\sqrt{\tau}$ dependent, but also $M_{ll'}$-dependent.

The "K-factor" was proposed to describe the difference of cross section between the theoretical calculation and the measured results [21].

$$\sigma_{measured} = K\sigma_{calculated} \tag{1.29}$$

In 1980s, K factor has been measured by several experiments, and the results was compared with the calculation of naïve Drell-Yan model. Each group finds the K factor is around 2 [19]. As the development of theoretical calculation, the higher-order calculation in QCD is now achieved. The work of the Drell-Yan cross section calculation is already much closer to the measured results. In 1993, W.J. Stirling and M.R. Whalley [30] published their calculation in QCD NLO calculation shown in Fig. 1.21 and they gave the K-factor of the most experiments are around 1.

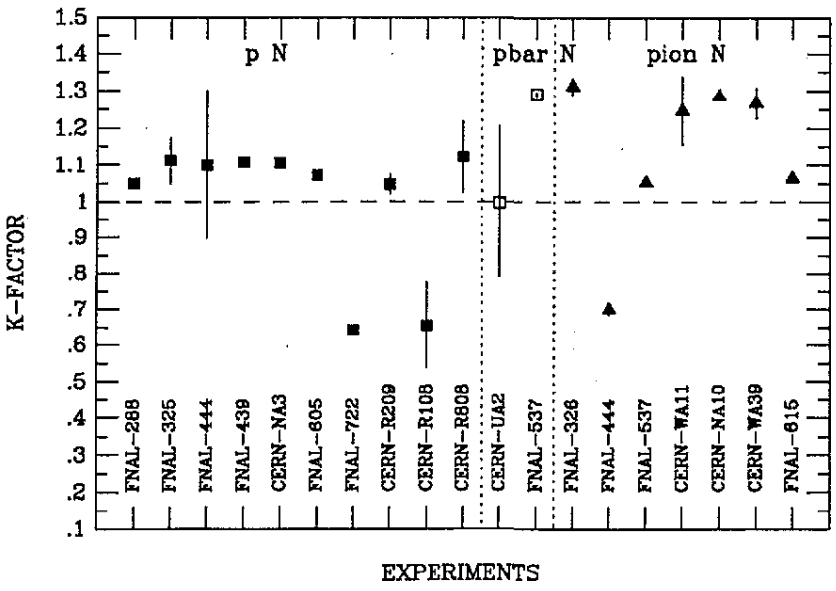

Figure 1.21: *The overall 'K-factors' from each experiments from W.J. Stirling's and M.R. Whalley's work in NLO QCD calculation [30].*

- **The mean square transverse momentum of dilepton pairs is in the order of few GeV which contradicted to the theoretical prediction around 0.3**

GeV. : In naïve Drell-Yan model, the mean square of the intrinsic transversed momentum of partons inside hadron is predicted in a very small value around 0.3 GeV. However, experimental results shows that the mean square of transverse moment $< p_t^2 >$ is in a few GeV order and linear-dependent with the center of mass energy s, as shown in Fig. 1.22 . The reason is that the gluon emission and gluon scattering provide kicks to the dileptons which give higher transverse momentum than the expectation which only considers the intrinsic transversed momentum.

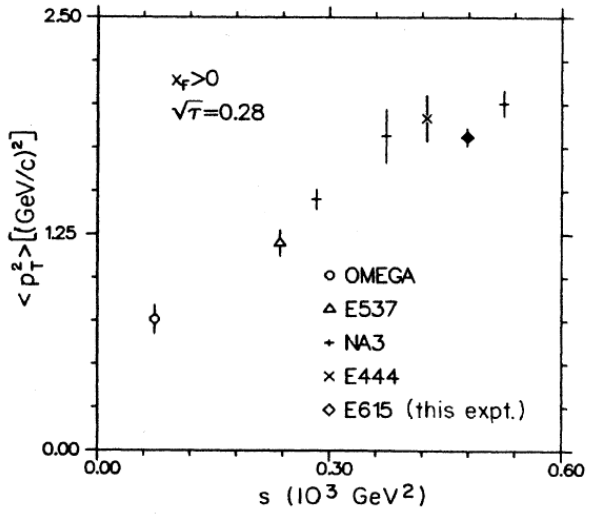

Figure 1.22: *The mean square of transverse momentum $< p_t^2 >$ verses the center-of-mass energy s from fixed-target experiments with π^- beam [21].*

The pp-collision experiment is usually performed at high Q level so the transversed momentum distribution of Drell-Yan process is calculable with pQCD ($Q > 0.2GeV$). Fig. 1.23 shows the good agreement between the $< p_t^2 >$ distribution of dilepton pairs measured by R209 experiments(pp collision experiment) and QCD NLO calculation [34]. However, for the fixed-target experiments which is at low Q level, where non-perturbative QCD effect dominates, thus the transverse momentum spectrum is incalculable. The study of of $< p_t^2 >$ distributions for fixed-target experiments remains in the phenomenological study. Joining with the data points from the other experiments, COMPASS results could make contribution of the intrinsic momentum distribution.

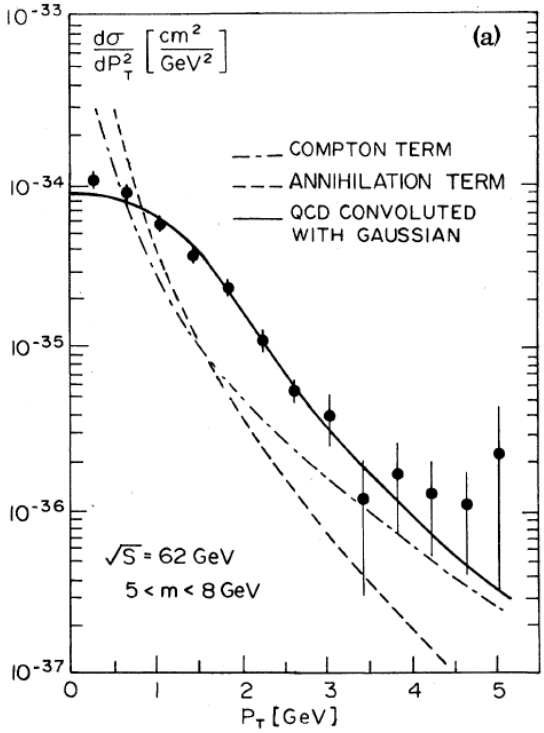

Figure 1.23: *The mean square of transverse momentum $< p_t^2 >$ distribution of dilepton pairs compares with QCD NLO calculation done by R209 group. One of the dash line is from the one gluon emission and another one is contributed from the gluon-quark or gluon-antiquark scattering. The solid line is the sum of the contributions of the dash line. R209 data fits pQCD calculation well [34].*

1.4 JPsi process

1.4.1 Introduction

J/ψ meson was discovered is 1974 by two groups, on in SLAC leaded by Burton Richter and another one lead by Samuel Ting in BNL. The plots of the J/ψ signals found by Burton Richter from e^+e^- annihilation and Samuel Ting from $p + Be$ scattering are shown in Fig 1.24. The discovery of J/ψ leads to a rapid development in particle physics in both experiment and theory. This is so-called well-known "November resolution". Burton Richter and Samuel Ting were awarded the 1976 Nobel Prize in Physics due to the discovery of J/ψ.

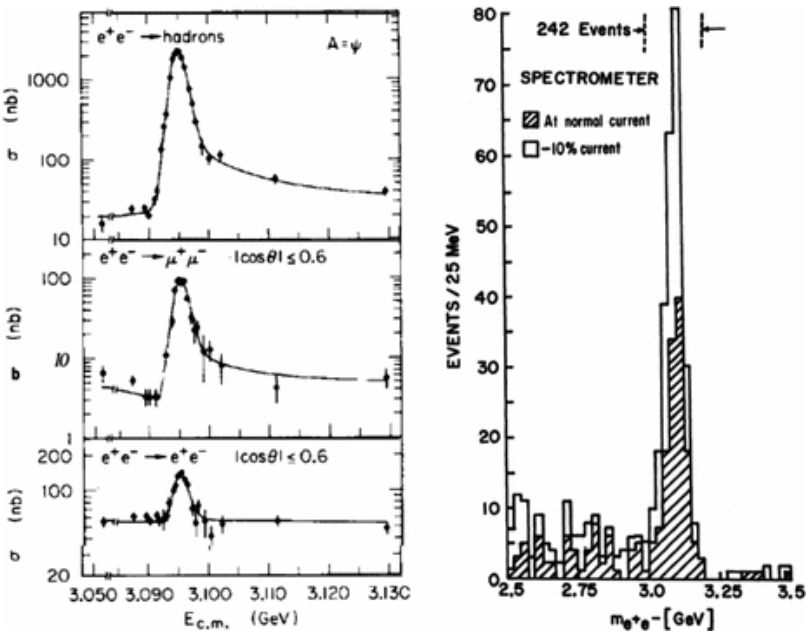

Figure 1.24: *The discoveries of J/ψ in 1984, (left)Burton Richter group from e^+e^- annihilation in SLAC, (right) Samuel Ting group from $p + Be$ scattering in BNL.*

J/ψ is a meson formed by a charm quark and a charm anti-quark so called "charmonium". J/ψ is the ground state of charmonium and its lifetime is long because of its mass lower than the threshold of open charm decay, 7.2×10^{21} s. It is a $Spin = 1$, $mass = 3.0969\ GeV/c^2$. The decay channels of J/ψ has significant amount goes dileptons. The primary decay modes of J/ψ are listed in Table. 1.4 [53]. Around 13% of J/ψ decays into di-leptons, e^+e^- or $\mu^+\mu^-$.

1.4.2 Charmonium spectrum

Since the discovery of the J/ψ, many other charmonium resonances have been comfirmed experimentally. The spectrum of the charmonium states are drawn in Fig. 1.25 [54]. There are multiple charmonium states, ex. J/ψ, $\psi(2S)$, χ_{C0}, χ_{C1}, etc. Each charmonium state has its own quantum state, derived from the quark model. The quantum numbers of the $c\bar{c}$ states in notations are :

$$n^{2S+1}L_J, \quad n = 1, 2, 3, \ldots$$

Table 1.4: *Branching ratios of the J/ψ decay modes [53].*

Decay Channel	Branching Ratios
$c\bar{c} \to 3g$	$64.1 \pm 1.0\%$
$c\bar{c} \to \gamma 2g$	$8.80 \pm 0.50\%$
$c\bar{c} \to \gamma$	$\sim 25.4\%$
$\gamma \to$hadrons	13.5 ± 0.30
$\gamma \to e^+e^-$	$5.94 \pm 0.06\%$
$\gamma \to \mu^+\mu^-$	$5.93 \pm 0.06\%$

where n is the principle quantum number, S is spin, L is the orbital angular momentum, and J is the total angular momentum $J = L + S$. The spin states can be categorized into spin-singlet S-wave and the spin-triplet P-wave. The quantum notation of the low-mass charmonium states shown in Fig. 1.25 and Table. 1.5.

Table 1.5: *Low-mass charmonium states*

$n^{2S+1}L_J$	Charmonium	J^{PC}	Mass(MeV)
1^1S_0	η_c	0^{-+}	2980
1^3S_0	J/ψ	1^{--}	3097
1^3P_0	χ_{c0}	0^{++}	3415
1^3P_1	χ_{c1}	1^{++}	3511
1^1P_1	h_c	1^{+-}	3526
1^3P_2	χ_{c2}	2^{++}	3556
2^1S_0	$\eta_c^{'}$	0^{-+}	3637
2^3S_1	$\psi(2S)$	1^{--}	3686

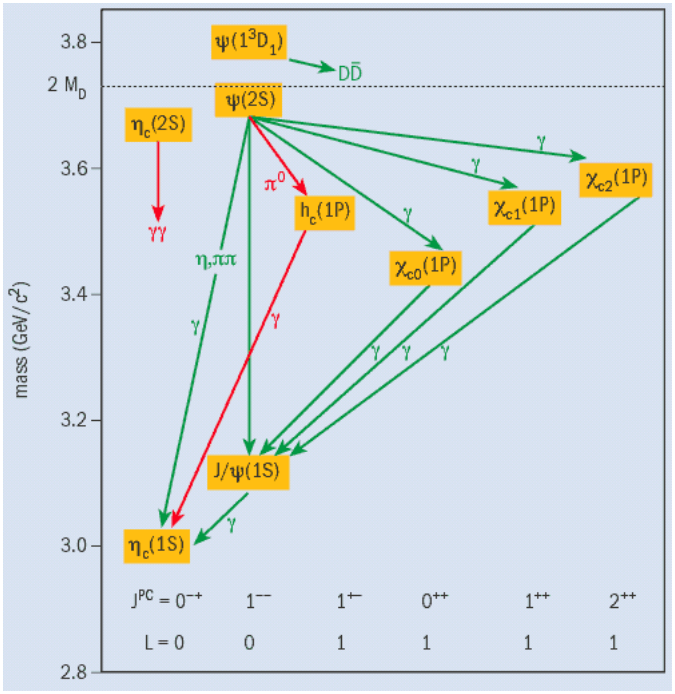

Figure 1.25: *Low-mass charmonium spectrum (below $D\bar{D}$) and the hadronic decays. Transitions are denoted by the arrows [54].*

Except for the direct production of J/ψ, the feed-down from the hadronic decays of $\psi(2S)$ and the radiative decays of three χ_{CJ} states produce J/ψ as well. The branching ratio (decay ratio) of them from PDG 2020 values are listed in Table. 1.6 [53] :

Table 1.6: *The branching ratio of the indirect J/ψ production [53].*

Indirect production of J/ψ	Branching ratio
$\psi(2S) \to J/\psi X$	61.4%
$\chi_{c0} \to J/\psi\gamma$	1.4%
$\chi_{c1} \to J/\psi\gamma$	34.3%
$\chi_{c2} \to J/\psi\gamma$	19.0%

1.4.3 The models of charmonium production

The mechanism of charmonium production has been studied since the discovery of J/ψ. There are many theoretical models proposed. There are three models have been discussed the most, Color Evaporation Model(CEM), Color Singlet Model(CSM) and the Non-Relativistic QCD model (NRQCD). NRQCD is often refereed as Color Octet Model(COM) with respect to CSM.

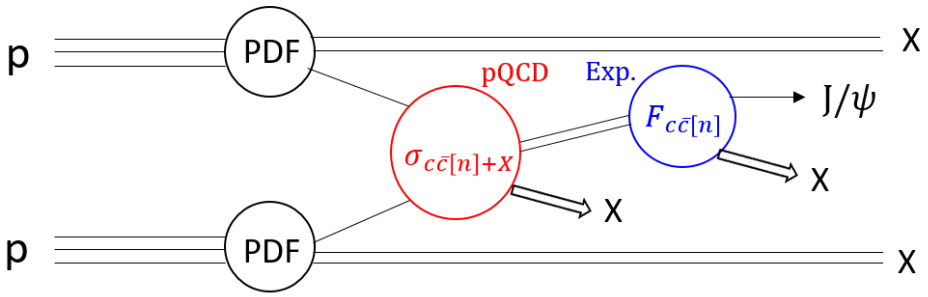

Figure 1.26: *The drawing charmonium production of hadron-hadron collision.*

In Fig. 1.26, the the production of J/ψ from pp collision is drawn and the formulation of the cross section is as folows :

$$d\sigma(J/\psi + X) = \sum_n \int d\Lambda \frac{d\sigma_{c\bar{c}[n]+X}}{d\Lambda} F_{c\bar{c}[n]}(\Lambda)$$

where n is the quantum state of the $c\bar{c}$ pair, Λ is the energy scale of the strong interaction, X is the fragmentation. All these three models, CSM, CEM, COM(NRQCD), try to factorize the charmonium production into two steps :

(1) First, $d\sigma_{c\bar{c}[n]+X}$ describes the production rate of charm and anti-charm which is a perturbative term also called as short-distance part or hard part in QCD. The hard process, $d\sigma_{c\bar{c}[n]+X}$, at leading-order(LO) $\mathcal{O}(\alpha_s^2)$ including quark-antiquark($q\bar{q}$) and gluon-gluon fusion (GG) diagrams. The NLO $\mathcal{O}(\alpha_s^3)$ calculations includes not only quark-antiquark($q\bar{q}$) and gluon-gluon fusion (GG) but also the gluon Compton scattering(Gq, $G\bar{q}$). The contributions of the partonic subprocesses in the fixed-order LO and NLO are listed below [55] :

$$\begin{aligned}
q + \bar{q} &\to c + \bar{c} && \alpha_s^2,\ \alpha_s^3 \\
G + g &\to c + \bar{c} && \alpha_s^2,\ \alpha_s^3 \\
q + \bar{q} &\to c + \bar{c} + G && \alpha_s^3 \\
G + g &\to c + \bar{c} + G && \alpha_s^3 \\
G + q &\to c + \bar{c} + G && \alpha_s^3 \\
G + \bar{q} &\to c + \bar{c} + G && \alpha_s^3
\end{aligned}$$

(2) Second, $F_{c\bar{c}[n]}(\Lambda)$ describes the bound state of charm and anti-charm, is an non-perturbative part also called an long-distance part or soft-part. The non-perturbative part can only be accessed by the experimental measurement. The treatment of the non-perturbative part, $F_{c\bar{c}[n]}(\Lambda)$, are different for different models :

- Color Evaporation Model (**CEM**)

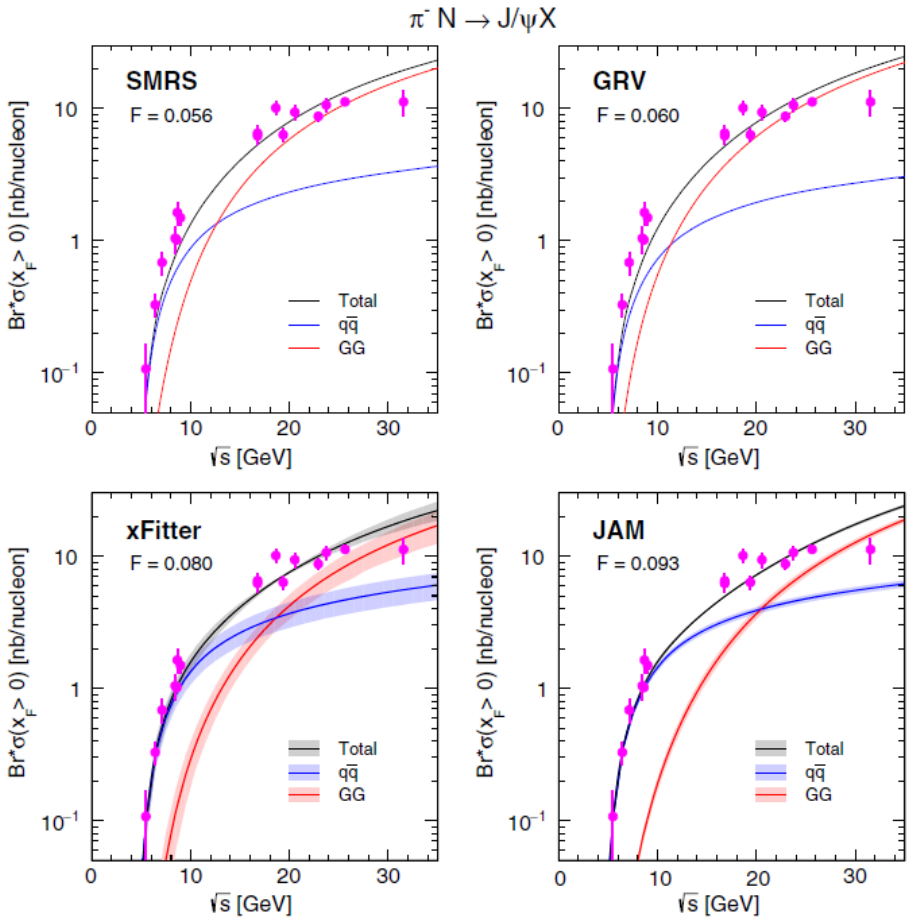

Figure 1.27: *The production cross-section of J/ψ including the direct production and the feed-down processes. The magenta points are the experimental data from the $\pi^- N$ experiments. The black solid lines are the calculations of CEM model in NLO with four pion PDFs, SMRS [15], GRV [13], xFitter [18], and JAM [16]) and nucleon PDF CT14nlo [3] under LHAPDF framework. $q\bar{q}$ and GG subprocesses are drawn in the blue and red curves, respectively.*

CEM [56] is was the earliest model to calculate the charmonium production. The non-perturbative part, $F_{H(c\bar{c}[n])}(\Lambda)$,is assumed to be non-zero and constant between $4m_c^2$ and $4m_D^2$ and zero for all the other energy, therefore $F_{H(c\bar{c}[n])}$ independent of the energy and the quantum states of the charmonium. The sum over all the quantum states gives the multiplication of a factor $\frac{1}{9}$. The charmonium production cross section can be simplified into :

$$d\sigma(J/\psi + X) = \frac{F_{c\bar{c}[J/\psi]}}{9} \sum_n \int_{2m_c}^{2m_D} dM \frac{d\sigma_{c\bar{c}[n]+X}}{dM}$$

where M is the mass of $c\bar{c}$ pair. If one use CME model to fit the experimental data, one could found that $F_{c\bar{c}[J/\psi]}$ is used to be as the normalization factor. This assumption of $F_{c\bar{c}[J/\psi]}$ greatly reduce the number of the free parameters in the CEM. CEM is actually more like a phenomenological parameterization of the charmonium

production than a model, however it describes the shape of J/ψ cross section really well. Fig. 1.27 [20] shows the production cross-section of J/ψ with π^- beam data and the calculation in NLO CEM model. The results shows nice agreement between the data and the calculation.

- Color Singlet Model (**CSM**)
  CSM [57] takes into account of the quantum state of $c\bar{c}$ pair, and requires the quantum state of $c\bar{c}$ is the same as the final bound state of J/ψ with the quantum state - color singlet state, $^3S_1$. The cross-section of J/ψ in CSM is written as follow :

$$d\sigma(J/\psi + X) = \sum_n \int_0^\infty dM \frac{d\sigma_{c\bar{c}[^3S_1]+X}}{dM} \psi_{J/\psi}(r=0)$$

  The non-perturbative part ($F_{c\bar{c}[J/\psi]}$) in CSM is calculated from the QCD potential, $V_{QCD} = -\frac{4}{3}\frac{\alpha_s}{r} + kr$ at $r = 0$, and result in a wavefunction $\psi_{J/\psi}(r = 0)$ allows the absorption all the non-perturbative terms into a single parameter. Unlike CEM, there is no free parameter left in CSM. However, the predicted J/ψ cross-section from CSM is several order below the measurements as shown in Fig. 1.28 [58]. It implies the model doesn't properly consider all the contributed diagrams therefore the Color Octet Model is later proposed.

- Color Octet Model (**COM**) / Non-relativistic QCD model (**NRQCD**)
  NRQCD [59] attempts to formalized the factorization of charmonium production for both perturbative and non-perturbative terms in a more rigorous way. It is considered as the most successful model for the heavy quarkonium production. It allows not just color singlet state of $c\bar{c}$, but also color octet state, therefore NRQCD is categorized as color octet model(COM). In another sense, the quantum state of $c\bar{c}$ doesn't have to be the same as J/ψ.

  The $c\bar{c}$ pair produced in short distance can evolve into bound-state J/ψ via emission soft gluons. The reason "non-relativistic" is named because the mass of charm quark 1.28 GeV is much higher than the QCD scale $\Lambda_{QCD} \sim 200GeV$ so that charm quark move slowly $v^2 \sim 0.3c^2 \ll c^2$. NRQCD is a general production mechanism of the heavy quarkonium including charmonia $c\bar{c}$, bottomonia $b\bar{b}$, B-meson $b\bar{c}$, $c\bar{b}$, and possible toponia $t\bar{t}$.

  The general expression of NRQCD model for J/ψ production is as follow :

$$d\sigma(J/\psi + X) = \sum_n \int_0^\infty dM \frac{d\sigma_{c\bar{c}[n]+X}}{dM} \langle \mathscr{O}^{J/\psi}_{[n]} \rangle$$

  NRQCD characterizes the cross section of heavy quarkonium production and their relative importance with respect to the strong coupling constant α_s and the $c\bar{c}$ velocity v. The hard part, $\sigma_{c\bar{c}[n]+X}$, is calculated as a series of α_s with pQCD. The soft part, $\langle \mathscr{O}^{J/\psi}_{[n]} \rangle$, long-distance matrix elements (LDMEs) characterizes the probability of harmonization for each quantum state in the powers of v, i.e. J/ψ is not just as simple as a bound state of $c\bar{c}$, but composed with many quantum states with the suppression factor in velocity v :

$$|J/\psi> \;=\; \underbrace{|c\bar{c}(^3S_1^1)>}_{\mathcal{O}(1)} \;+\; \underbrace{|c\bar{c}(^3P_J^8)\; g>}_{\mathcal{O}(v)} \;+\; \underbrace{|c\bar{c}(^3S_1^8)\; gg>}_{\mathcal{O}(v^2)} + \ldots$$

LDMEs are determined by the global fit to the experimental data. NRQCD model very well agree with the cross-section ash shown in Fig. 1.28 [58]. One of the important prediction of the LDMEs the universality, i.e. the elements extracted from a given experiment can be used in the other experiments. However, it is known that the LDMEs extracted from proton data (from both collier and fixed-target) under estimate the cross-section of pion fixed-target data. In this thesis, this issue is further discussed in Sec.4. We will perform the fit of LDMEs with fixed-target data from both pion and proton beam to determine a new parameterization of LDMEs. With the new LDMEs, we test the sensitivity of gluon distribution inside pion.

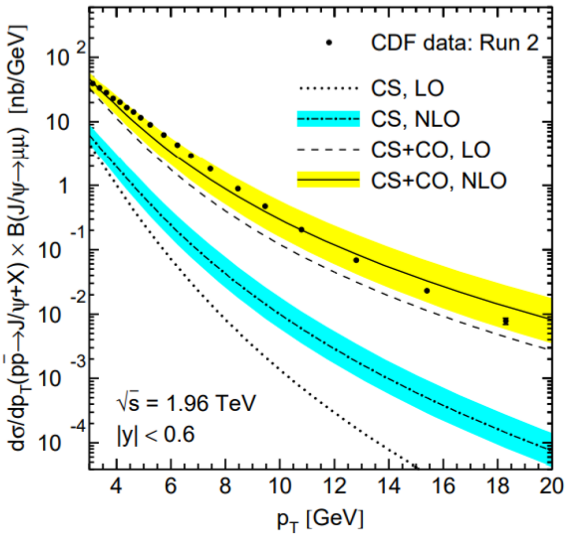

Figure 1.28: *The comparison of NLO CSM (labeled as CS) and COM (labeled as CO) calculation fit with CDF prompt J/ψ data. CSM underestimates the cross section. The sum of CSM and COM in NLO gives a nice agreement between data and calculation. [58].*

Chapter 2

The COMPASS experiment

2.1 General description of COMPASS

2.1.1 Introduction

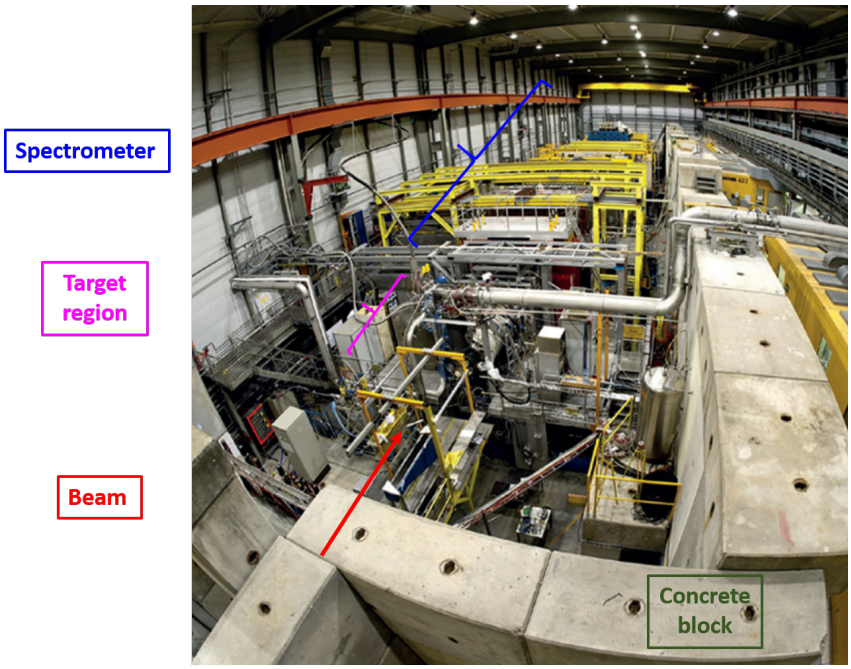

Figure 2.1: *The photo of COMPASS setup in 2018.*

COMPASS (standing for "Common Muon and Proton Apparatus for Structure and Spectroscopy" or so-called NA58 experiment) is a 60-meter-long fixed-target experiment located at M2 beam line of the SPS at CERN [60] [61]. It is a multi-purpose experimental setup to study the nucleon spin structure and hadron spectroscopy. The usage of different targets (longitudinal and transversely polarized nucleon target) and particle beams (muon, proton, pion, kaon beams) allow to investigate the physics with the various processes. There are 220 physicists from 13 different countries. COMPASS was the largest experiment at CERN until the LHC experiments started. Many advanced detectors and read-out electronics was developed here, such as MicroMegas, GEM detectors and most recently THGEM photon detection. There are two phases of COMPASS : COMPASS I

(2002-2011) [62] [63] and COMPASS II(2012-2021) [64]. Due to the high flexibility of the experimental setup, different physics programs were performed between these two phases.

COMPASS I Mainly the semi-inclusive deep inelastic scattering (SIDIS), hadron spectroscopy, and Primakoff reaction were taken. SIDIS experiment used muon beam collied with the polarised proton and deuteron targets to study the nucleon spin structure, gluon polarisation in nucleons, flavour(u,d,s) decomposition of the nucleon spin, and quark transverse momentum distribution. Hadron spectroscopy group used pion and proton beams scattering off a liquid hydrogen target and nuclear targets to search the exotic state of light-meson spectroscopy and baryon spectroscopy. Primakoff scattering used pion beam with heavy nucleus target to study pion polarisability.

COMPASS II Deeply virtual Compton scattering (DVCS), and Drell-Yan (DY) processes were performed. DVCS used muon beam collided with a long liquid hydrogen target with a huge recoil detector to study general parton distribution of nucleon (GPD). DY process used pion beam collides with polarized ammonia target to study universality of transverse momentum distribution (TMD). In the mean time, the alumina target and tungsten target were also used in DY data taking, therefore the cross section and nuclear effect can also be study simultaneously.

2018 DY Setup The experimental setup in 2018 is explicitly introduced in details since COMPASS 2018 data is analyzed in this thesis. In Fig. 2.2, it shows the simplified experimental setup in 2018, it could be divided into 4 parts from the beginning to the end : (1)beam telescopes, (2)target region, (3)spectrometer (tracking detectors and calorimeters), (4)trigger (sintillator counters). In general, for different physics program, the target, beam, triggers are designed differently, but the detectors are very similar with some slight modifications. Except for the beam type, targets, and beam telescopes, the arrangement of the other detectors are very similar between 2018 and the other years. One can also find more detailed COMPASS setup in Fig. 2.3 based on 2010 configuration. The content of 2018 DY setup are described as follows : Special design of beam and targets will be described in Sec. 2.1.2 and Sec. 2.1.3, respectively. Many different kinds of tracking detectors and calorimeters composing the spectrometer are described in Sec. 2.1.4. Trigger system is described in Sec. 2.1.5. Except for the experimental setup in the experimental hall, the data acquisition system(DAQ), the Monte-Carol simulation software called TGEAT, the event-reconstruction software called CORAL, the data-analysis software called PHAST, are also discussed in Sec. 2.1.6(DAQ), and Sec. 2.1.7(TGANT, CORAL, PHAST).

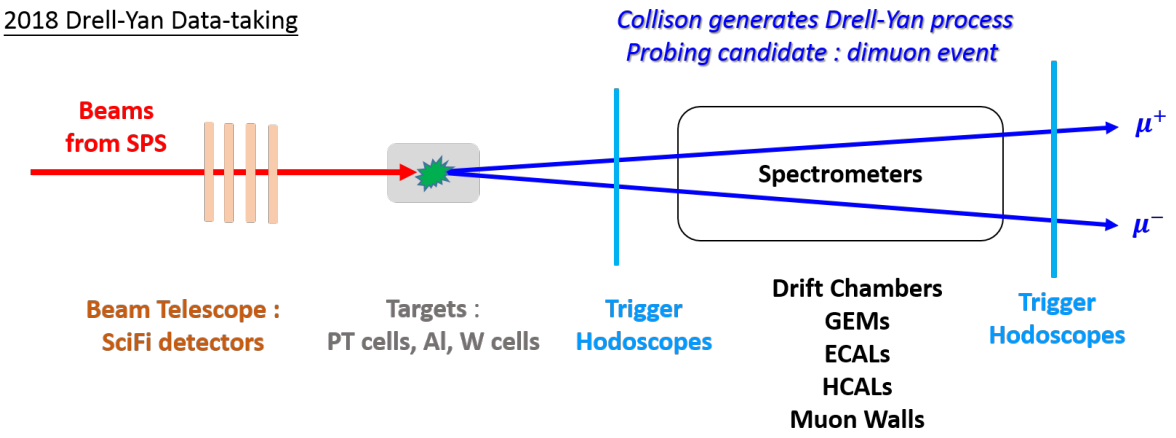

Figure 2.2: *The simplified sketch of COMPASS setup in 2018.*

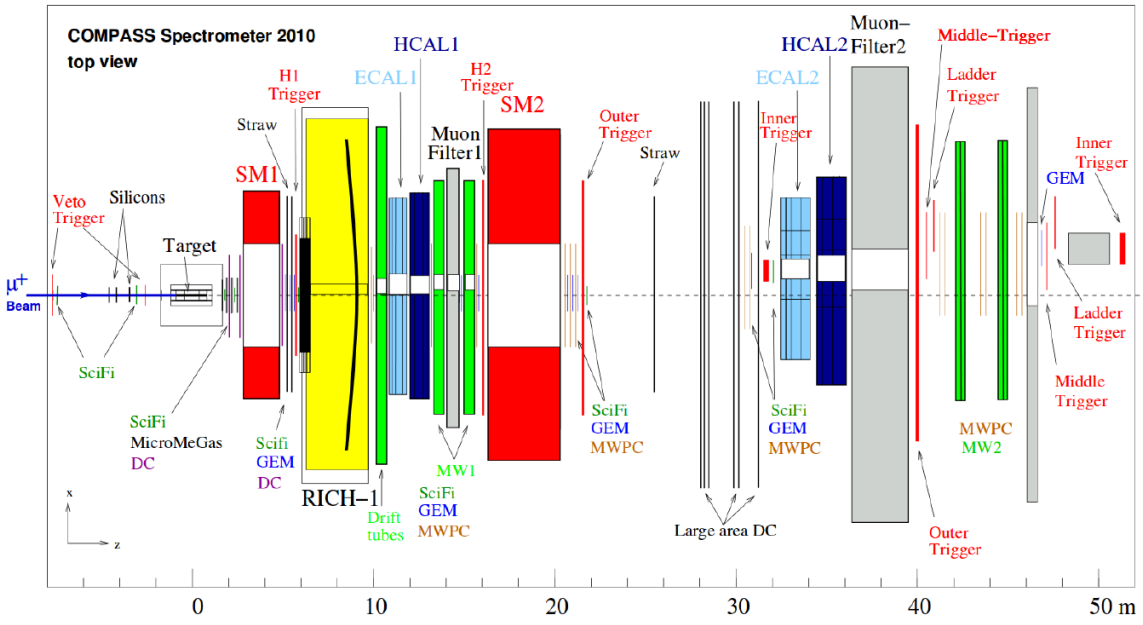

Figure 2.3: *The detailed sketch of COMPASS in 2010 [65].*

2.1.2 Beam

CERN M2 beam line The M2 beam line of SPS delivers various secondary beams : muon, proton, pion, and kaon beams for different physics purpose. The SPS super-cycle and spill length are varied according to the requirement of the experiments at CERN. Fig. 2.4 [66] shows the sketch of M2 beam line. The primary proton beam(400GeV and 10^{13} particles per super cycle) from SPS is scattering on a Beryllium target (T6) to produce secondary hadron beams, consisting of protons, anti-protons, pions and kaons. The thickness of T6 target is adjustable so that the secondary beam with various intensities are achieved. The momentum of secondary hadrons are selected by passing through a well-designed array of quadruples and dipoles magnets(TAX) after T6. After that, the secondary beam passes through a long decay tunnel around 650m, therefore a large fraction of pion decays into a muon and a neutrino. If muon beam is the one chosen to be used, a hadron absorber is placed after to stop all the hadrons. On the other hand, if hardon beams are the ones to be used, muon particels are removes with an array of quadrupoles again. Usually, five different beams are used by COMPASS :

- 160 GeV/c or 200 GeV/c muon($\mu^{\pm}$) beam
- positive hadron beams : 75% proton, 24% pions and 1% kaons, with momentum of 190 GeV/c.
- negative hadron beams : 97% pions, 2% kaons, and 1% anti-protons with momentum of 190 GeV/c.

As one can see, the beam types are used in COMPASS are mainly p, $\mu^{\pm}$, and π^{-}. The production rate of beam with $K^{\pm}$, $\bar{p}$, and π^{-} beam are still low. In 2018 Drell-Yan data taking, negative hadron beam(97 % π^{-}, 2% K^{-} and 1% $\bar{p}$) with the momentum of 190 GeV/c, in high intensity $\sim 6 \times 10^{7}/s$.

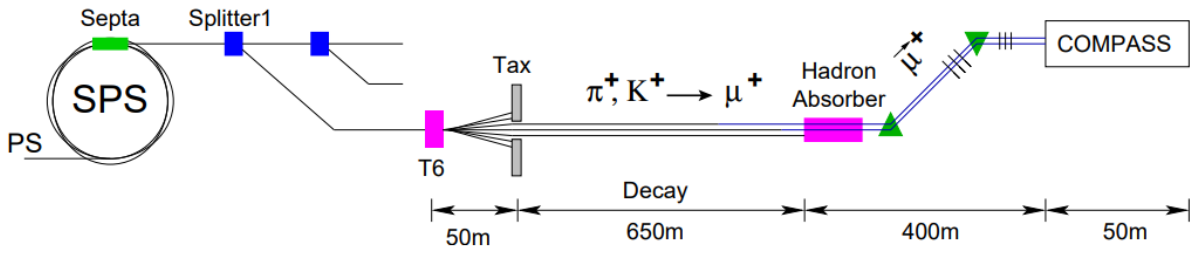

Figure 2.4: *Sketch of M2 beam line of SPS for COMPASS experiment at CERN [66].*

Beam Particle Identification Thanks to the diversity of beam CERN SPS delivered, there are various kinds of physics program to be studied. Muon beam is relative clean, while the pion, kaon, and proton from beam needs to be further disentangled. For this reason, Cherenkov Detector with Achromatic Ring focus (CEDAR) [67] detector in installed 30m upstream of the target region for the purpose of particle identification. CEDAR detector is a high pressure gas-Cherenkov counter composed by photo-multipliers tube (PMT) and optical lens in a high pressure environment with special gas. When particles enter the CEDAR chamber, it could radiate Cherenkov photons. Fig. 2.5 shows the sketch of CEDAR detector. The radiations from particles passing through lens can be focused on a ring whose opening angle is determined almost completely by the particle mass. Unfortunately, due to the high intensity beam, CEDAR did not function properly in 2018 Drell-Yan data taking. The beam particle identification between $\bar{p}$, π^-, and K^- was missing. Since negative hadron beam high percentage composition of π^- $\sim$ 97%, we claim that we use π^- beam with momentum of 190 GeV/c, high intensity $\sim 8 \times 10^7$, however it is not pure.

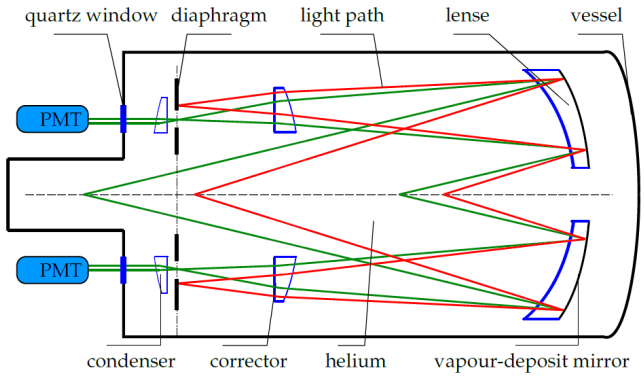

Figure 2.5: *A simplified schematic layout of CEDAR detector [67].*

Beam momentum Measurement Around 100m upstream of COMPASS experimental hall, there is a set of detectors called Beam Momentum Station (BMS) responsible for the measurement of beam momentum before entering the hall. However, it is turned off in 2018 DY data-taking because of the limitation of electronics responds to the high intensity $\sim 8 \times 10^7$. The incident momentum of beam in 2018 was not measured but extrapolated by the measurement of beam with lower intensity in 2014 (Fig. 2.6). The beam momentum given by the data reconstruction for real data is randomly assigned by COMPASS event reconstruction software based on the beam momentum profile measured in 2014. It is assumed that the beam momentum profile should be the same in this two years with the same beam energy 190 GeV/c.

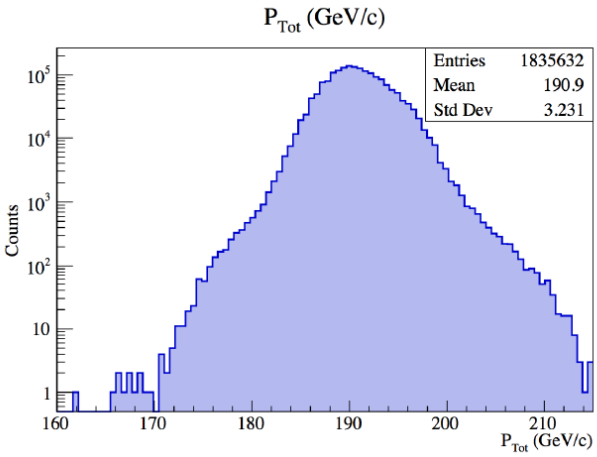

Figure 2.6: *The momentum profile of beam measured in 2014 with low intensity negative hadron beam. The same beam profile is also in 2018 [65].*

Beam Halo The ideal shape of beam is pencil-like. However, the beam delivered from M2 beam line has a halo component like a ring surround the concentrated beam. Halo beam hardly shots into the target but often fires a fact physics trigger. To avoid this, a set of hodoscopes made by sintillator counter placed right before the target area to detect halo beam. When the halo beam fires the hodoscopes, veto signal is generated and sent to the trigger system to block the generation of physics trigger at the same time. Veto hodoscopes take part of the trigger decision so it will be discussed further in the later trigger section, Sec. 2.1.5.

Beam Reconstruction Concerning the beam reconstruction, it is done by several fiber photon-multiplier detectors. The details of the beam telescopes will be discussed in Sec. 2.1.4.

2.1.3 Target setup

In 2018 Drell-Yan data taking, there are 3 kinds of targets used : two polarized ammonia targets (PT cells), alumina target(Al), and tungsten targets(W). Fig. 2.7 [65] shows the sketch of the target region, the relative positions of all the targets and hadron absorber. Two 55cm-long polarized targets are at the most upstream right. After polarized target, 7cm-long Al target and 120cm-long W targets are assembled inside the hadron absorber. W target are also used as beam dump therefore the total length is quite long. To avoid the reinteraction events, only the first 20cm W target is used in the analysis.

Absorber The hadron abosrber is a typical design for Drell-Yan experiment in order to absorb the decay hadrons and leave only muons pass. In the case for COMPASS, hadron absorbor is made of alumina tiles (Al_2O_3) inside a stainless steel frame. The front end is composed of aluminum. In the bottom surface, lithium plates are placed to reduce the radiation.

Polarized target The polarized targets are unique setups in COMPASS experiment. It allows us to have both transversely (perpendicular to beam direction) and longitudinally (parallel to beam direction) polarized nucleon targets so that the study of transverse and longitudinal spin asymmetries are possible. The machine of polarized targets are shown in Fig. 2.8. It is rather complex setup including the target material (NH_3) itself, the cooling system, the magnet system, and the microwave system. etc.

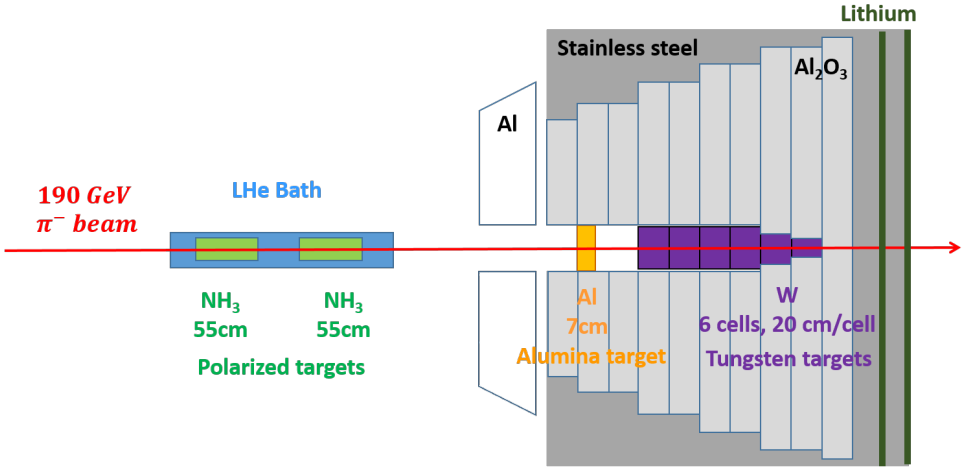

Figure 2.7: *The sketch of the hadron absorber and target cells. Two 55cm-long polarized targets are at the most upstream right. After polarized target, 7cm-long Al target and 120cm-long W targets are assembly inside the hadron absorber. W target are also used as beam dump.*

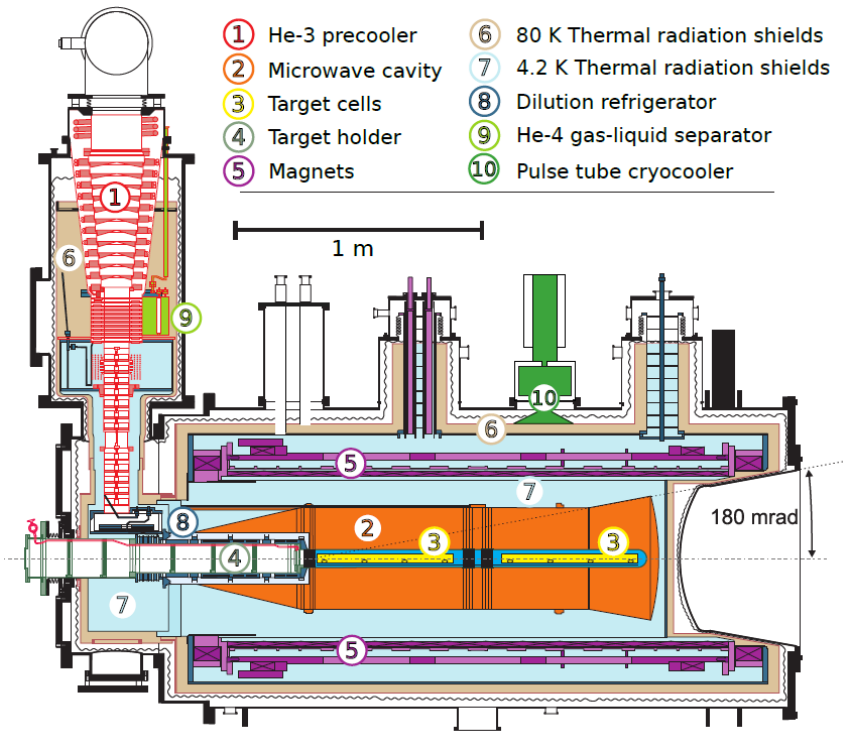

Figure 2.8: *The machine system of the polarized targets.*

Polarized targets are the mixture of solid ammonia beads (NH_3) and liquid helium (LHe) inside the 55cm-long target holders. Fig. 2.9 shows the materials used for polarized targets including a target holder(55cm long) and the Solid NH_3 beams. LHe bath is ^3He:^4He = 1:9 at the saturated vapor conditions∼60mK in order to keep the polarized target in very low temperature. The polarization of target uses the Dynamic Nuclear Polarization (DNP) technique [68] which transfers the polarization of the electrons to the polarization of the nucleons. The electrons are easier to be polarized than the nucleons, due to their larger magnetic moment. The transfer of the polarization from the electron to the proton is done using microwave radiation. The protons of NH_3 are polarized parallel or anti-parallel to the magnetic field. Note that, only the hydrogens are polarized. Longitudinal polarization requires a solenoid magnet and transversed polarization needs a dipole field.

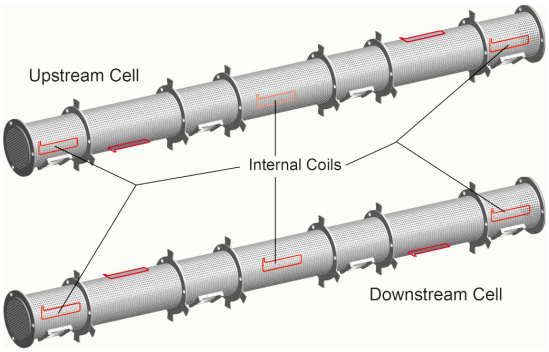

(a)

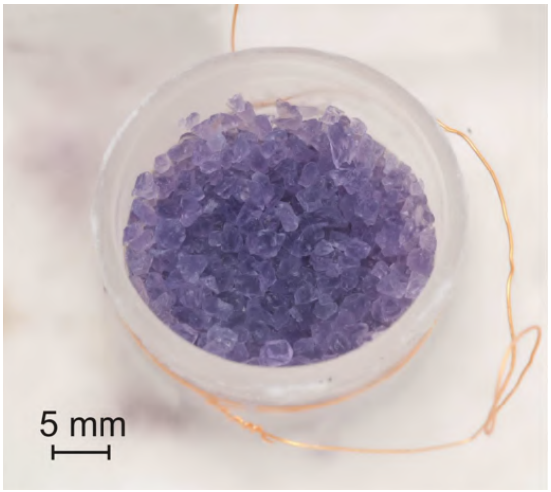

(b)

Figure 2.9: *The materials used for polarized targets : (a)target holder, (b)solid NH_3 beams.*

2.1.4 Detectors

The COMPASS spectrometer is drawn in Fig. 2.2 and Fig. 2.3. There are a large variety of tracking detectors divided into five groups :

- **Beam Telescope (BT)** : It measures the beam profile and intensity with two kinds of detectors, Scintillating Fiber(SciFi) detector with good time resolution $\sim 400ps$ and the Silicon Microstrip detector with good spatial resolution $\sim 10\mu m$. However, silicon microstrip detectors (maximum flux = $5 \times 10^7\ Hz/cm^2$) was not used in 2018 DY data-taking because they can't stand the high beam flux π^- beam $\sim 8 \times 10^6$.

- **Very Small Angle Trackers (VSAT)** : It is composed by tracking detectors measure the scattered particles. Since they cover the area very close to beam angle, the detectors stand high flux up to $5 \times 10^7\ Hz/cm^2$ and the fast electronics are required. Pixelized Micromesh Gaseous Structure(PMM) and Pixelized Gas Electron Multipliers(PGEM) are used for VSAT. PMM is in the center part of Micromesh Gaseous Structure (MM) detector and has a better spatial resolution.

- **Small Angle Trackers (SAT)** : It is composed of tracking detectors measures small angles covers from 8 mrad to 45 mrad. They stand the maximum flux up to 3×10^5 Hz/cm^2. There are two kinds of detectors, Micromesh Gaseous Structure (MM) and Gas Electron Multipliers(GEM).

- **Large Angle Trackers (LAT)** : It is composed of tracking detectors measuring the large angle tracks from 25 mrad to 165 mrad. They stand the maximum flux up to 1×10^4 Hz/cm^2. There are five kinds of detectors : Drift Chambers(DC), Straw Tube chambers(ST), Multiwire Proportional Chambers(MWPC), Large Size Drift Chamber(W45), and RichWall(RW). Since the requirement of detector response time is less demanding for LAT, the detector types here are usually drift-like detectors.

- **Detectors for Particle Identification (PID)** : To distinguish different kinds of particles, ex. proton, pion, kaon, and muons. Ring Imaging Cherenkov (RICH) detector identifies pions kaons and protons. Electromagnetic Calorimeter (ECAL) measures the energy of photons and electrons. Hadronic Calorimeters (HCAL) measures the energy of the hadrons. Muon walls (MW) are placed in the end of spectrometers to distinguish muons. In 2018 Drell-Yan data-taking, only the scattered muons are reconstructed, therefore only MW detectors are considered important in 2018 DY data-taking.

Except for the detectors, there are two magnets, SM1 and SM2. Both of them are dipole magnets with vertical fields perpendicular to the beam direction. The magnets allow us to determine the charge of particles and their momentum. The integrated field from top to bottom of SM1 and SM2 are 1 Tm and 4.4 Tm, respectively. The relative momentum resolution σ_p/p is about 0.5% in the SAS and 1.2% in LAS because of the bending power.

There are various kinds of detectors in COMPASS, so it will be too much to go through all the details of them. Some basic information of each detectors is provided in Table. 2.1 and the operation principle is described below :

- **Scintillating Fiber(SciFi)** : Scintillating fibre (SciFi) detectors in COMPASS provides the tracking of beams. It is a fast detector but can't built up with large size. It is made by several layers of very thin scintilator fibers as drawn in Fig. 2.10. The light outputs of groups of fibers are collected on photon-multipliers (PMT). Due to the large electronic signals after PMT, no front-end amplifiers are required. The fast leading-edge discriminators and TDCs are used. In COMPASS, there are different configurations of SciFi detectors : active area from $3.9 \times 3.9 cm^2$ to $12.3 \times 12.3 cm^2$, fibers diameter is 0.5nm, 0.75nm or 1nm. Depends on the configurations, The best spatial resolution 130 μm and time resolution 400 ps can be achieved.

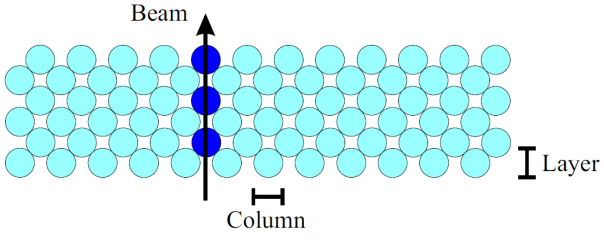

Figure 2.10: *Fiber configuration of a SciFi plane [69].*

Table 2.1: *Basic information of detectors in COMPASS 2018 Data Taking.*

Detector	# Det.	# Planes per Det.	Active area (cm^2)	Resolution
*** Beam Telescope (BT)**				
SciFi : 4 stations in different configurations, FI01, FI15, FI03, FI04				
FI01	1	X/Y	3.94 × 3.94	σ_s=130μm
FI15	1	X/Y/U(45°)	4.51 × 4.51	σ_s=150μm
FI03	1	X/Y/U(45°)	5.52 × 5.52	σ_s=130μm
FI04	1	X/Y/U(45°)	5.52 × 5.52	σ_s=130μm
*** Very Small Angle Trackers (VSAT)**				
PMM : 3 stations in the same configuration, MP01, MP02, MP03.				
MP[01-03]	3	X/Y/U(45°)/V(−45°)	2.5 × 2.5	σ_s=80μm
PGEM : 2 stations in the same configuration, GP02, GP03.				
GP[02-03]	2	X/Y/U(45°)/V(−45°)	10 × 10	σ_s=110μm
*** Small Angle Trackers (SAT)**				
MM : 3 stations in the same configuration, MM01, MM02, MM03.				
MM[01-03]	3	X/Y/U(45°)/V(−45°)	40 × 40	σ_s=110μm
GEM : 9 stations in the same configuration, GM01-GM09.				
GM[01-09]	9	X/Y/U(45°)/V(−45°)	32 × 32	σ_s=110μm
*** Large Angle Trackers (LAT)**				
DC : 4 stations in 2 kinds of configurations, DC00, DC01, DC04, DC05.				
DC[00-01]	2	2X/2Y/2U(10°)/2V(−10°)	180 × 130	σ_s=300μm
DC[04-05]	2	2X/2Y/2U(10°)/2V(−10°)	240 × 200	σ_s=300μm
ST : 2 stations in the same configuration, ST02, ST03.				
ST[02-03]	2	2X/2Y/U(10°)/V(−10°)	320 × 270	σ_s=400μm
MWPC : 14 stations with 4 kinds of configurations, PA*, PB*, PS*.				
PA[01-06], PA11	7	X/U(10°)/V(−10°)	180 × 120	σ_s=600μm
PB01, 03, 05	3	X/U(10°)/V(−10°)	180 × 120	σ_s=600μm
PB02, 04, 05	3	V(10°)/V(−10°)	180 × 120	σ_s=600μm
PS01	1	X/Y/U(10°)/V(−10°)	180 × 120	σ_s=600μm
W45 : 6 stations in 5 kinds of configurations, DW01-DW06.				
DW[01-02]	2	2X/2Y	520 × 260	σ_s=1500μm
DW03	1	2Y/2V(30°)	520 × 260	σ_s=1500μm
DW04	1	2Y/2U(−30°)	520 × 260	σ_s=1500μm
DW05	1	2X/2V(30°)	520 × 260	σ_s=1500μm
DW06	1	2X/2U(−30°)	520 × 260	σ_s=1500μm
RW : 1 station, DR.				
DR	1	4X/4Y	520 × 380	σ_s=600μm
*** Detectors for Particle Identification (PID)**				
RICH : 1 station, RICH.				
ECAL : 2 stations, EC01, EC02.				
HCAL : 2 stations, HC01, HC02.				
MW : 6 stations, MA[01-02], MB[01-02], MF[01-02].				

- **Micromesh Gaseous Structure(MM)** : MM was developed and first used in COMPASS. Fig. 2.11 shows the drawing of operation principle of it. It is composed by a conversion gap placed on the top an amplification gap below with a separation of a micro-mesh. The primary ionization takes place in the conversion gap, then drift to the micro-mesh. Afterwards, the primary ionization entering the amplification

gap creates the avalanche. The ions and electrons generated during the avalanche are collected by the mesh and readout strips. The mesh is designed to collect the ions in order to have a good time resolution. In COMPASS, it has $40 \times 40 cm^2$ active area with spatial resolution around $110 \mu m$. In 2015, all the MM were upgraded to have a pixelized region on its center (PMM in the center) so that the center parts $2.5 \times 2.5 cm^2$ can reach higher resolution $80 \mu m$.

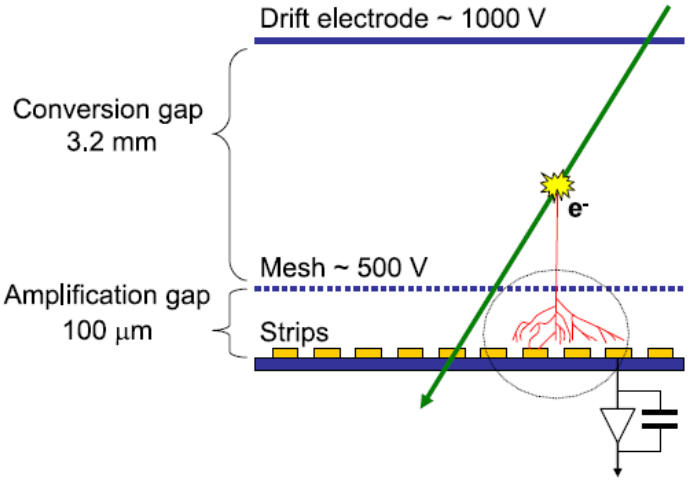

Figure 2.11: *Principle of MicroMega detector [69].*

- **Gas Electron Multipliers(GEM)** The GEM detector was also developed and first used in COMPASS, same as MM. Fig. 2.12 sketches the operation principle of the GEM detector. There are three amplification stages separated by 50 μm thin Polyimide foil with Cu coating on both sides. A large number of micro-holes $\sim 70 \mu m$ is drilled on the foil. A potential difference around 100V cross the foil holes. The primary ionization is created inside the drift gap and the avalanche multiplication happens in the holes. The 3-stages of the amplification guarantee the size of signals. In COMPASS, it has $32 \times 32 cm^2$ active area with spatial resolution around $110 \mu m$. There are two pixelised GEMs covers the small angle reconstruction with smaller active area $10 \times 10 cm^2$ and the same spatial resolution.

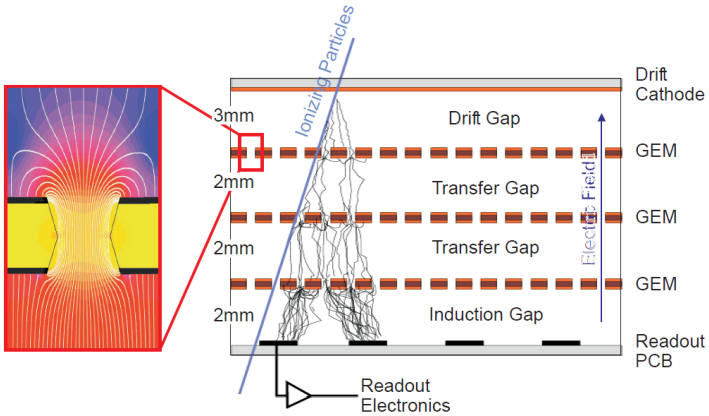

Figure 2.12: *Principle of GEM detector [69].*

Multiwire Proportional Chambers(MWPC) MWPC is one of the most basic wire chambers. It was invented by Georges Charpak and he got the Nobel Prize for Physics in 1992 because of this invention. The basic configuration of MWPC is drawn in Fig. 2.13. It is composed by two cathode planes and an array of anode wires. The wires are at ground potential and the cathode is applied with a high negative voltage. The particles fly through the gap, ionize gas atoms, and create the primary electron-ion pair. The avalanche generates when electron passing through the gap. In the end, the electron signal is collected by the anode wires then sent to the read-out in the end. The special resolution is decided by the space between wires. In COMPASS, there are 4 configuration of MWPC with wires in different orientations. The active area of them is $180 \times 120 cm^2$ and the special resolution is 600 μm.

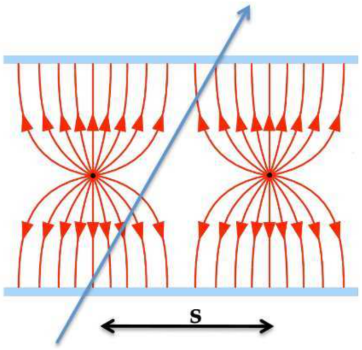

Figure 2.13: *Principle of MWPC detector [69].*

Drift Chambers(DC) One can consider it as the next generation of MWPC. A sketch of the operating principle is shown in Fig. 2.14. It is different from MWPC due to the special field wires are added to the design. Each stack of DC are made by two cathodes and a wire array composed by two kinds of wires, field wire and sense wire(blue). The negative cathodes and field wires are both applied to the same HV so that there is no potential between them. The sense wires(anode) are applied with positive voltage. MWPC and DC have a similar operation principle. The difference between MWPC and DC is the way how the avalanches "fly" to the anode. For MWPC, the potential in the gap changes intensively, therefore the avalanche moves towards the anode fast. For DC, the potential between field wire(cathode) and sense wire(anode) changes smoothly, therefore the avalanche slowly "drift" toward the sense wire and collected in the end. Since the drift velocity is predictable, the position of the ionization can be estimated from the time information of signal. In this way, the position resolution of DC is more precised than MWPC. More details of COMPASS drift chamber will be discuss in the next section Sec. 2.2. In COMPASS, there are two kinds of configurations of DC : one is with $180 \times 130 cm^2$ active area and another one is with larger active area $240 \times 200 cm^2$. All of them has spatial resolution around $300 \mu m$.

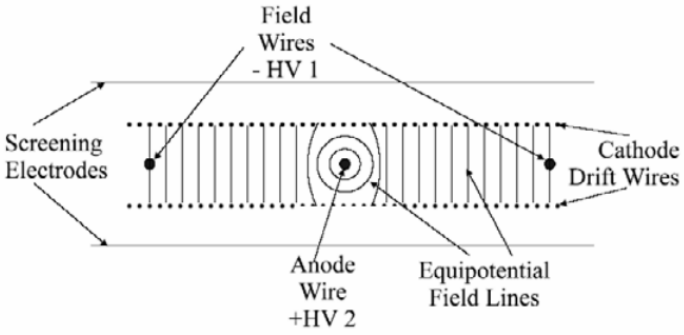

Figure 2.14: *Principle of DC detector [69].*

- **Rich-Wall(RW)** Fig. 2.15 shows the basic elements of RICH-Wall detector, Mini Drift Tube (MDB). A MDT module consists of eight aluminum cubes covered with a Noryl envelope. Each module has a gold plated tungsten wire placed in the center as an anode collects electron signal. The operation principle is just like other wire chamber. In COMPASS, RICH-Wall has active area $520 \times 380 cm^2$ and the special resolution is around half unit, $600 \mu m$.

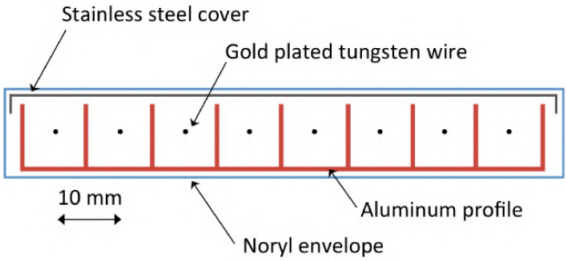

Figure 2.15: *Sketch of the basic elements of RICH-Wall detector - MDB module [69].*

- **Straw Tube Chamber(ST)** The basic configuration of straw tube is very similar to MDB but with round shape as meant for tube. The operation principle is also similar. In COMPASS, we have large area straw chamber with active area $320 \times 270 cm^2$ with spatial resolution around the size of the radius of the tube $400 \mu m$. The photo of basic element of ST is shown in Fig. 2.16.

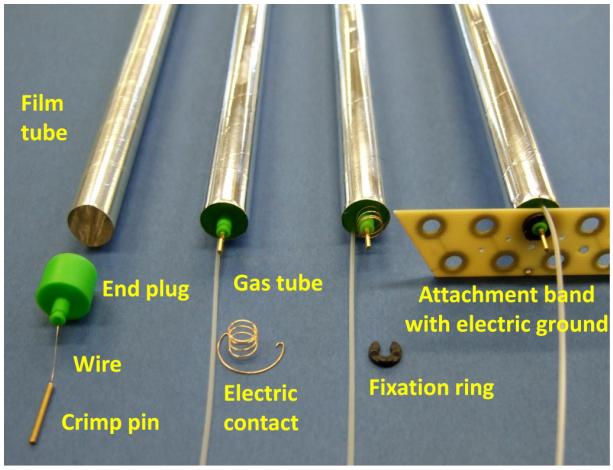

Figure 2.16: *The photo of basic element of ST from COSY experiment [70] .*

- **Ring Imaging Cherenkov detector(RICH)** RICH detector is used to separate hadrons(pions, kaons and protons) through Cherenkov effect. Cherenkov effect describes a particle travels in a medium with a velocity greater than the light speed and emits photons in a cone shape. The momentum and the type of hadrons affect the angle of the radiated photon - Cherenkov radiation. Fig. 2.17 shows the operation principle and the sketch of RICH in COMPASS. Cherenkov radiation is reflected and focused by two mirrors in the bottom of chamber and reflected to the windows collecting the photon signals. In COMPASS, the resolution of RICH is 1.2 mrad.

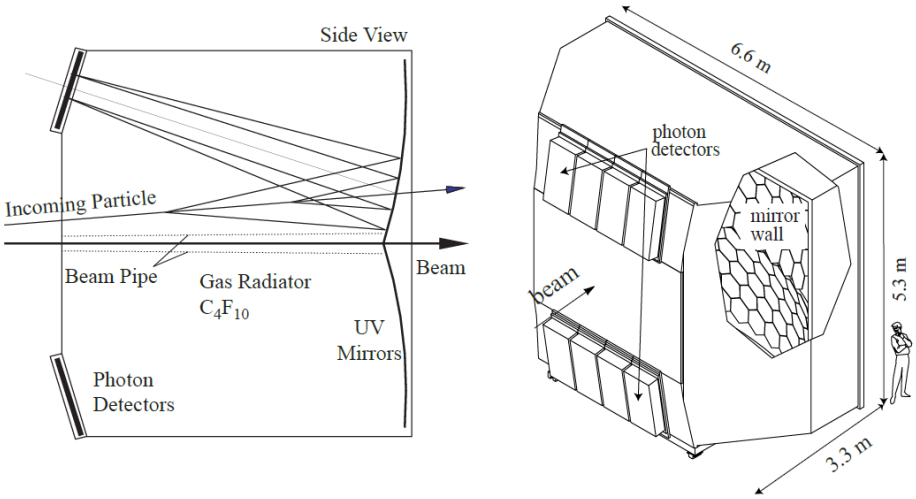

Figure 2.17: *Principle and sketch of RICH and detector in COMPSS [69].*

- **Electromagnetic Calorimeters (ECAL) and Hadronic Calorimeters (HCAL)** ECAL and HCAL are used to measure the energy of photons and electrons, and hadrons, respectively. In COPMPASS, both ECAL and HCAL are made by the stacks of iron absorbing the energy of particles and scintillator detectors to measure the energy lose of particle. Particle pass through iron and lose energy through the electromagnetic or hadronic cascades , measured by ADC. In COMPASS, the energy resolution are $\frac{\Delta E}{E} = 0.06 \pm 0.02$ and $\frac{\Delta E}{E} = 0.66 \pm 0.05$ for ECAL and HCAL, respectively.

- **Muon walls (MW)** MW system is composed of tracking stations and hadron absorbers made by heavy material shown in Fig. 2.18. Such design permits to distinguish the muons from the backgrounds like hadrons punch through from the HCAL placed in front of MW system. In COMPASS, there are two stations of MWs. They are important detectors for the DY data-taking since the measured particles are muons. MW1 is using 60cm-thick iron followed by 2 stations of MWPC and MW2 uses 2.4m-thick concrete block followed by 3 stations of MWPC. The special resolution of them are 3mm and 1mm for MW1 and MW2, respectively.

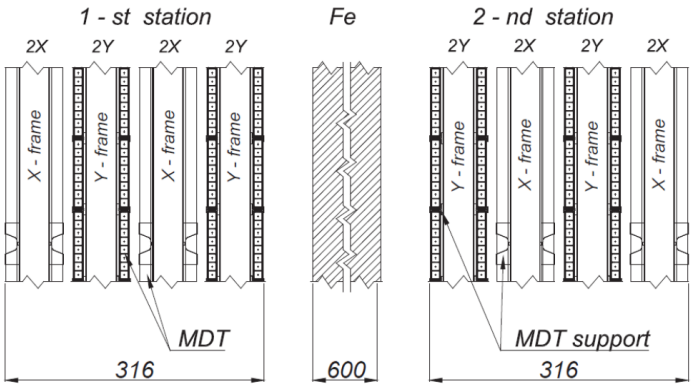

Figure 2.18: *Design of MW1 detector in COMPASS [69] : 60cm-thick iron followed by 2 stations of MWPC.*

2.1.5 Trigger system

The general purpose of trigger system is as follows : (1) It helps to be more precised in the selection of physics events and ease the stress toward data acquisition system, (2) A specific kinematics domain could be chosen through the design of trigger, (3) It provides a time reference of the whole redout system of detectors and DAQ. The trigger system is usually built based on scintillator counters or so called hodoscopes. Scintillator counter is feather with the good timing resolution up to a hundred picro-second and with a very fast responds time. Most of the triggers in COMPASS are composed by scintillator counter, such as Beam Halo Veto Trigger(BHVT), Large Angle Spectrometer Trigger (LAS), Outer Trigger(OT), Middle Trigger(MT). While calorimeter trigger(CT) is composed by HCAL signals and Random trigger(RT) is generated by the signal of natural radiation source. The sketch of COMPASS triggers in 2018 is shown in Fig. 2.19 and the details of each trigger are introduced as follows :

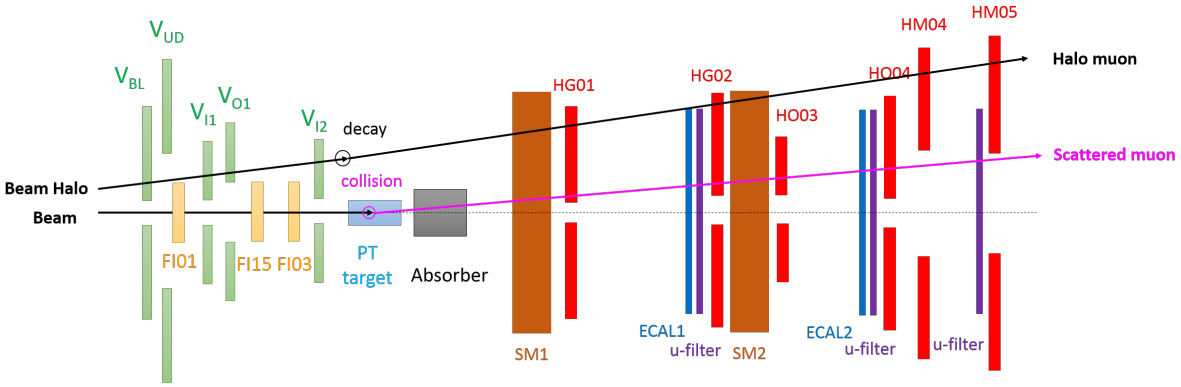

Figure 2.19: *Sketch of trigger hodoscopes in 2018 COMPASS DY data-taking.*

- **Beam Halo Veto Trigger (BHVT)** In Sec. 2.1.2, we had discussed the beam concerning its composition, etc. Ideally it is pencil like, while in reality there is a ring shape beam called beam halo. The beam halo does not collides with target but could also trigger the hodoscopes for physics process (HG, HO, HM labeled in red) due to the halo muon decays as drawn in Fig. 2.19. To avoid this situation, the hodoscopes for the beam halo detection are placed before target region, such

as $V_{beamline}(V_{BL})$, $V_{inner1}(V_{I1})$, $V_{inner2}(V_{I2})$, and $V_{outer1}(V_{O1})$ labeled in green. Beam Halo Veto Trigger (BHVT),in short VETO, is generated by the OR coincidence of all the veto hodoscopes, VETO $= V_{BL} \parallel V_{I1} \parallel V_{I2} \parallel V_{O1}$. VETO signals are anticoincidented with the signals of physics triggers. It is an effective trigger to avoid unwanted events when the experiment operates under high beam intensity condition like 2018 DY data-taking. However, it also creates the disadvantage, VETO deadtime, causes the lose of true physics triggers during the time window of the coincidence between VETO triggers and physics triggers. The measurement of VETO deadtime will be further discussed in Sec. 3.2 since it is required for the measurement of the Drell-Yan cross section.

- **Single Muon Trigger : LAS, OT, and MT** Single muon trigger detect muon tracks as it is named. There are three single muon triggers in COMPASS. From large opening angle to small opening angle, they are Large-angle Trigger(LAS or LT), Outer-angle Trigger(OUT or OT), Middle-angle Trigger(MT). They are all composed by horizontal hodoscopes (horizontal direction respects to the beam direction).

  Fig. 2.20 shows the concept of the generation of single muon trigger. Use LAS as an example, it consists of two sets of hodoscopes, HG01 and HG02. The scattered muon fires one strip of each HG01 and HG02. The signals from HG01 and HG02 are sent to coincidence matrix which decides the combination of two strips is validated as physics events we are interested or not. The coincident signal($HG01 \times HG02$) later coincides with VETO signal to exclude the possibility from beam halo. In the end, LAS trigger is formed by the logic of "$LAS = HG01 \times HG02 \times VETO$".

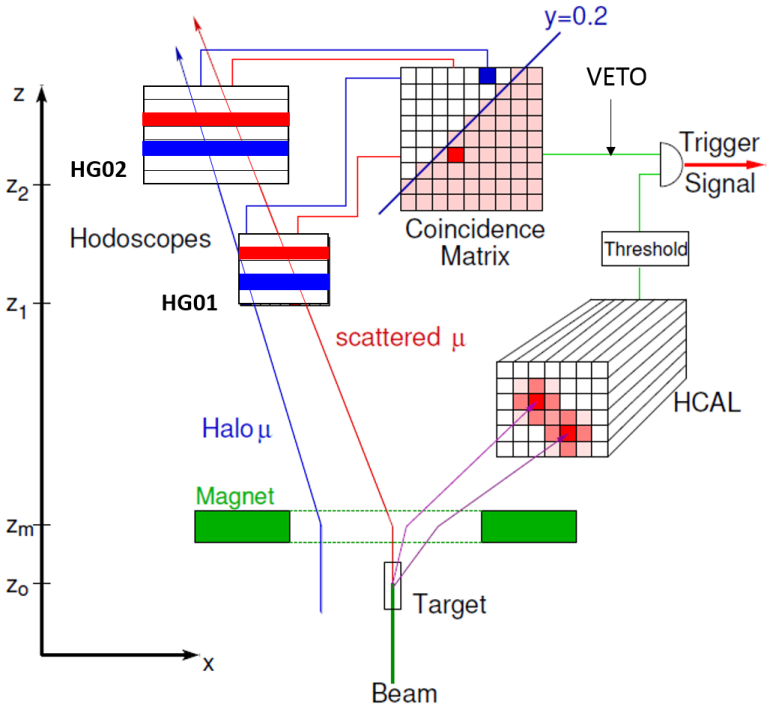

Figure 2.20: *Concept of trigger generation of LAS trigger and calorimeter trigger [69].*

The same concept can be applied to the other two single muon triggers, OT and MT. OT is formed by the signals of HO03, HO04, and VETO. MT is formed by HM04, HM05, and VETO. The coincidence matrix allows us to chose the kinematics of physics event and the sensitive target region (target-pointing). The design of the matrices are optimized with Monte-Carol simulation. The kinematic domain of each trigger is shown in Fig. 2.21.

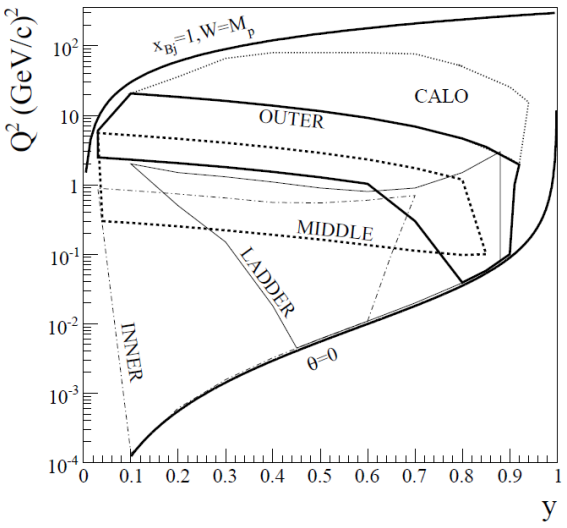

Figure 2.21: *The kinematic coverage of triggers in energy Q^2 and rapidity y. The black-solid linesat $x_{Bj} = 1$, $W = M_p$ and at $\theta = 0$ show the kinematic limits of the trigger system in COMPASS. LADDER and INNER triggers are not used in 2018 DY data-taking. LAS covers the same kinematics domain as CALO trigger(CT) [69].*

- **Dimuon Trigger : LAS⊗LAS, LAS⊗OT, and LAS⊗MT**

  The dimuon trigger is formed by two single muon triggers and there are 3 kinds of dimuon triggers : LAS⊗LAS, LAS⊗OT, and LAS⊗MT. Fig. 2.22 shows the kinematic coverage of dimuon triggers in terms of x_F and dimuon mass $M_{ll'}$. Dimuon events of LAS ⊗ LAS are distributed in higher mass and low x_F region. In contrast, events of LAS ⊗ MT are sitting in the lower mass and higher x_F region (x_F is another representative of rapidity y).

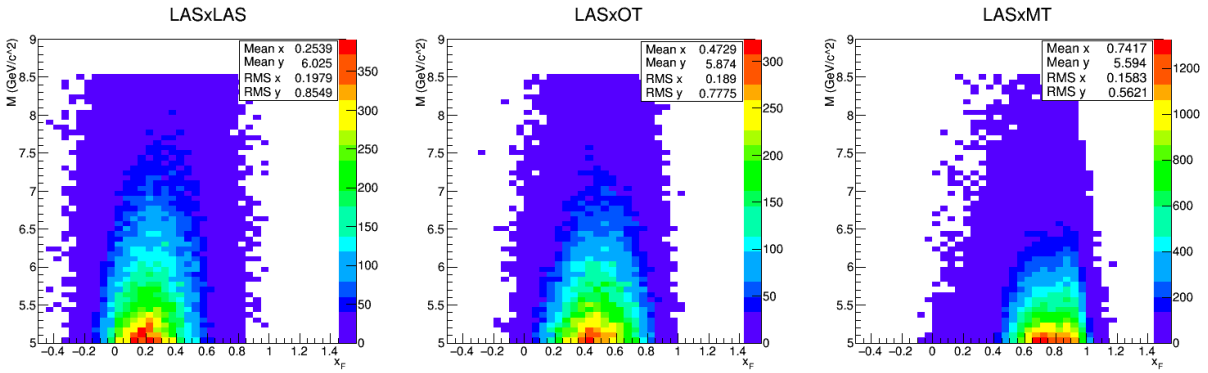

Figure 2.22: *The kinematic coverage of dimuon trigger in terms of x_F verse mass from the real data in 2018 DY data-taking. The x_F coverage from low to high are $LAS \times LAS$, $LAS \times OT$, then $LAS \times MT$.*

- **Calorimeter Trigger(CT)** The signals of hadron detection produced in the two hadronic calorimeters, HCAL1 and HCAL2 in COMPASS are used to form CT. A threshold is applied to ensure the energy of clusters of HCAL is above a certain value. The kinematic coverage of CT is as large as LAS. It is an unbiased trigger used for the dimuon trigger efficiency study.

- **Random Trigger(RT)** Two scintillator counters sandwich the Na-22 radiative source radiating the β photon and the coincidence signal of counters are used as RT. RT is an unbiased trigger not correlated with the timing of physics events so it is used for flux calculation mentioned in Sec. 3.1.

2.1.6 Data acquisition system

The Data Acquisition System(DAQ) in COMPASS receives data from more than 300k electronics channels. In the case of 2018 DY data-taking, DAQ has to deal with the event size per trigger around 45kB and the trigger rates is around 30 kHz in 6s spill time. During the off-spill time around 30s to 50s depending on the SPS super cycle, DAQ processes the data and send them to the 8 read-out engines.

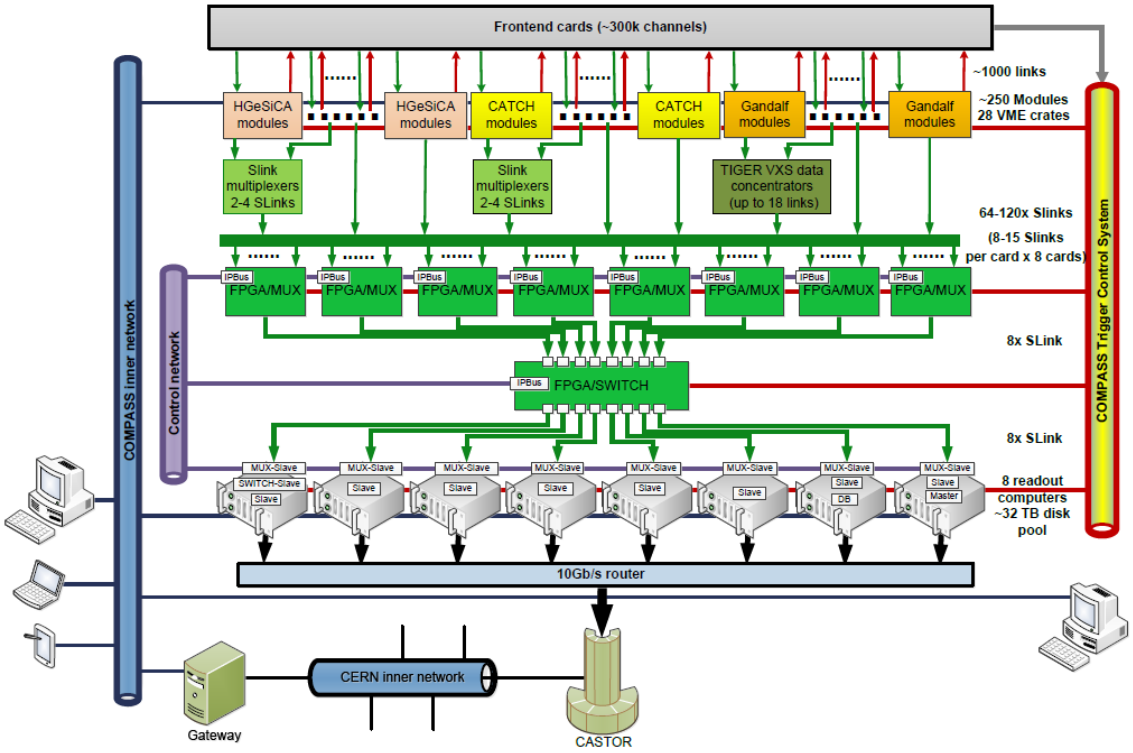

Figure 2.23: *Sketch of COMPASS DAQ system.*

COMPASS DAQ is a Field Programmable Gate Array (FPGA) based system as drawn in Fig. 2.23 [71]. The signals of the detectors are amplified and digitized by the front-end electronics(FEE) including Time-to-Digital Converters(TDC), Analog-to-digital converter(ADC). The digital signals are first sent to the first-stage data collection modules in COMPASS such as CATCH (COMPASS Accumulate, Transfer and Control Hardware), GeSiCA (GEM and Silicon Control and Acquisition), and GANDALF(Generic Advanced Numerical Device for Analog and Logic Functions). After the digitization of signals

from detectors, they are sent to the data-collection module responsible for collect data and build sub-event from several FEEs. The data-collection module also distributes the triggers and control signals sent from COMPASS Trigger Control System(TCS) to synchronize the events from multiple detectors. During the off-spill time, the data from FEE is processed through data-collection modules and sent to one of the eight read-out engine. The raw data needs to be reconstructed and then saved in the storage space at CERN, CASTER or EOS.

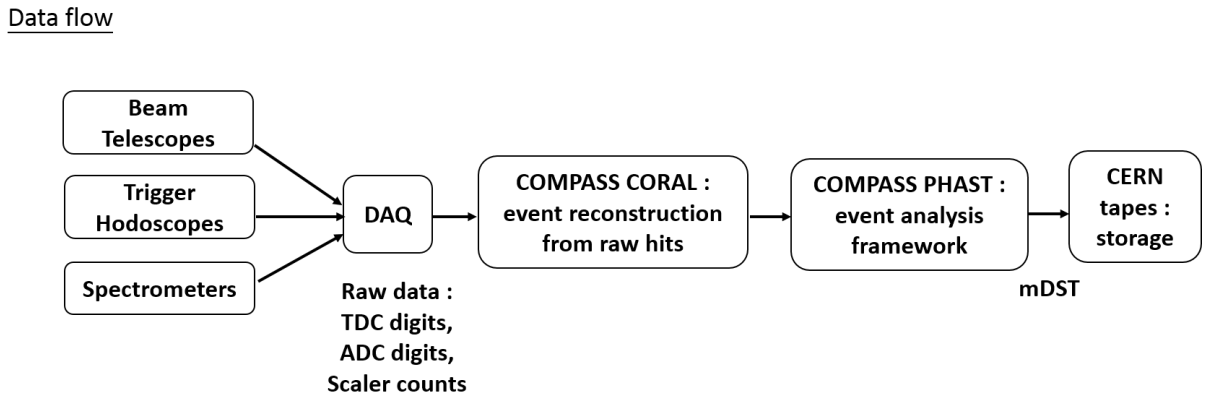

Figure 2.24: *The block digram of the data flow in COMPASS.*

In Fig. 2.24, it shows the whole data flow in COMPASS from detectors to CERN tapes. After saved the raw data collected from detectors, the construction of data is done with COMPASS softwares, CORAL and PHSAT. Afterward, the reconstructed data could be used for the physics studies.

2.1.7 COMPASS softwares

There are three kinds of softwares used for the COMPASS analysis : TGEANT, CORAL, and PHAST.

- TGEANT [72] : It is a Monte-Carlo software to simulate the experimental environments of COMPASS including detectors and targets. It is developed in C++ and based on Geant4 toolkit. To perform the Monte-Carol simulation, event generator, like PYTHIA, is operated with TGEANT.

- CORAL [73] : The track reconstruction software in COMPASS is named COMPASS RecOnstruction and AnaLysis, in short, CORAL. It reconstructs the events from raw data(hits) to the tracks and built up vertexes for the physics process. The information of tracks(momentum, energy, charges) and vertexes are all in the tree format called miniDSTs for the data-analysis.

- PHAST [74] : PHAST is a tool to analyze the data tree of COMPASS, miniDST. The full name is PHysics Analysis Software Tools. It is done with C++ language.

2.2 Drift chamber 05 in COMPASS

Drift Chamber 05 is a large-area planar chamber built as an upgrading project of COMPASS II to replace an old Straw Tube chamber(ST03). It is a joint project done by University of Illinois in US and Acadamia Sinica in Taiwan responsible for the construction of detector and electronics, respectively. DC05 were built in 2015-2016 and started to serve in COMPASS from 2016. It is a crucial detector for the track reconstruction in the large angle. In MC study, the reconstruction efficiency in large angle could drop 30 % without it [75]. Fig. 2.25 show the location of DC05 in COMPASS spectrometer, sits after the first-stage dipole magnet of COMPASS(SM1). In this section, the operation principle (Sec. 2.2.1), the construction of chamber (Sec. 2.2.2), the electronics (Sec. 2.2.3), and the performance (Sec. 2.2.4) of the detector will be discussed. Among the all, the electronics is going to be introduced in more details since it is the main hardware project for my phD journey.

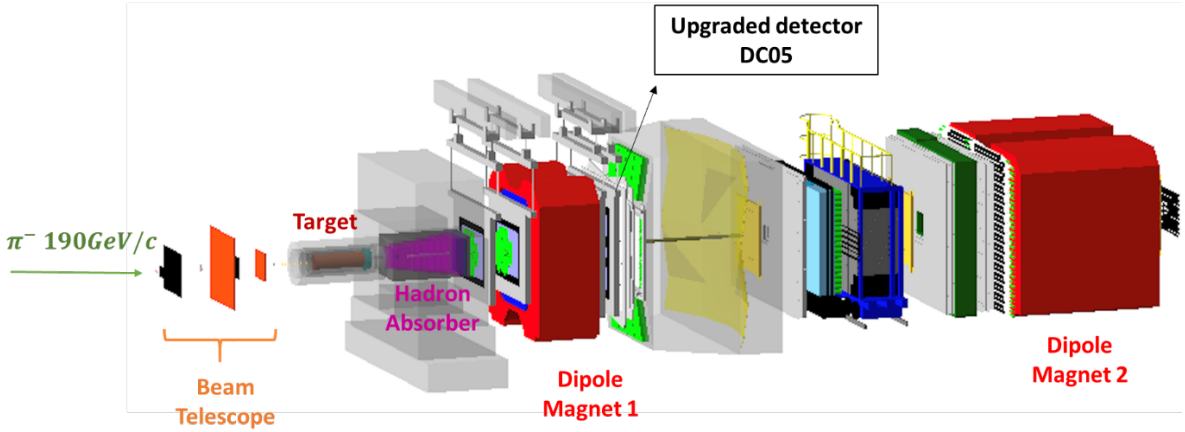

Figure 2.25: *Sketch of the location of DC05 in COMPASS spectrometer.*

2.2.1 Operation principle

A simple schematics of one basic unit of drift chamber is shown in Fig. 2.26. One basic unit is consist of two conductive planes sandwiching a wire array composed by two kinds of wires, field wires(Blue) and sense wires(Red) in a distance of 4mm. The two conductive planes and the field wires as cathodes are both applied with lower voltage compared to sense wires as anodes. In this structure, the field wires are also considered as cathodes since they are at the same electric potential as the conductive plates.

The formation of avalanches of drift chamber is just like the other gas chamber with with a small twist. The particles fly through the cell, ionize gas atoms, create the primary electron-ion pair, electron-ion pair move toward to anode, the avalanche generates during the movement, and the electron signals are collected by the anode in the end. An important feature of the drift chamber is that the position resolution is smaller than the cell size unlike the other kinds of gas chambers. A the good position resolution is resulted from the unique electric potential with the design of filed wires. The electric potential is nearly uniform between filed wires and sense wires so the primary electron-ion pair slowly drifts to toward to sense wire. The avalanche only occurs in the position very close to sense wire in the cell. The drift velocity is determined by the value of high voltage and the gas mixture. The location of the primary electron-ion pair is estimated by the drift

time, therefore the position resolution is better than the cell size, 8mm.

The gas mixture of drift chamber is similar to the other gas chamber : (1) noble gas to form the avalanches(ex. He, Ne, Ar, etc.), (2) quencher gas to absorb the emission of photon to prevent the second avalanches(ex. CH_4, C_4H_{10}), and (3) electronegative gas to limit the avalanche in a small area(ex. CF_3Br, CF_4). Different mixture of the gas could affect the amplification, the working HV, and the drift velocity of the chamber.

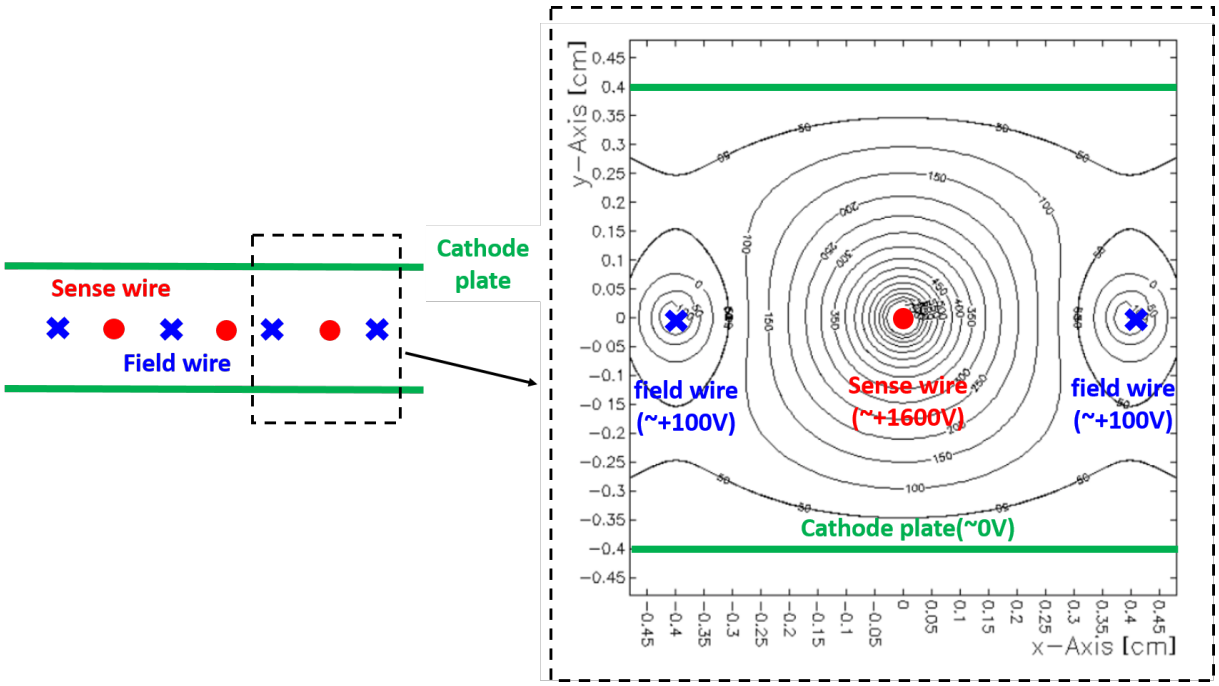

Figure 2.26: *Sketch of the profile of Drift chamber.*

2.2.2 Design and configuration of chamber

The design of DC05 follows that of the another drift detector in COMPASS, DC04. The active area is $249 \times 209 cm^2$. There are 8 planes (YY', XX', UU', VV') with 4 kinds of wire orientations : XX' in horizontal orientation, YY' in vertical orientation, UU' in $+10°$ orientation with respect to XX', VV' in -10° orientation with respect to XX'. X and X' plane are in the same orientation but with half cell shift with respect to each other as shown in Fig. 2.27. The design of the doublet planes with the same orientation allows us to decide weather the cluster is fired on the left-hand or right-hand of sense wire by judging the signal from the other plane. There are 256 sense wires for YY' and XX' planes, and 320 wires for UU' amd VV' planes. The space between sense wire is around 8mm called one cell. In total, DC05 includes 2304 sense wires and 2312 field wires.

The side view of the whole DC05 is drawn in Fig. 2.28. One stack (one doublet planes, XX', YY', UU', and VV') is composed by three layers of cathodes(drawn in black lines) sandwich the doublet planes composed by sense wires and field wires(drawn in red lines). The cathode plates are made from the carbon paint sprayed on a thin 25μm mylar layer. The sense wires is 20μm gold-plates tungsten wires. The field wire is 100 μm gold-plated-copper beryllium wires. G-10 frames (drawn in orange strips and blue strips) are used to support the structure of stacks and provide the isolation. The whole detector is closed with stainless steel stiffening frames (drawn in the grey strips).

In the right picture of Fig. 2.27, one can see the opening circles drawn in the center of

each plane called beam killer which is designed on the cathode planes. The inner parts of the opening circles are applied with smaller HV compared with the rest of cathode planes so that the efficiency of this area is lower than the rest of the area. The reason to do so is that drift chamber is a slow detector and it stand high intensity tracks mostly decay from the beam in the center region close to beam angle.

For DC05, the field wires and cathode plates are applied with -1675V and the sense wire is on the 0V. The distance between field wires is 8mm, same as sense wires. Beam killers are applied on -900V with a area of 30cm circular. The gas mixture of DC05 is 45% argon as ionization gas, 45% C_2H_6 (Ethane) as quencher and 10% CF_4 as electronegative gas. The nominal gain of DC05 is approximately 10^4, and the drift velocity is 67 $\mu m/ns$. Fig. 2.29 shows the photo of DC05 when moved into the experimental hall.

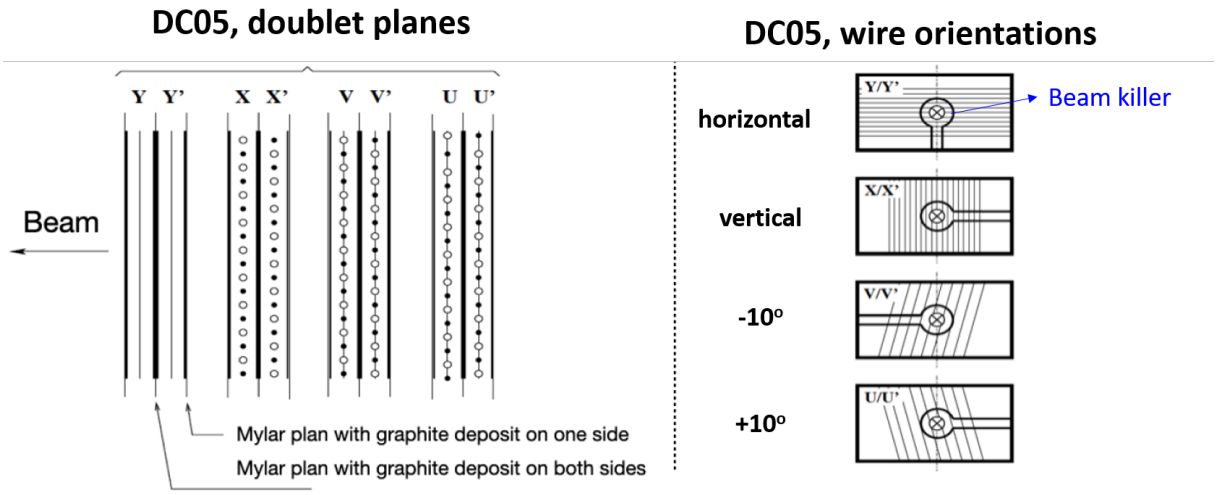

Figure 2.27: *The idea of doublet planes and the orientation of planes of DC05 [76].*

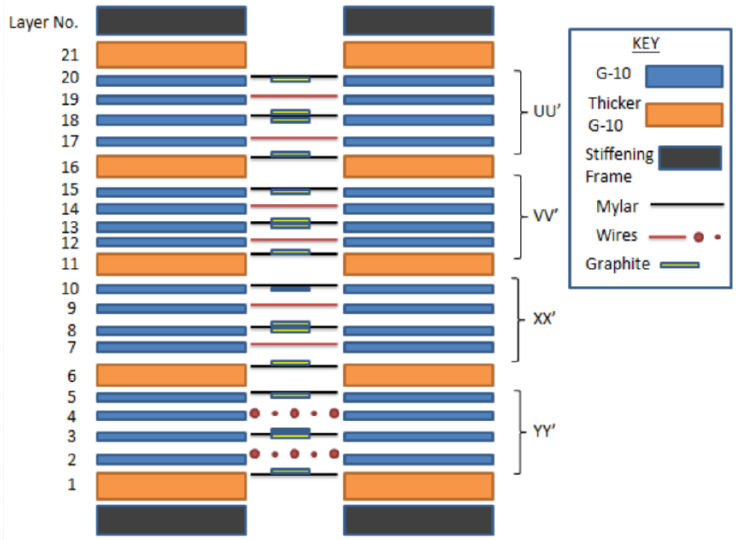

Figure 2.28: *The side view of DC05 [77].*

Figure 2.29: *The photo of DC05 when moved it to experimental hall.*

2.2.3 Front-end electronics

The Acedemia Sinica joined COMPASS and participated the DC05 project since 2012. The project of building the DC05 electronics is contributed by Dr. Wen-Chen Chang(project manager), Dr. Ming-Lee Chu(electronic engineer), Dr. Chih-Hsun Lin(electronics engineer), Yu-Sheng Teng(electronics engineer), Yu-Shiang Lian(graduate student) and myself. The significant helps from the phD student of Freiberg university in Germany, Tobias Grussenmeyer, and the postdoc of Illinois University in United States, Dr. Vincent Andrieux were essential.

There is 2304 readout channels(sense wires) of DC05. The goal of the DC05 electronics was to achieve 250um position resolution with 4fC threshold including the front-end electronics(FEEs). To satisfy this purpose, a high-gain and low-noise amplifier and TDC with resolution less than 1ns were designed.

Fig. 2.30 shows the block diagrams of electronic designed for one layer of DC05 (8 layer in total). The electronics of DC05 contains 3 modules, Front-End Module (FEM, 20 pieces per planes), Data Collection Module (DCM, 1 piece per plane), and a GANDALF module(8 planes share 1 pieces). FEM is the front-end electronics includes amplifier, discriminator and FPGA-based TDC to digitize the analog signal from chamber to readable signal. DCM is the first-stage multiplexer to collect TDC data from all the FEMs of one layer and sent them to the COMPASS-data-collection module, GANDALF. DCM serves not just as an data collection module for DC05 but also a trigger, clock, and control distributor sent from GANDALF and distributes them to all the FEMs. In order to simplify the cable mapping of the whole electronic system, DCM also serves as the power supply

for FEMs. GANDALF is a multiplexer commonly used in COMPASS experiment. It has almost the same purpose as DCM but without the function to distribute the low voltage to FEE. In total, there are 144 FEMs (16 FEMs for each plane of X, X', Y, Y' and 20 FEMs for each planes of U, U', V, V'), 8 DCMs (one layer for each), and 1 GANDALF used for DC05 with 8 planes.

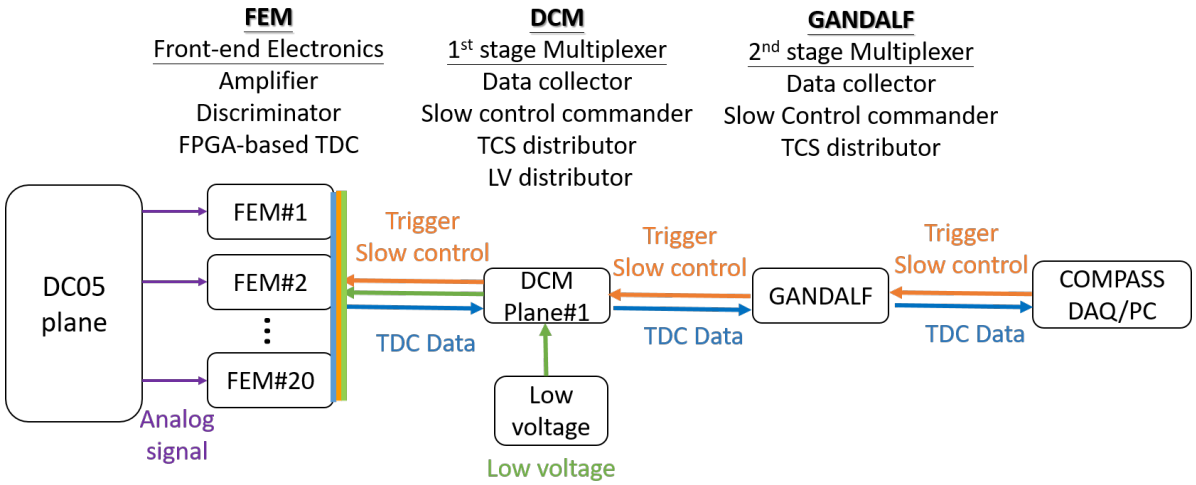

Figure 2.30: *The block diagram of DC05 electronics for one layer.*

The photo of FEM module is shown in Fig. 2.31 includes a chip called CMAD with the function of pre-amplifier and discriminator, and a FPGA-TDC. There are 16 channels on one FEM board. Two CMAD chips and one FPGA-TDC are placed on one FEM. The 5V low-voltage of FEM is provided by the next stage electronics, DCM. The data transmission, TCS signal from COMPASS DAQ, and the slow controls are communicated with DCM through Ethernet cable.

CMAD chip [78] is an 8-channel and ASIC chip combines amplifier and fast multi-stage discriminator, developed by INFN in Torino, ITALY. It is in the size of $4.7 \times 3.2mm^2$ with gain adjusted from 0.4 mV/fC to 1.2 mV/fC in steps of 0.08 mV/fC. The peaking time of the chip is 10ns with the speed 5MHz/ch. It consumes 26mW/Ch power from a 3.3V single source. It was designed and used for MWPC in COMPASS and later used in drift chamber.

After amplifying and digitizing the signals by CMAD, the drift time of DC05 are measured by FPGA-TDC. FPGA-TDC on FEM module is a RAM-based TDC. The block diagram of the design of FPGA-TDC is shown in Fig. 2.32. FPGA generates 233.328MHz clock from 38.888 MHz COMPASS global clock by using phase-lock-loop (PLL) technique, then shifting the 233.328MHz(4ns/period) clock by 0, 90, 270,360 degrees to reach the goal of TDC, 1.07ns time unit. The RAM-based buffer has 2047 addresses which could save the TDC inforamtion from 16 channels within 8761.16ns(2047 address*1.07 ns*4 phases). The timing of hits information are measured and saved in the RAM buffer before trigger arrives. When the trigger arrives, all the hits information contained in the buffer are transferred to DCM and the buffer is cleaned right afterward. FPGA-TDC can stand around 100kHz trigger beyond the requirement of 2018 Drell-Yan data taking with trigger rate around 30kHz.

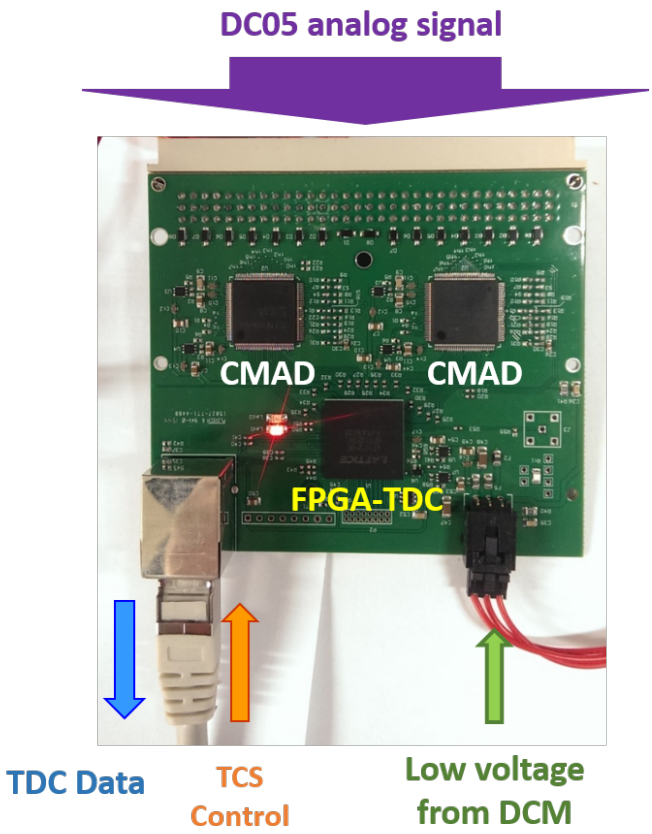

Figure 2.31: *The photo of FEM board.*

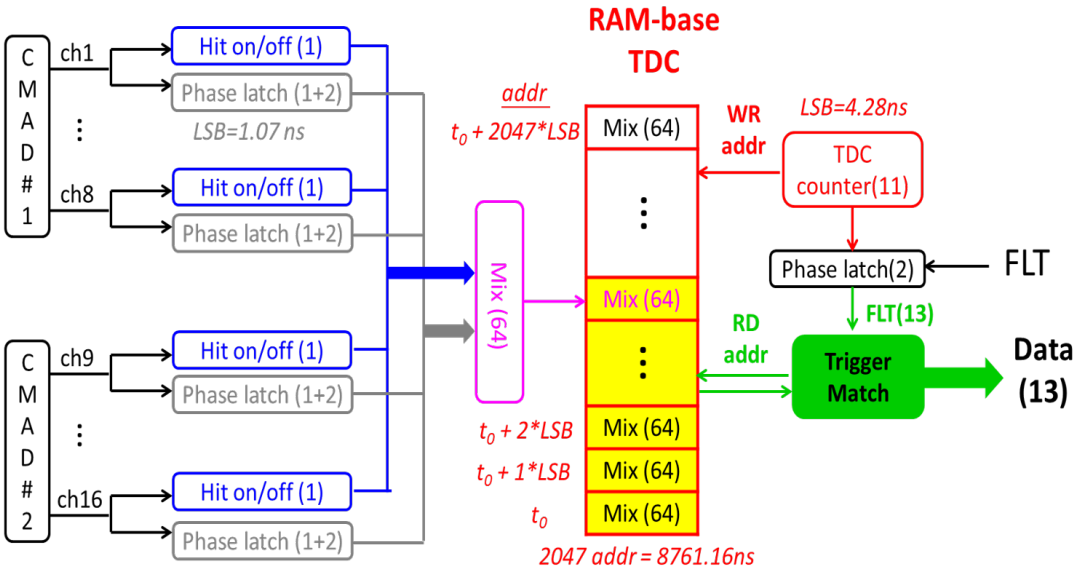

Figure 2.32: *The block diagram of the design of FPGA-TDC on FEM board.*

The photo of DCM module is shown in Fig. 2.33. It is a first order multiplexer which collect, encodes, buffers, and package the TDC data from 20 FEMs trough Ethernet, then transmits them to GAMDALF module through optical link. GANDALF module is an second stage multiplexer between DCM modules and DAQ system, which is developed and

designed by Freiburg University, Germany. The Trigger Control System (TCS) signal of COMPASS and the control of FEM/CMAD are distributed through Ethernet cable from DCM to FEM. To simplify the Low Voltage (LV) cabling, the power of FEMs are supplied by DCM through well-shielded twist pair. Note that the air cooling system was built to cool down the FPGA and power regulator since DCM board could be disfunctioned due to the overheat condition.

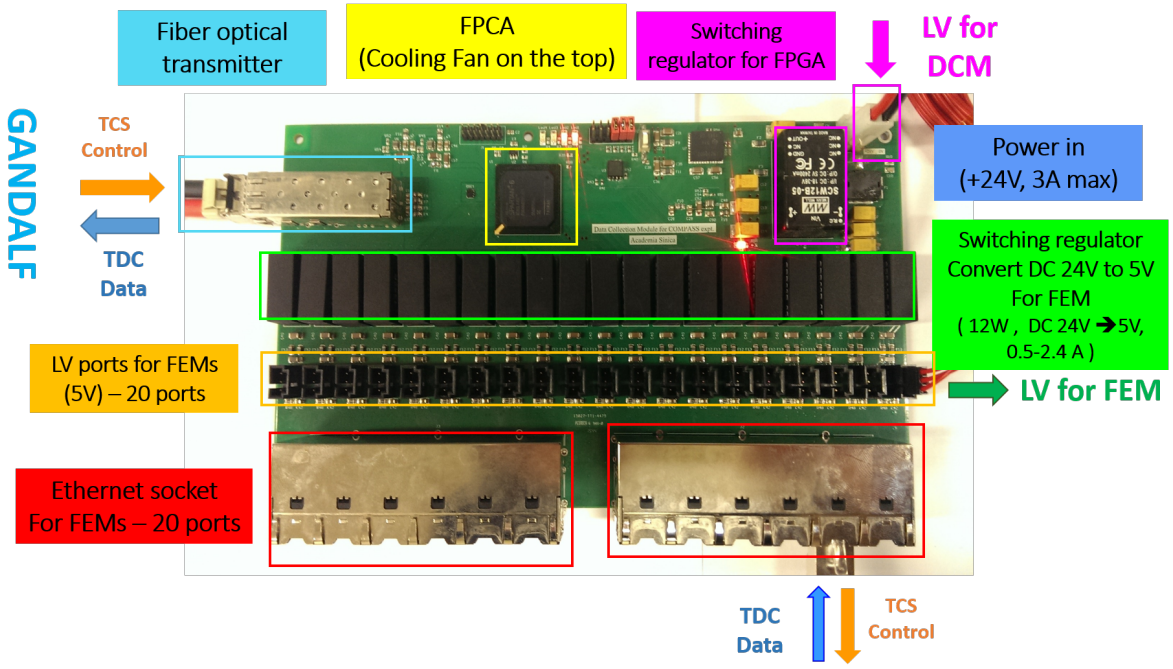

Figure 2.33: *The photo of DCM board.*

There was a serious issue occurred during the development of DC05 electronics. The first version of FEM was done already by the end of 2015. However, the FEMs were suffering with the power issue due to the neiboring strong magnetic field. The FEMs were installed very closely to the SM1 within 50cm distance. On FEM board, a power transformer used for the low voltage supply was placed inside the RJ-45 socket (RJ-45 also serves as a cable socket). It was a unique designed on purpose so that the signal line and power line between DCM and FEM are all bundled inside one Enternet cable with 4 twist pair inside. However, the power transformer made by coupling coil failed to function in the magnetic field. In 2015, we use iron plates to shield the RJ-45 socket from the magnetic field as a temperately solution. During the short break of the beam time from the end of 2015 to the beginning of 2016, we quickly produced the second version of FEM with another kind of RJ-45 socket without transformer on it. The low voltage cable between FEM and DCM were separated from Ethernet cable into another cable line. Power transformer is relocated on the DCM board.(DCM is further away from the magnetic filed.) Fig. 2.34 shows the comparison of FEM boards with the first version and the second version. The discussion above for FEM and DCM are based on the second version.

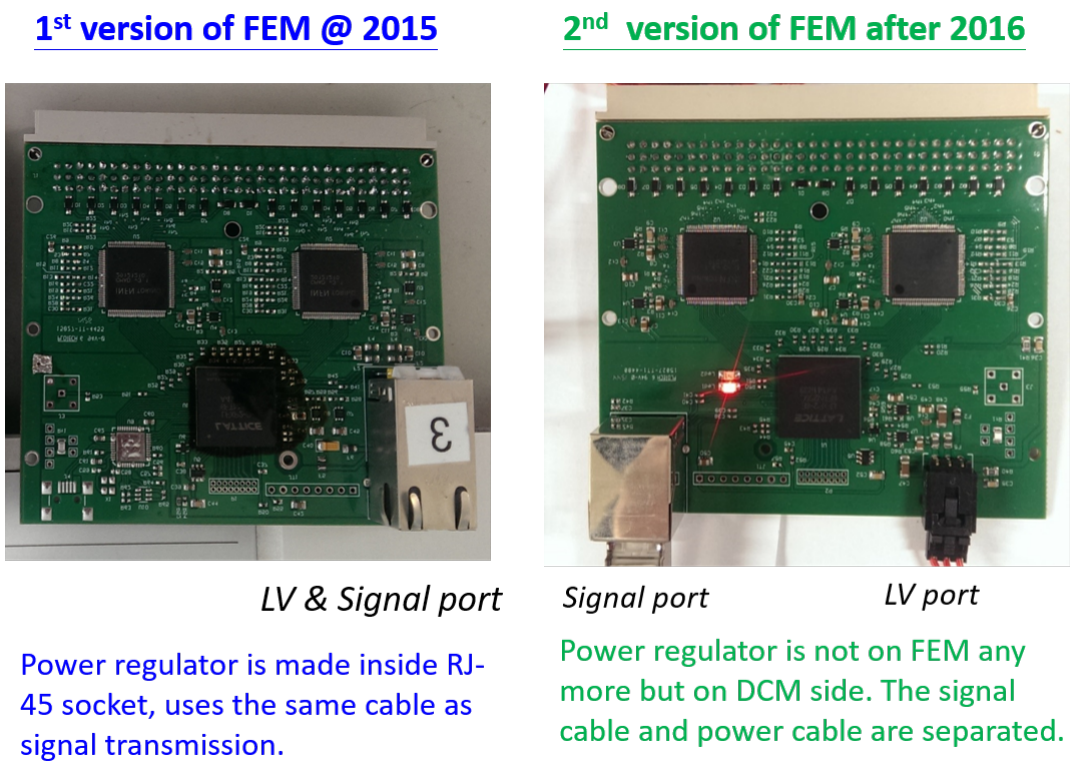

Figure 2.34: *The comparison of FEM boards between the first version and the second version.*

The project of electronics of DC05 started from the end of 2012 and was finally installed and ran without problems from 2016. During the development of DC05, there are numerous small problems, ex. noise issue(problem solved by reset the position of DCMs installed on chamber), event scrambling issue (due to the short buffering time designed in DCM software), etc. Fortunately, all of them were solved in the end. Fig. 2.35 and Fig. 2.36 show the photos of the work of the electronics installation in the COMPASS clean area.

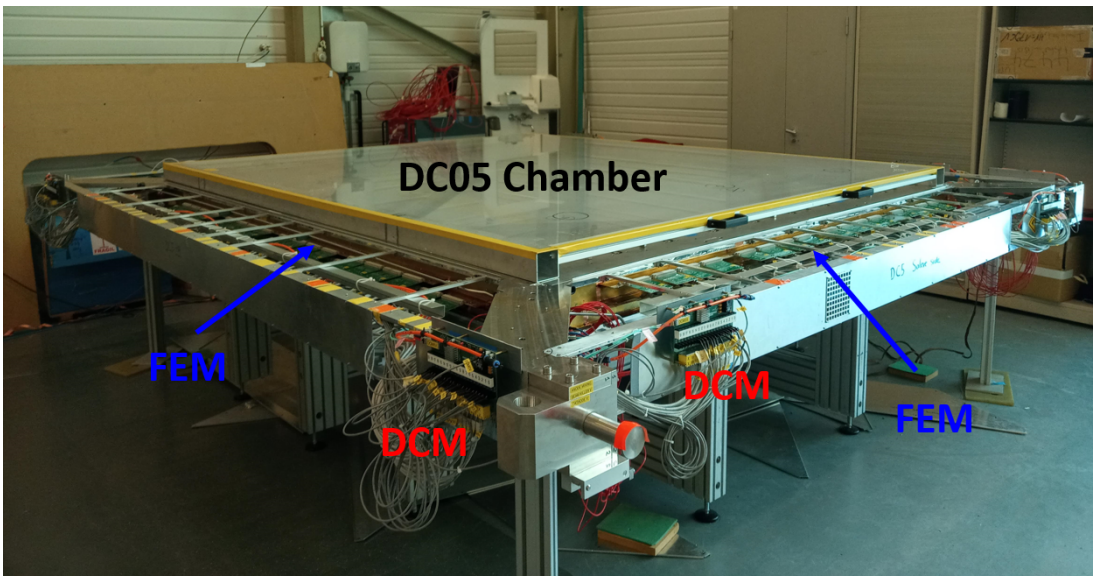

Figure 2.35: *The photo of electronics installation of DC05 in COMPASS clean area.*

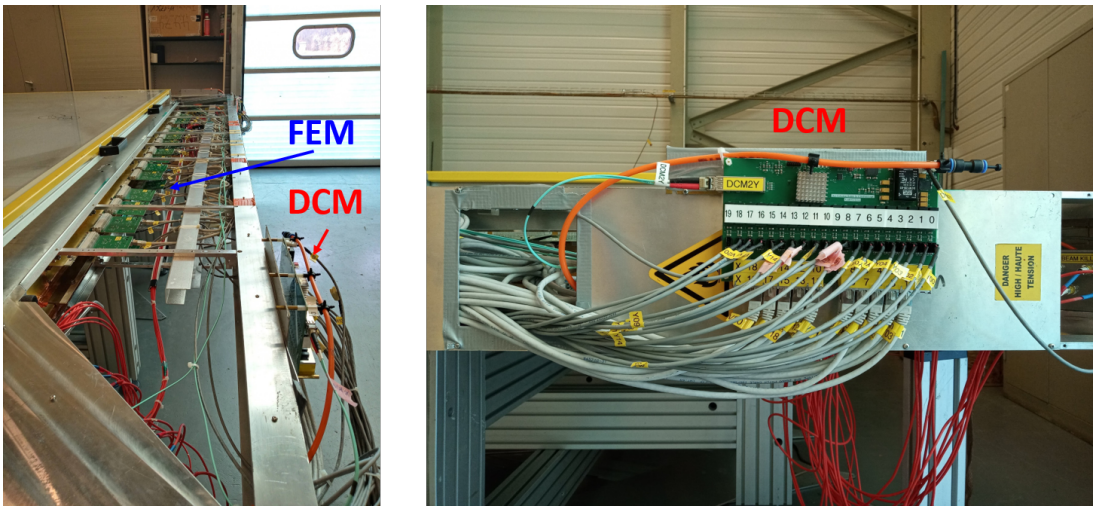

Figure 2.36: *The photo of electronics installation of DC05 in COMPASS clean area.*

2.2.4 Performance of DC05 chamber with FEE

As described in the operation principle of drift chamber, the position of track passing through the chamber could be determined with the drift time measured. The space-time correlation of drift chamber is mandatory to be prepared as the calibration material of drift chamber. Fig. 2.37 shows the drift-time spectrum on the left and space-time relation on the right of DC05 in high voltage of -1675V and 6fC threshold setup on CMAD. Here 6fC setup means the detected threshold of signal for electronics is 6fC. The working threshold of electronics and high voltage set of chamber were decided by the threshold scan and high voltage scan. The drift time spectrum on the right-hand side of Fig. 2.37 is the direct output of electronics without the trigger time calibration. The plot on the left-hand side is space-time relation(so called RT correlation) : T is the drift time with trigger time calibration and R is the drift distance between the extrapolated hit position of tracks and the sense wire. In this plot, R is determined by the other detectors in COMPASS spectrometer. With RT relation plot, the position of track can be determined by the drift time given by chamber. From the space-time correlation plot, the drift velocity of the electron cluster inside the chamber is estimated from the slope, $\frac{dR}{dT} \sim 67 \mu m/\text{ns}$.

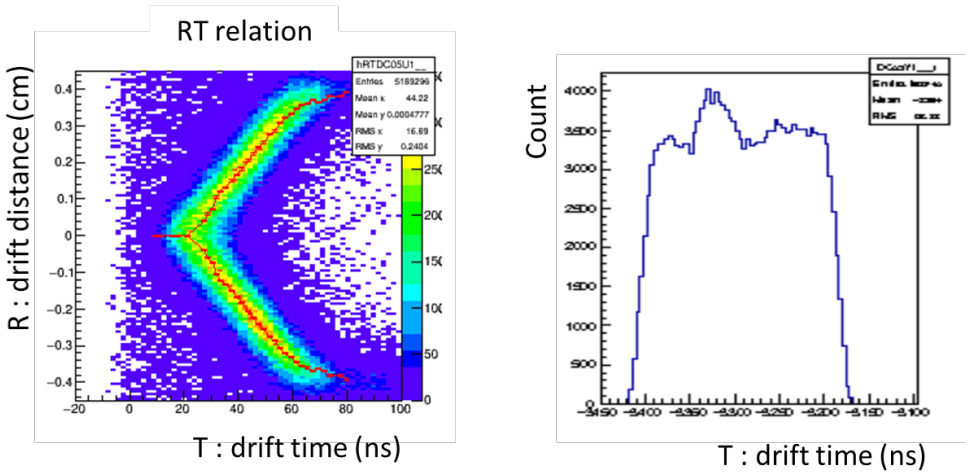

Figure 2.37: *(left)The space-time correlation of DC05.(right)The drift time spectrum of DC05 with π^- beam.*

In order to determine the working condition of chamber, the threshold scan and the high voltage scan were performed with 190 GeV muon beam in 2016. The results of threshold scan and high-voltage scan are shown in Fig. 2.38. The results given are all after the space-time calibration. As shown in the plot on left-hand side, with the increase of the high voltage applied on the cathode, the efficiency grows and the position resolution gets better. However, the efficiency of chamber starts to decrease slightly after -1675V. (Notice that the high voltage applied to DC05 is in the negative polarity.) It was suggested not to go beyond -1675V to keep the chamber working in the safe condition, therefore the high voltage scan stopped at -1675V. The ideal high voltage is chosen to be at -1675V which gives around 90% efficiency and 350μm position resolution. When the HV scan was performed, 6fC threshold was set on the signal discrimination.

The result of threshold scan is shown on the right-hand side of Fig. 2.38, in general the smaller the threshold set, the better efficiency and position resolution. However, the efficiency slightly drops around 6fC to 8fC. Notice that the threshold scan starts from 6fC, not zero. The electronics has its own intrinsic noise level, and 6fC is the threshold level which keeps the intrinsic noise level below 10Hz. The working threshold was decided at 6fC to 10fC depends on the noise condition during the data-taking. The efficiency and position resolution are around 90% and 350μm-400μm.

Fig. 2.39 shows the performance of the X plane of DC05 at working condition, high voltage = -1675V and threshold at 6fC. The plot on the most left-hand side is the space-time correlation of DC05. The red line is the calibration curve which is well aligned with the hits. The middle plot is the two-dimensional efficiency plot which gives 86.7±0.09%. The most right-hand side is the position resolutions after subtracting the tracking resolution which is 373.54μm. The goal of DC05 project was to achieve around 250 μm resolution with good efficiency. In the end, the performance is slightly worse than that but still reasonable.

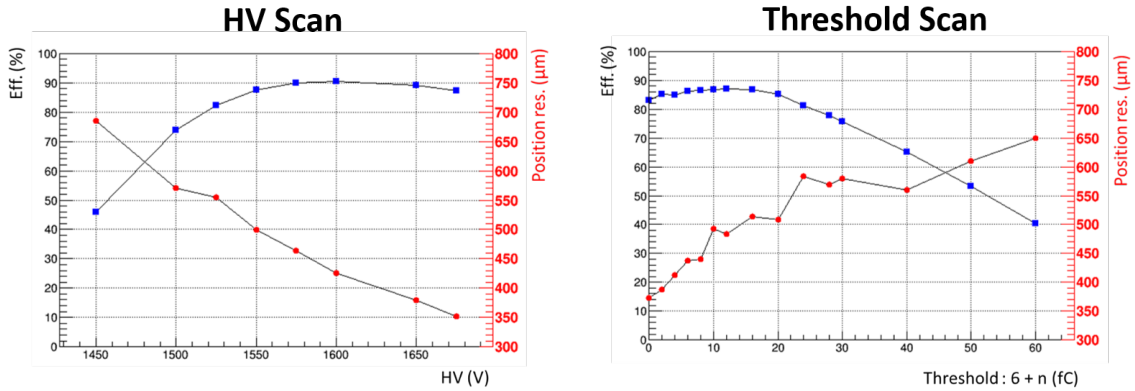

(a) *High voltage scan* **(b)** *Threshold scan*

Figure 2.38: *Efficiency and position resolution of DC05 with high-voltage scan. The scale on the left-hand side shows the averaged efficiency of one plane and on the right-hand side shows the position resolution. The high voltage is in the negative polarity.*

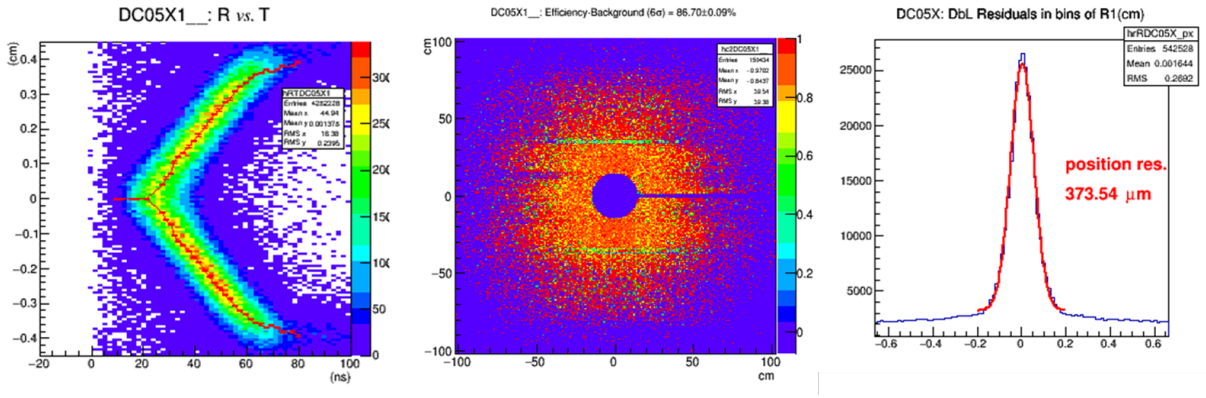

Figure 2.39: *Efficiency and position resolution of the X plane of DC05 at working condition, high voltage = -1675V and threshold at 6fC. (left) the space-time correlation. (middle) two-dimensional efficiency (right) postion resolution*

During the data taking, the online monitoring of DC05 was built. COOOL(Compass Object Oriented OnLine) is an online-monitoring software to consistently check the some important parameters of detectors. Fig. 2.40 and Fig. 2.41 shows the hit rate and drift time distribution of 8 planes of DC05 in 2016. The hit rate is around 10kHz to 100kHz. The high rate in the center of chamber is caused by the beam. The red line is the guided line gives the reference of nominal behavior of detector. During the data taking, if the drift-time spectrum or the hit spectrum is out of the reference, a warning will be issued and an action should be taken to improve.

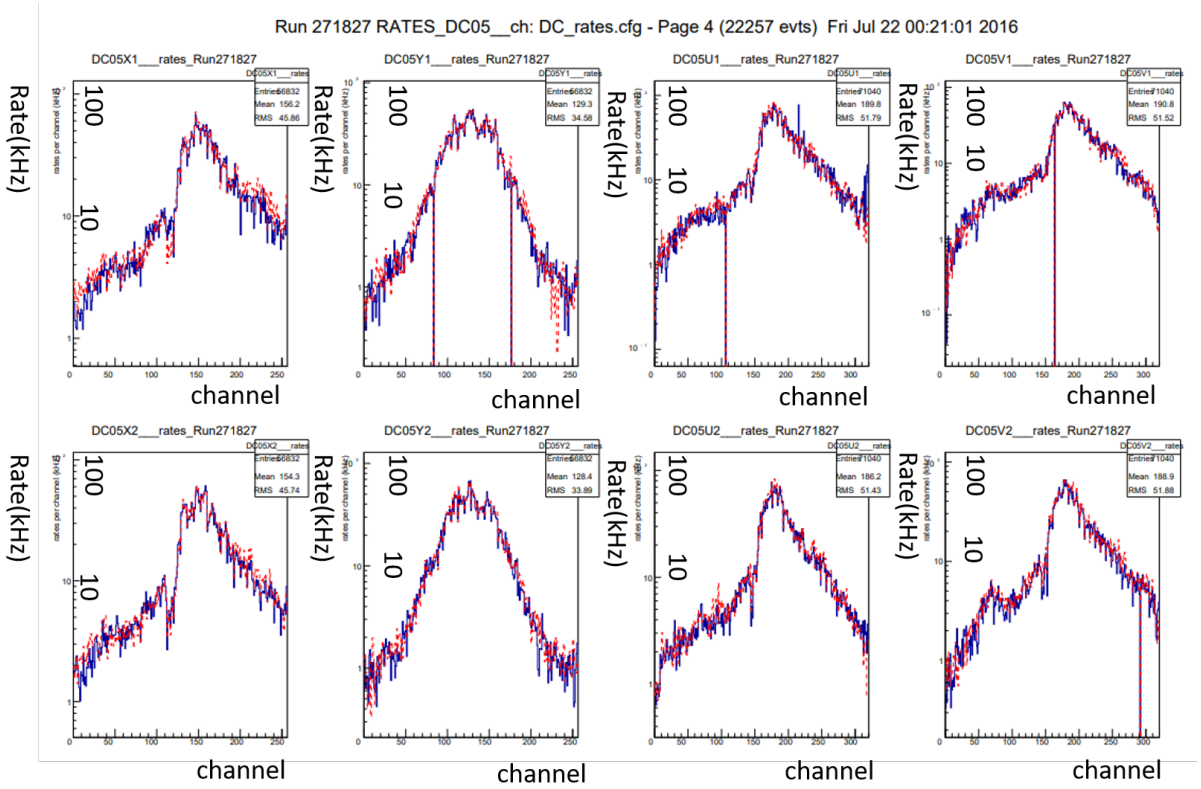

Figure 2.40: *The hit rate of DC05 from COOOL monitoring in 2016 data taking.*

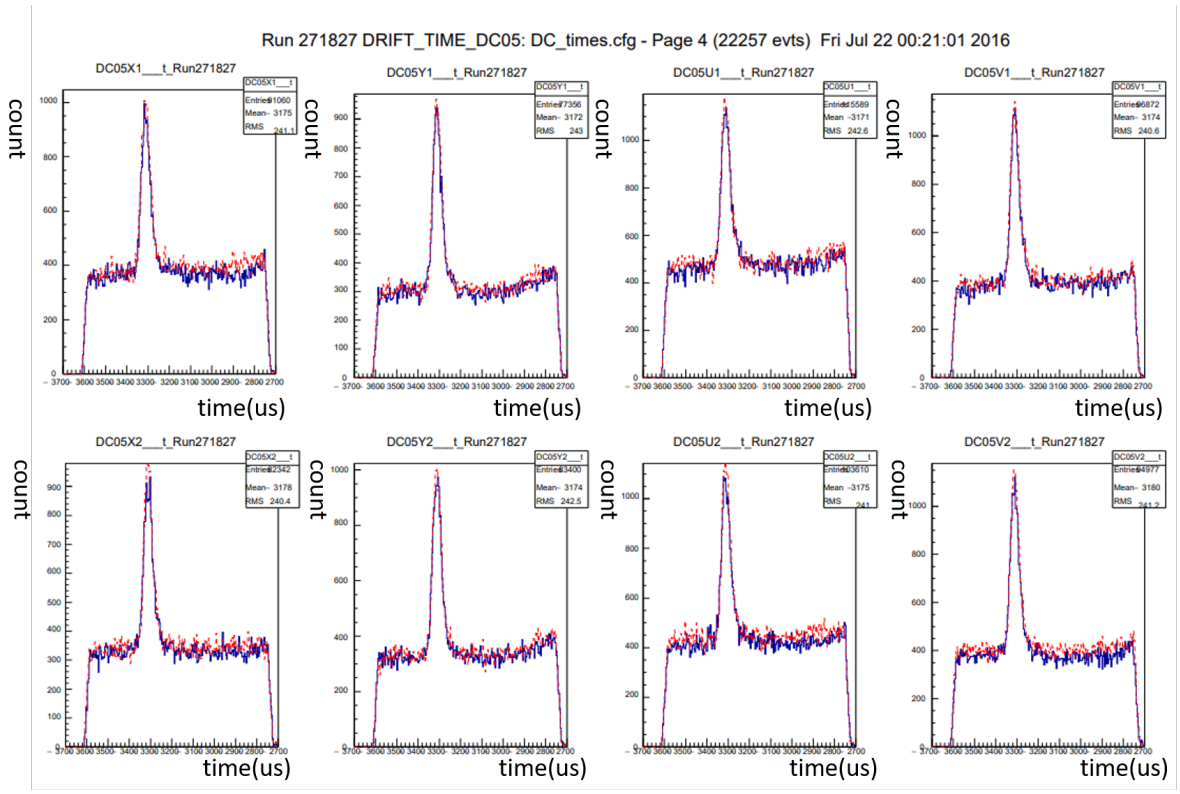

Figure 2.41: *The drift-time spectrum of DC05 from COOOL monitoring in 2016 data taking.*

Chapter 3

Measurement of Drell-Yan cross section in COMPASS experiment

The absolute Drell-Yan cross-section is an important result in QCD and in the determination of the pion PDF. This analysis presents pion-nucleus cross-sections obtained from the analysis of the COMPASS 2018 data on NH_3, Al and W targets. Furthermore, the COMPASS results are compared with the other pion-induced Drell-Yan cross-section measurements, NA10 and E615 experiments. The mean transverse momentum of Drell-Yan process is also extracted. Together with the global data, the mean transverse momentum extracted from COMPASS helps to the constrain of intrinsic transverse momentum of parton inside pion.

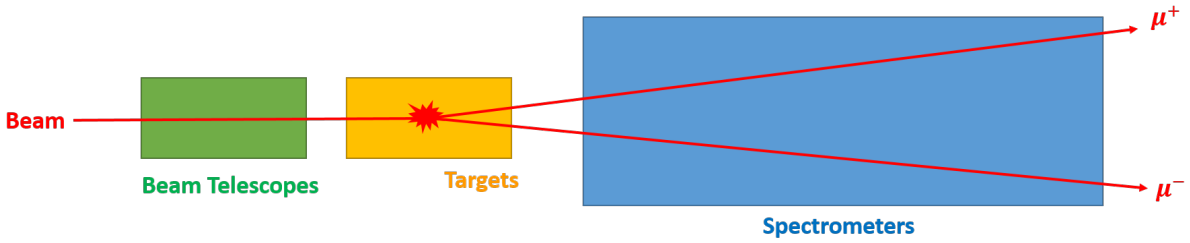

Figure 3.1: *The simplified illustration of the cross section measurement in the fixed-target experiment.*

The measurement of the cross section in a fixed-target experiment is illustrated in Fig. 3.1. The beams are injected into the fixed-targets. Most of the beams pass through the targets without any interaction, but some of them interacts with the nucleon inside the targets. In the case of COMPASS measurement in 2018, we tuned our triggers to interacts with two outgoing muon tracks with opposite signs. The beam telescopes measure the beams. The spectrometer measure the pathway, energy, and momentum of the outgoing dimuon pairs. The cross section is defined as follows :

$$\sigma = \frac{N_{true}}{\mathscr{L}} \tag{3.1}$$

where σ is the probability of a certain process $[cm^2]$, $\mathscr{L}$ is number of collisions per unit area so called luminosity $[cm^{-2}]$, and N_{true} is the number of events.

Luminosity $\mathscr{L}$ is further expressed as follows:

$$\mathscr{L} = N_{Beam} \times \rho_T$$

where N_{Beam} is the number of beams injected to the target cell measured by beam telescopes. ρ_T is the target density ρ_T $[cm^{-2}]$ calculated from the properties of targets.

The number of true physics events N_{true} is further expressed as below :

$$N_{true} = \frac{N_{measured}}{\varepsilon}$$

where N_{true} is the number of event happening, $N_{measured}$ is the number of events successfully constructed, ε is the efficiencies caused by the hardware limitations of the experiment such as the spectrometer acceptance, DAQ efficiency, VETO efficiency, etc. In the case of COMPASS experiment, the efficiencies are listed as follows :

$$\varepsilon = \varepsilon_{acc} \times \varepsilon_{DAQ} \times \varepsilon_{VETO}$$

where ε_{acc} represents the acceptance efficiency is obtained from MC including the spectrometers geometry acceptance, the detector efficiency, electronics efficiency, track reconstruction efficiency, beam telescope efficiency and analysis cuts. In COMPASS MC, there are only two efficiencies are not simulated, therefore they need to be estimated additionally. They are the DAQ lifetime ε_{DAQ} caused by tolerated rate capability of DAQ system and VETO lifetime ε_{VETO} caused by the beam halo VETO signals.

The cross-section is usually discussed in the multi-dimensional variable x_n, Eq. 3.1 is reformulated as below :

$$\frac{d^n\sigma}{dx_1dx_2...dx_n} = \frac{1}{\mathscr{L}} \times \frac{d^n(N_{measured}/\varepsilon)}{dx_1dx_2...dx_n}$$

where x_i is the kinematics studied. The analysis of Drell-Yan cross section will be presented in the details in the following sections :

- Sec. 3.1 : Measurement of Luminosity, $\mathscr{L}$.
- Sec. 3.2 : Measurement of DAQ Lifetime and VETO Lifetime, ε_{DAQ} and ε_{VETO}.
- Sec. 3.3 : Measured Drell-Yan dimuon as a function of kinematics, $\frac{d^nN_{measured}}{dx_1dx_2...dx_n}$.
- Sec. 3.4 : Extraction of acceptance, ε_{acc}, simulated from MC.
- Sec. 3.5 : Extraction of multi-dimensional Drell-Yan cross-section. $\frac{d^n\sigma}{dx_1dx_2...dx_n}$.
- Sec. 3.6 : Study of systematic uncertainties.

We will present the differential cross section in 3D, 2D, and 1D. The study of systematic uncertainty in multidimensional acceptance correction, period dependence, trigger dependence in cross-section, re-interaction effect, etc. The comparison with other experiments(*e.g.* NA10, E615) and pQCD calculation in NLO are also described.

3.1 Luminosity

In this chapter, the estimation of luminosity is introduced. As expressed in Eq. 3.1, luminosity is the product of the target density ρ_T $[cm^{-2}]$ and the number of beam particle N_{Beam}. The estimation of ρ_T and N_{beam} are in Sec. 3.1.1 and Sec. 3.1.2, respectively.

$$\mathscr{L} = N_{Beam} \times \rho_T$$

3.1.1 Estimation of target density

The target density ϱ_T represents the total number of the collision centers per unit area in the unit of [cm^{-2}]. It is formulated as follows :

$$\varrho_T = \frac{L_{\text{eff}} \times \rho \times \mathcal{N}_A}{M} \times A \qquad \mathrm{L}_{\text{eff}} = \frac{\bar{\lambda}_{\text{int, pion}}}{\rho}\left(1 - e^{-\rho L/\bar{\lambda}_{\text{int, pion}}}\right) \tag{3.2}$$

where ρ_T is the target density $[cm^{-2}]$
L_{eff} is the effective length $[cm]$.
L is the real length $[cm]$.
ρ is target density $[\frac{g}{cm^3}]$
$\bar{\lambda}_{\text{int,pion}}$ is the pion interaction length. $[\frac{g}{cm^2}]$
N_A is Avogadro constant, 6.022×10^{23} $[mole^{-1}]$.
M is the mass number $[\frac{g}{mole^1}]$.
A is number of nucleons per mole.(integer of M)

In the definition of target density, L_{eff} is introduced by considering the attenuation of beams inside the target cell. L_{eff} is shorter than the real target length L due to the beam attenuation. With the same target length L, heavy target has longer L_{eff} than the light one.

$\bar{\lambda}_{\text{int,pion}}$ represents the mean free path of material when interacting with pion. There are two kinds of pion interaction lengths with different units one can find in Particle Data Group (PDG) [80]. One is $\bar{\lambda}_{\text{int,pion}}$ in the unit of $[\frac{g}{cm^2}]$ and another one is $\lambda_{\text{int,pion}}$ in the unit of $[cm]$. $\bar{\lambda}_{\text{int,pion}}$ considers the density of material therefore it is independent of the state of material. The relation between them is shown as follows :

$$\lambda_{\text{int, pion}} = \frac{\bar{\lambda}_{\text{int, pion}}}{\rho}$$

In this analysis, we use 3 different material as targets, polarized ammonia targets (two cells), aluminum target (1 cell), and tungsten targets (two cells), 5 target cells in total. The relative position between target cells are sketched in Fig. 3.2. The most upstream ones are the two Polarized ammonia Targets (PT cells) composed by solid ammonia beans and liquid LHe kept in a low temperature ~60mK. The two PT cells allows COMPASS to study the transverse single spin asymmetry or so called the Sivers effect [46]. However, in the analysis of the Drell-Yan cross section the polarization feature is not considered as a factor in the Drell-Yan cross section analysis since the spin states of PT cells isn't a factor to impact the cross section. In the downstream of the two PT cells, one 7cm-long Al target and two 10cm-long W targets are placed. The light material Al and the heavy material W are chosen to study the nuclear effect. The 20cm-long W target is actually part of the 120cm-long beam plug. Only the first 20cm of beam plug used as target to

prevent the reinteration from the secondary pions. The target density ρ_T of each targets are described below.

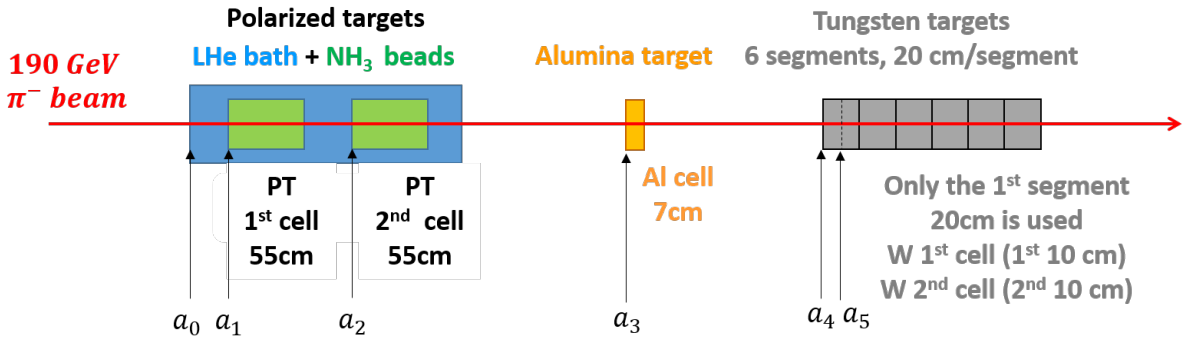

Figure 3.2: *The drawing the targets used in the analysis. The attenuation factors of a_i are assigned to the starting surface of each target and the values can be found in Table. 3.4.*

- Al and W cells
  Al and W cells are considered nearly the pure elements, therefore the estimation of ρ_T for them are relatively simple. Al target in COMPASS is composed of the pure ^{27}Al. W target in COMPASS is made of 99.5% ^{184}W and 0.5% of the mixture of its isotope ^{182}W, ^{183}W, ^{185}W. The effect caused by the isotope elements for W target is negligible. The related target parameters of Al and W used in the ρ_T estimation from Eq. 3.2 are taken from PDG [80]. Table. 3.1 shows the target density and its related target parameters for Al and W cells.

Table 3.1: *The related target parameters of Al and W used in the ρ_T estimation. They are mostly cited from PDG [80].*

Properties	Al	W cells
A	27	184
M (g/mol)	26.98	183.84
ρ (g/cm^3)	2.70	19.30
$\bar{\lambda}_{\text{int, pion}}$ (g/cm^2)	136.7	218.7
L(cm)	7.00	10.00
L_{eff} (cm)	6.54	6.64
ϱ_T (1/cm^2)	1.06×10^{25}	7.73×10^{25}

- PT cells
  PT cells are the mixture of solid ammonia beads (NH_3) and liquid helium (LHe), thus the evaluation of the target density of PT cells needs a specific treatment. To access the density ρ_{mix}, the mass number M_{mix}, and the pion interaction length $\bar{\lambda}_{int,mix}$ of a mixture of the NH_3 and LHe mixtures, we use the equations described as follows :

$$\begin{cases} \rho_{mix} & = & \rho_{NH_3} \times P_{NH3} & + & \rho_{LHe} \times (1 - P_{NH_3}) \\ \dfrac{1}{M_{mix}} & = & \dfrac{w_{NH_3}}{M_{NH_3}} & + & \dfrac{1 - w_{NH_3}}{M_{LHe}} \\ \dfrac{1}{\bar{\lambda}_{\mathbf{int},mix}} & = & \dfrac{w_{NH_3}}{\bar{\lambda}_{\mathbf{int},NH_3}} & + & \dfrac{1 - w_{NH_3}}{\bar{\lambda}_{\mathbf{int},LHe}} \end{cases} \tag{3.3}$$

where

$$\begin{cases} P_{NH3} & = & \dfrac{V_{NH_3}}{V_{NH_3} + V_{LHe}} & = & volume\ fraction\ of\ NH_3 \\ w_{NH3} & = & \dfrac{m_{NH_3}}{m_{NH_3} + m_{LHe}} & = & weight\ fraction\ of\ NH_3 \end{cases} \tag{3.4}$$

The volume fraction of NH_3 in the PT 1^{st} cell and PT 2^{nd} cell are 0.5580 and 0.5260, measured in advanced. The mass fraction is calculated through the volume fraction with simple formula, $mass = density \times volume$. Table. 3.2 gives the properties of pure LHe, pure NH_3, mixture PT 1^{st} cell, and mixture PT 2^{nd} cell. The density of the pure ammonia NH_3 was measured $\rho_{NH_3} = 0.853 \pm 0.036$ g/cm^3 by SMC collaboration [81]. Others properties from pure LHe and NH_3 are obtained either from Ref. [82] or PDG [80].

Table 3.2: *The related target parameters of pure LHe, solid NH_3 beans, and their mixture-PT cells, used in the ρ_T estimation. For pure LHe and solid NH_3 beans, they are mostly cited from PDG [80]. Concerning the PT cells, they are calculated based on Eq. 3.3.*

Properties	**LHe** (liquid, pure)	**NH_3** (solid, pure)	PT 1^{st} **Cell** (mixture)	PT 2^{nd} **Cell** (mixture)
P_{NH3}	–	–	0.5580	0.5260
M [g.mol^{-1}]	3.89	17.03	12.34	11.95
ρ [g.cm^{-3}]	0.1365	0.853	0.5363	0.5134
λ_{int} [g.cm^{-3}]	103.6000	111.5000	110.5518	110.4388
L [cm]	–	–	55.00	55.00
L_{eff} [cm]	–	–	48.3505	48.6864
ϱ_T [cm^{-2}]	–	–	1.52×10^{25}	1.51×10^{25}

Except for Eq. 3.3, there is an alternative method to calculate the ϱ_T of mixture shown in Eq. 3.5.

$$\varrho_T^{cell} = \frac{\mathcal{N}_A}{\pi R^2} \frac{L_{\text{eff}}}{L} \times [n_{\text{NH3}} A_{\text{NH3}} + n_{\text{He3}} A_{\text{He3}} + n_{\text{He4}} A_{\text{He4}}] \tag{3.5}$$

where n refers molar number of an element [mol]
A is the number of nucleons per mole of the element [uma]
R is the radius of PT cells around 125.66 cm.

It expresses ϱ_T in terms of the amount of each material in molar number. Table. 3.3 shows the values of molar number of liquid LHe, solid NH_3, and two PT cells. The target nucleon density ϱ_T of PT cells evaluated by Eq. 3.5 are 1.56×10^{25} and 1.51×10^{25} for PT 1^{st} cell and PT 2^{nd} cell, respectively. ϱ_T of PT 1^{st} cell give 2% inconsistency between Eq. 3.3 and Eq. 3.5. This 2% inconsistency is considered to be the systematic uncertainty of ρ_T calculation.

Table 3.3: *The amount of each material in molar number for PT cells and its target density ρ_T calculated based on on Eq. 3.5.*

Isotope	A_i	n_i of **PT Cell 1** [mol]	n_i of **PT Cell 2** [mol]
Proton	1	58.934 ± 0.317	49.974 ± 0.317
Deuteron	2	0.007 ± 0.001	0.006 ± 0.001
Helium-4	3	9.579 ± 0.070	11.492 ± 0.083
Helium-3	4	0.941 ± 0.006	1.128 ± 0.008
Nitrogen-14	14	19.574 ± 0.106	16.599 ± 0.106
Nitrogen-15	15	0.072 ± 0.001	0.061 ± 0.001

3.1.2 Estimation of beam flux

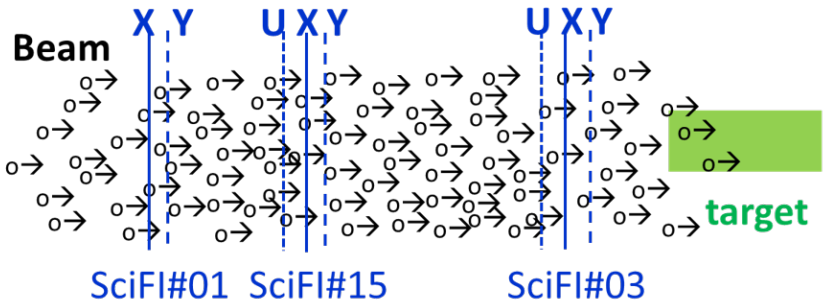

Figure 3.3: *The setup of beam telescopes in COMPASS Drell-Yan data taking.*

In COMPASS, there are three methods used to measure the beam flux : (1) Inside the SPS-M2 beam line (beam line of COMPASS from SPS), there is an ion chamber in downstream of the beam line close to the experimental hall of COMPASS. There are several scalers mounted on the chamber to counts the beams passing through the ion chamber. This method was frequently used in the past. However, this ion chamber was not calibrated for years so that the beam flux estimated is not accurate any longer. Therefore, in this analysis, it is not used. (2) COMPASS setups several SciFi stations to reconstruct the beam tracks for Drell-Yan data-taking as shown in Fig. 3.3. There are also scalers mounted on the SciFi detectors to count the beam flux. However, the SciFi detectors were suffered with the high intensity beam $\sim 10^7/s$, therefore the estimated beam flux was too low.

This option doesn't work either. (3) The third option is less straight forward but less biased by the detector performance, so called Random Trigger method(RT method). RT method is described below.

In COMPASS, random triggers are fired by the radiation sources. RT is used to sample the beam tracks. For each random trigger, a fixed time window is opened. The number of beam reconstructed within this time window $\sim 7ns$ is counted and divided by the width of the time window to estimated the averaged beam flux $[s^{-1}]$. The beam flux is estimated on spill basis. RT method is less affected by the performance of a single beam telescope plane. There are three SciFi stations with 8 planes in COMPASS. The redundancy is enough to reconstruct the beam tracks even if there is one plane out of order sometimes. The formulation of RT method is described as follows :

$$\mathscr{F}_{spill} = \frac{\sum N^{RT}_{beam}}{\sum \Delta t^{RT}_{window}} \tag{3.6}$$

where $\mathscr{F}_{spill}$ is the averaged bean flux per spill$[s^{-1}]$.
$\sum N^{RT}_{beam}$ is the sum of number of beams from several RTs within a spill.
$\sum \Delta t^{RT}_{window}$ is the sum of time window from several RTs within a spill $[s]$.
Δt^{RT}_{window} of each RT is $7ns$.

Fig. 3.4 shows the beam flux $\mathscr{F}_{spill}$ estimated on spill basis verse the run number in COMPASS 2018 data-taking. Beam flux estimated from RT method is around 60×10^6 $[s^{-1}]$ in 2018 Drell-Yan data taking. The beam intensity was quite stable over the year. If one is interested to learn more details of beam-flux estimation, the data-selection of the beam flux estimation is listed in Appendix. 4.3.

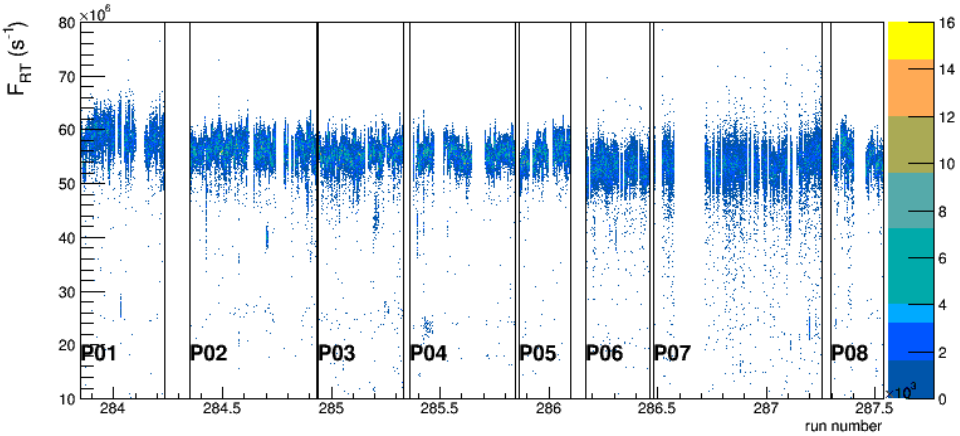

Figure 3.4: *The run number verses flux, $\mathscr{F}_{\mathscr{RT}}(1/s)$, in 2018 Drell-Yan data-taking. The beam intensity is quite stable around 60×10^6 over the year. P01 to P08 are labeled as the period of COMPASS data-taking in 2018.*

In COMPASS, the beams are reconstructed by the beam telescopes. After the beam telescopes, beams cross each target cells and start to attenuate. In Fig. 3.2, it shows that beams arrive the surface of each target cell with attenuation factor a_n with respect to the beam flux measured by the beam telescope. The formulation of the attenuation factor, a_i, is shown as follows :

$$\begin{cases} a_0 &= 100\%, & \text{for n} = 0 \\ a_n &= \prod_{k=1}^{n-1} a_k = \prod_{k=1}^{n-1} \exp\left(-\frac{\rho_k \times L_k}{\lambda_{\text{int},k}}\right), & \forall n > 0 \end{cases} \tag{3.7}$$

where $a_0 = 100\%$ means no attenuation before entering to any material.
a_k is the attenuation of beam "inside" the i-th target.
a_n is the attenuation factor "on the surface" of i-th target which accumulated from $a_{k=0}$ to $a_{k=i-1}$ targets.
L_k is length of the i-th target. $[cm]$
$\bar{\lambda}_{\text{int},k}$ is the pion interaction length of the i-th target. $[\frac{g}{cm^{-2}}]$
ρ_k is the target density of the i-th target $[\frac{g}{cm^{-3}}]$

The estimation of attenuation factor a_k is obtained according to the absorption model. The related target parameters, density ρ_k, pion interaction length $\bar{\lambda}_{int,k}$, target real length L_k, of each target can be founded in Table. 3.1 and Table. 3.2. The initial value , a_0 , is 100% measured by beam telescopes. The attenuation of beam passing the air is too small to be considered. The computed attenuation factors a_n of targets drawn in Fig.3.2, are listed in Table. 3.4.

Table 3.4: *The attenuation factors a_n of targets. The corresponding index of the targets are drawn in Fig.3.2.*

	Attenuation Coefficient a_n
Upstream LHe	$a_0 = 100\% \pm 0.00\%$
PT 1^{st} Cell	$a_1 = 99.08\% \pm 0.00\%$
PT 1^{st} Cell	$a_2 = 73.89\% \pm 0.66\%$
Al	$a_3 = 56.64\% \pm 0.68\%$
W 1^{st} cell	$a_4 = 49.33\% \pm 0.58\%$
W 2^{nd} cell	$a_5 = 20.68\% \pm 0.24\%$

The number of beam over spills is calculated with Eq. 3.8 with the preparations of a_n and $\mathscr{F}$ just introduced.The integrated number of beam over 2018 measured by beam telescopes is shown in Fig. 3.5.

$$N_{Beam} = a_n \sum_{spill} \mathscr{F}_{spill}\ \Delta t_{spill} \tag{3.8}$$

where a_n is the attenuation factor of each target.
$\mathscr{F}_{spill}$ is the averaged beam flux per spill $[s^{-1}]$.
Δt_{spill} is the spill length $[s]$, $\sim 4.6s$.

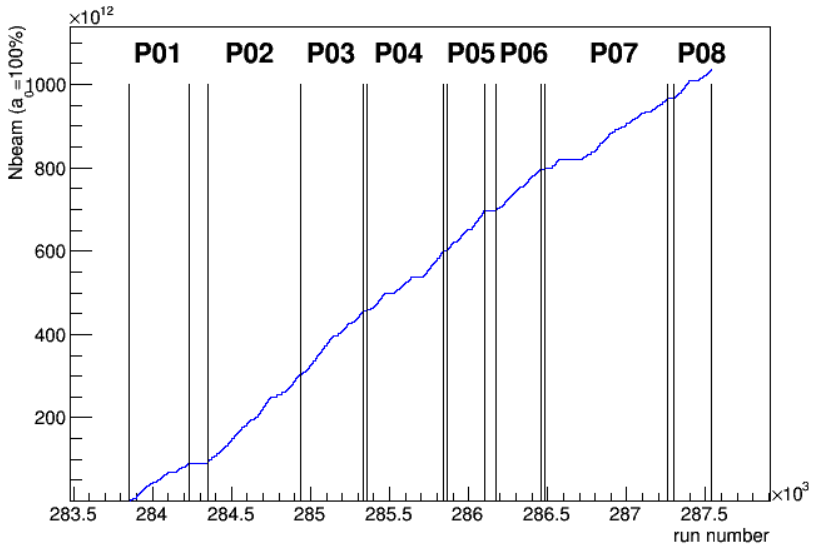

Figure 3.5: *The run number verses the integral N_{beam} measured by beam telescopes ($a_0 = 100\%$) over 2018 Drell-Yan data-taking. It is approaching $\sim \times 10^{15}$ in 2018. P01 to P08 are labeled as the period of COMPASS data-taking in 2018.*

3.1.3 COMPASS luminosity in 2018

Combining all the information, the target density ρ_T, beam flux $\mathscr{F}_{spill}$, beam attenuation factor a_n, finally the integral luminosity $\mathscr{L}$ of 5 target cells based on Eq. 3.1 are obtained and shown in Fig. 3.6. W cells have the highest luminosity compared with the other targets due to the large ρ_T. The integrated luminosity of Al cell is much less than W cells and PT cells because it is a light material and the thickness of Al target is relatively small (only $7cm$).

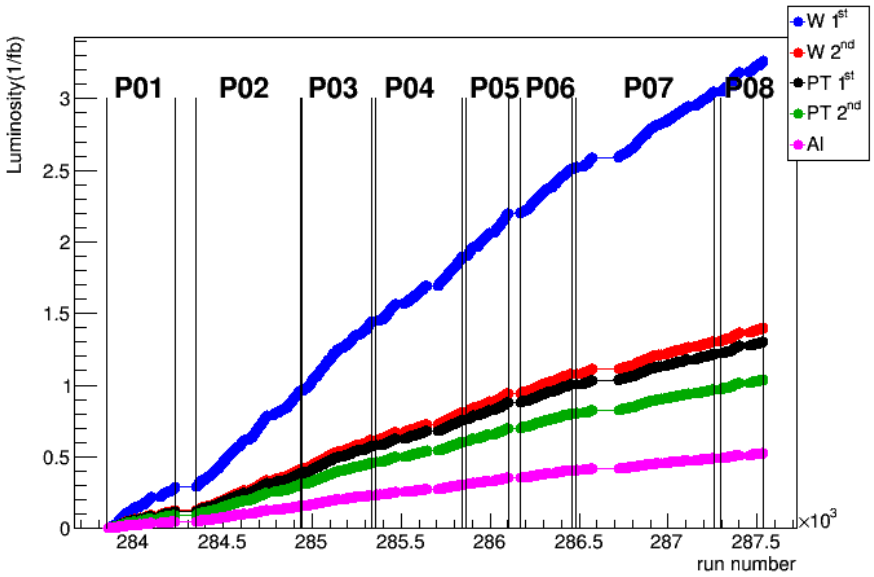

Figure 3.6: *The run number verses integral luminosity $\mathscr{L}(fb^{-1})$ in 2018. The integral luminosity over 2018 for W 1^{st} cell is up to 3 (fb^{-1}). P01 to P08 are labeled as the period of COMPASS data-taking in 2018.*

3.2 Measurement of lifetime

3.2.1 Lifetime in COMPASS

The percentage of lost triggers due to the system BUSY is defined as deadtime(DT). One the other hand, the survival percentage is called lifetime(LT) which is the supplement of deadtime. There are two kinds of lifetime needed to be measured in COMPASS, DAQ lifetime and VETO lifetime. They will be introduced in the following paragraphs.

3.2.2 DAQ lifetime

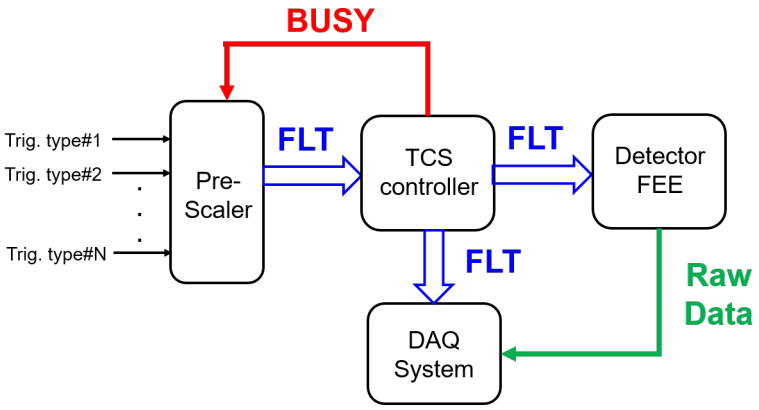

Figure 3.7: *The simplified block diagram of the cause of DAQ lifetime in COMPASS.*

The simplified block diagram of the generation of DAQ lifetime is drawn in Fig. 3.7. Detailed introduction of COMPASS DAQ system is written in Sec. 2.1.6. When the DAQ system is in a busy state, a BUSY signal is generated by COMPASS trigger-clock system(TCS). BUSY signal is sent to the pre-scaler - a coincident module OR and scale the trigger types to generate first-level trigger(FLT). BUSY signal inhibits the FLT sent to TCS system which distributes the triggers and clocks of COMPASS to the front-end electronics(FEE). As a result, BUSY signal limits the data rate. On the other hand, BUSY signal also cause the loss of physic FLT. The lose percentage of FLT caused by BUSY signals is defined as DAQ deadtime. The surviving percentage of FLT is defined as DAQ lifetime.

The measurement of DAQ lifetime in COMPASS is through the scaler. The count of FLT and RT are recorded with and without the anti-coincidence of BUSY signals. The formulation of the DAQ lifetime(efficiency) is defined as follows :

$$\varepsilon_{DAQ}^{RT} = \frac{N_{acc}^{RT}}{N_{att}^{RT}}, \quad \bar{\varepsilon}_{DAQ}^{RT} = 1 - \varepsilon_{DAQ}^{RT}$$

$$\varepsilon_{DAQ}^{FLT} = \frac{N_{acc}^{FLT}}{N_{att}^{FLT}}, \quad \bar{\varepsilon}_{DAQ}^{FLT} = 1 - \varepsilon_{DAQ}^{FLT}$$

where ε_{DAQ}^{RT} is DAQ lifetime measured by RT, $\bar{\varepsilon}_{DAQ}^{RT}$ is DAQ deadtime measured by RT, N_{acc}^{RT} is the number of RT "accepted" by the DAQ system (RTs anti-coincident with BUSY signals), N_{att}^{RT} is the number of RT triggers "attempted" to be recorded (RTs without BUSY signals). The same labeling is applied to FLT.

The DAQ lifetime measured is shown in Fig. 3.8. On average, it is around 86-87%. DAQ lifetime is slightly increased over the 2018. If one is interested in more details, the data selection of DAQ lifetime estimation is written in Appendix. 4.3.

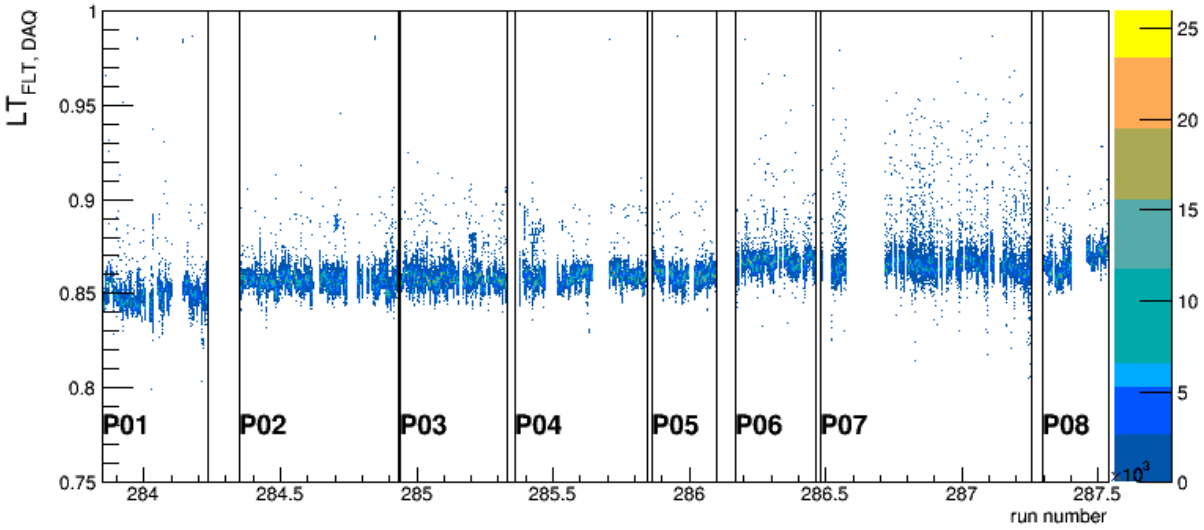

Figure 3.8: *DAQ lifetime estimated in 2018. One entry is one spill. It is around 87% and stable over the whole year.*

Theoretically, DAQ lifetime should be independent of trigger type. However the DAQ lifetime measure by RT and FLT give around 1% difference as shown in Fig. 3.9. It is considered as the systematic uncertainty of DAQ lifetime measurement. In this analysis, the DAQ lifetime estimated from FLT is used in this analysis.

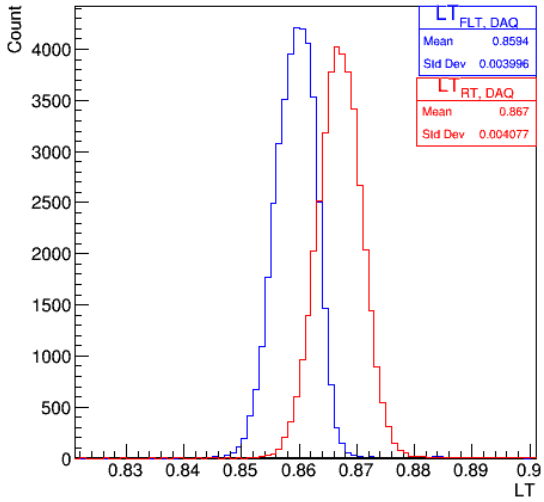

Figure 3.9: *DAQ lifetime distribution estimated from FLT trigger (in blue) and RT trigger(in red). One entry is one spill. There is around 1% difference between them.*

3.2.3 VETO lifetime

VETO lifetime is caused by beam-halo-veto triggers introduced explicitly in Sec. 2.1.5. VETO signal rejects ambiguous physics events triggered by halo beams to ease the pressure on DAQ system but it also prohibits some the physics triggers due to the opening

VETO time gate in the trigger coincidence. VETO lifetime is trigger-dependent since VETO time gates are adopted to the size of jitters of different trigger types. Veto lifetime is defined as follows :

$$\varepsilon_{VETO}^{dimuon} = 1 - \bar{\varepsilon}_{VETO}^{dimuon}$$

where ε_{VETO} and $\bar{\varepsilon}_{VETO}$ are the VETO lifetime and VETO deadtime of dimuon triggers, respectively. There are three kinds of dimuon triggers in COMPASS, LAS⊗LAS, LAS⊗OT, and LAS⊗MT, and the VETO lifetime of them are different.

VETO lifetime of dimuon triggers in 2018 unfortunately can't be accessed directly during the data-taking due to the hardware limitation. Therefore, we obtain them with an alternative way of combining the online measurement and offline measurement operated manually. Use $LAS \times LAS$ trigger as an example, the formulation of cable delay method is defined as follow :

$$\begin{aligned}
\bar{\varepsilon}_{VETO}^{LAS\times LAS} &= \left[\frac{\bar{\varepsilon}_{VETO}^{LAS\times LAS}}{\bar{\varepsilon}_{VETO}^{\mathbf{OT}}} \right]_{offline} \times \left[\bar{\varepsilon}_{VETO}^{\mathbf{OT}} \right]_{online}, \quad [\bar{\varepsilon}_{VETO}^{\mathbf{OT}}]_{online} = 1 - \frac{N_{VETO}^{OT}}{N_{att}^{OT}} \\
&= \left[\frac{\bar{\varepsilon}_{VETO}^{LAS\times LAS}}{\bar{\varepsilon}_{VETO}^{\mathbf{MT}}} \right]_{offline} \times \left[\bar{\varepsilon}_{VETO}^{\mathbf{MT}} \right]_{online}, \quad [\bar{\varepsilon}_{VETO}^{\mathbf{MT}}]_{online} = 1 - \frac{N_{VETO}^{MT}}{N_{att}^{MT}} \\
&= \left[\frac{\bar{\varepsilon}_{VETO}^{LAS\times LAS}}{\bar{\varepsilon}_{VETO}^{\mathbf{RT}}} \right]_{offline} \times \left[\bar{\varepsilon}_{VETO}^{\mathbf{RT}} \right]_{online}, \quad [\bar{\varepsilon}_{VETO}^{\mathbf{RT}}]_{online} = 1 - \frac{N_{VETO}^{RT}}{N_{att}^{OT}}
\end{aligned}$$

where $\bar{\varepsilon}_{VETO}^{LAS\times LAS}$, $\bar{\varepsilon}_{VETO}^{OT}$, $\bar{\varepsilon}_{VETO}^{MT}$, $\bar{\varepsilon}_{VETO}^{RT}$ are the VETO deadtime of $LAS \times LAS$(dimuon trigger), OT(single muon trigger), and MT(single muon trigger), and RT(random trigger) triggers. The ratios of VETO deadtime, $\left[\frac{\bar{\varepsilon}_{VETO}^{LAS\times LAS}}{\bar{\varepsilon}_{VETO}^{\mathbf{OT}}} \right]_{offline}$, $\left[\frac{\bar{\varepsilon}_{VETO}^{LAS\times LAS}}{\bar{\varepsilon}_{VETO}^{\mathbf{MT}}} \right]_{offline}$, $\left[\frac{\bar{\varepsilon}_{VETO}^{LAS\times LAS}}{\bar{\varepsilon}_{VETO}^{\mathbf{RT}}} \right]_{offline}$ are measured offline manually. One can find the ratios of VETO deadtime in Table. 3.5. VETO deadtime $\left[\bar{\varepsilon}_{VETO}^{OT} \right]_{online}$, $\left[\bar{\varepsilon}_{VETO}^{MT} \right]_{online}$, $\left[\bar{\varepsilon}_{VETO}^{RT} \right]_{online}$ are measured online from scaler and real data combined. $N_{VETO}^{OT,MT,RT}$ is the number of triggers convoluted with VETO gate counted from scaler. $N_{att}^{OT,MT,RT}$ is the number of triggers attempted counted from real data. The same formulation can be applied to the VETO deadtime measurement of the other two dimuon triggers $\bar{\varepsilon}_{VETO}^{LAS\times OT}$ and $\bar{\varepsilon}_{VETO}^{LAS\times MT}$.

In the estimation of VETO lifetime, the cuts are used the same as the ones for DAQ lifetime described in Appendix.4.3. Veto lifetime is obtained spill by spill and there are 3 possible values for each VETO deadtime of dimuon triggers from the ratios of OT, MT, and RT given as shown in Fig. 3.10. Estimated VETO deadtime of dimuon triggers from the ratio with respect to RT trigger deviates more from the ratio with respect to OT and MT because of the different spill structure between RT and physics triggers. Therefore the VETO deadtime measured from RT ratio is not used. VETO lifetime measured from the ratio of MT and the ratio of OT are considered to be more reliable with less than 1% systematic uncertainty between them. Veto lifetime of $LAS \times LAS$ trigger and $LAS \times OT$ trigger obtained from the ratio of OT are used in the cross-section analysis. The results over the whole 2018 are shown in Fig. 3.11. Veto lifetime of $LAS \times LAS$ trigger is around 75% and $LAS \times OT$ is around 70%. It is slowly increased from the beginning to the end of data-taking, same as the DAQ lifetime.

Table 3.5: *Ratios of VETO dead-time measured offline through the cable-delay method.*

	Ratio
$[\frac{\mathrm{DT_{LL,\ VETO}}}{\mathrm{DT_{OT,\ VETO}}}]_{offline}$	1.040 ± 0.010
$[\frac{\mathrm{DT_{LL,\ VETO}}}{\mathrm{DT_{MT,\ VETO}}}]_{offline}$	1.089 ± 0.013
$[\frac{\mathrm{DT_{LL,\ VETO}}}{\mathrm{DT_{RT,\ VETO}}}]_{offline}$	1.498 ± 0.008
$[\frac{\mathrm{DT_{LO,\ VETO}}}{\mathrm{DT_{OT,\ VETO}}}]_{offline}$	1.619 ± 0.023
$[\frac{\mathrm{DT_{LO,\ VETO}}}{\mathrm{DT_{MT,\ VETO}}}]_{offline}$	1.699 ± 0.028
$[\frac{\mathrm{DT_{LO,\ VETO}}}{\mathrm{DT_{RT,\ VETO}}}]_{offline}$	2.342 ± 0.024
$[\frac{\mathrm{DT_{LM,\ VETO}}}{\mathrm{DT_{OT,\ VETO}}}]_{offline}$	1.338 ± 0.012
$[\frac{\mathrm{DT_{LM,\ VETO}}}{\mathrm{DT_{MT,\ VETO}}}]_{offline}$	1.399 ± 0.014
$[\frac{\mathrm{DT_{LM,\ VETO}}}{\mathrm{DT_{RT,\ VETO}}}]_{offline}$	1.986 ± 0.009

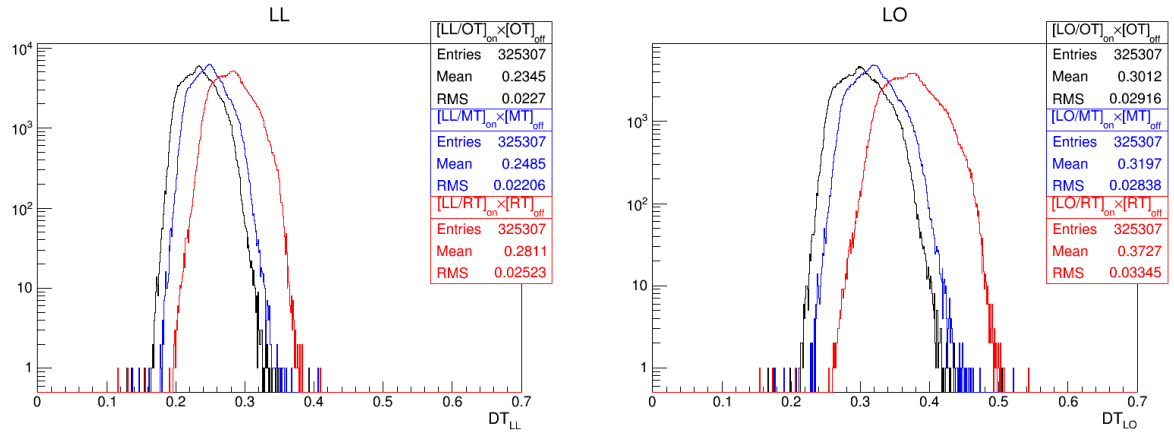

(a) $\bar{\varepsilon}^{LAS\times LAS}_{VETO}$ **(b)** $\bar{\varepsilon}^{LAS\times OT}_{VETO}$

Figure 3.10: *VETO dead-time of $LAS \times LAS$(LL) and $LAS \times OT$(LO) triggers on spill basis. There are 3 values each VETO deadtime of dimuon triggers from the ratios with respect to OT(black), MT(blue), and RT(red). The distributions given by the ratio of RT deviates more from the other two and it can be explained by the spill structure. The distributions given by ratios with respect to OT and MT triggers are closer, only $\sim 1\%$ difference considered to be systematic uncertainty of VETO lifetime in the cross-section measurement.*

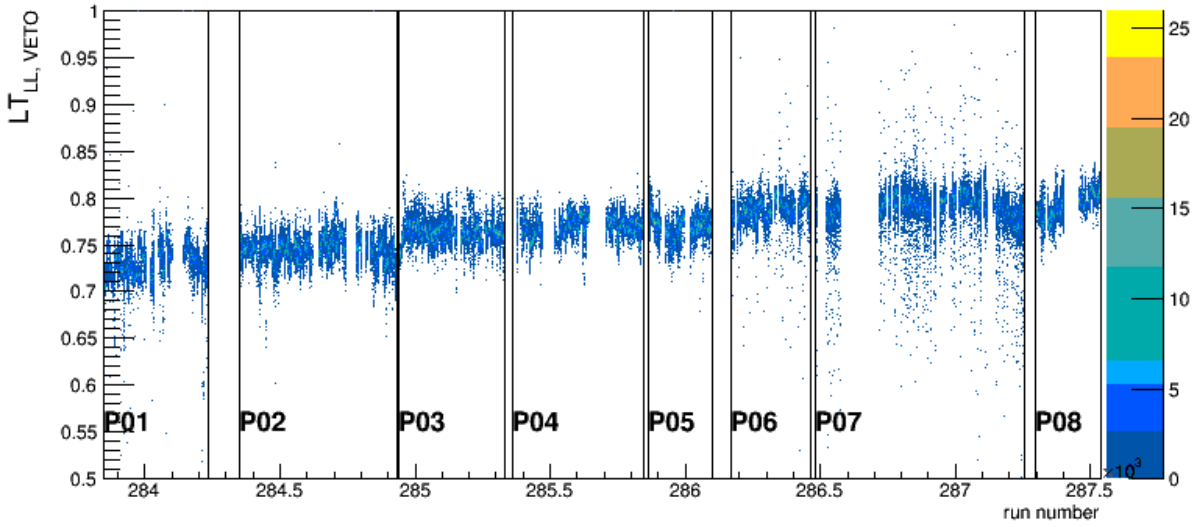

(a) $\varepsilon_{VETO}^{LAS \times LAS}$

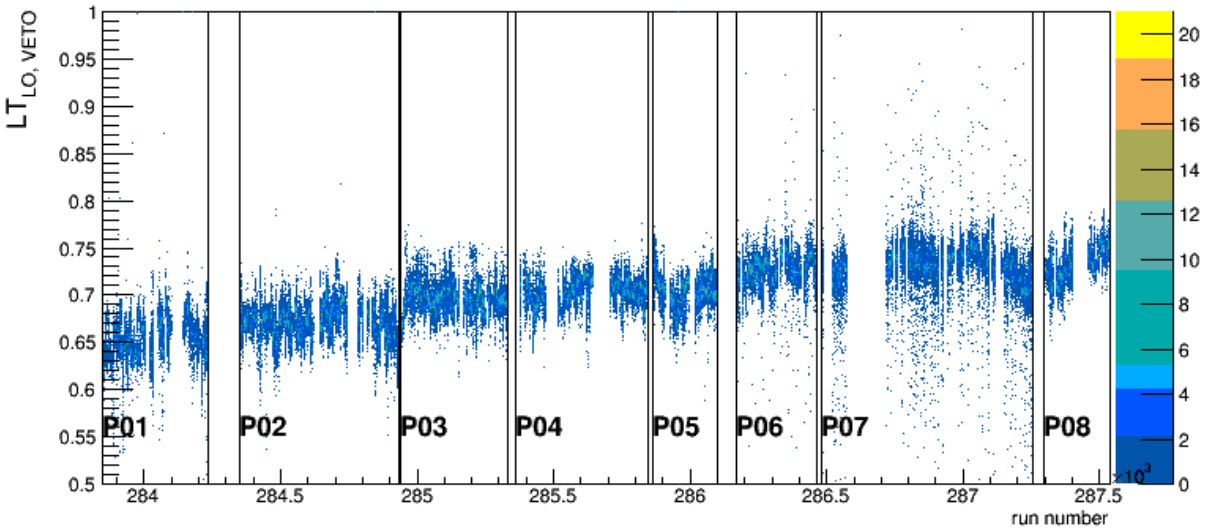

(b) $\varepsilon_{VETO}^{LAS \times OT}$

Figure 3.11: *Veto lifetime of (a)$LAS \times LAS$ and (b)$LAS \times OT$ triggers. VETO lifetime over the whole 2018 are around 75% for $LAS \times LAS$ and around 70% for $LAS \times OT$. It is slow increased from the beginning to the end of data-taking.*

3.3 Selection of dimuon events

In this section, the analysis of dimuon events from COMPASS 2018 Drell-Yan data is shown. The notations of kinematic variables(Sec. 3.3.1), the data selection of dimuon events(Sec. 3.3.2), and the kinematics distributions of the dimuon events(Sec. 3.3.3) will be presented.

3.3.1 Observables

The naïve Drell-Yan process proposed by Sidney D. Drell and Tung-Mow Yan in 1970 [19] describes the production of lepton–antilepton pairs (e^+e^- or $\mu^+\mu^-$) via a virtual photon or Z boson from a quark-antiquark annihilate of hadrons ($\pi^\pm$ beam, p beam, $\bar{p}$ beam or nucleon targets) : $h_A+h_B \rightarrow l^+ + l^- + X$, as shown in Fig. 3.12. In COMPASS experiment, $190GeV$ π^- beam collides with the fixed nucleus targets including two polarized ammonia targets (PT cells), one alumina target (Al), and two tungsten targets (W cells). The detected signals are the outgoing dimuon pairs $\mu^+\mu^-$(electron-positron pairs are the goal). The Drell-Yan data from COMPASS experiment gives chance to study the pion PDFs and the nuclear effect.

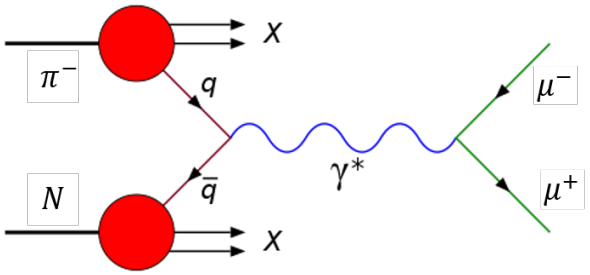

Figure 3.12: *The Feynman diagram of COMPASS π^-N collision in COMPASS experiment. The 190GeV π^- beam generated from SPS at CERN collides with the fixed nucleon targets include two polarized ammonia targets (PT cells), one alumina target (Al), and two tungsten targets (W cells). The outgoing $\mu^+\mu^-$ dimuon pairs are detected as the symptom of Drell-Yan process.*

The kinematic variables of the Drell-Yan process used in this analysis are summarized in Table. 3.6. The 4-momentum of π^- beam, nucleon target, and two opposite sign muons are referred as P_π, P_N, P_{μ^+}, P_{μ^-}. The 4-momentum of hadronic system composed by the beam hadron π^- and nucleon hadron N is $P = P_\pi + P_N$. The 4-momentum of two partons, one from beam hadron and another one from target hadron, is equal to the 4-momentum of the dimuon system and the 4-momentum of virtual photon, $q = P_{\mu^+} + P_{\mu^-}$. In the experimental of view, only the kinematic variables of dimuon system can be measured. The detailed discussion of the Drell-Yan variables had already been introduced in Sec. 1.3, therefore some crucial variables and its physics are discussed as follows :

- $M_{\mu\mu}$ and τ : The center-of-mass energy of hadronic system is defined as $s = P^2$. The interacted energy Q is equal to the mass of dimuon system, $Q = \sqrt{q^2} = M_{\mu\mu}$. The energy fraction of between the hadronic system and the dimuon system, $\tau = \frac{M^2_{\mu\mu}}{s}$, is often used when comparing the physics results between the experiments with different center-of-mass energy. τ is considered as an alternative observable with respect to $M_{\mu\mu}$. One of the successful prediction of the naïve Drell-Yan model is that the

rapid fall of Drell-Yan cross section is inversely proportional to the dimuon mass in the order of three as shown in Fig. 1.15 [32], $\frac{d\sigma}{dM_{\mu\mu}} \sim \frac{1}{M^3_{\mu\mu}}$. However, the amplitude of the measured Drell-Yan cross section along $M_{\mu\mu}$ was two times larger than the prediction made by the naïve Drell-Yan model due to the lack of the consideration of the gluon interactions with partons. Since after that, the Drell-Yan model has been developed with the QCD corrections. The QCD-improved Drell-Yan model has made the predictions of the cross section close to the experimental measurements. In Fig. 1.21 [30], it shows the K-factor, cross section ratio between the experimental measurements and the next-to-leading-order $\mathcal{O}(\alpha_s)$, is around 1.1 to 1.2. The inconsistency between the experimental results and theoretical calculation reduces from 2.0 to 1.2 after the QCD corrections.

- p_T : The transverse momentum of the dimuon pairs(partonic system) is defined as p_T. The intrinsic mean square of the transversed momentum of the dimuon pairs $< p_T^2 >$ is less than $1GeV$. However the measured $< p_T^2 >$ from multiple experiments showed that $< p_T^2 >$ is larger and it is linearly correlated with the center-of-mass energy s as shown in Fig. 1.22 [21]. Later it is understood that the unexpected large $< p_T^2 >$ is caused by the extra kicks from the gluons interact with the partons which is not considered by the naïve Drell-Yan model based on QED and parton model only. Furthermore, p_T is also an important observable to study the nuclear effect. In the hadron-nucleus interactions, the past experiments found that the collisions with the heavier targets tend to give larger $< p_T^2 >$ due to the stronger multiple scattering compared to the light targets.

- x_F : The longitudinal momentum of dimuon system is defined as p_L. In center-of-mass frame, the maximum longitudinal momentum is half of the center-of-mass energy, $p_L^{max} = \frac{\sqrt{s}}{2}$. The Feynman-x of dimuon system is defined as the ratio of the longitudinal momentum with respect to the possible maximum longitudinal momentum $x_F = \frac{p_L}{\sqrt{s}/2}$. x_F is considered as the an alternative representation of the longitudinal momentum of dimuon system (partonic system). x_F is an comprehensive observables with respect to p_T to described the dimuon system and partonic system. The reasonable x_F region is $-1.0 < x_F < 1.0$. The fixed-target experiments are usually sensitive to $x_F > 0$ region since the spectrometer along the beam direction after the interaction target. The study of x_F is a valuable input for the pion PDF study. Fig. 3.13 on the right-hand side shows the kinematic distributions of x_F verses p_T extracted from COMPASS 2018 data.

- x_π and x_N : x_π is the longitudinal momentum fraction of parton inside the π^- beam. x_N is the longitudinal momentum fraction of parton inside the nucleus target. x_π and x_N can't be measured directly (not experimental observables). They are derived from the longitudinal momentum of dimuon system p_L and the energy fraction of between the hadronic system and the dimuon system τ : $x_\pi = [\ x_F + \sqrt{x_F^2 + 4\tau}]/2$ and $x_N = [-x_F + \sqrt{x_F^2 + 4\tau}]/2$. In Fig. 3.13 on the left-hand side shows the kinematic distributions of x_π verses x_N extracted from COMPASS 2018 data, a strong correlation is observed between x_π and x_N as expected due to Eq.1.16 and Eq.1.17 derived from the momentum conservation between partonic system and hadron system.

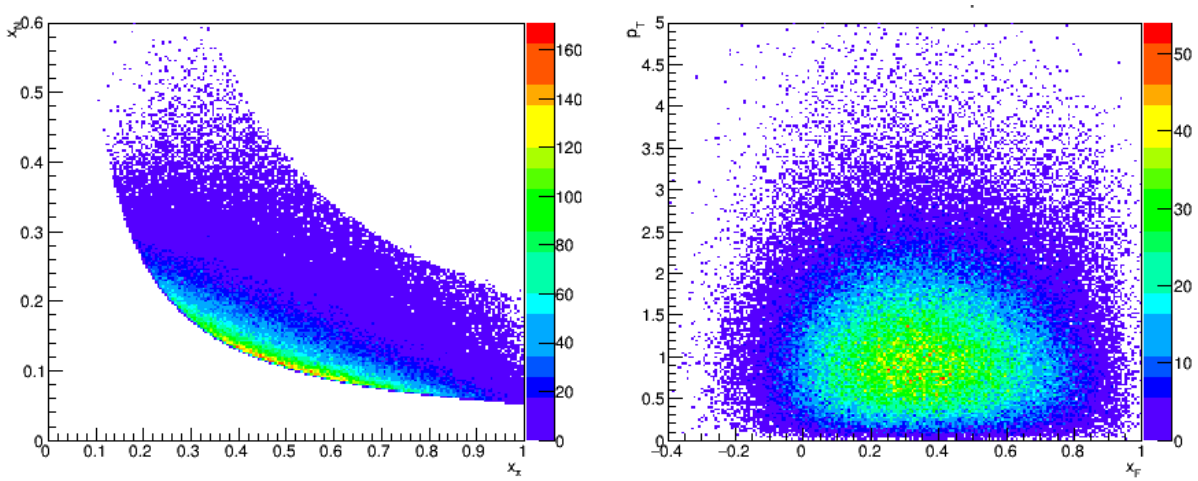

Figure 3.13: *The 2D kinematics distributions of dimuon events from COMPASS 2018 data: (Left) x_π VS x_N, (Right) x_F VS p_T.*

The comprehensive descriptions of dimuon system and partonic system are either $[M_{\mu\mu}(\sqrt{\tau}), p_T, p_L]$, $[M_{\mu\mu}(\sqrt{\tau}), p_T, x_F]$, or $[M_{\mu\mu}(\sqrt{\tau}), p_T, x_1, x_2]$. The kinematics p_L, x_F, and $[x_1, x_2]$ sets equally represent the same physics - longitudinal momentum of dimuon system.

In this analysis, the multi-dimensional Drell-Yan cross-section is presented. For one-dimensional Drell-Yan cross section, it is presented in six variables : $M_{\mu\mu}$, $\sqrt{\tau}$, p_T, x_F, x_1, and x_2. For two-dimensional cross section, it is done with $[\sqrt{\tau}, x_F]$, $[M_{\mu\mu}, p_T]$, and $[x_F, p_T]$. For three-dimensional cross section, it is shown in $[M_{\mu\mu}, p_T, x_F]$.

Table 3.6: *Notations for Drell-Yan kinematic variables used in this analysis*

Variable	Description
P_π, P_N	4-momenta of the π^-, and of the target nucleon
P_{μ^+}, P_{μ^-}	4-momenta of the μ^+, and of the μ^-
$P = P_\pi + P_N$	4-momenta of hadronic system
$q = P_{\mu^+} + P_{\mu^-}$	4-momenta of virtual photon/dimuon system/partonic system
$s = P^2$	Center-of-mass energy of hadronic system
$Q^2 = q^2$	Energy square of virtual photon/dimuon system/partonic system
$M_{\mu\mu} \sim \sqrt{Q}$	Invariant mass of the dimuon
$\tau = M_{\mu\mu}^2/P^2 = x_\pi x_N$	Fraction of energy between hadronic system and dimuon
p_T	Transverse momentum of the virtual photon/dimuon system/parton system (with respect to the beam direction)
p_L	Longitudinal momentum of the virtual photon/dimuon system/parton system (with respect to the beam direction)
$x_\pi = [\, x_F + \sqrt{x_F^2 + 4\tau}]/2$	Momentum fraction of parton inside π^- (often refereed as x_1)
$x_N = [-x_F + \sqrt{x_F^2 + 4\tau}]/2$	Momentum fraction of parton inside nucleon target (often refereed as x_2)
$x_F = p_L/(\sqrt{s}/2) = x_\pi - x_N$	Feynman-x of the virtual photon/dimuon/quarkonium

3.3.2 Data selections

To select clean dimuon events, the special design in the hardware setup and the specific selection criteria are investigated.

Hardware-wise, a hadron absorber and the dimuon triggers are used. In the general designed of Drell-Yan measurement, a hadron absorber made by heavy material is place

right after the collision points so that most of the tracks pass through the spectrometers are mostly muons. There are three single muon triggers designed to detect the muon triggers with different opening angle (different Feynman-x x_F, different rapidity y) : Large-Angle Single muon trigger(LAS), Outer-angle single muon trigger(OT), and Middle-angle single muon trigger(MT). The customized dimuon triggers are composed by single muon triggers : $LAS \times LAS$, $LAS \times OT$, and $LAS \times MT$. The kinematics coverage of dimuon triggers are designed to be sensitive to different Feynman-x x_F(rapidity y) coverage shown in Fig. 3.14. $LAS \times LAS$ trigger covers mainly in low x_F region, $-0.2 < x_F < 0.6$. $LAS \times OT$ covers $0.2 < x_F < 0.8$. $LAS \times MT$ covers in high x_F region, $0.4 < x_F < 1.0$. In $x_F < 0.2$ region, Drell-Yan cross section helps to constrain to gluon and sea distributions of pion PDF. In high $x_F \to 1$ regions, Drell-Yan cross section helps to resolve the ambiguity concerning the shape of valance distribution $(1 - x_\pi)^\beta$. β is predicted in the range of $[1, 2]$ depends on the pQCD models. In this data-analysis, the events from $LAS \times MT$ are not used unfortunately due to the high background contamination from the beam-decay muons. Only the dimuon events from $LAS \times LAS$ and $LAS \times OT$ triggers are used studied.

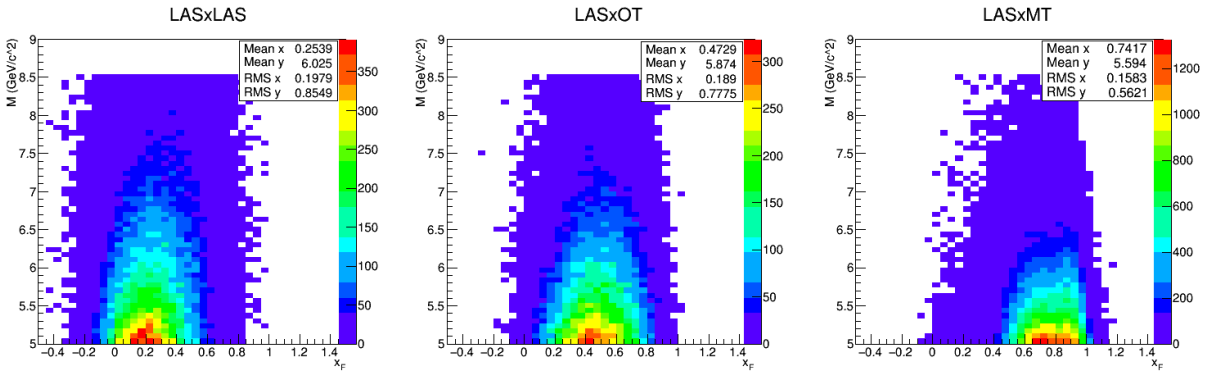

Figure 3.14: *The kinematic coverage of dimuon trigger in terms of x_F verse mass from the real data in 2018 DY data-taking.*

Except for the hardware selection, the selection criteria of dimuon events in the analysis also helps to remove unwanted background. All the dimuon events firing dimuon triggers are saved in COMPASS data set. The data used in this analysis collected between May to November in 2018 are divided into 9 periods from P00 to P08. Except for P00, the rest periods are used in this analysis. In order to have a clean and reliable dimuon sample from the Drell-Yan process, several cuts are performed in dimuon kinematics, target selections, beam track quality, muon track quality, vertexing quality, data stability, etc. Here some of the important ones are introduced. The full descriptions of the cut are given in Appendix. 4.3.

- Dimuon $M_{\mu\mu}$ selection
  The $M_{\mu\mu}$ selection is based on the background estimation and the MC simulation. Fig. 3.15 shows the dimuon mass spectrum of PT cells in 2015. COMPASS data is well described by the sum of the MC simulation and the background estimation. The contributions of J/ψ, ψ', open-charm, and background are significant when $M_{\mu\mu} < 4\ GeV$, therefore the Drell-Yan mass region of PT cells and Al cell are chosen in $4.3 < M_{\mu\mu} < 8.5$ GeV/c^2 and of W cells, the mass range chosen is narrower, $4.7 < M_{\mu\mu} < 8.5$ GeV/c^2. The multiple scattering of muon tracks in the heavy target is worse than the light target, as a results, the W cells have worse mass

resolution than the others. The mass cut chosen keeps the background level less than 5%.

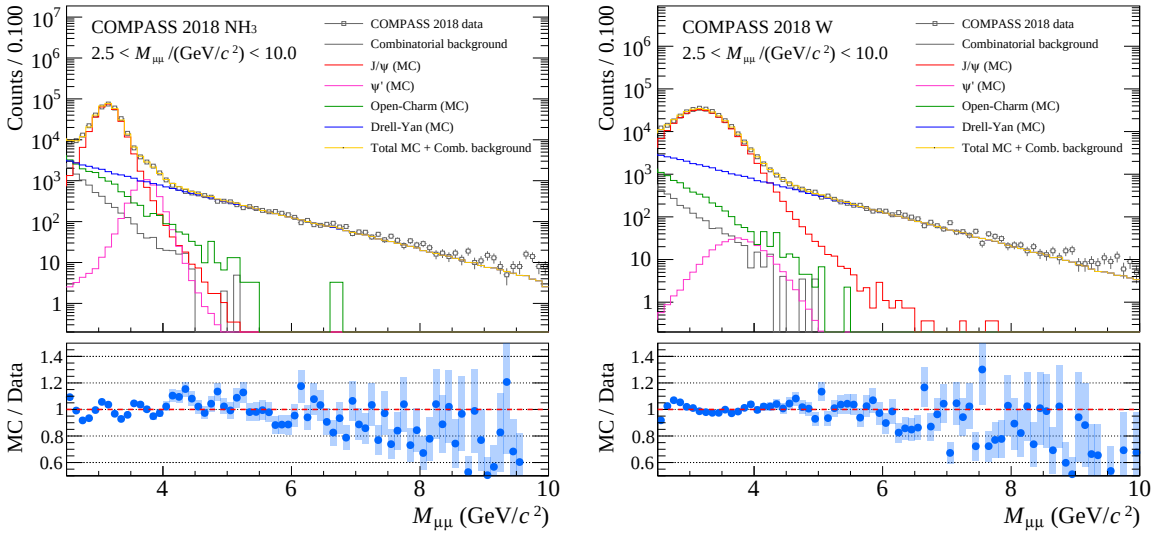

(a) *PT cells* **(b)** *W cells*

Figure 3.15: *Dimuon mass spectrum of (a)PT cells and (b)W cells in 2018 data-taking. COMPASS data is black dots. The background is in the black dash line. The Monte-Carol(MC) simulations of J/ψ, $\psi^{'}$, open-charm, and Drell-Yan processes are in the red, magenta, green dash lines, respectively. COMPASS data has nice agreement with the sum of the MC simulations and the backgrounds except for the high mass region. Drell-Yan mass region of PT cells and Al cell are chosen in $4.3 < M_{\mu\mu} < 8.5$ GeV/c^2 and of W cells, the mass range chosen is narrower, $4.7 < M_{\mu\mu} < 8.5$ GeV/c^2, due to the worse mass resolution caused by the multiple scattering inside the hadron absorber.*

- Z_{vtx} selection
  There are three kinds of materials used as targets : two polarized ammonia targets (PT cells), ammonia target(Al), and tungsten targets(W). The relative position of them is shown in Fig. 2.7. Fig: 3.16 shows the vertex distribution of targets along beam direction, Z_{vtx}, in COMPASS. The 4 peaks represents the target positions : Two 55cm-long PT cells are in the most upstream, then 7cm-long Al target, and in the end two 10cm-long W cells taken from the first 20cm of beam plug. Table. 3.7 shows the real potions and the cut position of each target. For PT cells and W_{2nd} cell, the selected Z_{vtx} positions are same as the real position given by survey. However it is not the case for Al and W_{1st} targets. In order to increase the statistics, the migrated events are included so that the selected Z_{vtx} positions of them are larger than the real range. The gain of statistics for Al cell and W^{1st} cell are 30% and 10% after include the migrated events. The comparison between Monte-Carol(MC) and Real Data (RD) along Z_{vtx} is made to check if the choice of Z_{vtx} regions are reasonable or not. The MC and RD comparison along Z_{vtx} shown in Fig. 3.17. A nice agreement along Z_{vtx} is achieved.

Table 3.7: *The Z_{vtx} cut of each target.*

Target cell	Real Position(cm)	Z_{vtx} (cm) selected
$PT\ 1^{st}$	[-294.5, -239.4]	same as real position
$PT\ 2^{ns}$	[-219.5, -163.9]	same as real position
Al	[-73.5, -66.5]	[-80.0, -60.0]
$W\ 1^{st}$	[-30.0, -10.0]	[-40.0, -10.0]
$W\ 2^{nd}$	[-10.0, 0.0]	same as real position

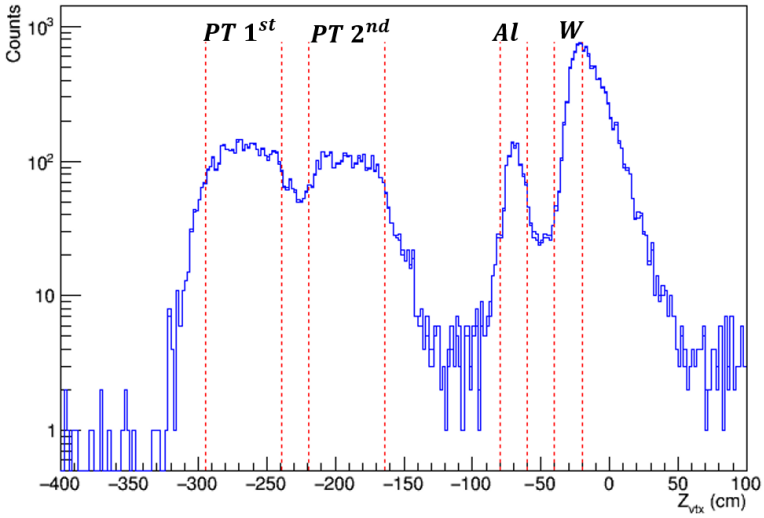

Figure 3.16: *The Z_{vtx} distribution of dimuon pairs in 2018 COMPASS data. The 4 peaks represents the target positions : Two 55cm-long PT cells are in the most upstream, then 7cm-long Al target, and in the end two 10cm-long W cells taken from the first 20cm of beam plug. The red dashlines show the Z_{vtx} cuts of target cells.*

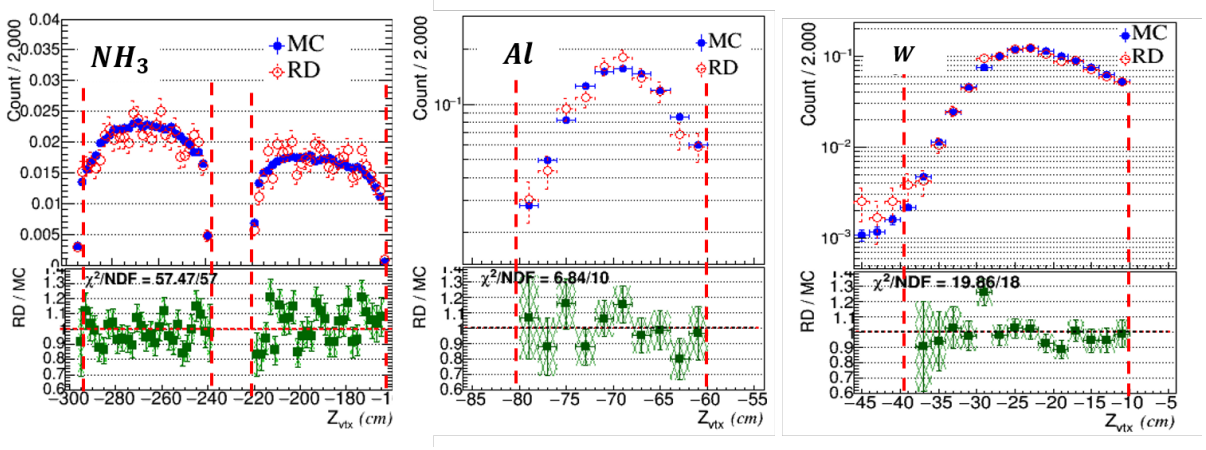

Figure 3.17: *The comparison between MC and RD of Drell-Yan sample selected in Z_{vtx} distribution for all the target cells. (top) Z_{vtx} distributions of MC and RD. (bottom) The ratio between RD and MC. The red dashlines show the selected Z_{vtx} region in this analysis. In the chosen Z_{vtx} regions, a reasonable agreement achieved between RD and MC.*

- Kinematic cuts in x_π, x_N, x_F, and p_T
  The kinematics in x_π, x_N, x_F, and p_T are shown in Table. 3.8. The kinematic selection of x_π and x_N are chosen in the physics ranges, $0.0 < x_\pi < 1.0$ and $0.0 < x_N < 1.0$. The selected ranges of p_T and x_F are decided by the 1D acceptance larger than 1% and the relative statistical error of it is less than 10% in order to have a stable acceptance correction. The large uncertainty of acceptance could leads to an unreliable cross section results. The discussion of acceptance will be further elaborated in Sec.3.4.

Table 3.8: *The kinematic cuts.*

	Selected range
p_T	$[0.0, 0.36]$
x_π	$[0.0, 1.0]$
x_N	$[0.0, 1.0]$
x_F	$[-0.1, 0.7]$ for $LAS \times LAS$
	$[0.2, 0.9]$ for $LAS \times OT$

3.3.3 Kinematics distributions

The one-dimensional kinematics distributions of the selected dimuon events of PT cells, Al cell, and W cells are shown in Fig. 3.18, Fig. 3.19, and Fig. 3.20 for both $LAS \times LAS$, and $LAS \times OT$ triggers. The binning of each kinematics is listed in Table 3.9. The rapid fall of Drell-Yan cross-section in $M_{\mu\mu}$ is observed. The kinematics coverage between $LAS \times LAS$ and $LAS \times OT$ are similar in $M_{\mu\mu}$ and p_T. However, they covers different x_F, x_π, and x_N. The mean value of each kinematic distributions are listed in Table. 3.10.

Table 3.9: *The binning 1D kinematics distribution.*

Kinematics	Nbin	Binning
$M_{\mu\mu}$	10	[4.30, 4.70, 5.10, 5.50, 5.90, 6.30, 6.70, 7.10, 7.50, 7.90, 8.50]
$\sqrt{\tau}$	10	[0.23, 0.25, 0.27, 0.29, 0.31, 0.33, 0.35, 0.38, 0.40, 0.42, 0.45]
p_T	11	[0.00, 0.30, 0.60, 0.90, 1.20, 1.50, 1.80, 2.10, 2.40, 2.70, 3.00, 3.60]
x_π	9	[0.00, 0.10, 0.20, 0.30, 0.40, 0.50, 0.60, 0.70, 0.80, 1.00]
x_N	10	[0.00, 0.05, 0.10, 0.15, 0.20, 0.25, 0.30, 0.35, 0.40, 0.45, 0.6]
x_F	9	[-0.10, 0.00, 0.10, 0.20, 0.30, 0.40, 0.50, 0.60, 0.70, 0.90]

Table 3.10: *The mean value of the kinematic distributions after event selections. "Both" means $LAS \times LAS$ and $LAS \times OT$ data combined.*

Target cell	Tigger	M	$\sqrt{\tau}$	p_T	x_π	x_N	x_F
PT cells	$Both$	5.34	0.28	1.01	0.52	0.17	0.35
	$LAS \times LAS$	5.41	0.29	1.13	0.45	0.20	0.25
	$LAS \times OT$	5.22	0.28	1.05	0.64	0.12	0.52
Al cell	$Both$	5.35	0.28	1.15	0.51	0.17	0.34
	$LAS \times LAS$	5.43	0.29	1.17	0.42	0.20	0.22
	$LAS \times OT$	5.27	0.28	1.13	0.63	0.13	0.50
W cells	$Both$	5.70	0.30	1.20	0.54	0.19	0.35
	$LAS \times LAS$	5.77	0.31	1.22	0.45	0.22	0.22
	$LAS \times OT$	5.61	0.30	1.17	0.65	0.14	0.51

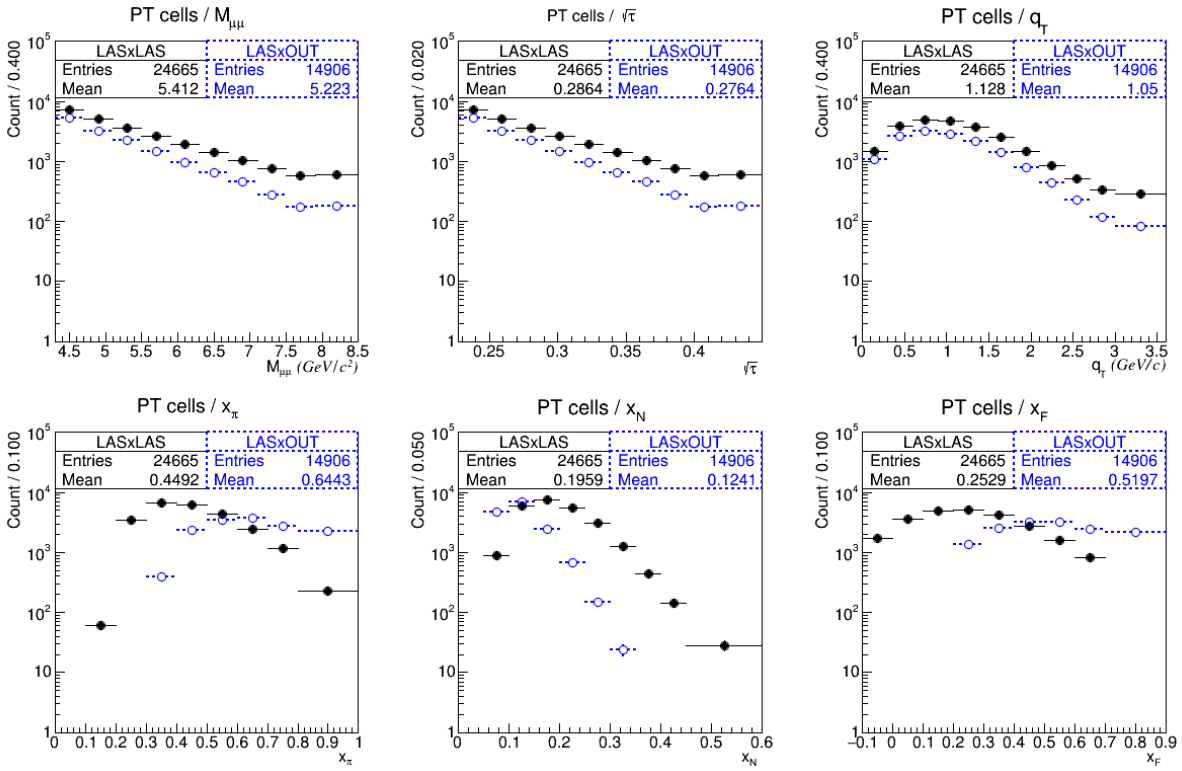

Figure 3.18: *1D kinematic distributions of two PT cells combined : (Black) $LAS \times LAS$ trigger and (Blue) $LAS \times OT$ trigger.*

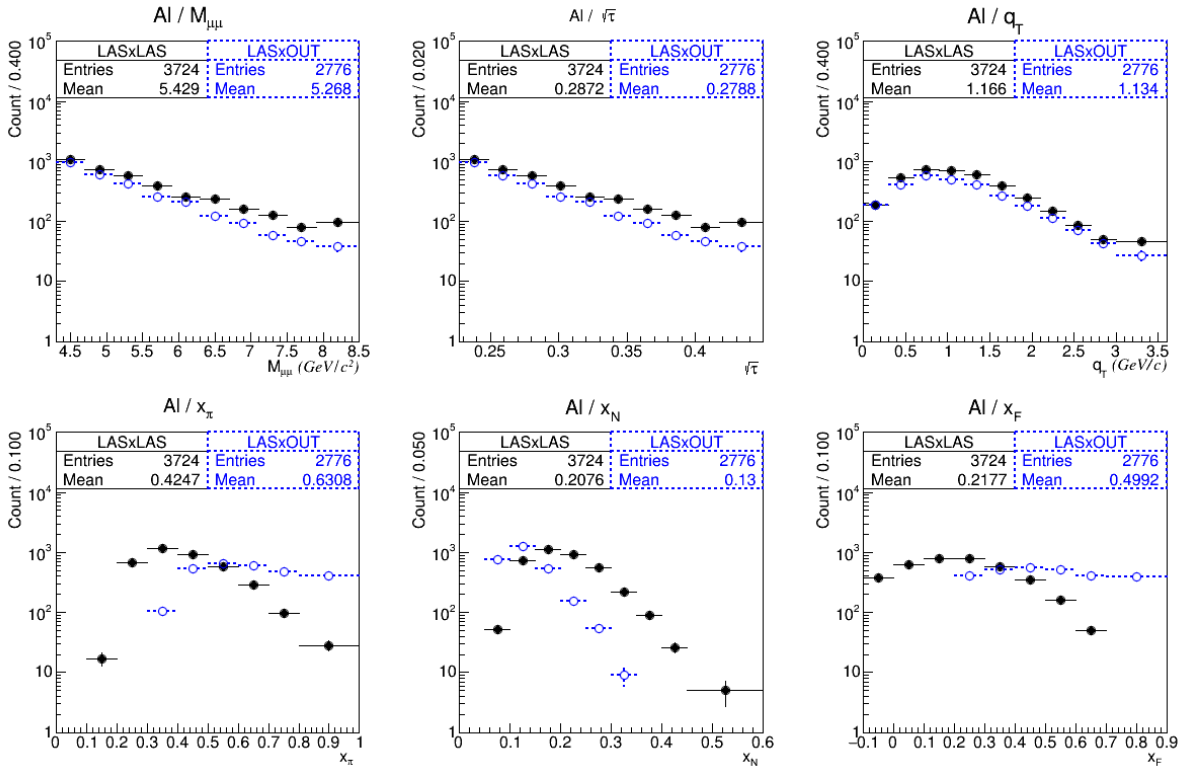

Figure 3.19: *1D kinematic distributions of Al cell : (Black) LAS × LAS trigger and (Blue) LAS × OT trigger.*

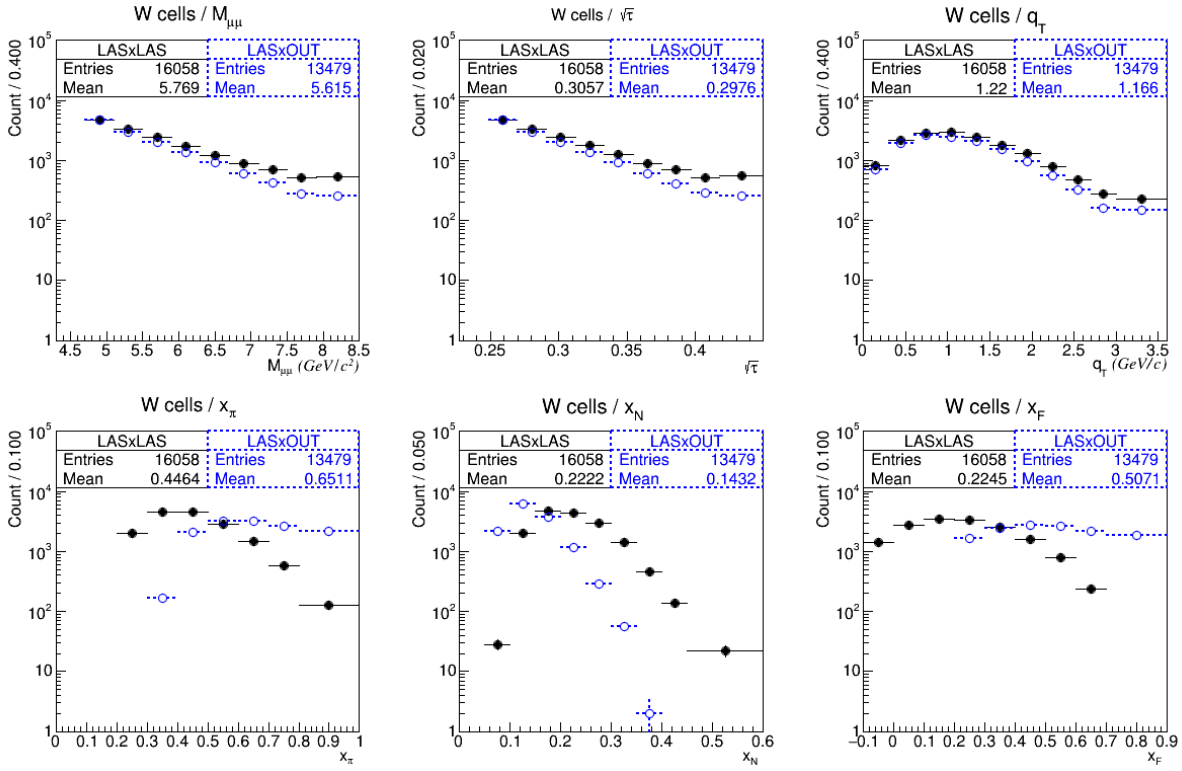

Figure 3.20: *1D kinematic distributions of two W cells combined : (Black) LAS × LAS trigger and (Blue) LAS × OT trigger.*

3.4 Extraction of acceptance

The efficiency extracted from Monte-Carol ,ε_{acc}, is described. Acceptance efficiency includes the efficiency of spectrometer geometry, trigger, detector, front-end electronics, and reconstruction. In Fig. 3.21, shows the block diagram of the comparison between the MC simulation and the real situation in COMPASS.

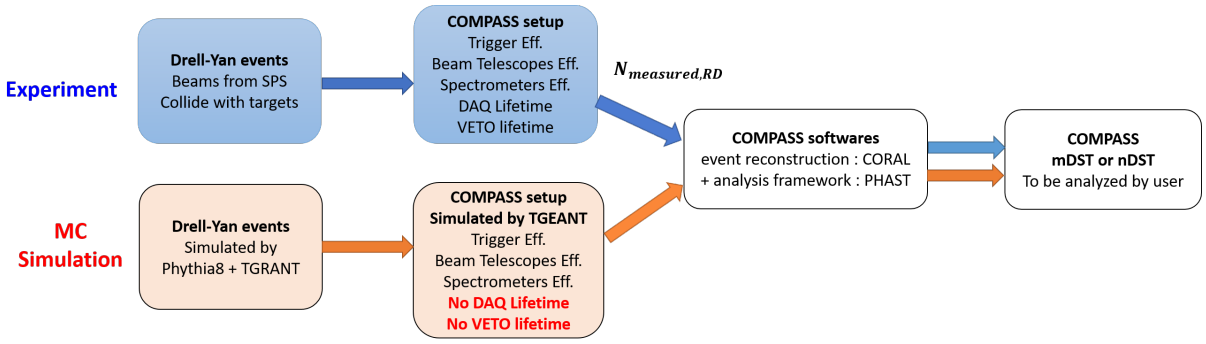

Figure 3.21: *The block diagram of the comparison between the MC simulation(Orange) and the real experiment (Blue).*

The starting point of the MC simulation is the Drell-Yan events simulated by Pythia8 [83] combined with TGEANT [72]. Pythia8 is a popular physic event generator widely used. TGRANT is the simulation tool customized for COMPASS experimental environment including the simulation of beams, triggers, spectrometers, etc. TGEANT simulates almost all the experimental conditions except for DAQ lifetime ε_{DAQ} and VETO lifetime ε_{VETO}. In the Drell-Yan cross-section analysis, almost all the efficiencies are simulated in MC except for DAQ lifetime ε_{DAQ} and VETO lifetime ε_{VETO}. TGEANT outputs the digitized information of hits from detectors then fed into CORAL which is the event reconstruction software in COMPASS. CORAL reconstructs tracks, vertexes of events. After the dimuon events reconstructed by the CORAL, the COMPASS analysis framework, PHAST, builds the event tree called mDST for analysis purpose. All the COMPASS softwares are described in more details in Sec. 2.1.7. CORAL and PHAST are commonly used for both MC and RD.

The acceptance simulated from MC is defined as follows :

$$\varepsilon_{Acc} = \frac{N_{rec}^{MC}}{N_{gen}^{MC}}$$

where N_{rec}^{MC} is the number of physics events reconstructed COMPASS spectrometers with the effect of trigger efficiency, efficiency of beam telescopes, efficiency of spectrometer, the geometry coverage of the spectrometer, and the reconstruction efficiency (affected by the reconstruction algorithm written in CORAL and the event selection cuts). N_{gen}^{MC} is the number of generated physics events from Pythia8.

There are several materials needed to be prepared to feed into MC : (1) Drell-Yan process setting in Pythia8, (2) Information of beam profile, beam intensity, and pile up, (3) Efficiency of trigger including geometric descriptions, hodoscopes plus electronics efficiency. (4) Efficiency of detectors including the geometry descriptions, detector plus electronics efficiency. The MC samples generated period by period on the stage because the trigger efficiency are extract period by period. The beam condition is quite stable over 2018, therefore beam profile(in space) extracted from P02 is used. The detector

efficiencies is taken from P03. The ideal case is to extract the detector efficiencies period by period same as trigger efficiencies. In this analysis, P03 detector efficiency is applied to all the periods. All the items required for MC in the following paragraphs will be presented. Furthermore, the acceptance, ε_{acc}, in one dimensional and three dimensional will be shown later. In the end of this section, the comparison of real data and MC data will be discussed.

3.4.1 Pythia8 settings

In this part, the setting of the Drell-Yan production used in Pythia8 is given. The Drell-Yan process involved in "Weak boson processes", which generates the production of a single electroweak gauge boson, i.e. γ^*/Z^0 or W^{+-}. The energy scale of COMPASS DY run is too low to produce Z^0 or W^{+-}, therefore only the production of γ^* is considered. The mass of γ^* is set to $3.5 \sim 11.0\ GeV/c^2$. Both initial and final state radiations were turned-off in the generator. Since the observed events are dimuon pairs, the appearance of muons in the final state is required. It is known that the p_T is not well calculated in Pythia8 because p_T is strongly affected by non-perturbative QCD effect. Consequently it's necessary to tune p_T parameters in order to obtain reasonable transverse momentum spectrum for this analysis.

The nucleon PDF and pion PDF used in Pythia8 are GRV98lo [84] and GRVPI0 [13] parameterizations. The Q-evolution is done via LHAPDF5 interface [85]. The Drell-Yan cross section of $\pi(\bar{u}d) - p(uud)$ collision is twice than $\pi(\bar{u}d) - n(udd)$ collision due to quark composition. In reality, it is not exactly two, but energy and kinematic dependent. $\sigma^{DY}_{\pi^- p}/\sigma^{DY}_{\pi^- n} = 1.83$ is obtained. The Pythia options used in this analysis can be found in Appendix. 4.3.

3.4.2 Beam setting

The setting of the beam conditions are mostly based on on the experimental condition. The beams profile in space is characterized by four parameters θ_x, θ_y, x_{beam}, y_{beam}, which are extracted from the experimental data collected with random trigger and beam triggers. The random trigger events serve as an unbiased input, but they are few. In order to increase the statistics also the beam trigger events are used. It was tested the beam profiles produced from random trigger and beam trigger are consistent. Traditionally, the amplitude of beam momentum is measured by the beam momentum station then input to the MC. However, the beam intensity in 2018 was too high to have the detector functioned properly. The amplitude of beam momentum in MC is simulated according to the past beam condition measured in 2014. The beam pile-up time window is set to $\Delta T = \pm\ 20ns$. The beam rate is set to 10^8 per second which is slightly higher than the experimental condition 6×10^7 per second.

3.4.3 Trigger efficiency

The physics trigger used are three dimuon triggers, $LAS \times LAS$, $LAS \times OT$, $LAS \times MT$. LAS and OT, MT are the single muon triggers composed by two hodoscopes. The signals of two hodoscopes are coincident with a designed matrix pattern in order to select the dimuon events cover the desired kinematics. This designed coincident matrix is so called the trigger matrix. Two single muon triggers construct a dimuon trigger. In this analysis,

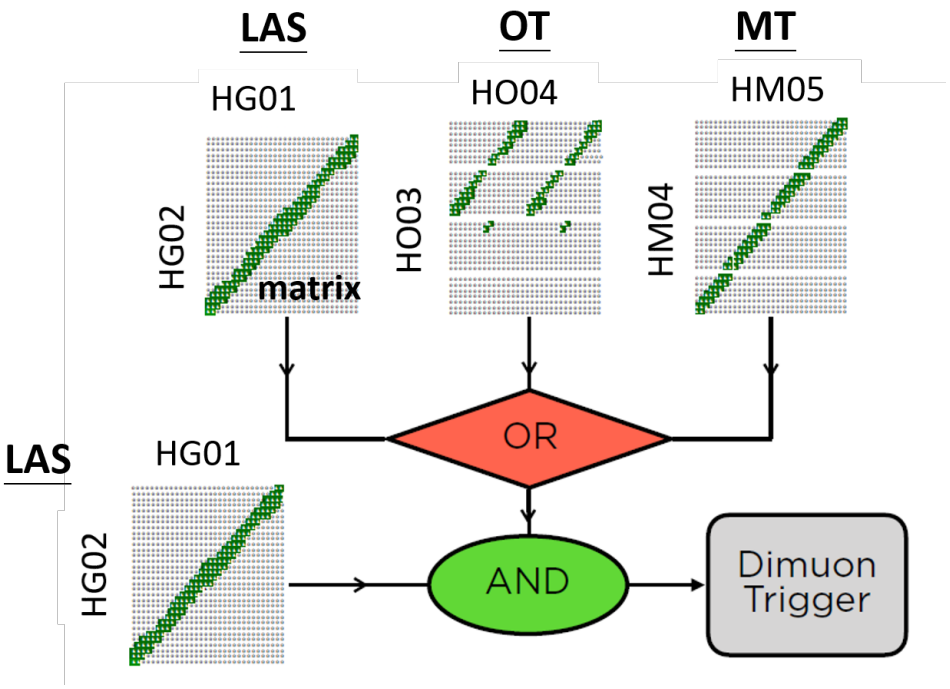

Figure 3.22: *The sketch of the formation of dimuon triggers from the hodoscopes and matrices [65].LAS trigger is composed by two hodoscopes, HG*01 *and HG*02*, and the trigger matrix of LAS is in a diagonal shape. The same concept is applied to OT and MT triggers : OT = HG*03 $\otimes$ *HG*04*, MT = HM*04 $\otimes$ *HM*05*. The dimuon triggers are composed by the AND logic of LAS, OT, and MT : LAS* $\times$ *LAS, LAS* $\times$ *OT, LAS* $\times$ *MT.*

$LAS \times MT$ events are not used due to the high background contamination. As drawn in Fig. 3.22, LAS trigger is composed by two hodoscopes, $HG01$ and $HG02$, and the trigger matrix of LAS is in a diagonal shape. The same concept is applied to OT and MT triggers : $OT = HG03 \otimes HG04$, $MT = HM04 \otimes HM05$. (One could find more detailed descriptions of the COMPASS trigger system in Sec. 2.1.5.) The efficiency of dimuon trigger is defined as follows :

$$\begin{aligned} \varepsilon_{LAS\otimes LAS} &= \varepsilon_{LAS} \times \varepsilon_{LAS} \\ \varepsilon_{LAS\otimes OT} &= \varepsilon_{LAS} \times \varepsilon_{OT} \\ \varepsilon_{LAS\otimes MT} &= \varepsilon_{LAS} \times \varepsilon_{MT} \end{aligned}$$

where

$$\begin{aligned} \varepsilon_{LAS} &= \varepsilon^{hodo}_{HG01} \times \varepsilon^{hodo}_{HG02} \times \varepsilon^{matrix}_{HGO1\otimes HG02} \\ \varepsilon_{OT} &= \varepsilon^{hodo}_{HO03} \times \varepsilon^{hodo}_{HO04} \times \varepsilon^{matrix}_{HO03\otimes HO04} \\ \varepsilon_{MT} &= \varepsilon^{hodo}_{HM04} \times \varepsilon^{hodo}_{HM05} \times \varepsilon^{matrix}_{HM04\otimes HM05} \end{aligned}$$

where $\varepsilon_{LAS\otimes LAS}$, $\varepsilon_{LAS\otimes OT}$, and $\varepsilon_{LAS\otimes MT}$ are the trigger efficiency of dimuon triggers multiplied by two single muon trigger efficiency, ε_{LAS}, ε_{OT}, or ε_{MT}. Efficiency of single muon trigger is multiplied by the hodoscope efficiency ε^{hodo} and matrix efficiency ε^{matrix}.

In the extraction of hodoscopes efficiency,ε^{hodo}, the good muon tracks are selected, then extrapolated to position of the hodoscopes. If there are hits of hodoscopes found in the passing slab or the neighboring slabs, the hodoscopes is considered efficient with this

track. The idea of the extraction of hopdoscope efficiency ε^{hodo} is drawn in Fig. 3.23. The hodoscope efficiencies can be defined as follows :

$$\varepsilon^{hodo} = \frac{N_{HitFound}}{N_{Track}} \tag{3.9}$$

where N_{Track} is the number of track passing through the hodoscopes, $N_{HitFound}$ is the number of hits found in the hodoscopes.

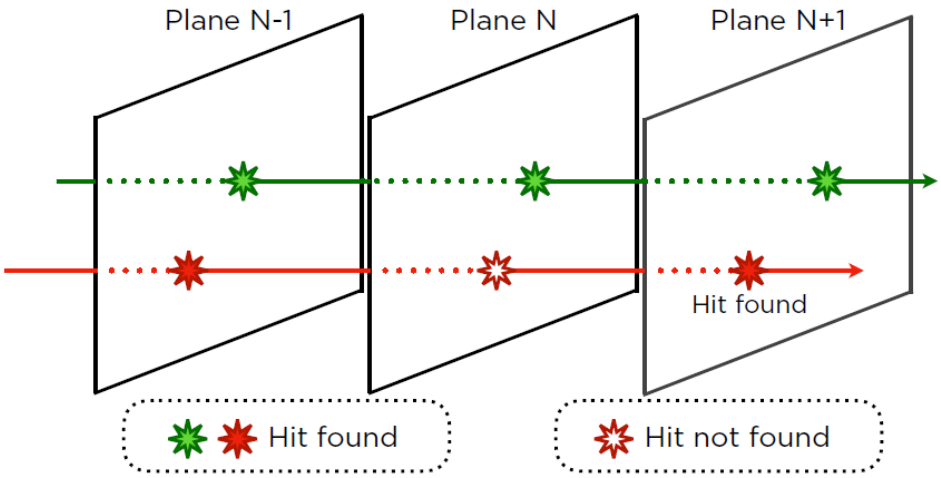

Figure 3.23: *The idea of the extraction of hopdoscope efficiency and detector efficiency [65].*

The 2-dimensional hodoscope efficiencies of P03 are shown in Fig. 3.24. 2D Efficiency of hodoscope is done period by period, but here only one period is shown. All the slabs are with the efficiency close to 100% except for the center slabs of $HG01$ of $LAS \sim 50\%$ efficiency. The low efficacy of the center slab of LAS bring significant impact for this analysis since high percentage of the muon tracks pass through this area.

The extraction of the efficiency of trigger matrix, ε^{matrix}, is straightforward : (1) All the hits from two hodoscopes are looped one by one, (2) The hits from two hodoscopes are paired from the same event and checked to see if the hit pairs occurs within the time window required by the single muon trigger setting hardware-wise, (3) The paired hits not only have to pass not only the the check of time window, but also the pattern of trigger matrix, (4) If paired hits pass all the requirement mentioned and also the corresponding trigger bit fires, then the matrix is considered efficient. The trigger matrix efficiency is defined as follows :

$$\varepsilon^{matrix} = \frac{N_{TriggerBitFired}}{N_{HitPairsFound}} \tag{3.10}$$

where $N_{TriggerBitFired}$ is the number of trigger bit fired, $N_{HitPairsFound}$ is the number of paired hits pass the requirement of time window and the pattern of matrix. The results of coincidence matrix efficiencies of P03 are shown in Fig. 3.25. The matrix efficiency is around 70% to 100%.

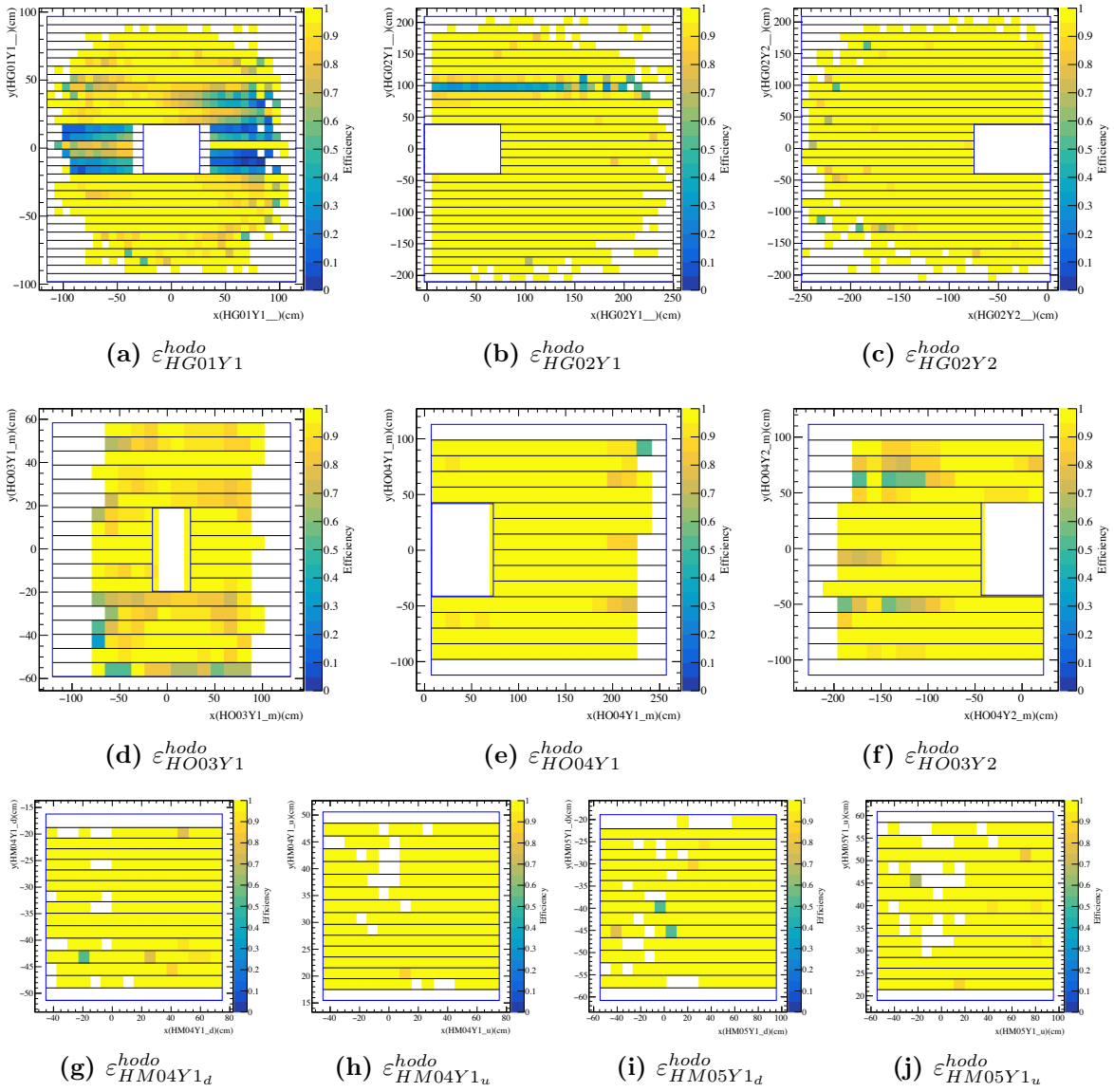

(a) $\varepsilon^{hodo}_{HG01Y1}$ **(b)** $\varepsilon^{hodo}_{HG02Y1}$ **(c)** $\varepsilon^{hodo}_{HG02Y2}$

(d) $\varepsilon^{hodo}_{HO03Y1}$ **(e)** $\varepsilon^{hodo}_{HO04Y1}$ **(f)** $\varepsilon^{hodo}_{HO03Y2}$

(g) $\varepsilon^{hodo}_{HM04Y1_d}$ **(h)** $\varepsilon^{hodo}_{HM04Y1_u}$ **(i)** $\varepsilon^{hodo}_{HM05Y1_d}$ **(j)** $\varepsilon^{hodo}_{HM05Y1_u}$

Figure 3.24: *The 2-dimensional hodoscope efficiencies : (top tow) LAS trigger, (middle row) OT trigger, (bottom tow) MT trigger. All the slabs are with the efficiency close to* 100% *except for the center slabs of* $HG01$ *of LAS trigger only with* $\sim 50\%$ *efficiency. The inefficiency of the center slab of LAS bring significant impact for this analysis since high percentage of the muon tracks pass through this area.*

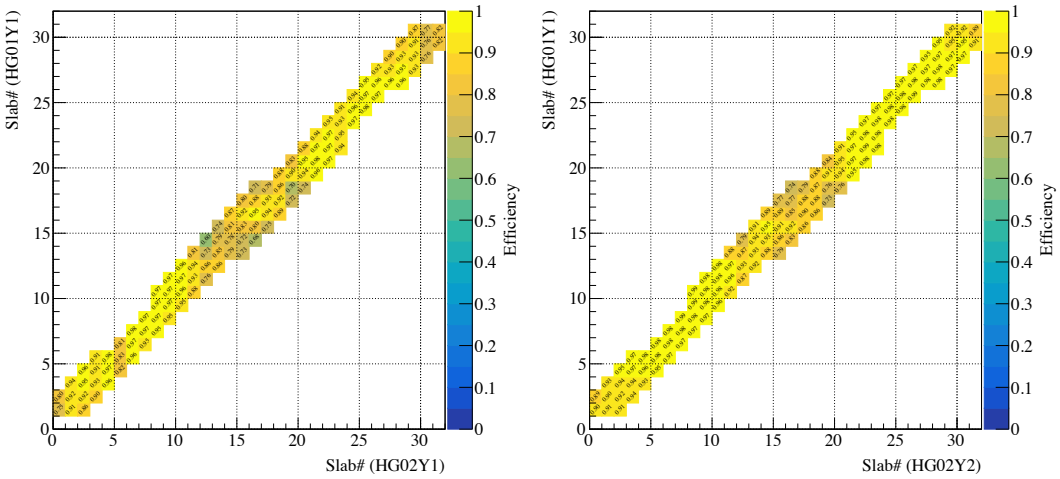

(a) $\varepsilon_{LAS1}^{matrix}$: $HG01Y1 \otimes HG02Y1$ **(b)** $\varepsilon_{LAS1}^{matrix}$: $HG01Y1 \otimes HG02Y2$

(c) $\varepsilon_{OT}^{matrix}$: $HG03 \otimes HO04$ **(d)** $\varepsilon_{MT}^{matrix}$: $HM04 \otimes HM05$

Figure 3.25: *The coincidence matrices efficiency of $LAS \times LAS$, $LAS \times OT$, and $LAS \times MT$ trigger. The matrix efficiency is around 70% to 100%.*

3.4.4 Detector efficiency

The extraction of detector efficiency is the same as the extraction of hodoscope efficiency sketched in Fig. 3.23 and defined in Eq. 3.9. Detector efficiency used in MC is extracted from real data, P03. Around 10% P03 data is used. The future goal is to implement it period by period. The detector efficiency of $DC01X1$ plane is shown in Fig. 3.26 as an example. The efficiency map is done in 2-dimensional.

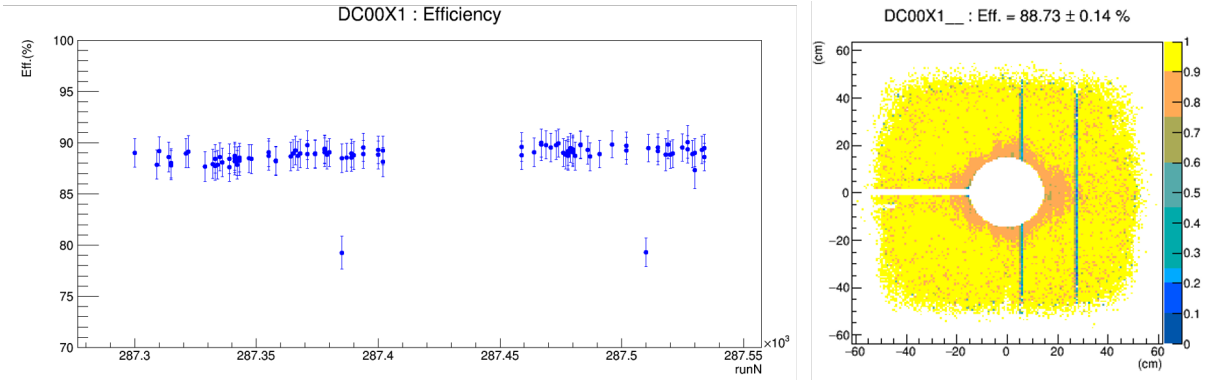

Figure 3.26: *The efficiency of DC00X1 in P03 : (Right) 1D efficiency verse run number. The efficiency is stable over the period. (Left) 2D efficiency averaged from 10% P03 data,* $\sim 88\%$.

3.4.5 Acceptance distribution

The multidimensional acceptance is determined in the generated kinematic space for bin i is defined as follows :

$$\frac{d\varepsilon^{acc}}{dx_i} = \frac{dN_i^{rec}}{dN_i^{gen}}$$

where N_i^{gen} is the MC truth and N_i^{rec} is the MC events after passing COMPASS hardware setup like spectrometers, triggers, beam telescopes, but not including DAQ lifetime and VETO lifetime (as described in Fig. 3.21). The selection criteria of N_i^{gen} and N_i^{rec} are described in Appendix. 4.3.

The acceptances used in this analysis are extracted target by target (5 cells, PT 1^{st}, PT 2^{nd}, Al cell, W 1^{st} cell, W 2^{nd} cell), trigger by trigger (2 triggers, LAS and $LAS \times OT$), also period by period (8 periods, P00-P08). In total, there are 80 acceptance sets generated dependents on the type of targets, triggers and periods. They are obtained from the same MC truth but different the experimental conditions/cuts lead to different N_i^{rec}, as consequence, different ε_{acc}.

The period-dependent acceptance of PT 1^st cell in x_F distribution is shown in Fig. 3.27. The acceptance of each period is compared with the P01. The difference between periods could go up to 20% due to the period-dependent trigger efficiency.

The one-dimensional acceptance of PT cells, Al cell, and W cells targets in six kinematics $M_{\mu\mu}$, $\sqrt{\tau}$, p_T, x_π, x_N, x_F are shown in Fig 3.28, Fig 3.29, Fig. 3.30. The acceptances shown in the plots are the weighted average acceptance of all periods and its weighting factor of each period is based on the real data statistics. In general, the average acceptance in COMPASS is around 10%. The 1D acceptance are quite uniform along $M_{\mu\mu}$, $\sqrt{\tau}$, and q_T distributions. However, it varies along x_π, x_N, and x_F distributions.

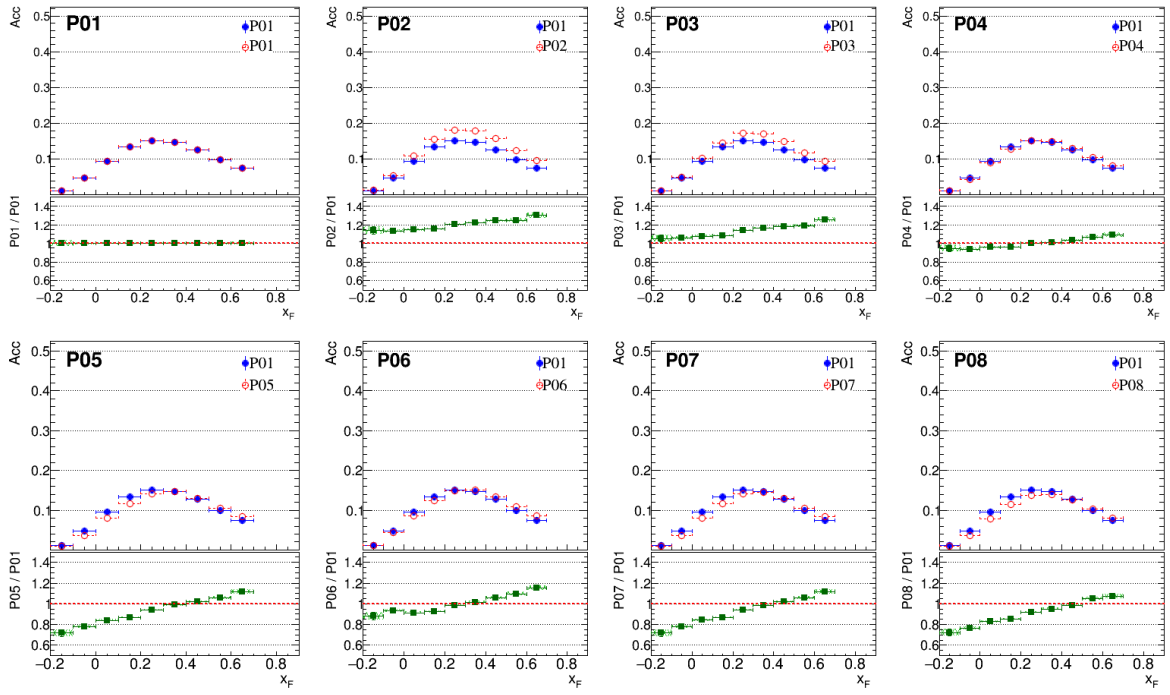

(a) *LAS* × *LAS trigger*

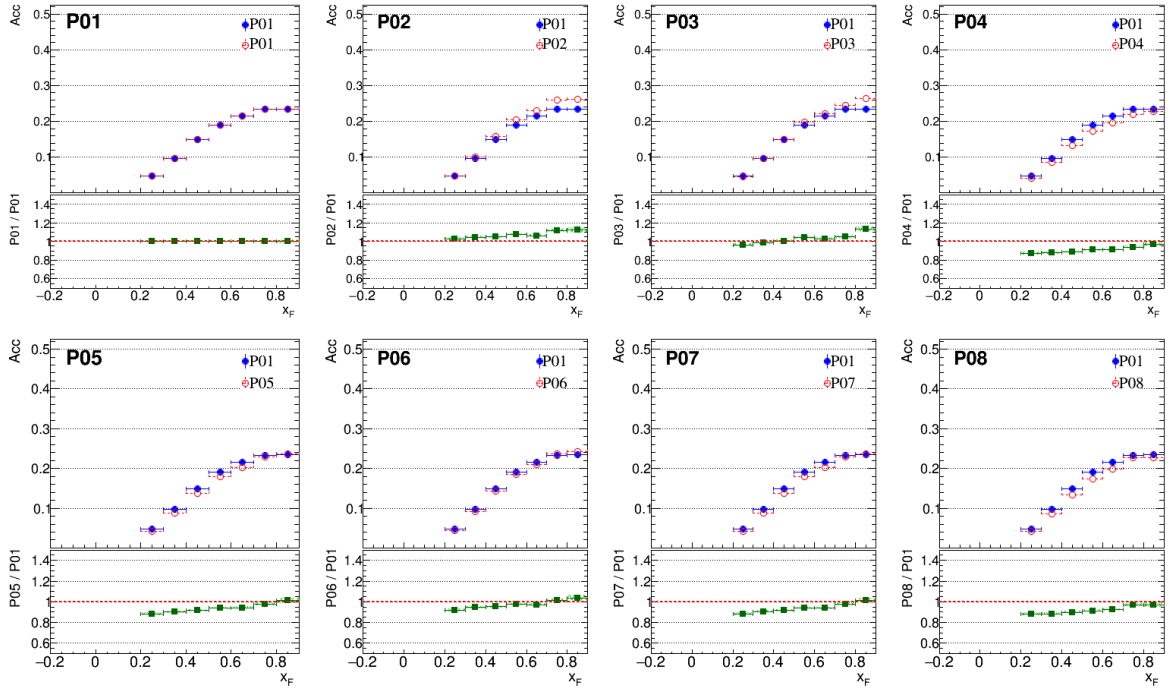

(b) *LAS* × *OT trigger*

Figure 3.27: *One-dimensional acceptance of PT 1st cell in x_F is shown period by period : (a) LAS × LAS (b) LAS × OT. The comparison of acceptance of each period with respect to period P01 is shown. The difference of acceptance between periods could go up to 20% because of the trigger efficiency.*

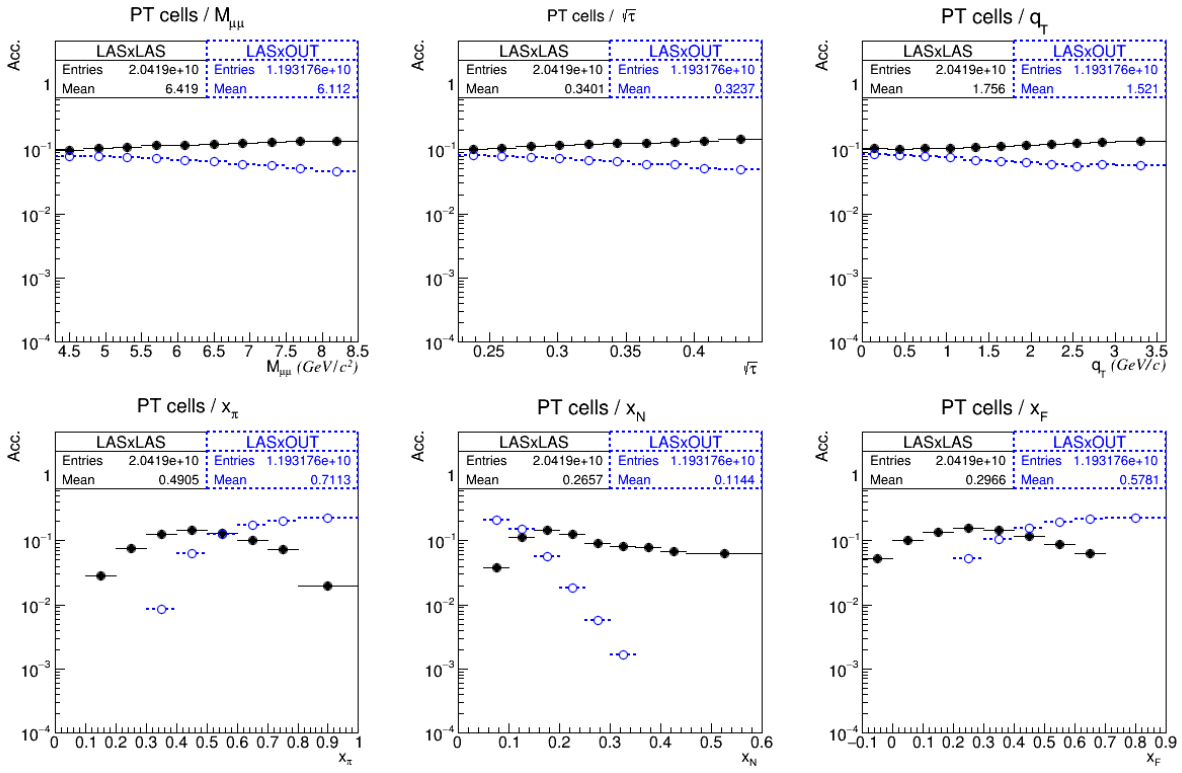

Figure 3.28: *One-dimensional acceptance of two PT cells : (Black) LAS × LAS (Blue) LAS × OT.*

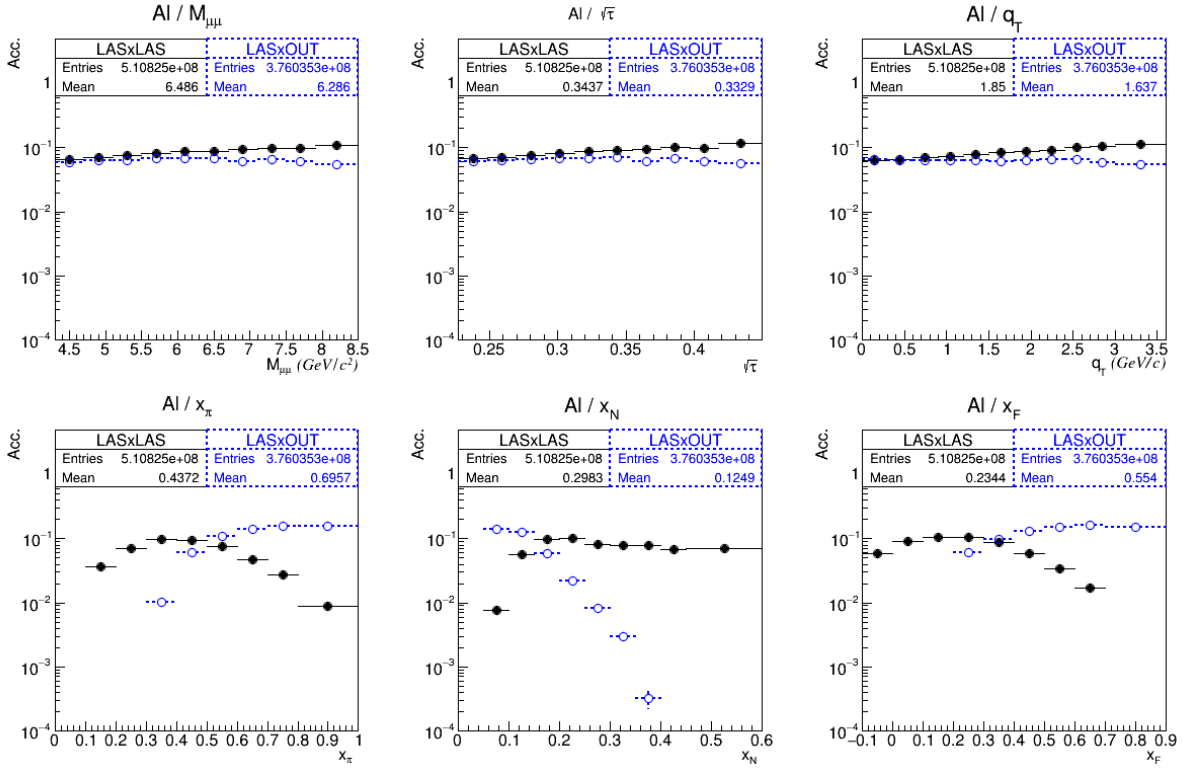

Figure 3.29: *One-dimensional acceptance of Al cell : (Black) LAS × LAS (Blue) LAS × OT.*

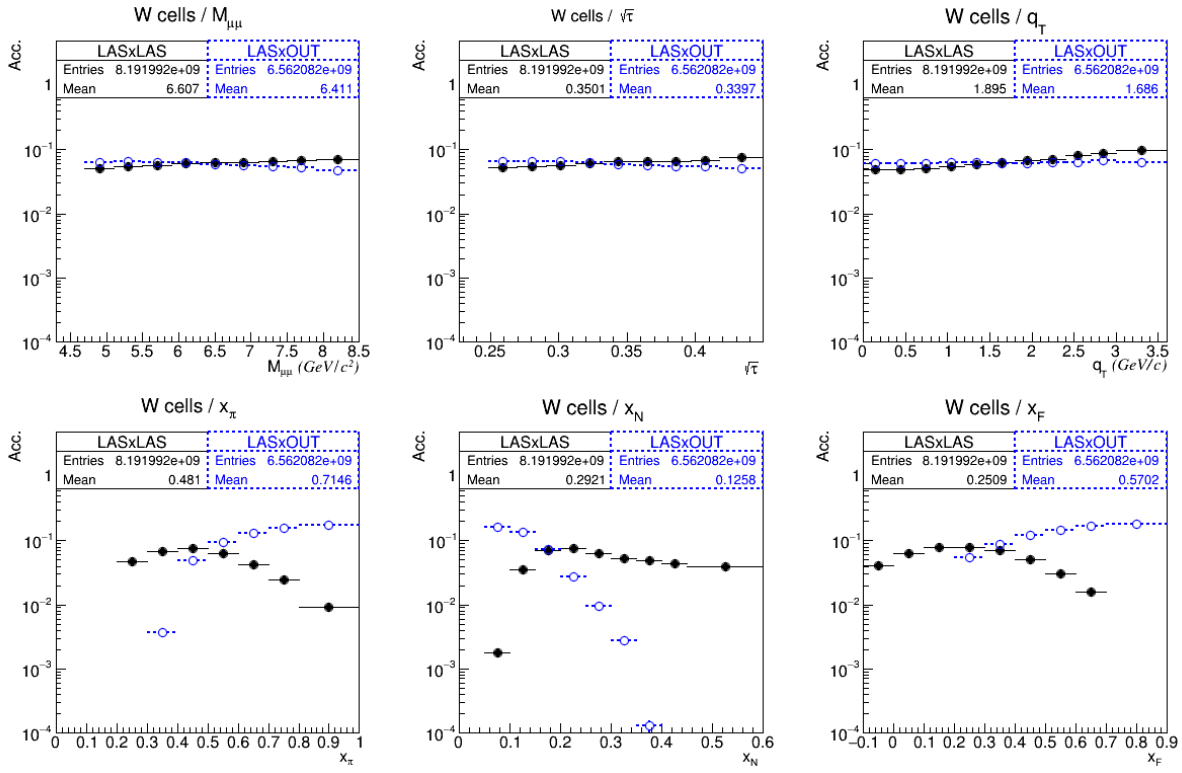

Figure 3.30: *One-dimensional acceptance of two W cells : (Black) LAS × LAS (Blue) LAS × OT.*

3.4.6 Monte-Carlo and real data comparison

To verify the reliability of the MC simulation, the comparison between MC reconstructed N_{rec} and real data is validated and shown in Fig. 3.31, Fig. 3.32, Fig. 3.33 for PT cells, Al cell, and W cells, respectively. In general, a nice agreement between MC and real data is achieved within 20% deviation. However, there are some kinematics regions gives unsatisfied MC/RD ratio :

- $M_{\mu\mu}$ region at $8.0 < M_{\mu\mu} < 8.5(GeV/c^2)$
- $\sqrt{\tau}$ region at $0.40 < \sqrt{\tau} < 0.45$
- p_T region at $2.0 < p_T < 3.5(GeV/c)$
- x_π region at $0.9 < x_\pi < 1.0$
- x_N region at $0.5 < x_N < 0.6$ for $LAS \times LAS$
- x_N region at $0.3 < x_N < 0.4$ for $LAS \times OT$
- x_F at $0.8 < x_F < 0.9$ for $LAS \times LAS$

Overall, the inconsistencies between RD and MC are located at high $M_{\mu\mu}$, high p_T, high x_π, high x_N, and high x_F regions which are also the regions has less MC events populated. For the inconsistency in p_T, it might be expected because the event generator Pythia8 does not have good description for the p_T spectrum. The special settings are made in Pythia8 in the Drell-Yan process generation to tune the p_T customized for this

analysis. For the rest kinematics in $M_{\mu\mu}$, $\sqrt{\tau}$, x_π ,x_N, and x_F, the detector efficiency might play the role since it is not implemented on period basis. The problem might be solved after the detector efficiency implemented period by period in the future. Another suspection is that the trigger efficiency estimated is still not perfect. Despite of some small inconsistencies, the MC simulation used in this analysis is considered in a good shape.

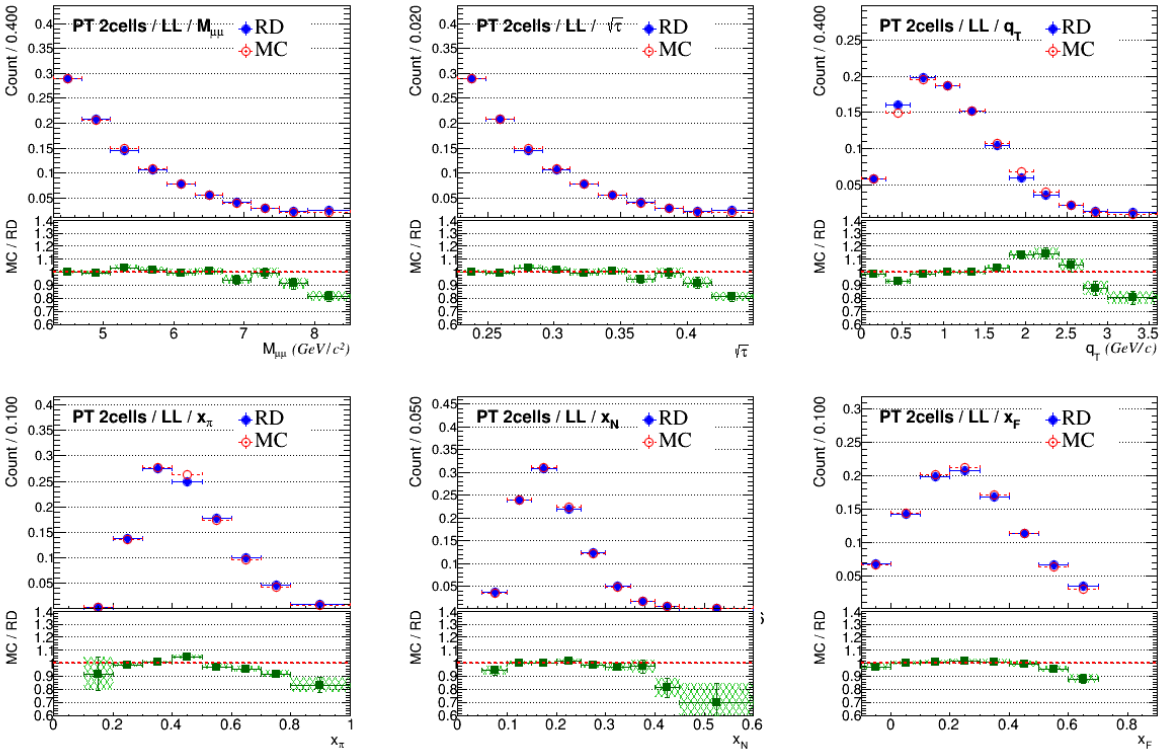

(a) *LAS × LAS trigger*

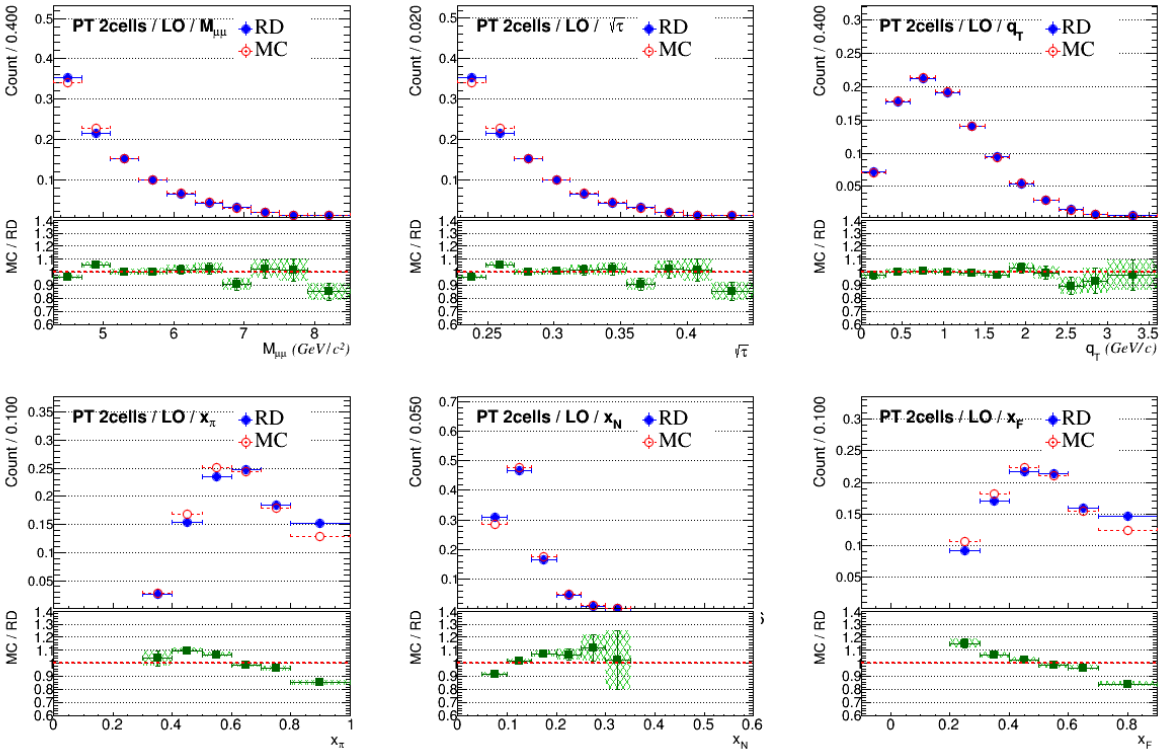

(b) *LAS × OT trigger*

Figure 3.31: *The Comparison between MC and real data in one dimension for two PT cells : (a) LAS × LAS (b) LAS × OT.*

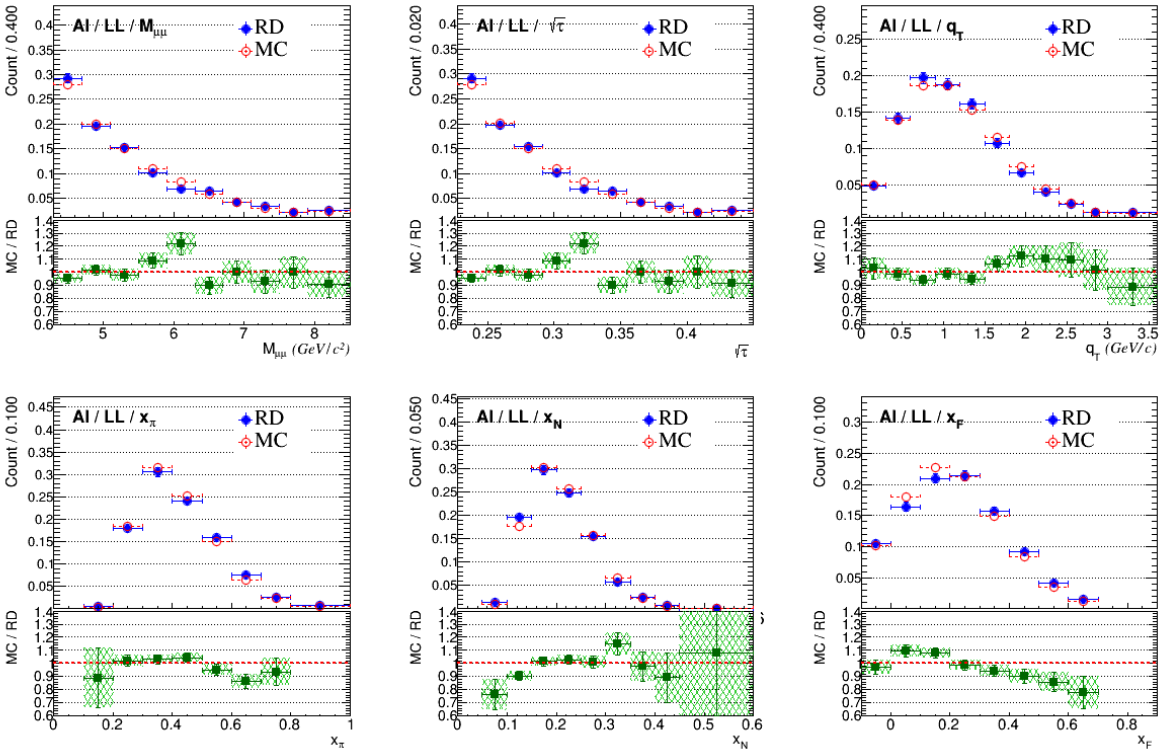

(a) *LAS × LAS trigger*

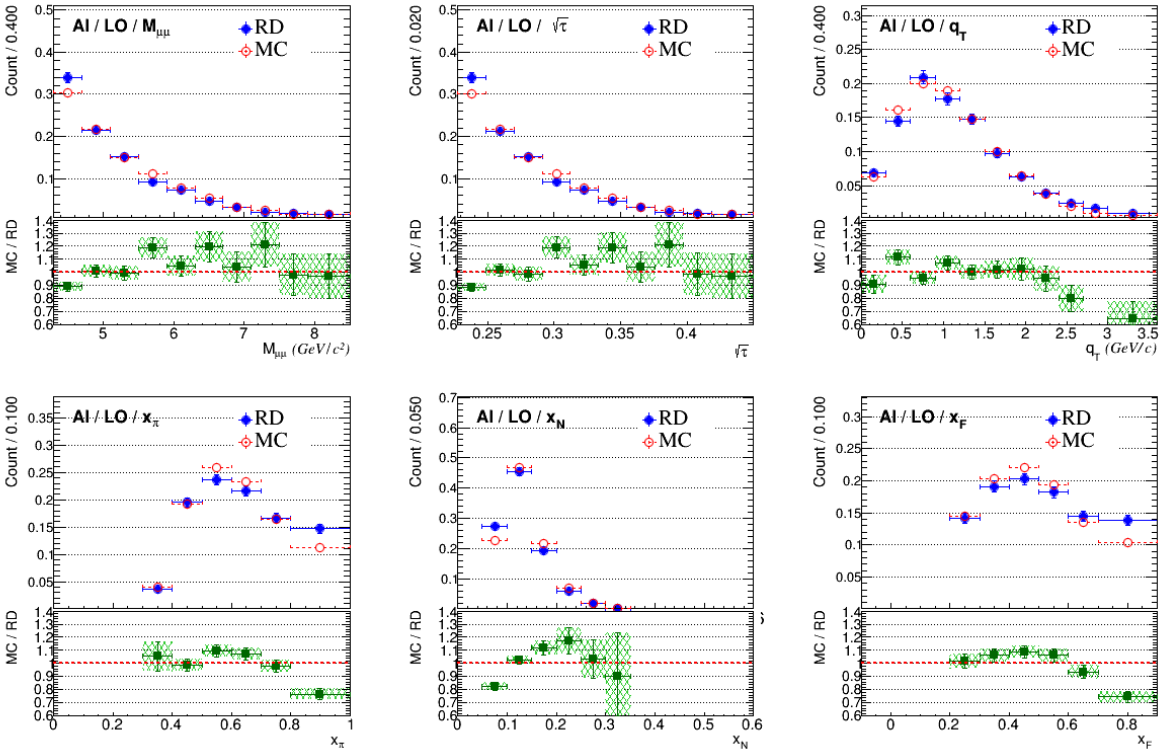

(b) *LAS × OT trigger*

Figure 3.32: *The Comparison between MC and real data in one dimension for Al cell: (a)LAS× LAS (b) LAS × OT.*

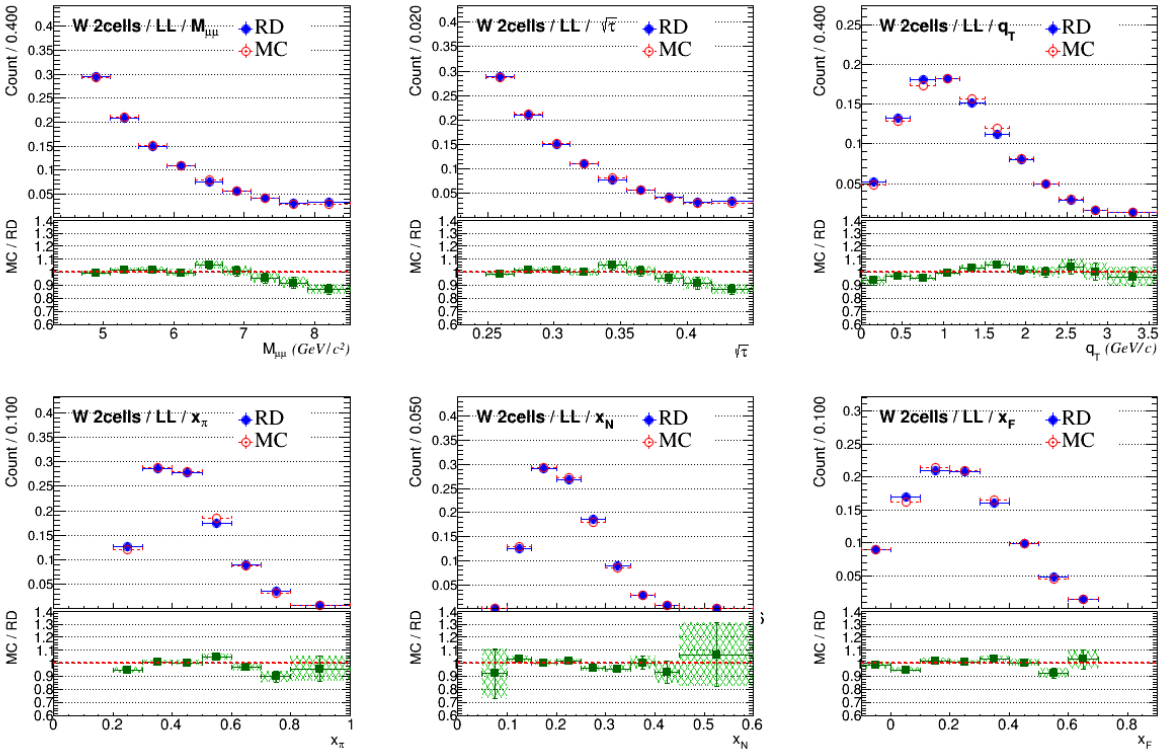

(a) *LAS × LAS trigger*

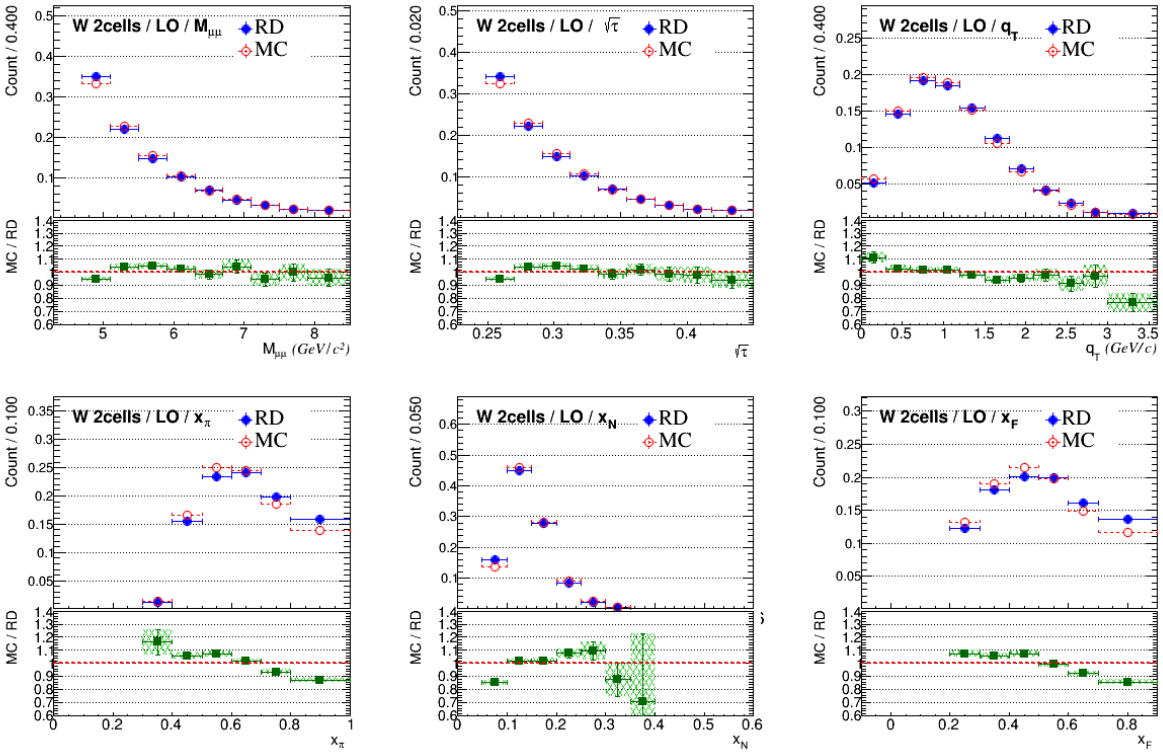

(b) *LAS × OT trigger*

Figure 3.33: *The Comparison between MC and real data in one dimension for W 1^{st} cell : (a) LAS × LAS (b) LAS × OT.*

3.5 Extraction of differential Drell-Yan cross-section

In this section, the multidimensional cross section are extracted and the results are compared with the theoretical calculation under Drell-Yan Next-to-Next-to-Leading Order(DYNNLO) framework in QCD perturbation theory [86] and the past experiments, NA10 [22] and E615 [21].

3.5.1 Method to extract differential cross-section

The extraction method of the cross section is called event-weighted method, the formulation is as follows :

$$\frac{d^n\sigma}{dx_1dx_2...dx_n} = \frac{1}{\mathscr{L}} \times \frac{d^n(N_{measured,i}/w_i)}{dx_1dx_2...dx_n} \ , \ w_i = \varepsilon_{acc,i}\varepsilon_{DAQ,i}\varepsilon_{VETO,i} \tag{3.11}$$

Each pair of dimuon event finds its corresponding efficiencies : (1) Acceptance efficiency $\varepsilon_{acc,i}$ depends on its trigger type and kinematic region, (2) DAQ efficiency $\varepsilon_{DAQ,i}$ depends on its trigger type and the unique spill number, (3) VETO efficiency $\varepsilon_{VETO,i}$ depends on its trigger type and the unique spill number. Afterwards the dimuon pair is corrected with a given weight, $w_i = \varepsilon_{acc,i} \times \varepsilon_{DAQ,i} \times \varepsilon_{VETO,i}$. The corrected kinematic distribution is divided by the luminosity in the end to access the cross section in multidimensional.

3.5.2 Three-dimensional cross-section

The three-dimensional cross section is extracted in the kinematics of $M_{\mu\mu}$, p_T, and x_F with event-weighted method and three-dimensional acceptance correction. The binning and kinematics chosen is listed in Table. 3.11. The kinematics ranges chosen are $-0.1 < x_F < 0.9$, $0.0 < p_T(GeV) < 3.6$ and $4.3 < M_{\mu\mu}(GeV) < 8.5$. A coarse binning is selected in $M_{\mu\mu}$ and q_T, and a finer binning in x_F. The global analysis of the pion PDFs are mainly fitted with the cross section in x_F distribution therefore finer binning in x_F is chosen. The JAM group recently starts to include the Drell-Yan cross section as a function of p_T in the global analysis of the pion PDFs [87]. The ideal case is to have a finer binning in both x_F and p_T, however it is not done in this analysis due to the limited statistics. Nevertheless, it is still interesting to see the variation of the cross section in more than two dimensions which was mostly done by the past experiments.

Table 3.11: *Binning of three-dimensional cross section*

Kinematics	Nbin	Binning
$M_{\mu\mu}(GeV)$	3	[4.3, 4.7, 5.4, 8.5]
$p_T(GeV)$	4	[0.0, 0.7, 1.1, 1.6, 3.6]
x_F	11	[-0.1, 0.0, 0.1, 0.2, 0.3, 0.4, 0.5, 0.6, 0.7, 0.8, 0.9]

The three-dimensional cross-sections of PT cells, Al cell, and W cells are shown as a function of x_F distribution over different p_T and $M_{\mu\mu}$ bins given in Fig. 3.34, Fig. 3.35, and Fig. 3.36, respectively. Note that the mass range of W cells is narrower, $4.7 < M_{\mu\mu}(GeV) < 8.5$. The multiple scattering of muon tracks in the heavy target is worse than the light target, as a results, the W cells have worse mass resolution than the others. The mass cut chosen keeps the background level less than 5%. As shown in the plots,

Drell-Yan cross section is rapidly decreased with the increase of the dimuon mass. In the range of p_T studied, the peak of Drell-Yan cross section appears around $p_T \sim 1(GeV)$.

The systematic uncertainty bands are drawn in the bottom of the plots. The systematic band is discontinuous along the kinematic distribution due to the extraction method described in Sec. 3.6. The numerical values of three-dimensional cross-sections are given in Appendix. 4.3.

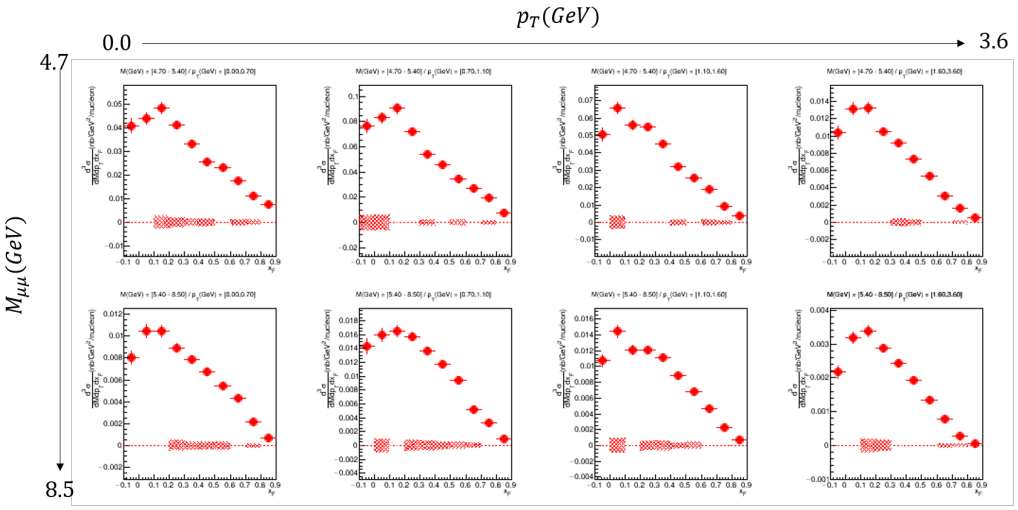

Figure 3.34: *The **three-dimensional** cross section of **W cells**. They are shown as a function of x_F distribution over different p_T and $M_{\mu\mu}$ bins. An systematic uncertainty bend in red is shown in the bottom of the plot.*

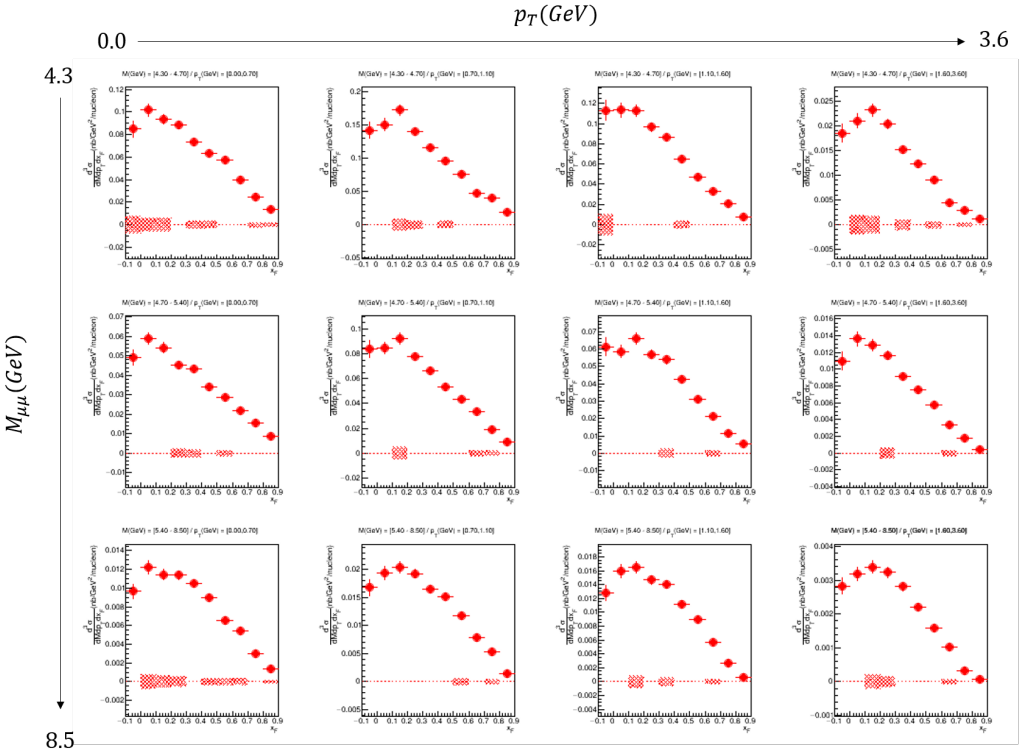

Figure 3.35: *The **three-dimensional** cross section of **PT cells**. They are shown as a function of x_F over different p_T and $M_{\mu\mu}$ bins. The red bend is the systematic uncertainty.*

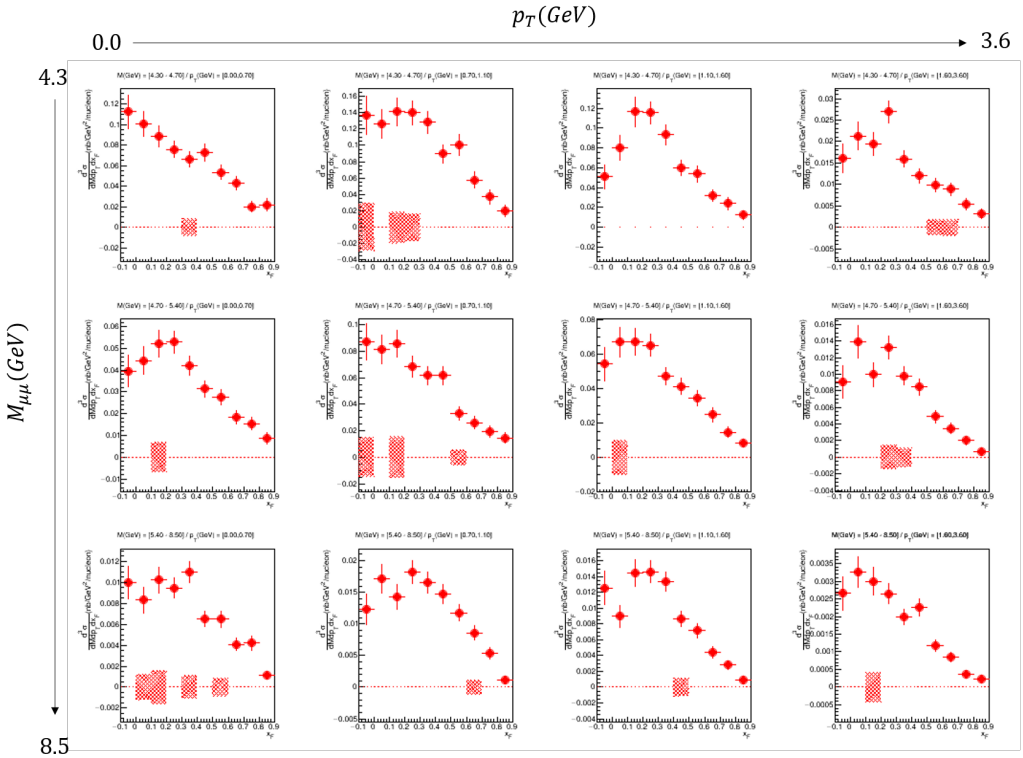

Figure 3.36: *The **three-dimensional** cross section of **Al cell**. They are shown as a function of x_F over different p_T and $M_{\mu\mu}$ bins. The red bend is the systematic uncertainty.*

3.5.3 Two-dimensional cross-section

The two-dimensional cross sections are evaluated with two-dimensional-acceptance correction and the event-weighted method. Among kinematic ranges chosen, $-0.1 < x_F < 0.9$, $0.0 < p_T(GeV) < 3.6$ and $4.3 < M_{\mu\mu}(GeV) < 8.5$, any of the two combinations are studied in the two-dimensional cross-section, $d^2\sigma/d\sqrt{\tau}dx_F$, $d^2\sigma/dM_{\mu\mu}dp_T$, and $d^2\sigma/dx_F dp_T$. The third dimension is integrated. The advantage of the two-dimensional cross-section compared to three-dimensional one is that the binning of the kinematics is finer so that the physics is better observed. In the publication of the past experiments, the cross-sections are mostly extracted in two dimensions. In order to compare the Drell-Yan cross section with the other experiments, the binning of the two-dimensional extraction follows the binning of the cross-section results published in E615 [21] and NA10 [22] experiments which are the pion-tungsten experiments with 252 GeV and 196 GeV pion beams, respectively. Their two-dimensional cross-sections are discussed as follows :

- $d^2\sigma/d\sqrt{\tau}dx_F$

  COMPASS results The pion-induced Drell-Yan cross sections in $d^2\sigma/d\sqrt{\tau}dx_F$ is a valuable to access the pion PDFs based on Eq. 1.19. The high statistics Drell-Yan cross sections data in the $x_F < 0.2$ helps to improve the sea and gluon distributions as well [18]. However the pion-induced data was not updated for 30 years since the publication of E615 experiment**??**. The pion-induced Drell-Yan cross sections in from 2018 COMPASS data-taking could make contributions to the global analysis of pion PDF.

  The two-dimensional Drell-Yan cross-section in x_F and $\sqrt{\tau}$, $d^2\sigma/d\sqrt{\tau}dx_F$, is extracted with the binning shown in Table. 3.12 follows the binning of E615 experi-

ment [21]. The reason to study the Drell-Yan cross-section in $\sqrt{\tau} = M_{\mu\mu}/\sqrt{s}$ instead of $M_{\mu\mu}$ is to normalize the effect from the center-of-mass energy so that it is more convenient to compare the results from different experiments so-called scaling effect. The corresponding $M_{\mu\mu}$ ranges with different $\sqrt{\tau}$ ranges are also given in Table. 3.12. The $\sqrt{\tau}$ range, $0.231 < \sqrt{\tau} < 0.438$ $(4.37 < M_{\mu\mu}(GeV) < 8.28)$ is slightly smaller than the cut limitations chosen $4.3 < M_{\mu\mu}(GeV) < 8.5$ in this analysis in order to adopt to the binning of E615 reported. The x_F range chosen is in the range of $-0.1 < x_F < 0.9$.

The two-dimensional Drell-Yan cross-section of PT cells, Al cell, and W cells are shown in Fig. 3.37. The Drell-Yan cross section rapidly drops with the increase of $\sqrt{\tau}$ as expected. Along x_F kinematic, the cross section shows a Poisson distribution with a high point around x_F=0.2. The systematic uncertainty is drawn in the bottom of the plots. The systematic uncertainty is discontinuous due to the extraction method studied in Sec. 3.6. The systematic uncertainty is high in the range of $0.0 < x_F < 0.3$ due to the effect of trigger dependence discussed in Sec. 3.6.6. The fluctuation of the two-dimensional cross section for Al cell is large due to the low statistics. For W cells, the cross-section of $0.231 < \sqrt{\tau} < 0.454$ $(4.37 < M_{\mu\mu}(GeV) < 4.80)$ is not reported due to the cut limitation, $M_{\mu\mu} > 4.7(GeV)$. The numerical values are given in Appendix. 4.3.

Table 3.12: *Binning of two-dimensional cross section in $\sqrt{\tau}$ and x_F.*

Kinematics	Nbin	Binning
x_F	10	[-0.10, 0.0, 0.10, 0.20, 0.30, 0.40, 0.50, 0.60, 0.70, 0.80, 0.90]
$\sqrt{\tau}$	9	[0.231, 0.254, 0.277, 0.300, 0.323, 0.346, 0.369, 0.392, 0.415, 0.438]
$M_{\mu\mu}$	9	[4.37, 4.80, 5.24, 5.67, 6.10, 6.54, 6.97, 7.41, 8.44, 8.28]

Comparison with E615 and NA10 results E615 experiment at Fermilab($252GeV$ π^- beams) [21] and NA10 at CERN($196GeV$ π^- beams) [22] measured the Drell-Yan cross sections with π^- beams incident on the tungsten target, as COMPASS(190 GeV π^- beams) does. The global fit of pion PDFs were all extracted from pion-induced NA10 and E615 results only. However, it was found that the normalization of cross section is around 20% different between them [30]. COMPASS results will be compared with NA10 and E615 as follows.

Fig. 3.38 shows the comparisons of Drell-Yan cross section of W cells as function of x_F in several $\sqrt{\tau}$ bins : (a)COMPASS VS NA10 and (b)COMPASS VS E615. The scaling factor $M^3/\sqrt{s}$ is applied in order to compare the cross section between different experiments with different beam energy. The Drell-Yan cross section of NA10 experiment was first published in Ref. [22] and later updated in Ref. [30] due to the problem found in the analysis. Here the results of NA10 published in Ref. [30] is used. Fig. 3.38(a) shows that NA10 and COMPASS results have a nice agreement except for the low x_F region, $x_F < 0.2$ in all the $\sqrt{\tau}$ bins. Fig. 3.38(b) shows that E615 and COMPASS have a nice agreement in the range of $0.346 < \sqrt{\tau} < 0.415$, however COMPASS results are higher than E615 results by a factor of 10% to 50% in the range of $0.254 < \sqrt{\tau} < 0.346$. Overall, Drell-Yan cross section of COMPASS and NA10 are agreed but both of them larger than E615 estimated. The disagreement in low $x_F < 0.2$ is also observed in the comparison with E615 data. The inconsistency in low x_F region might be caused by the unrealistic MC, multidimensional comparison between RD and MC will be investigated.

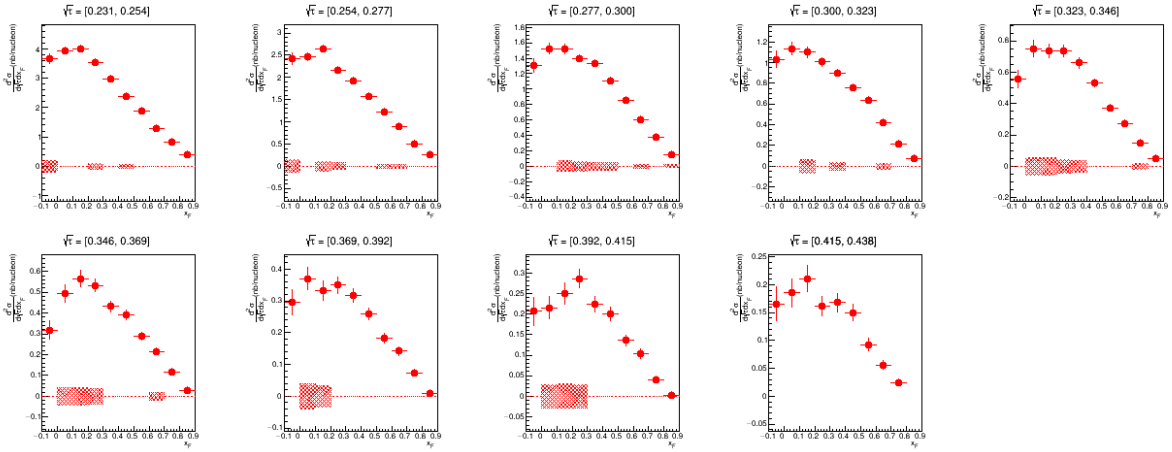

(a) *PT cells.*

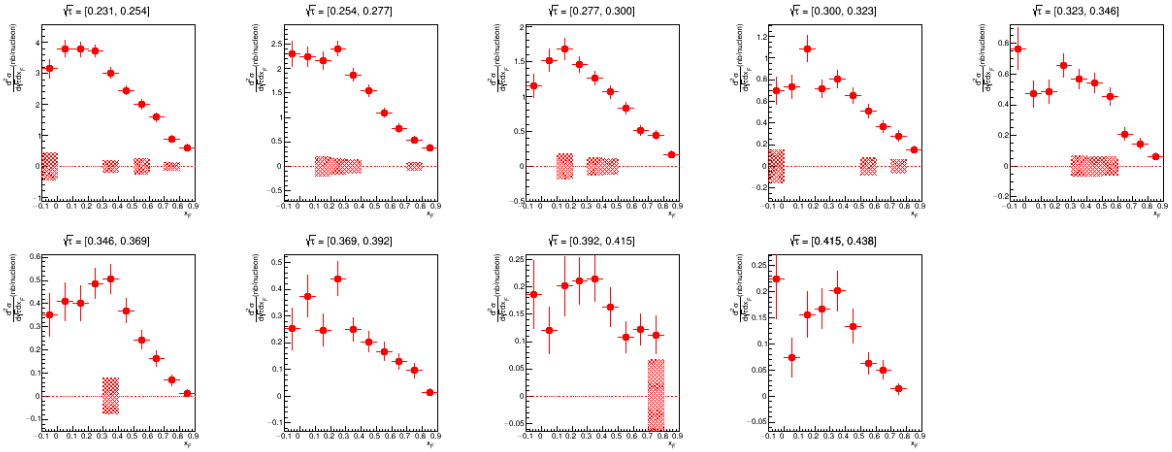

(b) *Al cell*

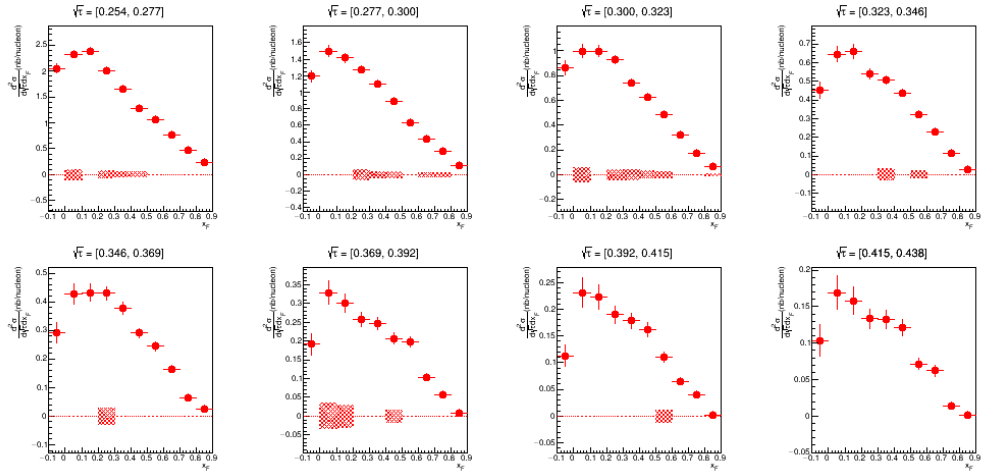

(c) *PT cells*

Figure 3.37: $d^2\sigma/d\sqrt{\tau}dx_F$ *: The two-dimensional cross section as a function of* x_F *in different* $\sqrt{\tau}$ *bins. The systematic uncertainties are shown in the bottom with the cred bend.*

Comparison with the pQCD calculations In Fig. 3.39, it shows the pQCD calculation in NLO compares with COMPASS results as a function of x_F integrated over $0.254 < \sqrt{\tau} < 0.438$ for (a)PT cells, (b)Al cell, and (c)W cells. The supplementary plots in different $\sqrt{\tau}$ bins are shown in Fig. 3.40 for PT cells, Fig. 3.41 for

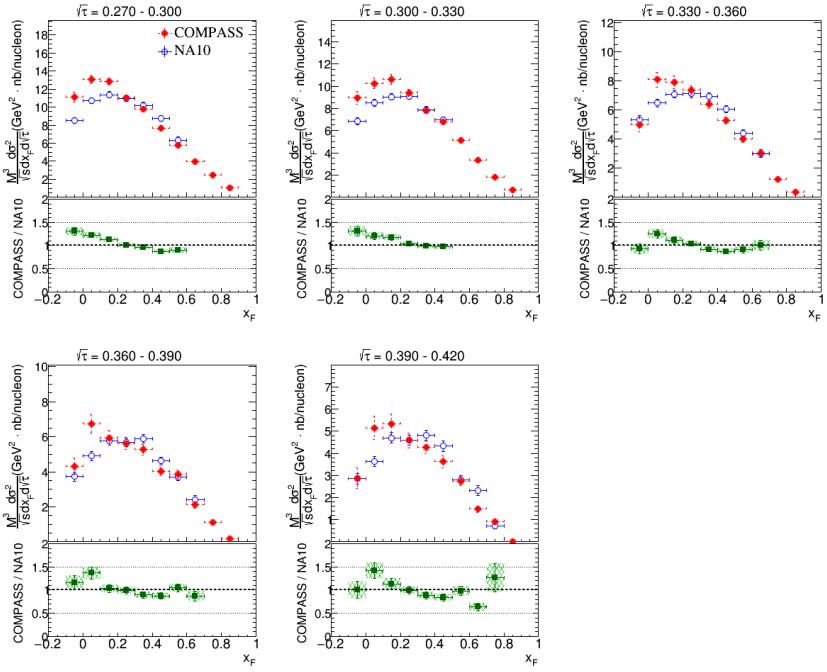

(a) *Comparison between COMPASS(red) and NA10(blue)*

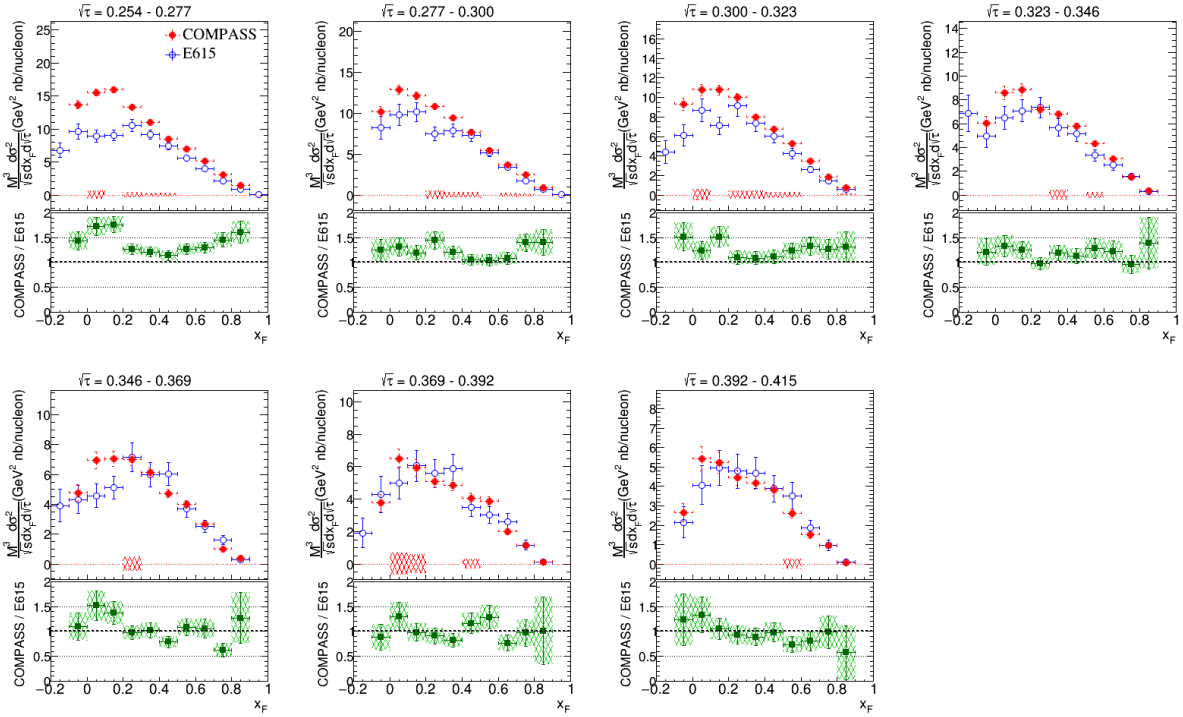

(b) *Comparison between COMPASS (red) and E615(blue)*

Figure 3.38: *The comparison of Drell-Yan cross section of W cells as function of x_F at several $\sqrt{\tau}$ bins between COMPASS, E615, and NA10 experiments. Scaling factor of beam energy $\frac{M^3}{\sqrt{\tau}}$ is applied.*

Al cell, Fig. 3.42 for W cells.

The pQCD calculation is done under DYNNLO framework [86] doesn't include the logarithm resummation contribution in large x (non-perturbative QCD effect).

There are three pion PDFs are tested with pQCD calculation, GRV [13], JAM [16], and xFitter [18]. There are three pion PDFs are tested with pQCD calculation, GRV [13], JAM [16], and xFitter [18]. GRV was published in 1992 and widely used. XFitter and JAM are published recently in 2018 and 2020, respectively. The detailed discussion on the current pion PDF is in Sec. 1.2.1. The target structure is calculated with nucleon PDF, CT14 [3]. The isospin average of proton and neutron is considered($\sigma_W \sim 0.4\sigma_p + 0.6\sigma_n$, $\sigma_{Al} \sim 0.5\sigma_p + 0.5\sigma_n$, and $\sigma_{PT} \sim 0.6\sigma_p + 0.4\sigma_n$. Unit is per nucleon). There is no nuclear effect included in the calculation.

As shown in Fig. 3.39, the theoretical calculations using different pion PDFs give great differences. In terms of the amplitude, $\sigma_{xFitter} > \sigma_{JAM} > \sigma_{GRV}$. The normalization of the cross-section shows around 30% difference between GRV and xFitter, even though the same data sets are used in their global fits(pion-induced DY from E615 and NA10, pion-induced J/ψ from WA70). The calculation with GRV is too low compared to the ones from JAM and xFitter results because its low valance composition with respect to the other pion PDFs shown in Fig. 1.10. The DY cross section as a function of x_F of PT cells and Al cell agree on the pQCD calculation in NLO using xFitter. However, W cells results is aligned in between the pQCD calculations with JAM and pQCD calculation with xFitter. Overall, COMPASS results have nice consistencies with pQCD calculation in NLO using JAM and xFitter considering the overall uncertainty of statistics and systematic. The data does not have enough discriminated power to judge which one is in favor. The differential cross-section of COMPASS as function of x_F in different $\sqrt{\tau}$ is shown in Fig. 3.40 for PT cells, Fig. 3.41 for Al cell, Fig. 3.42 for W cells. The conclusion stays the same when looking into different different $\sqrt{\tau}$ bins.

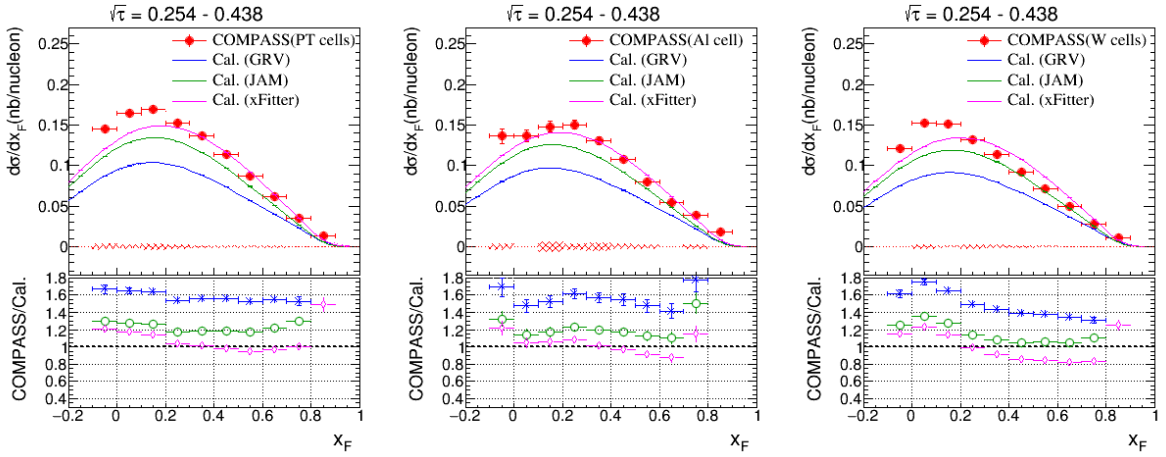

(a) *PT cells* **(b)** *Al cell* **(c)** *W cells*

Figure 3.39: *(Top) The comparison of cross section as a function of x_F integrated in the range of $0.254 < \sqrt{\tau} < 0.438$ between COMPASS and pQCD calculations in NLO with pion PDFs. COMPASS data is drawn in the red dots with the systematic uncertainty been given in the bottom aligned with zero. The calculations are done with three kinds of pion PDFs, GRV in blue lines, JAM in green lines, xFitter in magenta line and proton PDF CT14. (Bottom)The ratio between COMPASS data and pQCD calculations in NLO.*

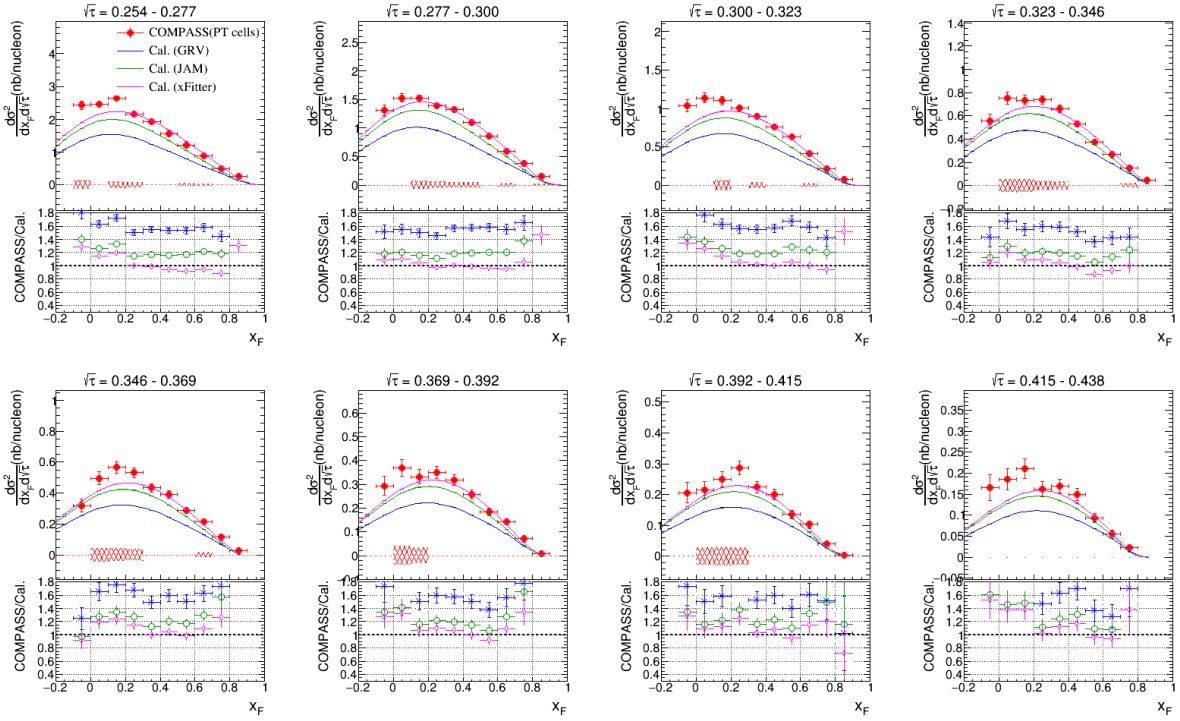

Figure 3.40: *The supplemental plots of Fig. 3.39(a). The comparison of cross section as a function of x_F in different $\sqrt{\tau}$ bins between COMPASS and DYNLO calculations for* ***PT cells****.*

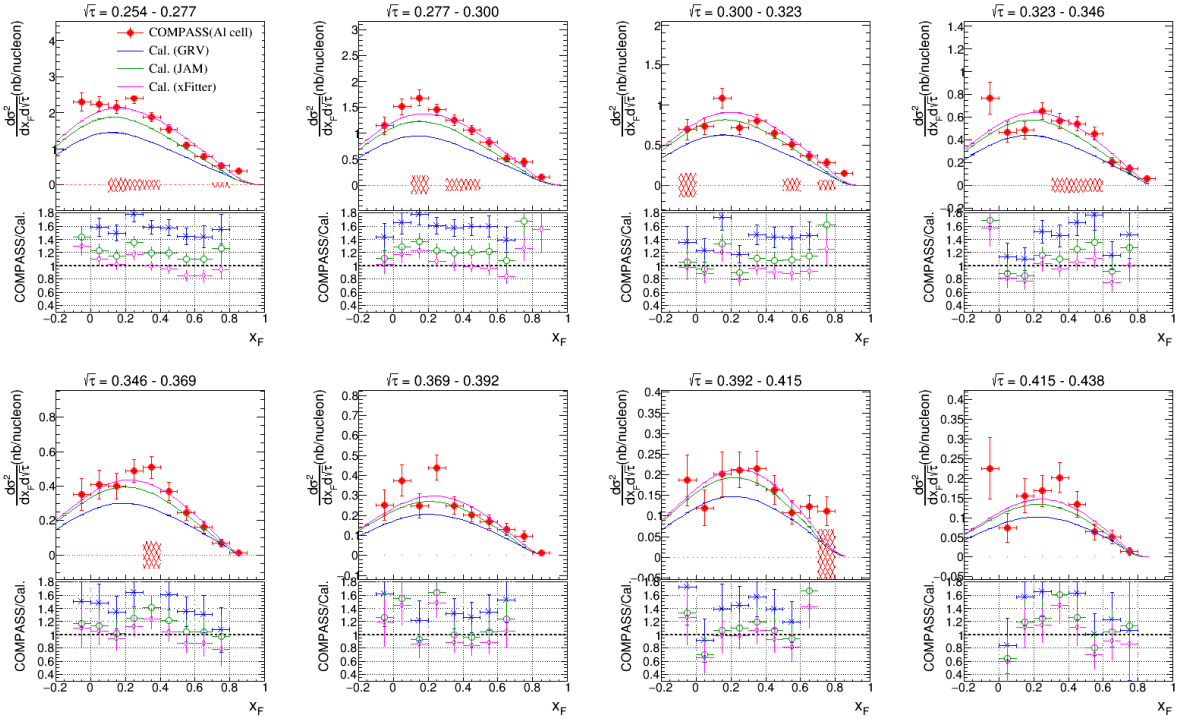

Figure 3.41: *The supplemental plots of Fig. 3.39(b). The comparison of cross section as a function of x_F in different $\sqrt{\tau}$ bins between COMPASS and pQCD calculations in NLO for* ***Al cell****.*

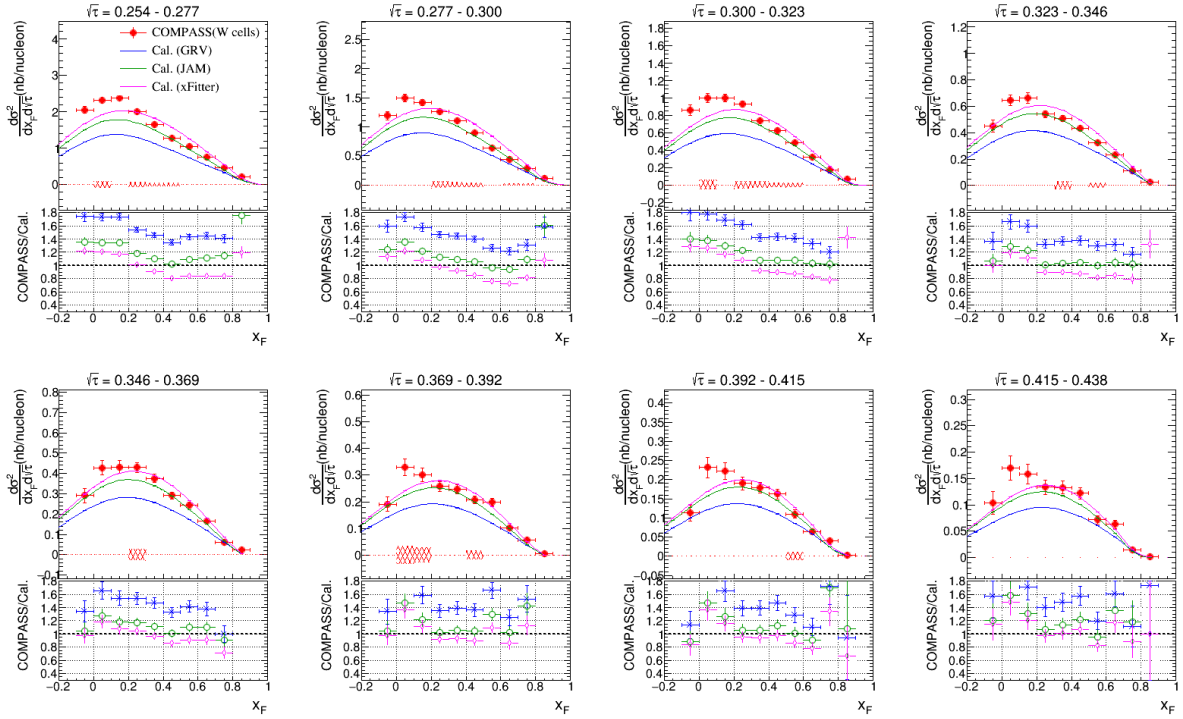

Figure 3.42: *The supplemental plots of Fig. 3.39(c)W cells. The comparison of cross section as a function of x_F in different $\sqrt{\tau}$ bins between COMPASS and pQCD calculations in NLO for* ***W cells****.*

- $d^2\sigma/dx_F dp_T$ and $d^2\sigma/dM_{\mu\mu}dp_T$

  The transverse momentum p_T distributions of pion-induced Drell-Yan cross sections from fixed-target experiments are valuable for several physics studies : (1) It is sensitive to the transverse momentum parton distribution function(TMD). The small $p_T < 10GV$ spectrum of Drell-Yan process is not predictable from the pQCD calculation. A reliable theoretical estimate of the p_T distribution based on TMD factorization is not available until very recent [89]. The study of p_T spectrum gives the insights of the non-perturbative QCD physics, (2) The intrinsic transverse momentum distribution of partons induced by the gluon contributions inside the pion. The fixed-target experiments with low-energy pion beam especially bring a good constrain power of it, therefore the contribution of COMPASS experiment with 190 GeV pion beam is essential, (3) The study of p_T distribution is also interesting for the nuclear effect. When a parton propagates in a nucleus, the multiple scatterings with the medium inside nucleus lead to a broadening effect in the p_T spectrum of parton. Study the broadening effect of p_T spectrum with different nucleus targets serve as a tool to study the nuclear effect [90].

  In this paragraph, the two-dimensional Drell-Yan cross-section in $d^2\sigma/dx_F dp_T$ and $d^2\sigma/dM_{\mu\mu}dp_T$ are extracted. The p_T spectrum of Drell-Yan cross section in different x_F bins and $M_{\mu\mu}$ bins are investigated. The binning of $d^2\sigma/dM_{\mu\mu}dp_T$ given in Table. 3.13 and $d^2\sigma/dx_F dp_T$ given in Table. 3.14 are based on the binnings reported by E615 [21] since the COMPASS results will be compared to them.

Table 3.13: *Binning of 2D-dimensional cross section in $M_{\mu\mu}$ and p_T.*

Kinematics	Nbin	Binning
p_T	18	[0.0, 0.25, 0.50, 0.75, 1.00, 1.25, 1.50, 1.75, 2.00, 2.25, 2.50, 2.75, 3.00, 3.25, 3.50, 3.75, 4.00, 4.25, 4.50]
$M_{\mu\mu}$	8	[4.50, 4.95, 5.40, 5.85, 6.30, 6.75, 7.20, 7.65, 8.10]

Table 3.14: *Binning of 2D-dimensional cross section in x_F and p_T.*

Kinematics	Nbin	Binning
p_T	18	[0.0, 0.25, 0.50, 0.75, 1.00, 1.25, 1.50, 1.75, 2.00, 2.25, 2.50, 2.75, 3.00, 3.25, 3.50, 3.75, 4.00, 4.25, 4.50]
x_F	10	[-0.10, 0.0, 0.10, 0.20, 0.30, 0.40, 0.50, 0.60, 0.70, 0.80, 0.90]

The two-dimensional Drell-Yan cross-section in $d^2\sigma/dx_F dp_T$ and $d^2\sigma/dM_{\mu\mu}dp_T$ of PT cells, Al cell, and W cells are shown in Fig. 3.43, Fig. 3.44, and Fig. 3.45, respectively. Note that $d^2\sigma/dx_F dp_T$ and $d^2\sigma/dM_{\mu\mu}dp_T$ are scaled with 10^i for the convenience of display. The numerical values of $d^2\sigma/dx_F dp_T$ and $d^2\sigma/dM_{\mu\mu}dp_T$ are listed in Appendix. 4.3 and Appendix. 4.3, respectively. The Drell-Yan cross section as a function of p_T distributions in different $M_{\mu\mu}$ and x_F bins are in Poisson distribution with the mean around 0.5 GeV to 1.5 GeV. With the increase of the x_F, p_T spectrum tends to move to the smaller values. The statistical fluctuation of in the region larger than $2.5GeV$ is large for all 3 targets. As for Al cell, the binning is too small with its the statistics. The cut limitation might need to be tighten or a coarse binning will be studied in the future. For now, the binning E615 reported is chosen in order to compare the results.

As described above, there is no pQCD calculation is compared with COMPASS results because the p_T spectrum is distributed below $10GeV$. The p_T spectrum is mainly studied phonologically by the extraction of mean square transverse momentum.

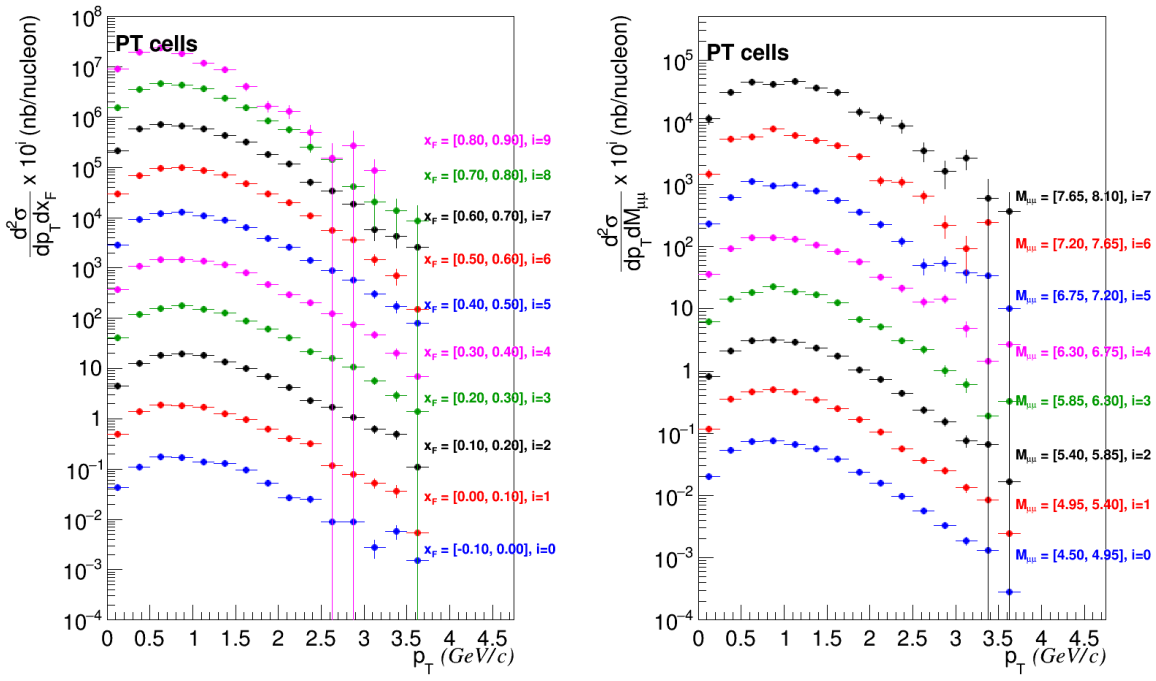

(a) $d^2\sigma/dx_F dp_T$ **(b)** $d^2\sigma/dM_{\mu\mu} dp_T$

Figure 3.43: *The cross section as a function of p_T in different x_F bins and $M_{\mu\mu}$ bins for* ***PT cells****.*

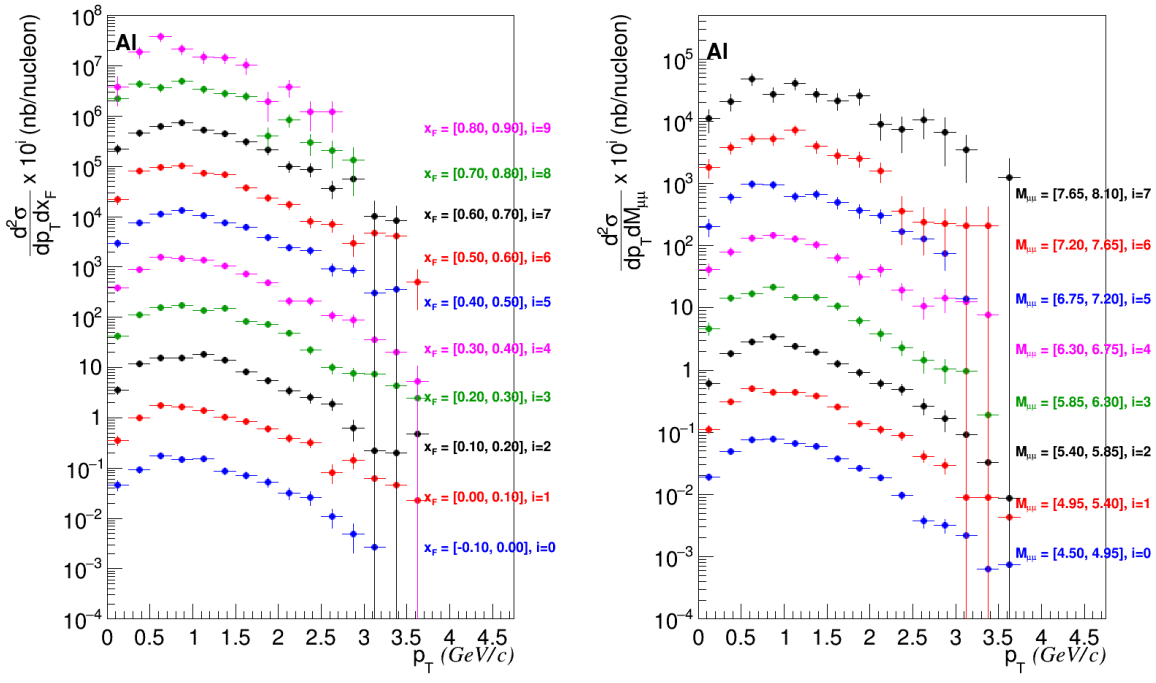

(a) $d^2\sigma/dx_F dp_T$ **(b)** $d^2\sigma/dM_{\mu\mu} dp_T$

Figure 3.44: *The cross section as a function of p_T in different x_F bins and $M_{\mu\mu}$ bins for* ***Al cell****.*

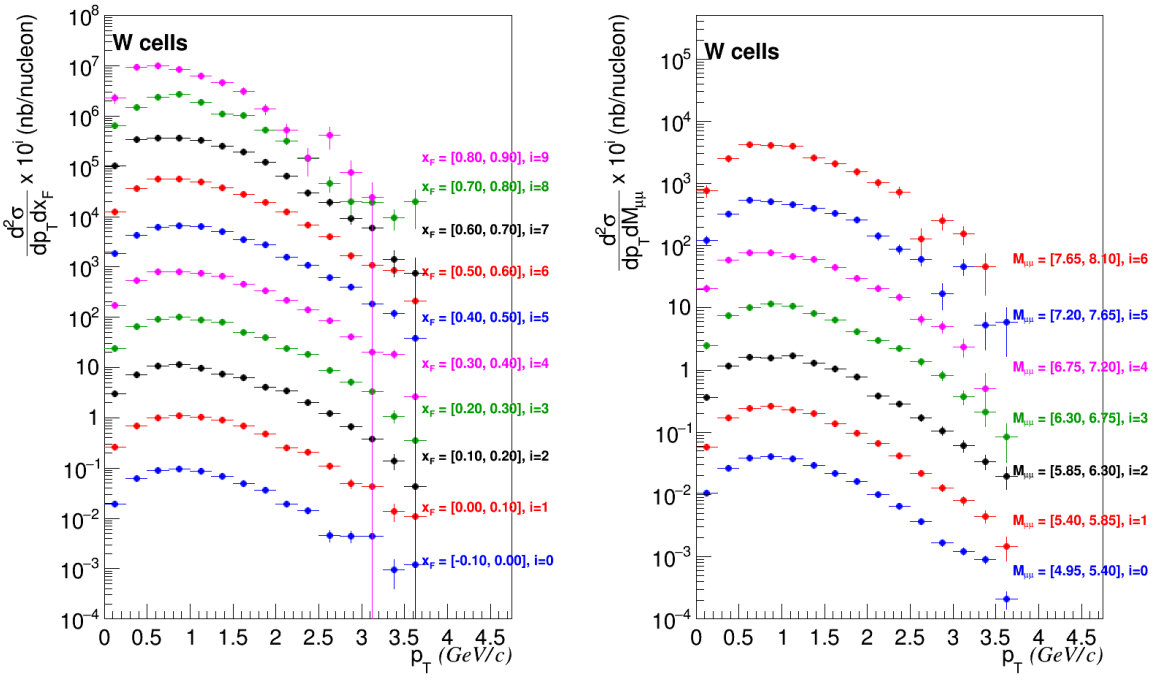

(a) $d^2\sigma/dx_F dp_T$ **(b)** $d^2\sigma/dM_{\mu\mu}dp_T$

Figure 3.45: *The cross section as a function of p_T in different x_F bins and $M_{\mu\mu}$ bins for* ***W cells****.*

Extraction of mean square transverse momentum The mean square of transverse momentum of dimion, $< p_T^2 >$, is evaluated from the cross-section as function of p_T distribution in different $M_{\mu\mu}$ and x_F bins.

There are two methods are used. One is the bin summation method described as follows :

$$< p_T^2 >= \frac{\sum_{bin=1}^{N} p_T^2(i) \frac{d\sigma}{dp_T} dp_T(i)}{\sum_{bin=1}^{N} \frac{d\sigma}{dp_T} dp_T(i)} \tag{3.12}$$

where $p_T(i)$ is the bin center of bin=i, $d\sigma/dp_T(i)$ is the differential cross-section (bin content) of bin=i, $dp_T(i)$ is the bin width of bin=i.

Another one is reported by E615 [21] to fit the cross section as function of p_T for any x_F and $M_{\mu\mu}$ bins with :

$$P(p_T, x_F, M_{\mu\mu}) = \frac{5\frac{a}{b}[\frac{p_T}{b}]^{a-1}}{[1+(p_T/b)^a]^6}, \qquad < p_T^2 >= \frac{2b^2}{a} B(2/a, 5-2/a) \tag{3.13}$$

where $a \equiv a(x_F, M_{\mu\mu})$ and $b \equiv b(x_F, M_{\mu\mu})$ are fitting parameters. $B(x, y)$ is the Euler beta function. This equation is chosen completely empirical and found to described the distributions well over the measured kinematics.

Fig. 3.46 shows the fitting of the cross section as function of p_T with Eq. 3.13 proposed by E615 group [21] on different x_F bins for W cells. The fitting quality looks reasonable. Fig. 3.47 compares the mean square of transverse momentum

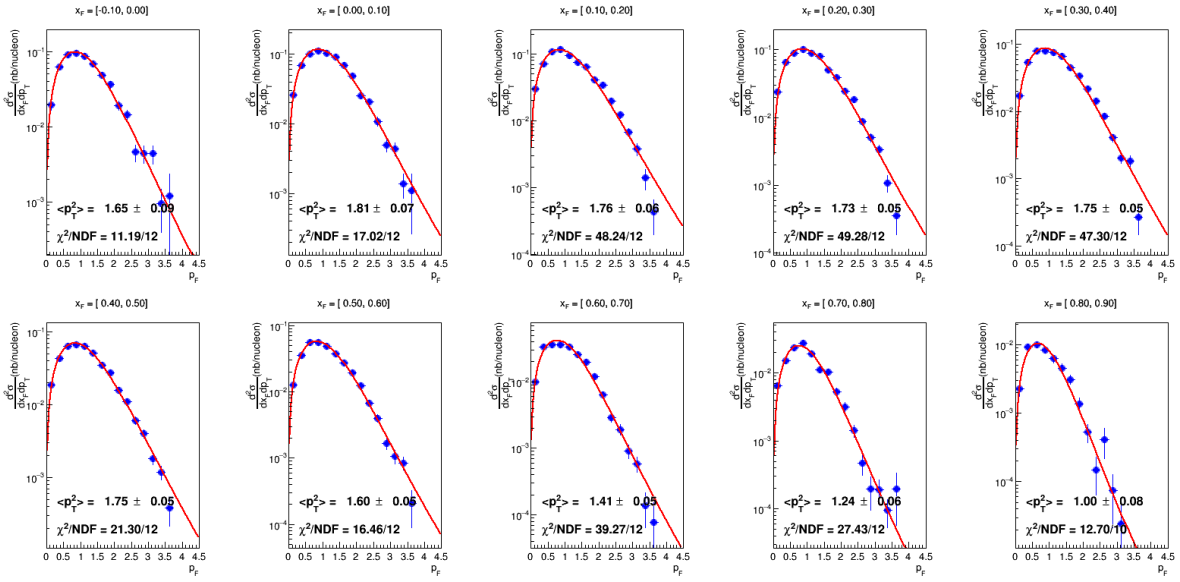

Figure 3.46: *The fitting of the cross section as function of p_T with Eq. 3.13 proposed by E615 group [21] on different x_F bins for W cells.*

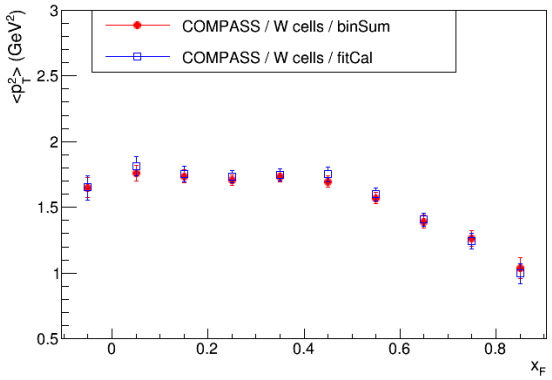

Figure 3.47: *The mean square of transverse momentum $< p_T^2 >$ calculated from bin summation method from Eq. 3.12(labeled as "binSum") and Eq. 3.13(labeled as "fitCal"). The two extracted methods give the consistent results.*

p_T^2 calculated from bin summation method (Eq. 3.12,labeled as "binSum") and fit method (Eq. 3.13, labeled as "fitCal"). The two extracted methods give the consistent results. In the following analysis, the bin summation method is chosen.

The mean square of transverse momentum of W cells and PT cells in various x_F bins and $\sqrt{\tau}$ dins, are estimated and compared with E615 results [21] shown in Fig. 3.48. The comparison is made in $\sqrt{\tau}$ bins instead of $M_{\mu\mu}$ bins in order to take the beam energy into account. Both COMPASS and E615 results show that $< p_T^2 >$ decreases with the x_F and slightly increases with $M_{\mu\mu}$. In the region of $0.35 < \sqrt{\tau} < 0.45$, E615 enters Υ mass region therefore $< p_T^2 >$ distribution is higher than the rest regions dominated by Drell-Yan events.

The $< p_T^2 >$ of W target from COMPASS and from E615 are consistent in various x_F bins, however it is not expected. In general, the higher center-of-mass energy gives a larger $< p_T^2 >$. As shown in Fig. 3.49, it gives the center-of-mass energy

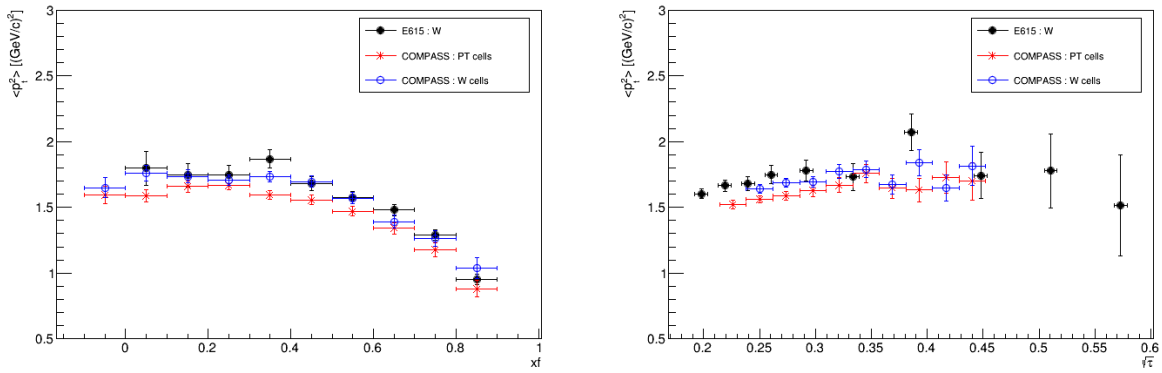

(a) $< p_T^2 >$ *in different* x_F *bins.* **(b)** $< p_T^2 >$ *in different* $\sqrt{\tau}$ *bins.*

Figure 3.48: $< p_T^2 >$ *of W cells and PT cells in various* x_F *and mass bins. The comparison is made with E615 data with 190GeV pion beam collides with tungsten target.*

verses $< p_T^2 >$ for different experiments. The $< p_T^2 >$ extracted from E615 seems to be below the linear extrapolation. A linear fit is performed in Fig. 3.49 to extract the intrinsic $< p_T^2 >$. The intrinsic $< p_T^2 >$ of parton inside pion obtained is $0.731 \pm 0.066[(GeV/c)^2]$.

$< p_T^2 >$ is frequently measured to characterize the nuclear effect. The nuclear effect is studied through comparing the $< p_T^2 >$ of W cells(heavy target) and PT cells(light target). Al target is not used due to the poor statistics. The difference of $< p_T^2 >$ between PT cells and W cells in various x_F and $\sqrt{\tau}$ bins are listed in Table. 3.15 and also show in Fig. 3.48. COMPASS data shows that W target has stronger broadening effect compare to PT cells, as expected [89]. The input of the theoretical calculation will be performed in the future.

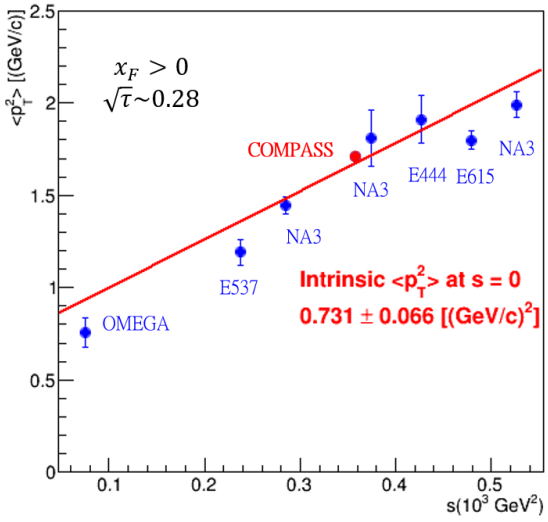

Figure 3.49: $< p_T^2 >$ *verses center-of-mass energy s for different pion-induced experiments. The data points except for COMPASS are collected in Ref. [21].A linear fit is performed in Fig. 3.49 to extract the intrinsic* $< p_T^2 >$. *The intrinsic* $< p_T^2 >$ *of parton inside pion obtained is* $0.731 \pm 0.066[(GeV/c)^2]$ *though a linear fit.*

Table 3.15: *The mean square of transversed momentum $< p_T^2 >$ calculated from bin summation method in different x_F and $\sqrt{\tau}$ bins of PT cells and W cells and their difference.*

Kinematics		$< p_T^2 >_W$ $[(GeV/c)^2]$	$< p_T^2 >_{PT}$ $[(GeV/c)^2]$	$< p_T^2 >_W - < p_T^2 >_{PT}$ $[(GeV/c)^2]$
x_F	[-0.10, 0.00]	1.65±0.08	1.59±0.07	0.06±0.10
x_F	[0.00, 0.10]	1.76±0.06	1.59±0.05	0.17±0.08
x_F	[0.10, 0.20]	1.74±0.05	1.66±0.04	0.08±0.06
x_F	[0.20, 0.30]	1.71±0.04	1.67±0.04	0.04±0.06
x_F	[0.30, 0.40]	1.73±0.04	1.59±0.03	0.14±0.05
x_F	[0.40, 0.50]	1.69±0.04	1.56±0.04	0.13±0.06
x_F	[0.50, 0.60]	1.57±0.04	1.47±0.04	0.10±0.06
x_F	[0.60, 0.70]	1.39±0.05	1.34±0.04	0.05±0.06
x_F	[0.70, 0.80]	1.26±0.06	1.18±0.05	0.08±0.08
x_F	[0.80, 0.90]	1.04±0.08	0.88±0.06	0.16±0.10
$\sqrt{\tau}$	[0.238, 0.262]	1.64±0.03	1.56±0.03	0.08±0.04
$\sqrt{\tau}$	[0.262, 0.286]	1.69±0.03	1.59±0.03	0.10±0.04
$\sqrt{\tau}$	[0.286, 0.310]	1.69±0.04	1.62±0.04	0.10±0.04
$\sqrt{\tau}$	[0.310, 0.333]	1.77±0.05	1.67±0.06	0.10±0.08
$\sqrt{\tau}$	[0.333, 0.357]	1.79±0.06	1.76±0.07	0.03±0.09
$\sqrt{\tau}$	[0.357, 0.381]	1.67±0.07	1.64±0.08	0.03±0.11
$\sqrt{\tau}$	[0.381, 0.405]	1.84±0.10	1.63±0.09	0.21±0.13
$\sqrt{\tau}$	[0.405, 0.429]	1.65±0.10	1.73±0.12	-0.08±0.15
$\sqrt{\tau}$	[0.429, 0.452]	1.82±0.15	1.70±0.14	0.12±0.21

3.5.4 One-dimensional cross-section

The one-dimensional Drell-Yan cross-section is extracted in six kinematics : $d\sigma/dM_{\mu\mu}$, $d\sigma/d\sqrt{\tau}$, $d\sigma/dp_T$, $d\sigma/dx_\pi$, $d\sigma/dx_N$, and $d\sigma/dx_F$. The binning is shown in Table. 3.16. Fig. 3.50, Fig. 3.51, and Fig. 3.52 show the one-dimensional cross-section of PT cells, Al cell, and W cells, respectively. The mean of the 1D cross section of six kinematics are listed in Table. 3.17. The systematic uncertainty bends are given and described in Sec. 3.6. The numerical values of the one-dimensional cross-section are listed in the Appendix, Sec. 4.3.

Table 3.16: *The binning of 1D cross section.*

Kinematics	Nbin	Binning
$M_{\mu\mu}$	10	[4.30, 4.70, 5.10, 5.50, 5.90, 6.30, 6.70, 7.10, 7.50, 7.90, 8.50]
$\sqrt{\tau}$	10	[0.23, 0.25, 0.27, 0.29, 0.31, 0.33, 0.35, 0.38, 0.40, 0.42, 0.45]
p_T	11	[0.00, 0.30, 0.60, 0.90, 1.20, 1.50, 1.80, 2.10, 2.40, 2.70, 3.00, 3.60]
x_π	9	[0.00, 0.10, 0.20, 0.30, 0.40, 0.50, 0.60, 0.70, 0.80, 1.00]
x_N	10	[0.00, 0.05, 0.10, 0.15, 0.20, 0.25, 0.30, 0.35, 0.40, 0.45, 0.6]
x_F	9	[-0.10, 0.00, 0.10, 0.20, 0.30, 0.40, 0.50, 0.60, 0.70, 0.90]

Table 3.17: *The mean of 1D cross section.*

Kinematics	PT cells	Al cell	W cells
$< M_{\mu\mu} >$	5.31±0.89	5.26±0.87	5.66±0.83
$< \sqrt{\tau} >$	0.28±0.05	0.28±0.05	0.30±0.04
$< p_T >$	1.01±0.61	1.10±0.62	1.13±0.62
$< x_\pi >$	0.45±0.17	0.45±0.17	0.46±0.16
$< x_N >$	0.19±0.08	0.19±0.08	0.21±0.08
$< x_F >$	0.25±0.22	0.26±0.22	0.25±0.22

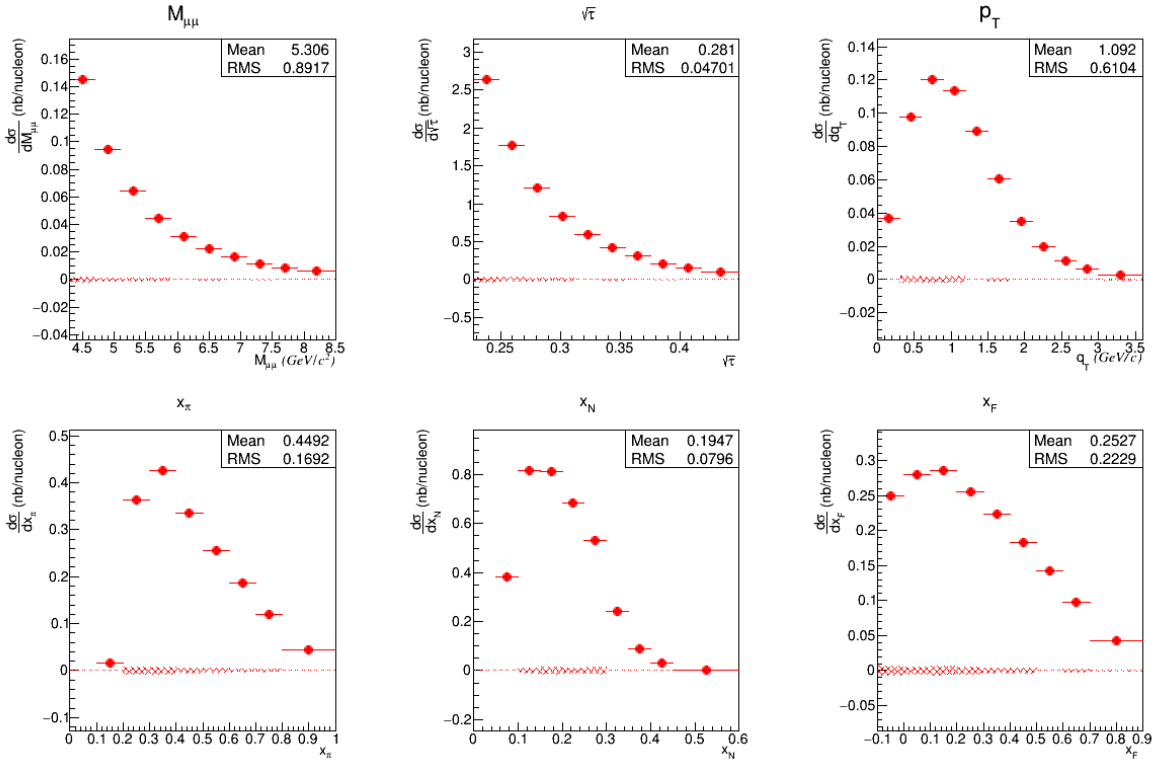

Figure 3.50: *One-dimensional cross-section of* ***PT cells****.*

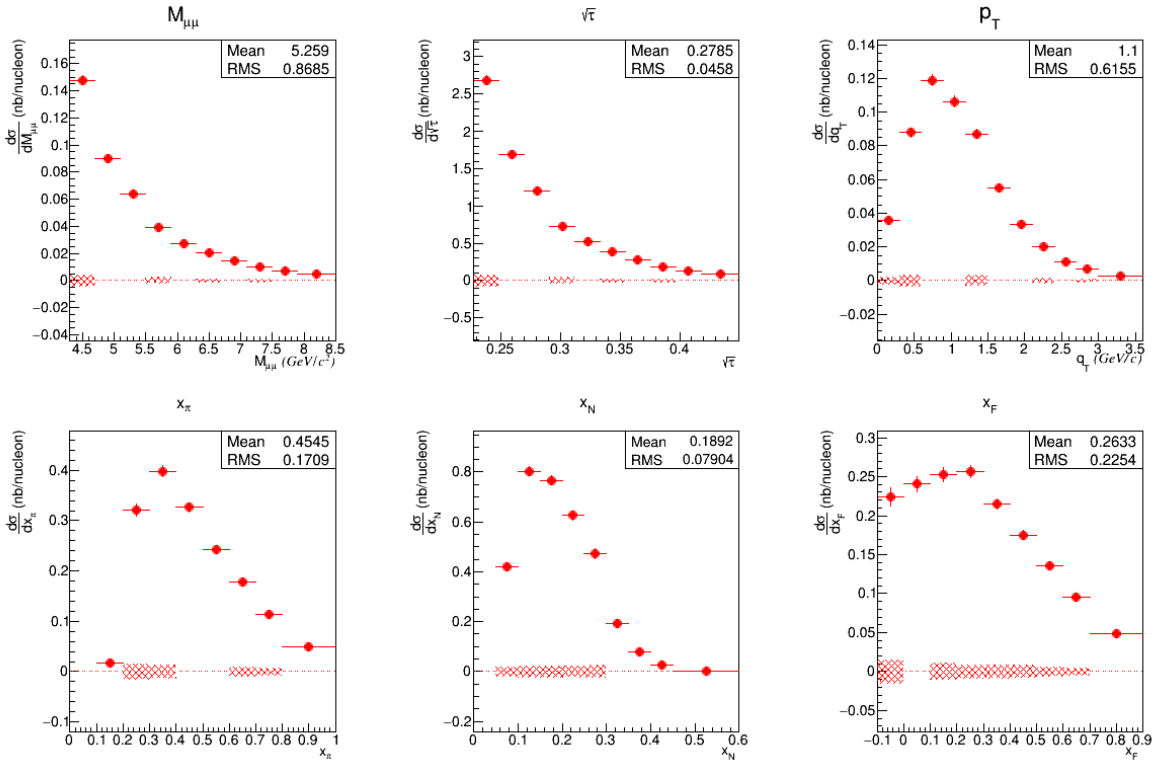

Figure 3.51: *One-dimensional cross-section of* ***Al cell****.*

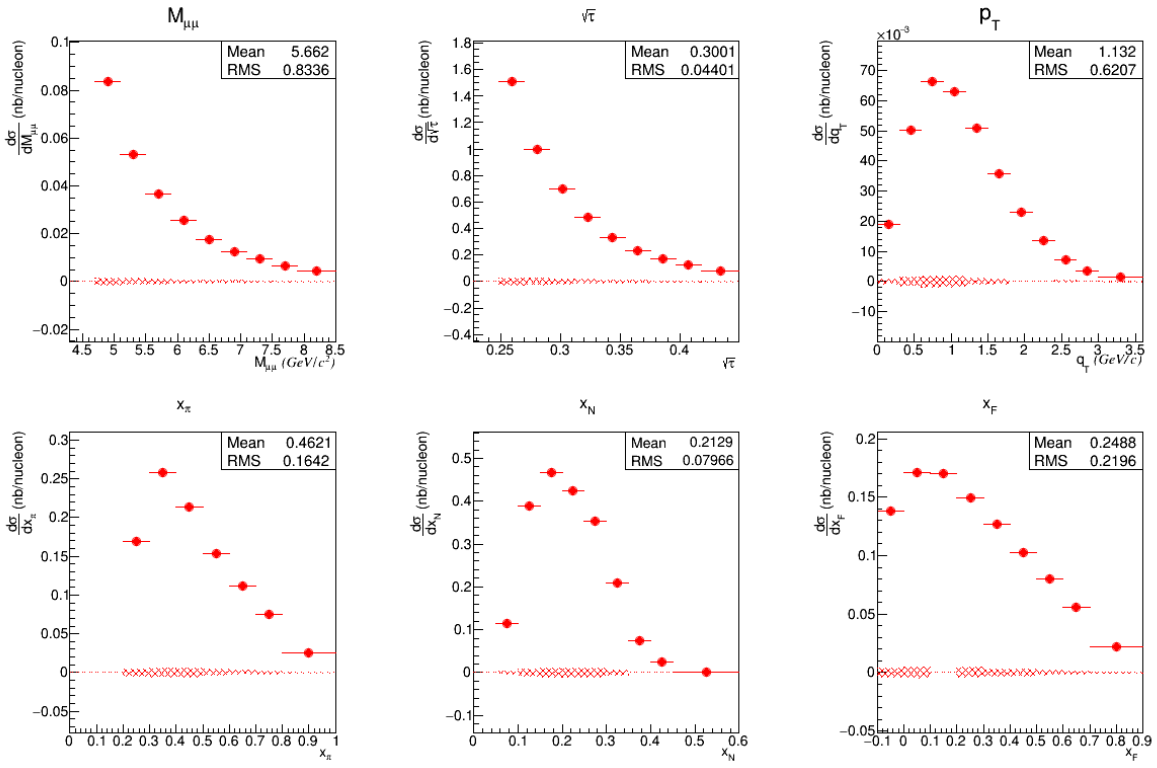

Figure 3.52: *One-dimensional cross-section of* ***W cells****.*

3.6 Systematic uncertainty

In this section, the estimation of the systematic uncertainties of the cross-section measurements is presented. All the possible systematic uncertainties will be discussed one by one.

3.6.1 Luminosity estimation and lifetime

The systematic uncertainties contributed by the beam flux measurement, the target composition, the DAQ lifetime estimation, and the VETO lifetime estimation, are already discussed in the previous sections. More details to be founded in Sec. 3.1 for luminosity and Sec. 3.2 for lifetime estimation.

For the **extraction of DAQ lifetime**, there are two triggers to be used, random triggers(RT) and first-level triggers(FLT). The DAQ lifetime measure by RT and FLT give around 1% difference considered as the systematic uncertainty.

For the **extraction of VETO lifetime**, there are also two triggers can be used from the cable delay method, and they gives the systematic uncertainties of the measurement is less than 1%.

For the **target composition**, there is no uncertainty given for Al cell and W cells since they are pure element. As for PT cells, it is a mixture of liquid LHe and solid NH_3. The mass density and volume density of PT cells are measured to estimate transverse target density ρ_T used in the luminosity estimation. Around 2% systematic uncertainty is obtained for the measurement of transversed target density ρ_T of PT cells.

For the **beam composition**, the incident $190GeV$ π^- beam is composed of 97% π^-, 2% K^- and 1% $\bar{p}$. The beam particle identification was absent because the CEDAR detector couldn't operated under high intensity beam $\sim 6 \times 10^7/s$. There is around 3% impurities of π^- beam. The measured cross section is a sum of the three individual cross sections:

$$\sigma_{meas} = a_1\sigma_{\pi^-} + a_2\sigma_{K^-} + a_3\sigma_{\bar{p}}, \tag{3.14}$$

where the coefficients a_i are the relative fractions of π^-, K^- and $\bar{p}$ in the beam. The cross section can also be expressed as:

$$\sigma_{meas} = \sigma_\pi \times (a_1 + a_2R_K + a_3R_{\bar{p}}) = \sigma_\pi \times R, \tag{3.15}$$

The overall factor R was evaluated by taking the kaon/pion and antiproton/pion dimuon rate ratios (R_K and $R_{\bar{p}}$, respectively) from the measurements made by the NA3 collaboration [23]. In the mass region between 5 and 8 GeV/c^2, these ratios are 0.6 and 1.1, respectively. The uncertainties on the ratios are estimated to be about 25%. Combining the rate ratios with the relative beam composition numbers results in $R = 0.991 \pm 0.005$. The pure pion-induced cross section is then: $\sigma_\pi = \sigma_{meas} \times (1/R)$. It gives around 1% systematic uncertainty.

In Table. 3.18, the systematic uncertainties of each terms related to the luminosity and deadtime measurements are summarized. They are all below 2 %, therefore they are considered negligible.

Table 3.18: *The overall systematic uncertainties of the Drell-Yan cross section contributed by the luminosity and the lifetime estimation.*

	PT cells	Al cell	W cells
Beam Flux	1 %	1%	1%
DAQ Lifetime	1%	1%	1%
VETO Lifetime	1%	1%	1%
Beam Composition	1%	1%	1%
Target Composition	2%	-	-

3.6.2 Multidimensional acceptance correction

In the cross section analysis, the higher-dimensional-acceptance correction is preferred to minimize the model dependence in MC event generator level. The three-dimension-acceptance correction is considered to be better than one-dimensional-acceptance correction. In order to know the possible model-dependent effect in this analysis, a comparison between the cross-section in one-dimensional-acceptance correction and the cross-section three-dimensional-acceptance correction is made. In Fig. 3.53, the top plot shows the cross-section of PT cells with one-dimensional-acceptance correction in blue dots and the three-dimensional-acceptance correction in red dots. The three-dimensional cross-section with three-dimensional acceptance correction is integral to one-dimensional cross-section in this plot drawn in red dots in order to make the comparison. The bottom plot in Fig. 3.53 shows the ratio between one-dimensional-acceptance correction and three-dimensional-acceptance correction, which is close to 1. A small inconsistency less than 3% is shown in high p_T and high x_F regions. It indicates that the Drell-Yan process generated by Pythia8 with the customized p_T tuning is well simulated in this analysis.

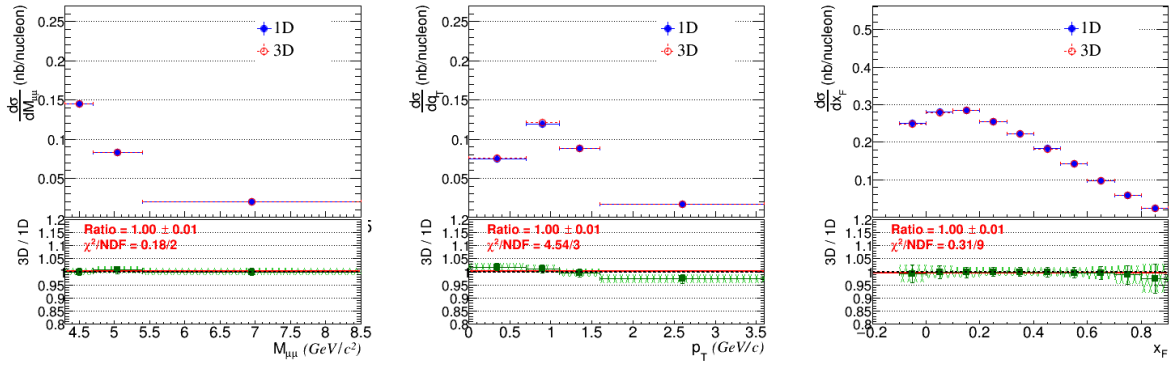

Figure 3.53: *The comparison between 3D-acceptance correction and 1D-acceptance correction for the cross-section of PT cells. On the top plots, the blue dots show the results of 1D-acceptance correction and the red dots show the 3D-acceptance correction. The ratio is shown in the bottom plots with green dots. A small inconsistency less than 3% is shown in high p_T and high x_F regions.*

3.6.3 Re-interaction effect on W cells

The re-interaction effect is defined as the Drell-Yan cross section contributed by the secondary pions scatter the target. The secondary pion is produced from the hadronization

of the primary pion beam and target interaction. The re-interaction effect is not simulated in the MC simulation, therefore it has to be corrected. The re-interaction effect increases with longer and heavier targets. In this analysis, only W cells requires the correction of re-interaction effect. In Ref. [91], the formulation of the re-interaction effect is defined as follows :

$$\sigma_{measure} = \sigma_{direct} + \sigma_{reint}\ [1 - \frac{L/\lambda_{int,pion}}{exp(L/\lambda_{int,pion}) - 1}]$$

where L is the physical length of target, $\lambda_{int,pion}$ is the pion interaction length in the unit of cm, $\sigma_{measure}$ is the measured cross section, σ_{direct} is the true cross section, σ_{reint} is the re-interacted cross-section.

Fig. 3.54 shows the measured cross-section $\sigma_{measure}$ of 30cm-long W cells along beam direction, Z_{vtx}. In the nominal Drell-Yan cross section analysis, only 20cm-long W target is used. In the study of the reinteraction effect, an extract 10cm is extended to better observer the reinteraction effect. The measured cross-section is fitted with the reinteraction formulation with fixed parameters, $\lambda_{int,pion} = 11.3\ cm$. The fitted results shows the true cross-section is 0.01062 ± 0.00045 and the reinteraction cross-section is 0.0003156 ± 0.000981. The reinteraction effect is smaller than the statistical uncertainty of the true cross-section. There is no strong reinteraction effect observed - the measure cross-section doesn't increase obviously along the Z_{vtx} distribution. In this analysis, the systematic uncertainty caused by the reinteraction effect of W cells is negligible.

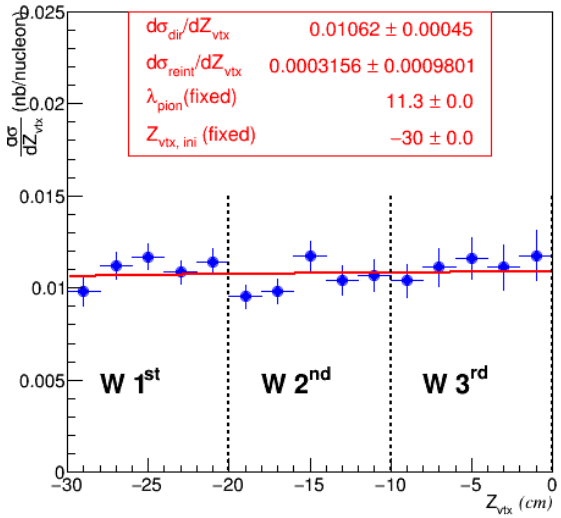

Figure 3.54: *The cross-section of 30cm-long W cells along Z_{vtx} fitted with the formulation of the reinteraction effect. The true Drell-Yan cross-section is* 0.01062 ± 0.00045 *and the reinteraction cross-section is* 0.0003156 ± 0.000981 *which is smaller than the statistical uncertainty of the true cross-section, therefore the systematic uncertainty caused by the reinteraction effect of W cells is negligible.*

3.6.4 Z_{vtx}-dependent cross-section

The comparison of the cross-section with the same material but located in different Z_{vtx} positions is made. There are two PT cells used in this analysis, one is PT 1^{st} cell located

in more upstream than the another one, PT 2^{nd}. For W targets, the comparison of the cross section between the first 10cm-long cell, W 1^{st} cell and the second 10cm-long cell, W 2^{nd} are studied.

Fig. 3.55 shows the the cross section comparison in x_F distribution for PT cells and W cells : (a) PT 1^{st} cell/PT 2^{nd} cell, (b) W 1^{st} cell/W 2^{nd} cell. The ratio between two PT cells is 0.98 ± 0.01 gives a nice agreement. However, the ratio between W cells is 1.07 ± 0.01 gives around 5% inconsistency possible given by the unrealistic acceptance extraction.

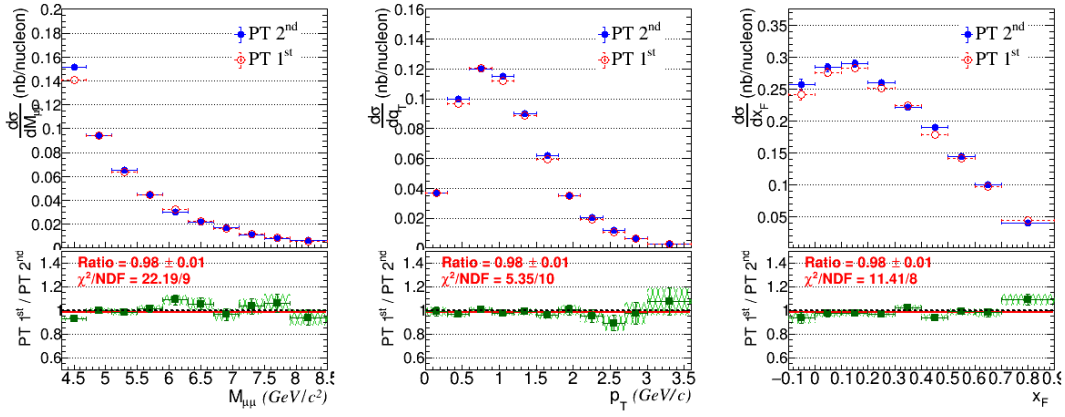

(a) *PT 1^{st} cell/PT 2^{nd} cell*

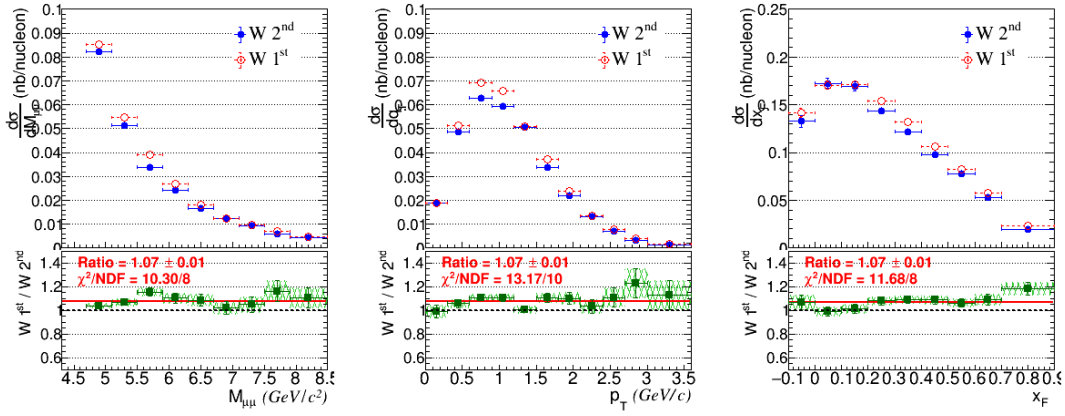

(b) *W 1^{st} cell/W 2^{nd} cell*

Figure 3.55: *The comparison of cross-section for the same materials : (a) PT 1^{st} cell/PT 2^{nd} cell (b) W 1^{st} cell/W 2^{nd} cell. The ratio between two PT cells is* 0.98 ± 0.01 *gives perfect agreement. The ratio between W cells is* 1.07 ± 0.01 *gives around 5% inconsistency contributes to the systematic uncertainty of the Z_{vtx} depednent.*

3.6.5 Period-dependent cross-section

The cross-section is extracted period by period since the acceptance simulated from MC is done also period by period. Fig. 3.56 shows the cross-section in Feynman-x xF of PT cells, Al cell, and W cells period by period and its comparison with the results averaged from the whole 2018 data. Only P01 and P04 gives around 10% difference compared to the other periods. The rest periods give nice consistency between each other.

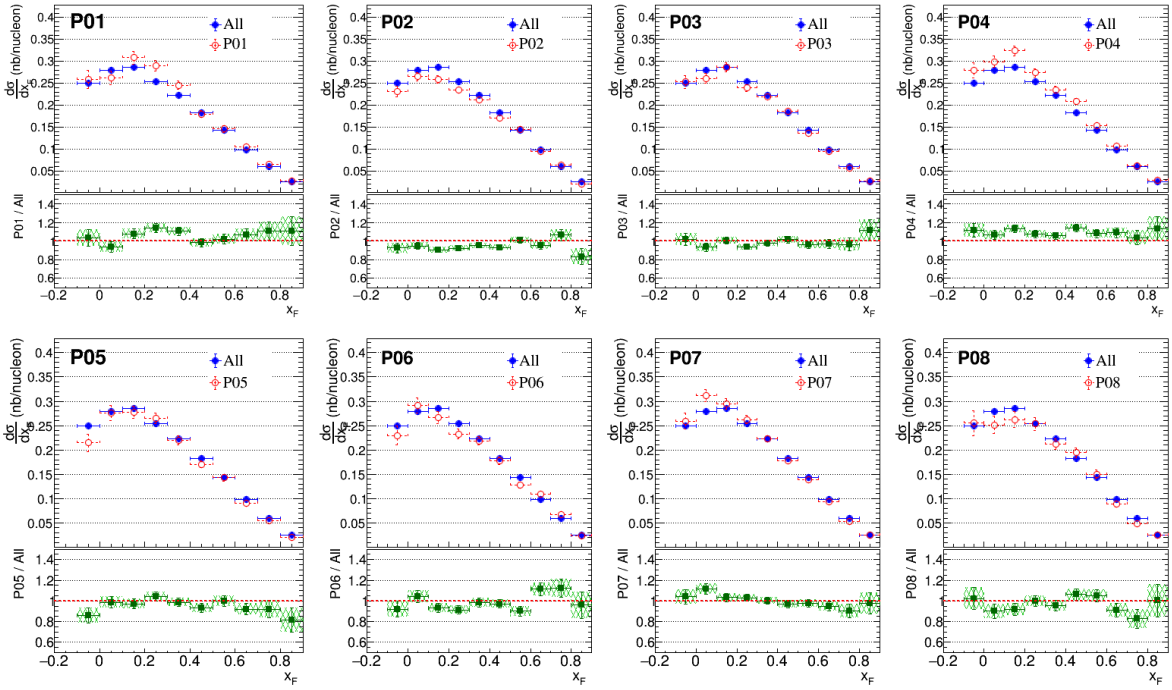

(a) *PT cells*

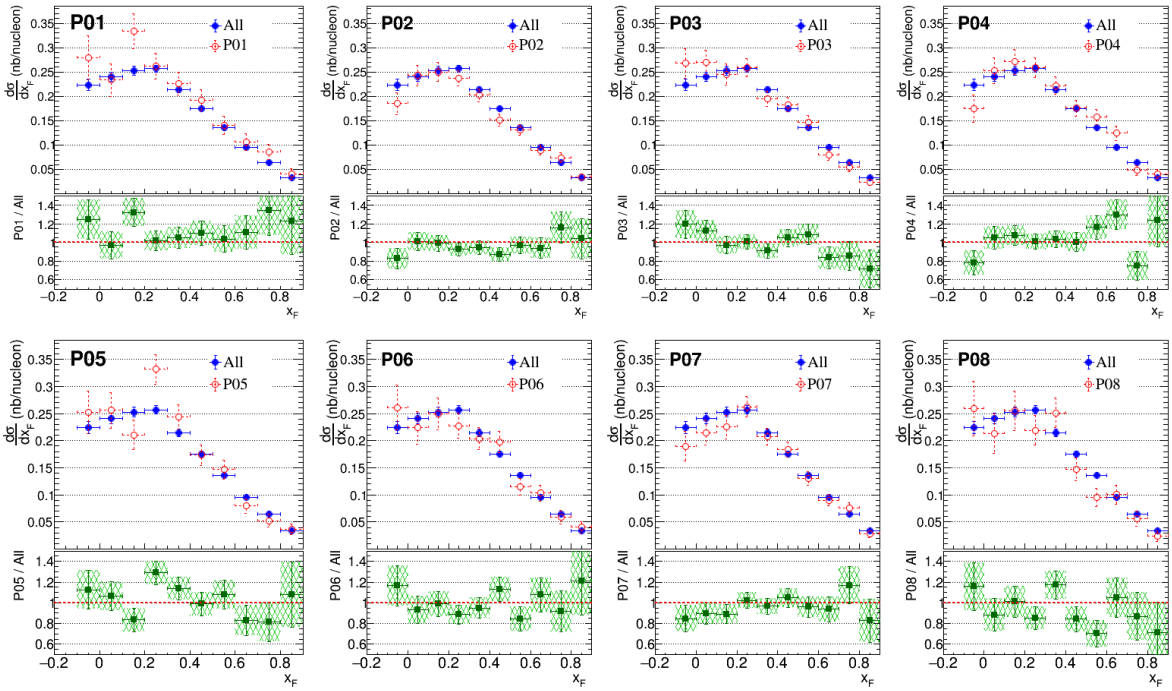

(b) *Al cell*

Figure 3.56: *The cross-section period by period and the comparison with the overall 2018 cross-section : (a) PT cells (b) Al cell. Blue dots : The overall cross section of 2018 data. Red dots : the cross-section of each period. Green dots : the ratio of cross-section, each period divides by all 2018 data.*

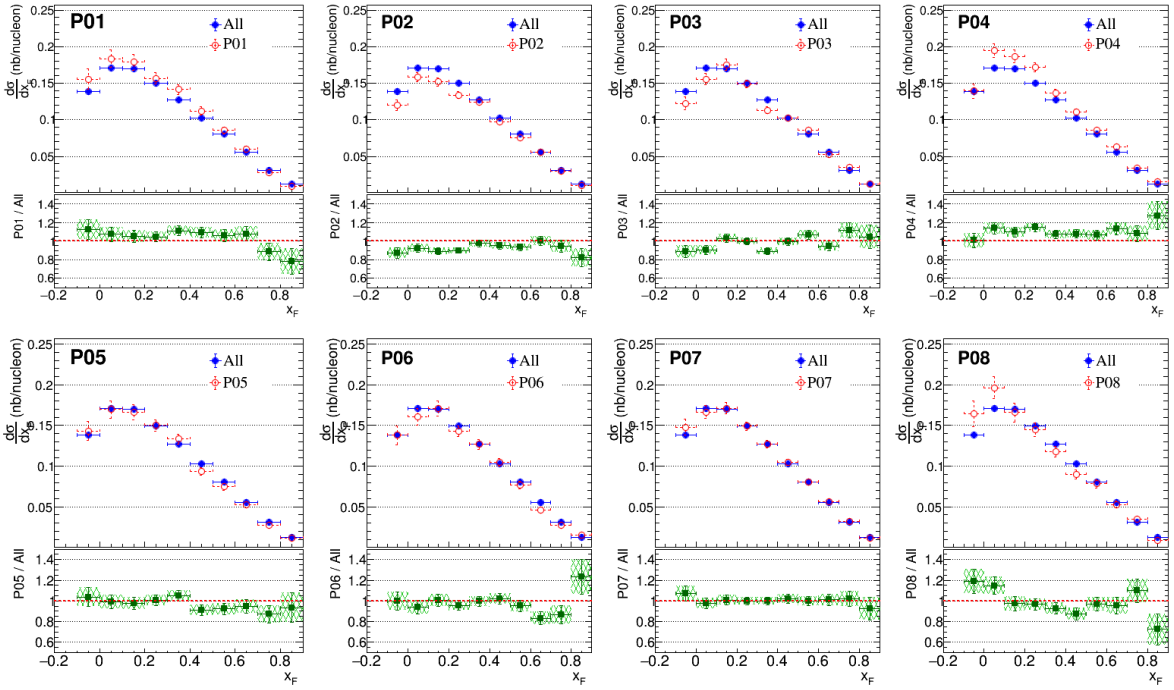

(c) *W cells*

Figure 3.56: *The cross-section period by period and the comparison with the results from all the 2018 data : (c) W cells.*

3.6.6 Trigger-dependent cross-section

There are two dimuon triggers used in this analysis, LAS×LAS and LAS×OT triggers covers different kinematics regions in x_F, $-0.1 < x_F < 0.7$ for LAS×LAS and $0.2 < x_F < 0.8$ LAS×OT. The cross section of LAS×LAS and LAS×OT triggers are compared in x_F shown in Fig. 3.57. LAS×LAS and LAS×OT have the same x_F coverage in $0.2 < x_F < 0.7$ however they gives inconsistent cross section, around 5% for PT cells and around 20% for Al and W cells. The systematic uncertainty from trigger-dependence is the greatest one in this analysis. The reason of this problem is still under investigation.

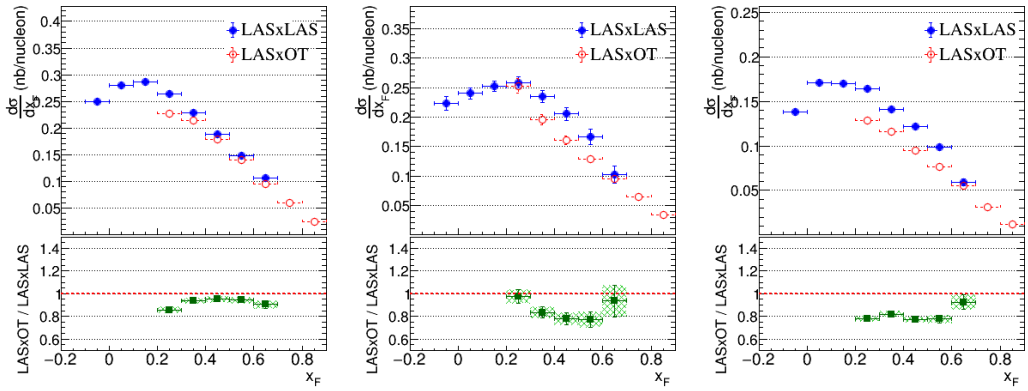

(a) *PT cells* **(b)** *Al cell* **(c)** *W cells*

Figure 3.57: *The cross-section comparison between LAS×LAS and LAS×OT triggers in x_F. Blue dots : LAS×LAS trigger. Red dots : LAS×OT trigger. Green dots : the ratio of cross-section between two triggers, LAS×OT/LAS×LAS.*

3.6.7 Overall systematic uncertainty

The possible contributions of the systematic uncertainties of the Drell-Yan cross-section measurements are discussed in the previous paragraphs including the extraction of the luminosity, the reinteraction effect from the secondary pion, the extracted methods of cross-section, Z_{vxt} dependence in cross-section, period-dependence in cross-section, and trigger-dependence in cross-section. Among all of them, only Z_{vxt} dependence in cross-section, period-dependence in cross-section, and trigger-dependence in cross-section shows the systematic uncertainties larger than 5%. The other contributions are negligible. In order to quantify the overall systematic uncertainties from them, the χ^2 method [92] is applied.

The χ^2 method is used to average the physics results from various experiments by Particle Data Group. A typical example is given in the Fig. 3.58 [92] shows a set of data measured by several experiments. Assuming all the measurements are independent and uncorrelated, the weighted average of the physics results is evaluated to represent the overall physics results :

$$\bar{x} \pm \delta\bar{x}_{stat} = \frac{\sum_i w_i x_i}{\sum_i w_i} \pm \frac{1}{\sqrt{\sum_i w_i}} \quad , \quad w_i = \frac{1}{(\delta x_i)^2}$$

where $x_i \pm \delta xi$ is the physics results given by the ith experiment from N experiments in total. The χ^2 and the number degree of freedom $(N-1)$ is evaluated under the assumption that the distribution of all the measurements is a Gaussian distribution.

$$\chi^2 = \sum_i w_i(\bar{x} - x_i)^2$$

If $\chi^2/(N-1)$ is less than or equal to 1, the measurements from various experiments are consistent. There is no known problem with the data sets. If $\chi^2/(N-1)$ is larger than 1, the results from the measurements are inconsistent. A systematic uncertainty need to be assigned additionally. The ratio between the systematic uncertainty and the statistical uncertainty is defined as below :

$$\frac{\delta\bar{x}_{sys}}{\delta\bar{x}_{stat}} = \sqrt{\chi^2/(N-1)}$$

In the evaluation of the systematic uncertainty of the COMPASS Drell-Yan cross-section measurement, the data sample is separated into sub-samples according to its Z_{vtx} position, period, and trigger type, which are the three parameters contribute most of the systematic uncertainty. Due to the limitation of statistics of Al cell (only 7cm-long), the Z_{vtx}-position dependence is not studied. In total, there are 32 sub-samples for both PT cells and W cells, and 16 sub-samples for Al cell.

- 32 sub-samples for W cells = 2 cells (W 1^{st} cell and W 2^{nd} cell) × 8 periods (P01-P08) × 2 triggers (LAS×LAS and LAS ×OT)
- 32 sub-samples for PT cells = 2 cells (PT 1^{st} cell and PT 2^{nd} cell) × 8 periods (P01-P08) × 2 triggers (LAS×LAS and LAS ×OT)
- 16 sub-samples for Al cells = 1 cell (Al cell) × 8 periods (P01-P08) × 2 triggers (LAS×LAS and LAS ×OT)

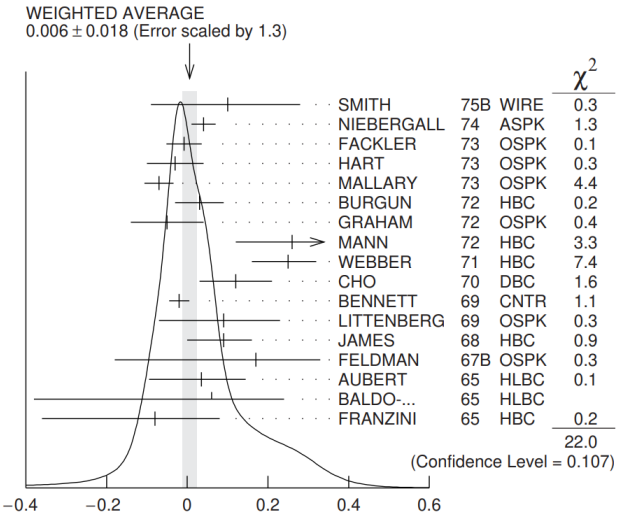

Figure 3.58: *An example of the evaluation of the averaged results from various measurements given in Ref. [92]. The grey band is the weighted average of all the data points.*

The systematic uncertainty is calculated bin by bin of the multi-dimensional cross section. An example of the systematic uncertainty estimated for the one-dimension cross-section of PT cells in the $M_{\mu\mu}$ is shown in the following. Fig. 3.60 shows the cross-section of 32 sub-samples of PT cells in different mass bins fitted with pol0 function to extract the weighted average mean $\bar{x}$, weighted averaged statistical uncertainty $\delta\bar{x}_{stat}$, and the systematic uncertainty calculated $\delta\bar{x}_{sys} = \sqrt{\chi^2/(N-1)} \times \delta\bar{x}_{stat}$. The final results of one-dimension cross-section of PT cells in the $M_{\mu\mu}$ is shown in Fig. 3.59. The systeamtic uncertainty band is drawn in the bottom, which includes the effects of Z_{vtx} position, period, and trigger type. The systematic uncertainties of the multi-dimensional cross-sections shown in Sec. 3.5 are calculated through the χ^2 method.

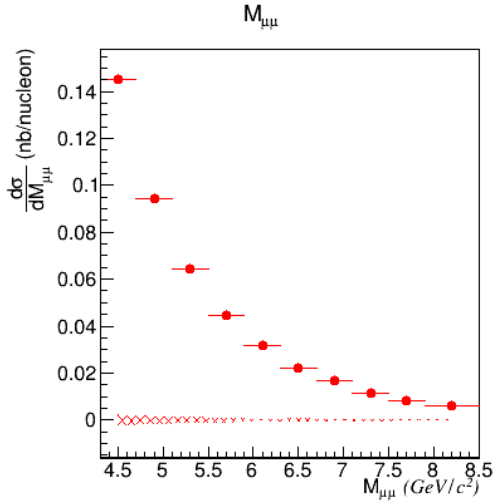

Figure 3.59: *The final results of one-dimension cross-section of PT cells in the $M_{\mu\mu}$ with the systematic uncertainty band drwan in the bottom, including the effects of Z_{vtx} position, period, and trigger type*

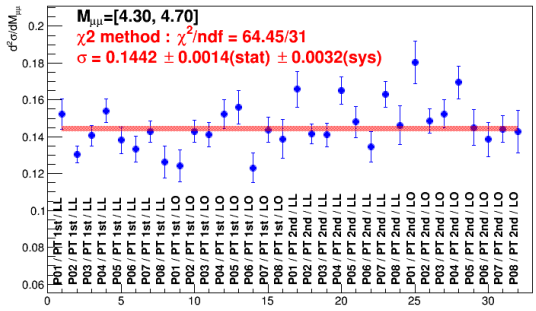

(a) $M_{\mu\mu} = [4.30, 4.70]$

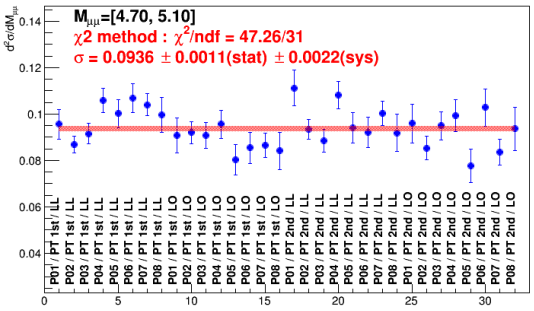

(b) $M_{\mu\mu} = [4.70, 5.10]$

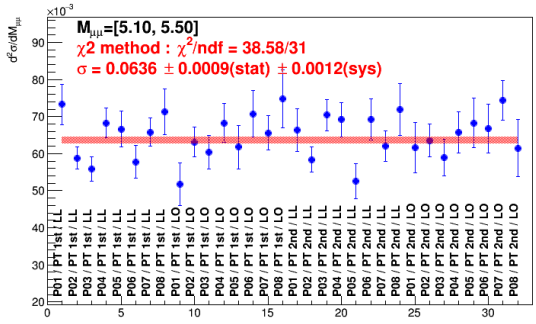

(c) $M_{\mu\mu} = [5.10, 5.50]$

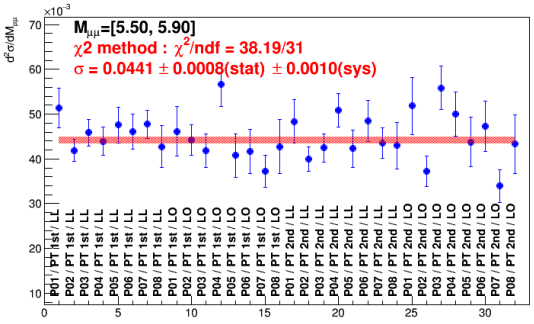

(d) $M_{\mu\mu} = [5.50, 5.90]$

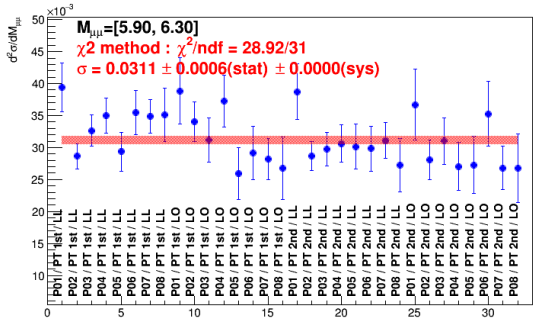

(e) $M_{\mu\mu} = [5.90, 6.30]$

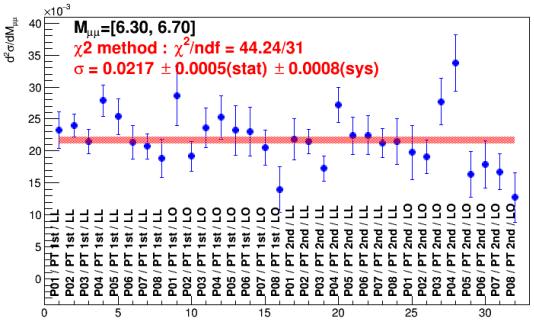

(f) $M_{\mu\mu} = [6.30, 6.70]$

Figure 3.60: *The cross-section of 32 sub-samples of PT cells in $M_{\mu\mu}$ and its fit with polynomial0 (1).*

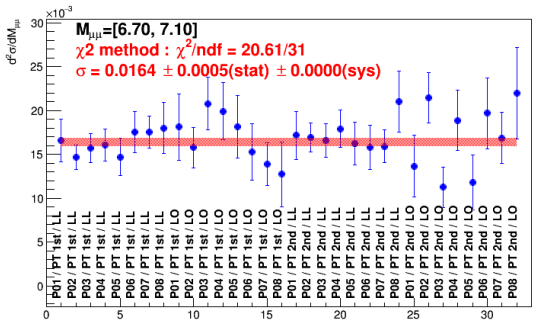

(g) $M_{\mu\mu} = [6.70, 7.10]$

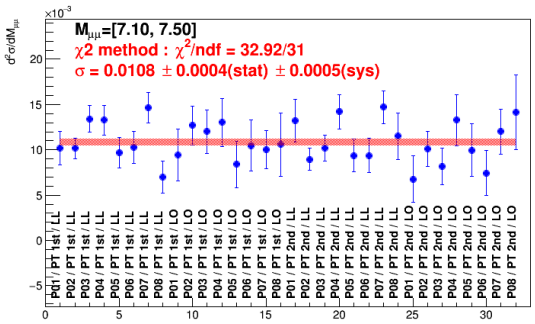

(h) $M_{\mu\mu} = [7.10, 7.50]$

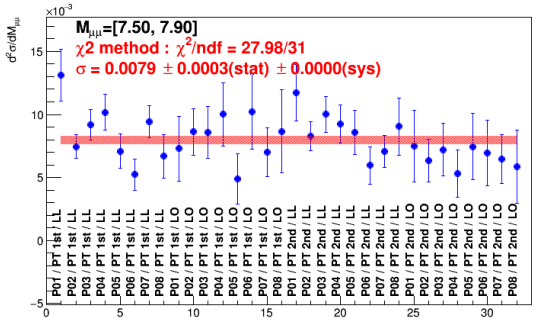

(i) $M_{\mu\mu} = [7.50, 7.90]$

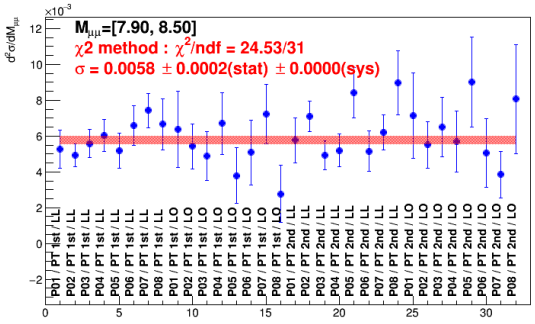

(j) $M_{\mu\mu} = [7.90, 8.50]$

Figure 3.60: *The cross-section of 32 sub-samples of PT cells in $M_{\mu\mu}$ and its fit with polynomial0(1).*

Chapter 4

Phenomenology study of J/ψ mechanism under NRQCD framework

The study of J/ψ production mechanism is important tool understand the QCD, also it serves as a tool to explore the pion PDF. In Sec. 1.4.3, we introduce the production mechanism of J/ψ cross-section. Historically, there are three models to describe the J/ψ production : color-evaporation model (CEM), color single model (CSM), and none-relativistic QCD (NRQCD). Among them, NRQCD model is considered the most successful one. The J/ψ production cross-section from proton data (either fixed-target or collision) is well aligned with the theoretical prediction of NRQCD model, however the pion data is not the case. The suspection is that the Long-Distance-Matrix Elements(LDMEs) of NRQCD obtained from proton data is not universal as it is claimed in the model, i.e. the LDMEs extracted from one experiment can be used to another one. In this section, a new LDMEs is extracted considering the data from both pion-nucleon fixed-target and proton-nucleon fixed-target. With the new parameterized LDMEs, the sensitivity of gluon distribution inside pion is explored.

4.1 Charmonium cross-section in NRQCD

In Ref. [93], the production cross section of a quarkonion generated by hadron-hadron collision is described as follows :

$$h_A \ + \ h_B \to H \ + \ X$$

$$\sigma_H = \sum_{i,j} \int_0^1 dx_A dx_B \ f_{i/h_A}(x_A) \ f_{j/h_B}(x_B) \ \hat{\sigma}(ij \to H),$$

$$\hat{\sigma}(ij \to H) = \sum_n C^{ij}_{QQ[n]} \langle \mathscr{O}^H_n \rangle$$

where two hadrons are labeled as h_A and h_B, quarkonion is labeled as H, the other hadronization is labeled as X. $f_{i/A}(x_1)$ and $f_{j/B}(x_2)$ represents the hadron PDFs of hadrons h_A and h_B, respectively. x_A and x_B are the Bjorken-x - momentum fraction of parton, of of hadrons h_A and h_B, respectively. $\sum_{i,j}$ sum over all the possible partons. $\int_1^0$ integrate over the momentum of partons from maximum 1 (equal to hadron momentum) to 0 (none). The production cross-section of the quarkonium $\hat{\sigma}(ij \to H)$ in NRQCD is divided into two parts :

(1) The perturbative part, $C_{QQ}^{ij}[n]$, describes the production of a quark-antiquark pair $Q\bar{Q}$ in a color state n. $C_{QQ}^{ij}[n]$ is a expansion of series terms with order of strong coupling constant $\alpha_s(2m_Q)$. The color state n is either in $n = 1$ so called color singlet(CS) state or $n = 8$ so called color octet(CO) state.

(2)The non-perturbative part, $< \mathscr{O}_n^H >$ describes the probability of quark-antiquark harmonizing into bound states H. It is demonstrated in the form of matrix so called Long-Distance-Matrix Elements(LDMEs). LDMEs is estimated from the experimental data since it is of a nonperturbative nature in QCD

The charmonium production cross-section of J/ψ, $\psi(2S)$, χ_{cJ} up to NLO $\mathscr{O}(\alpha_s^3)$ could comes from three possible sub-processes, quark-antiquark annihilation $q\bar{q}$, gluon fusion gg, and quark-gluon scattering gq. The formulation of the charmonium production described in Ref. [93] is listed below :

For J/ψ and $\psi(2S)$

$$\begin{aligned}
\hat{\sigma}(gg \to J/\psi,\psi(2S)) &= \frac{5\pi^3\alpha_s^2}{12(2m_c)^3 s}\delta(x_1x_2-4m_c^2/s)\Big[\langle \mathscr{O}_8^{J/\psi,\psi(2S)}(^1S_0)\rangle + \frac{3}{m_c^2}\langle \mathscr{O}_8^{J/\psi,\psi(2S)}(^3P_0)\rangle + \frac{4}{5m_c^2}\langle \mathscr{O}_8^{J/\psi,\psi(2S)}(^3P_2)\rangle\Big] \\
&\quad + \frac{20\pi^2\alpha_s^3}{81(2m_c)^5}\Theta(x_1x_2-4m_c^2/s)\langle \mathscr{O}_1^{J/\psi,\psi(2S)}(^3S_1)\rangle z^2\Big[\frac{1-z^2+2zlnz}{(1-z)^2}+\frac{1-z^2-2zlnz}{(1+z)^3}\Big] \\
\hat{\sigma}(gq \to J/\psi,\psi(2S)) &= 0 \\
\hat{\sigma}(q\bar{q} \to J/\psi,\psi(2S)) &= \frac{16\pi^3\alpha_s^2}{27(2m_c)^3 s}\delta(x_1x_2-4m_c^2/s)\langle \mathscr{O}_8^{J/\psi,\psi(2S)}(^3S_1)\rangle
\end{aligned}$$

For χ_{c0}

$$\begin{aligned}
\hat{\sigma}(gg \to \chi_{c0}) &= \frac{2\pi^3\alpha_s^2}{3(2m_c)^3 s}\delta(x_1x_2-4m_c^2/s)\frac{1}{m_s^2}\langle \mathscr{O}_1^{\chi_{c0}}(^3P_0)\rangle \\
\hat{\sigma}(gq \to \chi_{c0}) &= 0 \\
\hat{\sigma}(q\bar{q} \to \chi_{c0}) &= \frac{16\pi^3\alpha_s^2}{27(2m_c)^3 s}\delta(x_1x_2-4m_c^2/s)\langle \mathscr{O}_8^{\chi_{c0}}(^3S_1)\rangle
\end{aligned}$$

For χ_{c1}

$$\begin{aligned}
\hat{\sigma}(gg \to \chi_{c1}) &= \frac{2\pi^2\alpha_s^3}{9(2m_c)^5}\Theta(x_1x_2-4m_c^2/s)\frac{1}{m_c^2}\langle \mathscr{O}_1^{\chi^{c1}}(^3P_1)\rangle\Big[\frac{4z^2lnz(z^8+9z^7+26z^6+28z^5+17z^4+7z^3-40z^2-4z-4)}{(1+z)^5(1-z)^4)} \\
&\quad + \frac{z^9+39z^8+145z^7+251z^6+119z^5-153z^4-17z^3-147z^2-8z+10}{3(1-z)^3(1+z)^4}\Big] \\
\hat{\sigma}(gq \to \chi_{c1}) &= \frac{8\pi^2\alpha_s^3}{81(2m_c)^5}\Theta(x_1x_2-4m_c^2/s)\frac{1}{m_c^2}\langle \mathscr{O}_1^{\chi^{c1}}(^3P_1)\rangle\Big[-z^2lnz+\frac{4z^3-9z+5}{3}\Big] \\
\hat{\sigma}(q\bar{q} \to \chi_{c1}) &= \frac{16\pi^3\alpha_s^2}{27(2m_c)^3 s}\delta(x_1x_2-4m_c^2/s)\langle \mathscr{O}_8^{\chi_{c1}}(^3S_1)\rangle
\end{aligned}$$

For χ_{c2}

$$\begin{aligned}
\hat{\sigma}(gg \to \chi_{c2}) &= \frac{8\pi^3\alpha_s^2}{45(2m_c)^3 s}\frac{1}{m_c^2}\delta(x_1x_2-4m_c^2/s)\frac{1}{m_s^2}\langle \mathscr{O}_1^{\chi_{c2}}(^3P_2)\rangle \\
\hat{\sigma}(gq \to \chi_{c2}) &= 0 \\
\hat{\sigma}(q\bar{q} \to \chi_{c2}) &= \frac{16\pi^3\alpha_s^2}{27(2m_c)^3 s}\delta(x_1x_2-4m_c^2/s)\langle \mathscr{O}_8^{\chi_{c2}}(^3S_1)\rangle
\end{aligned}$$

where $z=\frac{(2m_c)^2}{sx_1x_2}$, $\sqrt{s}$ is the center-of-mass-energy, m_c is the charm quark mass.

For J/ψ and $\psi(2S)$:
J/ψ and $\psi(2S)$ have the same production mechanism. They are produced with gg and $q\bar{q}$ processes. The contribution from gq is close zero. In gg fusion, they are generated by CS production $\sim \frac{\alpha_s^2}{m_c^3}\triangle_8^{J/\psi,\psi(2S)}$, where $\triangle_8^{J/\psi,\psi(2S)} = \Big[\langle \mathscr{O}_8^{J/\psi,\psi(2S)}(^1S_0)\rangle + \frac{3}{m_c^2}\langle \mathscr{O}_8^{J/\psi,\psi(2S)}(^3P_0)\rangle + \frac{4}{5m_c^2}\langle \mathscr{O}_8^{J/\psi,\psi(2S)}(^3P_2)\rangle\Big]$ and by CO production $\sim \frac{\alpha_s^3}{m_c^5}\langle \mathscr{O}_8^{J/\psi,\psi(2S)}(^3S_1)\rangle$. Through $q\bar{q}$, they are produced by CO state $\sim \frac{\alpha_s^2}{m_c^3}\langle \mathscr{O}_8^{J/\psi,\psi(2S)}(^3S_1)\rangle$.

For χ_{c1} :
χ_{c1} is produced as a CS state through GG fusion and qg scattering $\sim \frac{\alpha_s^3}{m_c^5}\langle \mathscr{O}_1^{\chi_{c1}}(^3P_1)\rangle$. The $q\bar{q}$ production is with CO state $\sim \frac{\alpha_s^2}{m_c^3}\langle \mathscr{O}_8^{\chi_{c1}}(^3S_1)\rangle$.

For χ_{c0} and χ_{c2} :
The production mechanism at LO are relatively simple. They are produced as CS states by gg fusion and as COs by $q\bar{q}$ annihilation. The corresponding LDMEs for these two subprocesses are $\mathscr{O}_1^{\chi_{c0,c2}}(^3P_0)$ and $\mathscr{O}_8^{\chi_{c0,c2}}(^3S_1)$.

The relations of LDMEs in different sub-processes, quark-antiquark annihilation $q\bar{q}$, gluon fusion gg, and quark-gluon scattering gq, are summarized in Table. 4.1.

Table 4.1: *The relations of NRQCD LDMEs in the different sub-processes, quark-antiquark annihilation $q\bar{q}$, gluon fusion gg, and quark-gluon scattering gq, in the order of α_S, i.e.* $\triangle_8^H = \left[\langle \mathscr{O}_8^H(^1S_0)\rangle + \frac{3}{m_c^2}\langle \mathscr{O}_8^H(^3P_0)\rangle + \frac{4}{5m_c^2}\langle \mathscr{O}_8^H(^3P_2)\rangle\right]$

H	$q\bar{q}$	gg	qg
$J/\psi,\ \psi(2S)$	$\langle \mathscr{O}_8^H(^3S_1)\rangle \mathscr{O}(\alpha_s^2)$	$\triangle_8^H \mathscr{O}(\alpha_s^2)$ $\langle \mathscr{O}_1^H(^3S_1)\rangle \mathscr{O}(\alpha_s^3)$	
χ_{c0}	$\langle \mathscr{O}_8^H(^3S_1)\rangle \mathscr{O}(\alpha_s^2)$	$\langle \mathscr{O}_1^H(^3P_0)\rangle \mathscr{O}(\alpha_s^3)$	
χ_{c1}	$\langle \mathscr{O}_8^H(^3S_1)\rangle \mathscr{O}(\alpha_s^2)$	$\langle \mathscr{O}_1^H(^3P_1)\rangle \mathscr{O}(\alpha_s^3)$	$\langle \mathscr{O}_1^H(^3P_1)\rangle \mathscr{O}(\alpha_s^3)$
χ_{c0}	$\langle \mathscr{O}_8^H(^3S_1)\rangle \mathscr{O}(\alpha_s^2)$	$\langle \mathscr{O}_1^H(^3P_2)\rangle \mathscr{O}(\alpha_s^3)$	

As a results of the spin symmetry relation. The number of the LDMEs are further reduced:

$$\begin{aligned}
\langle \mathscr{O}_8^{J/\psi,\psi(2S)}(^3P_J)\rangle &= (2J+1)\langle \mathscr{O}_8^{J/\psi,\psi(2S)}(^3P_0)\rangle \text{ for } J=2 \\
\langle \mathscr{O}_8^{\chi_{cJ}}(^3S_1)\rangle &= (2J+1)\langle \mathscr{O}_8^{\chi_{c0}}(^3S_1)\rangle \text{ for } J=1,2 \\
\langle \mathscr{O}_1^{\chi_{cJ}}(^3P_J)\rangle &= (2J+1)\langle \mathscr{O}_1^{\chi_{c0}}(^3P_0)\rangle \text{ for } J=1,2
\end{aligned}$$

Note that LEMDs are obtained from the experimental fits, therefore the LEMDs of χ_{c1} and χ_{c2} could be evaluated from the fit-LDMEs of χ_{c0}.

In Ref. [93], they published the best-fit of LDMEs in Table. 4.2. The CS LDMEs $\langle \mathscr{O}_1^H[^3S_1]\rangle$ for J/ψ and $\psi(2S)$, and $\langle \mathscr{O}_1^H[^3P_0]\rangle$ for χ_{c0}, are given by the potential models [94], and the CO LDMEs $\langle \mathscr{O}_8^H[^3S_1]\rangle$ for J/ψ, $\psi(2S)$ and χ_{cJ}, are taken from the fits to Tevatron collider data of p_T spectra [95]. The Δ_8^H parameters for the individual J/ψ and $\psi(2S)$ production were determined by a fit of NRQCD calculation to the proton-induced data.

A later study by Maltoni *et al.* [96] performed with a full NLO calculation. LDMEs given in Ref. [96] paper show an additional reduction factor of about 0.1 for $\langle \mathscr{O}_8^H[^3S_1]\rangle$ and $\langle \mathscr{O}_8^H[^1S_0]\rangle$ of J/ψ and $\psi(2S)$, was required in the calculations to achieve a good description of fixed-target proton-induced data. The CS LDMEs used in these two studies are either identical or very similar, as they were obtained from a potential model. The CO $\langle \mathscr{O}_8^H[^3S_1]\rangle$ for χ_{c0} are nearly identical. In contrast, the remaining CO LDMEs obtained in Ref. [93] are about a factor of 1.5-5 larger than those determined in Ref. [96].

Table 4.2: *The best-fit LDMEs for the charmonium production given in Ref [93].(unit=GeV^3.)*

H	$\langle \mathscr{O}_1^H(^3S_1)\rangle$	$\langle \mathscr{O}_1^H(^3P_0)\rangle/m_c^2$	$\langle \mathscr{O}_8^H(^3S_1)\rangle$	$\triangle_8^H$
J/ψ	1.16		6.6×10^{-3}	3×10^{-2}
$\psi(2S)$	0.76		4.6×10^{-3}	5.2×10^{-2}
χ_{c0}		0.044	3.2×10^{-3}	

With the information of LDMEs, the direct production cross sections of J/ψ, $\psi(2S)$ and χ_{cJ} can be calculated. Furthermore, taking into account the direct production of J/ψ and the feed-down from hadronic decays of $\psi(2S)$ and χ_{cJ}, the total J/ψ cross section is estimated as follow :

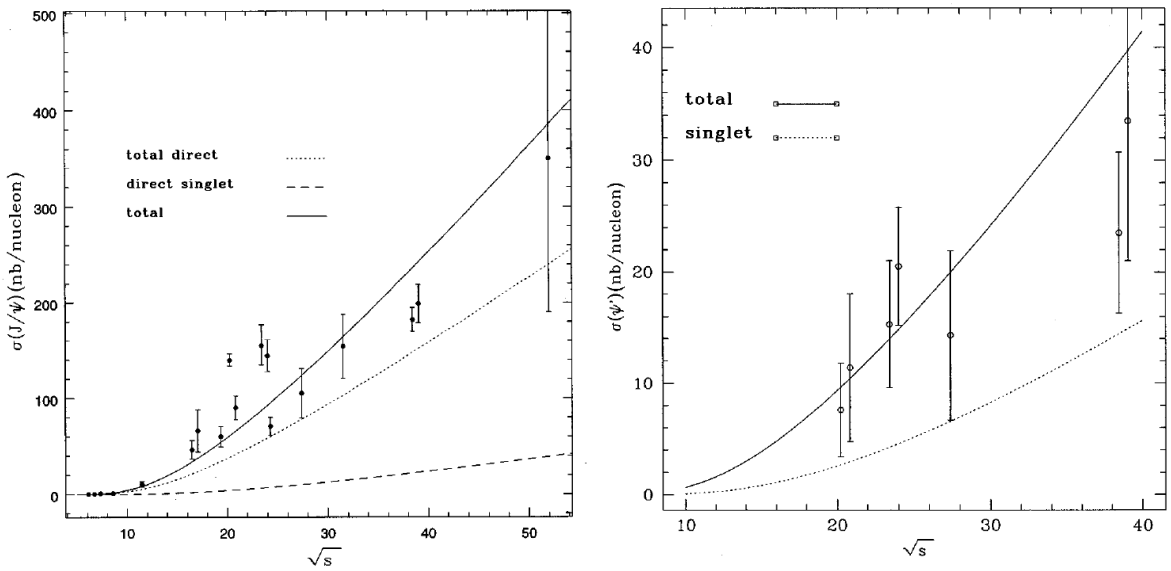

(a) J/ψ **(b)** $\psi(2S)$

Figure 4.1: *The comparison between J/ψ and $\psi(2S)$ cross section compared from* ***proton-nucleon*** *collision and NRQCD calculation from Ref. [93]. The dotted line is from the contribution of color-singlet(CS) processes. The dash line is the color-octet(CO) processes. The solid line is the total cross section includes both CS and CO states. Both J/ψ and $\psi(2S)$ data are well agreed with the NRQCD predictions include CS and CO processes.*

$$\sigma_{J/\psi} = \sigma^{direct}_{J/\psi} + Br(\psi(2S) \to J/\psi + X) + \sum_{J=2}^{2} Br(\chi_{cJ} \to J/\psi + \gamma)$$

The branching ratios of the indirect J/ψ production from $\psi(2S)$ and χ_{cJ} can be found in Table. 1.6. In Ref. [93], they shows the J/ψ and $\psi(2S)$ cross section of proton-nucleon collisions compared with their NRQCD calculation from in Fig. 4.1. Additionally, they also fit the $\psi(2S)$ cross section of pion-nucleon collisions with their NRQCD calculation shown in Fig. 4.2. Pion PDF, GRV [13], is used in the calculation. The discrepancy given by the pion data is not well understood. The suspection is either the unrealistic pion PDF used or the violation of the universality LDMEs (The nucleon PDF is consider well constrained due to high statistic data from LHC). To untangle the suspections, a new set of LDMEs is extracted with both fixed-target proton-induced data and fixed-target pion-induced data, shown in Sec.4.2. In the later Sec.4.3, the sensitivity of gluon distribution inside pion from different pion PDF sets is tested with this new LDMEs.

4.2 Extraction of LDEMs includes pion data

In this section, the extraction of new LDMEs of NRQCD with the fixed-target data of J/ψ and $\psi(2S)$ production with proton and pion beams. The differential cross section as a function of x_F for a charmonium state H ($H = J/\psi$, $\psi(2S)$, or χ_{cJ}) from the hN, ($h = p$, $\bar{p}$, or π) collisions :

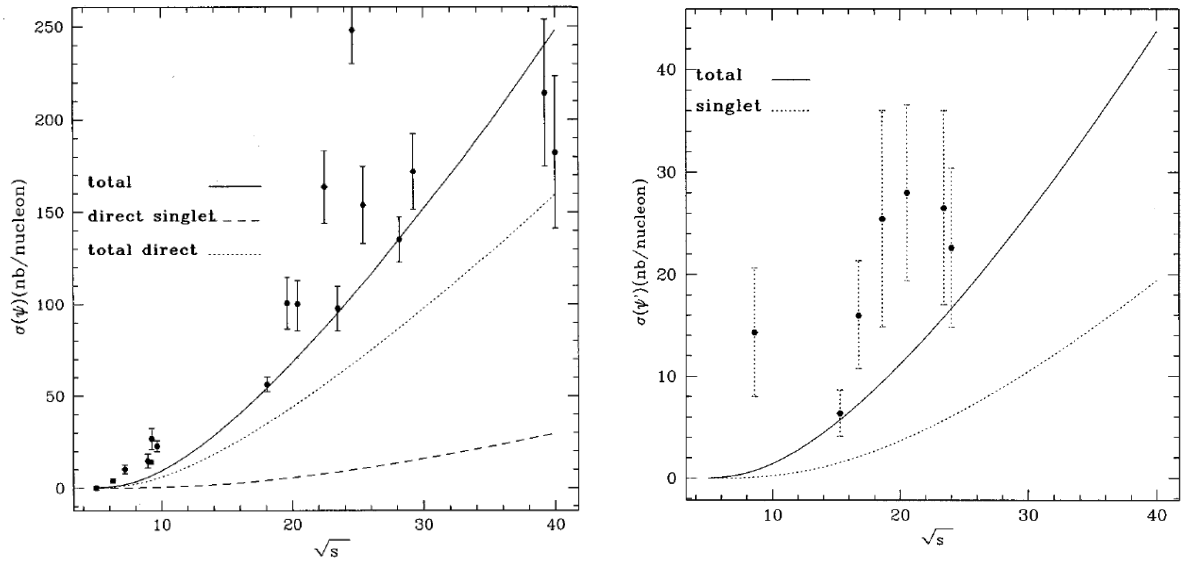

(a) J/ψ **(b)** $\psi(2S)$

Figure 4.2: *The comparison between J/ψ and $\psi(2S)$ cross section compared from* ***pion-nucleon*** *collision and NRQCD calculation from Ref. [93]. The dotted line is from the contribution of color-singlet(CS) processes. The dash line is the color-octet(CO) processes. The solid line is the total cross section includes both CS and CO states. NRQCD calculation is lower than the data.*

$$\frac{d\sigma^H}{dx_F} = \sum_{i,j=q,\bar{q},G} \int_0^1 dx_1 dx_2 \delta(x_F - x_1 + x_2)$$
$$\times f_i^h(x_1,\mu_F) f_j^N(x_2,\mu_F) \hat{\sigma}[ij \to H](x_1 P_h, x_2 P_N, \mu_F, \mu_R, m_c), \tag{4.1}$$
$$\hat{\sigma}[ij \to H] = \sum_n C^{ij}_{c\bar{c}[n]}(x_1 P_h, x_2 P_N, \mu_F, \mu_R, m_c) \times \langle \mathscr{O}_n^H[^{2S+1}L_J] \rangle \tag{4.2}$$

$$x_F = 2p_L/\sqrt{s},\ x_{1,2} = \frac{\sqrt{x_F^2 + 4{M_{c\bar{c}}}^2/s} \pm x_F}{2} \tag{4.3}$$

where h is the beam hadron and N the target nucleon, i and j label the type of interacting partons (gluons, quarks and antiquarks), and the $c\bar{c}$ pair is denoted by its color (n), spin (S), orbital angular momentum (L) and total angular momentum (J). Here m_c and $M_{c\bar{c}}$ are the charm quark and $c\bar{c}$ pair masses, f^h and f^N are the incoming hadron and the target nucleon parton distribution functions, evaluated at their respective Bjorken-x values, x_1 and x_2. The μ_F and μ_R are the factorization and renormalization scales. The total cross sections are obtained by integrating over x_F.

The NRQCD formulation of charmonium production cross section is based on Ref. [93]. The cross sections are evaluated with a charm quark mass $m_c = 1.5$ GeV/c^2 and renormalization and factorization scale $\mu_R = \mu_F = 2m_c$. The nucleon PDFs and pion PDFs are used with PDFs [3] and GRV in NLO PDFs [13] under the Q-evaluation LHAPDF framework [**?**, 85], respectively.

The pion-induced data for J/ψ and $\psi(2S)$ are taken from Refs. [97, 98]. In addition, three measurements of R_ψ from HERA [99] and NA38 [100], and the pion-induced data of

$\sigma(J/\psi)$ and $\sigma(\psi(2S))$ from NA38 [101] and WA92 [36] are added. The cross sections for proton-induced J/ψ and $\psi(2S)$ and their ratios $R_\psi = \sigma(\psi(2S)))/\sigma(J/\psi)$ are taken from Ref. [96]. The cancellation of systematic uncertainties in $R_\psi = \sigma(\psi(2S)))/\sigma(J/\psi)$ brings additional constraining power in the fit.

The fit results are shown in Fig. 4.3. The fitting procedures are performed in 3 steps. First, the parameterization of LDMEs from Ref. [93] is used to utilized the analysis framework, named as "Fit-R"(reference fit). After confirming the reliability of the analysis framework, we include only the proton-induced data in the fitting named as "Fit-1" to extract LDMEs. Fit-1 is converged, however the CO contribution of LDMEs is close to zero. The LDMEs can't be decided with proton data alone. Finally, we use both proton-induced and pion-induced data in the fitting names as "Fit-2". Fit-2 demonstrate a good consistency between data and the fitting, furthermore the CS and CO contributions of LDMEs are all reasonable, The new LDMEs includes both proton-nucleon data and pion-nucleon data are decided. The details of each steps are describes as follows :

Table 4.3: *The reduced χ^2/ndf of the whole data sets, the χ^2 is divided by the number of data point (ndp) for each data set in "Fit-R", "Fit-1" and "Fit-2" NRQCD calculations and the corresponding input or best-fit LDMEs. All LDMEs are in units of* GeV^3.

	Fit-R	Fit-1	Fit-2
χ^2_{total}/ndf	16.8	6.0	3.3
$\chi^2/ndp\|^p_{\sigma(J/\psi)}$	9.2	4.1	5.4
$\chi^2/ndp\|^p_{\sigma(\psi(2S))}$	2.2	1.4	1.7
$\chi^2/ndp\|^p_{R(\psi(2S))}$	1.1	0.7	1.0
$\chi^2/ndp\|^{\pi^-}_{\sigma(J/\psi)}$	46.8	15.3	3.7
$\chi^2/ndp\|^{\pi^-}_{\sigma(\psi(2S))}$	2.8	0.9	0.7
$\langle \mathscr{O}_1^{J/\psi}(^3S_1)\rangle$	0.16	0.16	0.16
$\langle \mathscr{O}_8^{J/\psi}[^3S_1]\rangle$	6.6×10^{-3}	$(1.47 \pm 0.07) \times 10^{-1}$	$(9.5 \pm 0.4) \times 10^{-2}$
$\Delta_8^{J/\psi}$	3×10^{-2}	$(0 \pm 8) \times 10^{-4}$	$(1.8 \pm 0.2) \times 10^{-2}$
$\langle \mathscr{O}_1^{\psi(2S)}(^3S_1)\rangle$	0.76	0.76	0.76
$\langle \mathscr{O}_8^{\psi(2S)}[^3S_1]\rangle$	4.6×10^{-3}	$(2.5 \pm 0.2) \times 10^{-2}$	$(2.6 \pm 0.2) \times 10^{-2}$
$\Delta_8^{\psi(2S)}$	5.2×10^{-3}	$(0 \pm 8) \times 10^{-4}$	$(4 \pm 6) \times 10^{-4}$
$\langle \mathscr{O}_1^{\chi_{c0}}(^3P_0)\rangle/m_c^2$	0.044	0.044	0.044
$\langle \mathscr{O}_8^{\chi_{c0}}(^3S_1)\rangle$	3.2×10^{-3}	3.2×10^{-3}	3.2×10^{-3}

- **Fit-R (LDMEs from Ref. [93] used)**

  We first compare these data with the NRQCD calculations with LDMEs determined in Ref. [93], named as "Fit-R". It is not really a fitting but a demonstration of the the work of Ref. [93] to verify the reliability of our analysis framework. The difference of proton PDFs selected for the study of Ref. [93] (CTEQ3L) and here (CT14nlo) has a negligible effect on the final results. The results are plotted as black dashed lines in Fig. 4.3. The total reduced χ^2/ndf, together with the deviations between data and calculations per data point (χ^2/ndp) for each data set, are displayed in Fig. 4.3

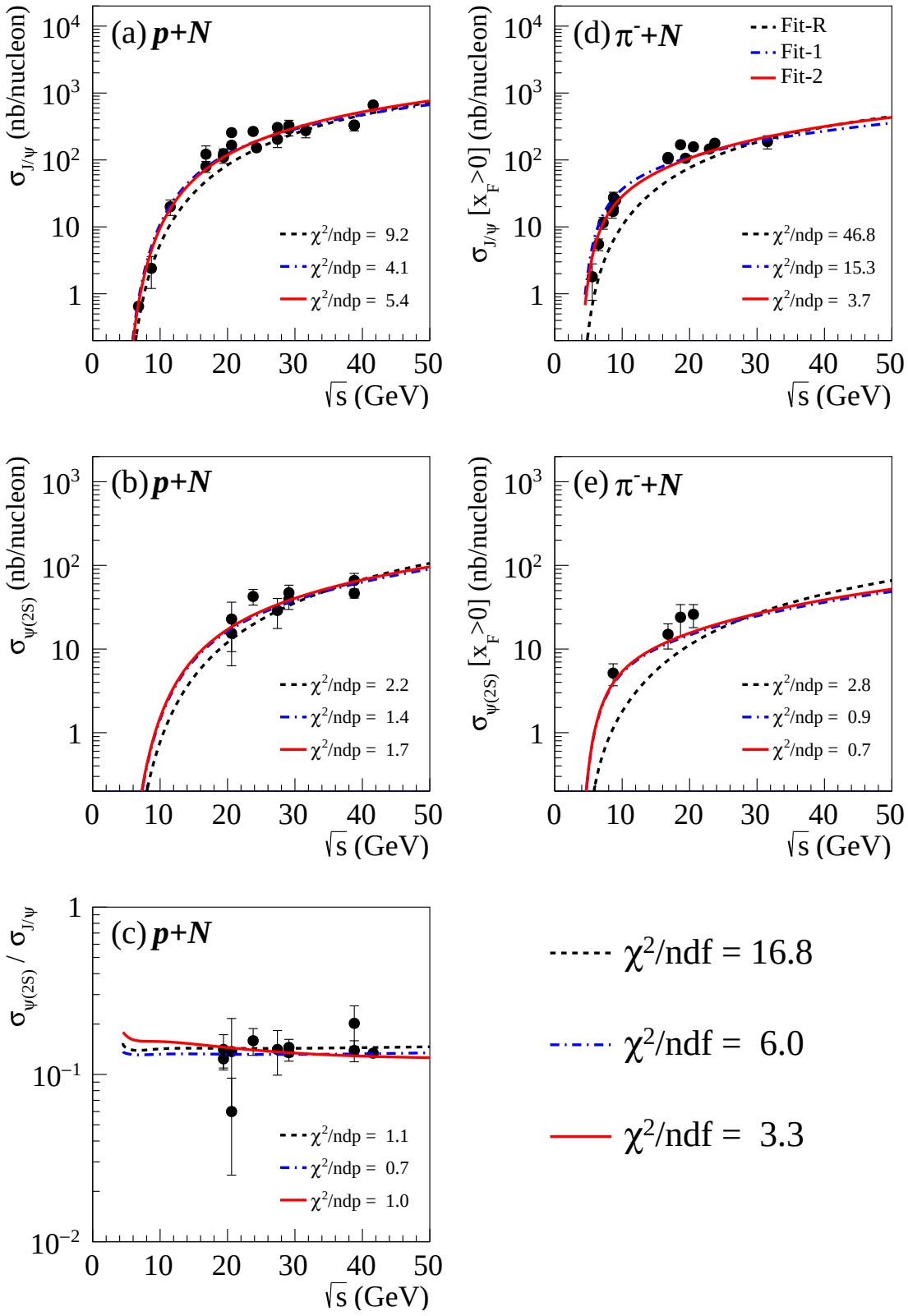

Figure 4.3: *J/ψ and $\psi(2S)$ production cross sections and the $\psi(2S)/(J/\psi)$ ratios in the $p+N$ reactions, and J/ψ and $\psi(2S)$ production cross sections in the $\pi^- + N$ reactions, labeled as (a)-(e) in the plot. The dashed (black), dot-dashed (blue) and solid (red) curves represent the NRQCD results using the LDMEs obtained in "Fit-R", "Fit-1" and "Fit-2", respectively. The reduced χ^2/ndf for all data are displayed in the bottom-right. The values of χ^2 divided by the number of data point (ndp) for each data set are also shown.*

and listed in Table 4.3. Fit-R show the consistent plots results as shown in Fig. 4.1. The reduced χ^2/ndf of the entire data sets is 16.8. Clearly, the pion-induced data below $\sqrt{s} = 20$ GeV are significantly underestimated by the calculations as already observed.

- **Fit-1 (Fit of the proton-induced data)**

  It is known that the $q\bar{q}$ contribution plays an important role in the pion-induced J/ψ production near threshold because the parton density at large x is dominated by the valence antiquarks in pions. In Fit-R taken from Ref. [93], The CO contribution $\langle \mathscr{O}_8^H[^3S_1] \rangle$ LDMEs are responsible for the $q\bar{q}$ contribution, as shown in Table 4.1, and their values were taken from the fits to the Tevatron data [95] at high energies (same as what Ref. [93] does). The observed underestimation of low-energy pion-induced data in "Fit-R" could arise from too smaller value for the input $\langle \mathscr{O}_8^H[^3S_1] \rangle$.

  To seek an improved description of the pion-induced data, we take a different approach, called "Fit-1", of leaving both CO contributions of LDMEs $\langle \mathscr{O}_8^H[^3S_1] \rangle$ and Δ_8^H J/ψ and $\psi(2S)$ as free parameters in the global fit of the proton-induced data. In the mean time, the CS contribution $\langle \mathscr{O}_1^H[^3S_1] \rangle$ LDMEs of J/ψ and $\psi(2S)$ are taken from potential model [94] same as Ref. [93] and Ref. [96]. The CO LDME of χ_{c0} is also fixed at the values given in Ref. [93]. The best-fit LDMEs are required to be positive-definite. The resulting fit is shown as blue dot-dashed lines in Fig. 4.3. The cross sections for both proton- and pion-induced data are significantly enhanced, compared to the results of Fit-R. The agreement between the data and calculation is greatly improved. As shown in Table 4.3, the overall χ^2/ndf is reduced from 16.8 to 6.0, compared to Fit-R. While the pion-induced data are not used in the global fit for Fit-1 LDMEs determination, these data are included in the evaluation of χ^2/ndf for comparison purposes.

  More specifically, the agreement between the pion-induced J/ψ data alone and the calculations with best-fit LDMEs of "Fit-1" is improved by a factor of 3, compared to "Fit-R". The values of newly determined $\langle \mathscr{O}_8^H[^3S_1] \rangle$ are 1.5×10^{-1} and 2.5×10^{-2} for J/ψ and $\psi(2S)$, respectively. Both are significantly larger than the "Fit-R" values of 6.6×10^{-3} and 4.6×10^{-3} determined from collider data. The increase of the values of $\langle \mathscr{O}_8^H[^3S_1] \rangle$ clearly accounts for better agreement between NRQCD calculations and pion-induced data, even though the pion data were not included in the fit.

  The values of the CO Δ_8^H for J/ψ and $\psi(2S)$ resulting from "Fit-1" are compatible with zero, as shown in Table 4.3. Despite an improved description of data in this approach, "Fit-1" finds vanishing values of Δ_8^H for both J/ψ and $\psi(2S)$. It appears that these LDMEs cannot be determined from the proton-induced J/ψ and $\psi(2S)$ production data alone. This suggests the need to include also the pion data in the global fit, as discussed next.

- **Fit-2 (Fit of both the pion- and proton-induced data)**

  Because of the different nature of valence quarks in the protons and pions, the energy dependence of the relative contributions of $q\bar{q}$ and GG processes is different for the J/ψ and $\psi(2S)$ production, especially at low energies. Under the assumption

that higher-twist effects are negligible, a combined fit of these two data sets should further constrain the CO LDMEs. The results of this new fit, referred to as "Fit-2", are shown in Table 4.3 and displayed as the solid red lines in Fig. 4.3.

Comparing the results of "Fit-2" and "Fit-1", it is found that the description of the pion-induced data is improved, while maintaining the good agreement between the proton data and the calculations. The CO matrix elements are also better constrained. The total reduced χ^2/ndf is further decreased to about 3.3. The agreement between the pion-induced J/ψ data and the NRQCD calculation is improved by a factor of 4, from a χ^2/ndp of 15.3 in "Fit-1" to 3.7 in "Fit-2". The values of the newly determined CO $\langle \mathscr{O}_8^H[^3S_1] \rangle$ LDMEs are 9.5×10^{-2} and 2.6×10^{-2} for J/ψ and $\psi(2S)$, respectively, either smaller than or consistent with those obtained in "Fit-1".

With the inclusion of the pion-induced data, non-zero values of the CO Δ_8^H LDMEs can now be obtained. As shown in Table 4.3, the values of CO Δ_8^H LDMEs are found to be 2.2×10^{-3} and 5.0×10^{-5} for J/ψ and $\psi(2S)$, respectively. The best-fit $\langle \mathscr{O}_8^H[^3S_1] \rangle$ LDMEs responsible for the contribution of the $q\bar{q}$ process are larger by about a factor of 10, while the Δ_8^H related to the contribution of the GG process are reduced by a factor of 2-10, in comparison with the LDMEs determined from collider data [93,95]. The new CO LDMEs indicate that the $q\bar{q}$ contribution determined by the fixed-target data is significantly larger than the corresponding contribution at collider energies.

The systematic uncertainties of these results are studied by setting m_c to 1.2 GeV/c^2 or 1.5 GeV/c^2 and the normalization scale $\mu = \mu_F = \mu_R$ to m_c, $2m_c$, and $3m_c$. Figure 4.4 shows the comparison of the pion-induced J/ψ data and NRQCD calculation with the corresponding settings of m_c and μ. The total cross sections and the $q\bar{q}$, GG, and qG contributions are denoted as black, blue, red and green lines, respectively. The parameter of charm quark mass m_c plays a significant role in the systematic effect. With m_c set to 1.2 GeV/c^2, the CO LDMEs as free parameters are not well constrained, and the quality of fit significantly deteriorates as seen from the increased χ^2/ndp. Judging from the contributions of various subprocesses, the GG process is enhanced too much to provide a good description of data in the calculations with this reduction of m_c. When m_c is set as 1.5 GeV/c^2, the quality of the fit is equally good with μ varying among m_c, $2m_c$, and $3m_c$. Even though one of CO LDMEs cannot be obtained with good accuracy when μ is set at m_c, the best-fit LDMEs for three different scales are consistent with having large values of $\langle \mathscr{O}_8^H[^3S_1] \rangle$ LDMEs, reflecting a non-negligible $q\bar{q}$ contribution.

A new set of LDMEs for J/ψ and $\psi(2S)$ production at fixed-target energies has been obtained in an analysis of data with proton and pion beams (Fit-2). Our analysis differs from that of Ref. [93] in two aspects. First, the LDMEs $\langle \mathscr{O}_8^H[^3S_1] \rangle$ are now allowed to vary in the global fit. This leads to a much improved description of fixed-target data with proton beam. Second, the pion data are included in the global fit. This allows for the determination of the LDMEs Δ_8^H. To better understand the reasons for the significantly improved description of the J/ψ and $\psi(2S)$ production data, it is instructive to compare the NRQCD calculations using the "Fit-R" LDMEs of Ref. [93] and the "Fit-2" LDMEs of the present analysis. In particular, we examine the decomposition of the J/ψ production cross section into individual contributions in three fashions: (i) $q\bar{q}$, GG, and qG subprocesses; (ii) color singlet versus color octet $c\bar{c}$ states; (iii) direct production of J/ψ versus feed-down from $\psi(2S)$ and χ_c.

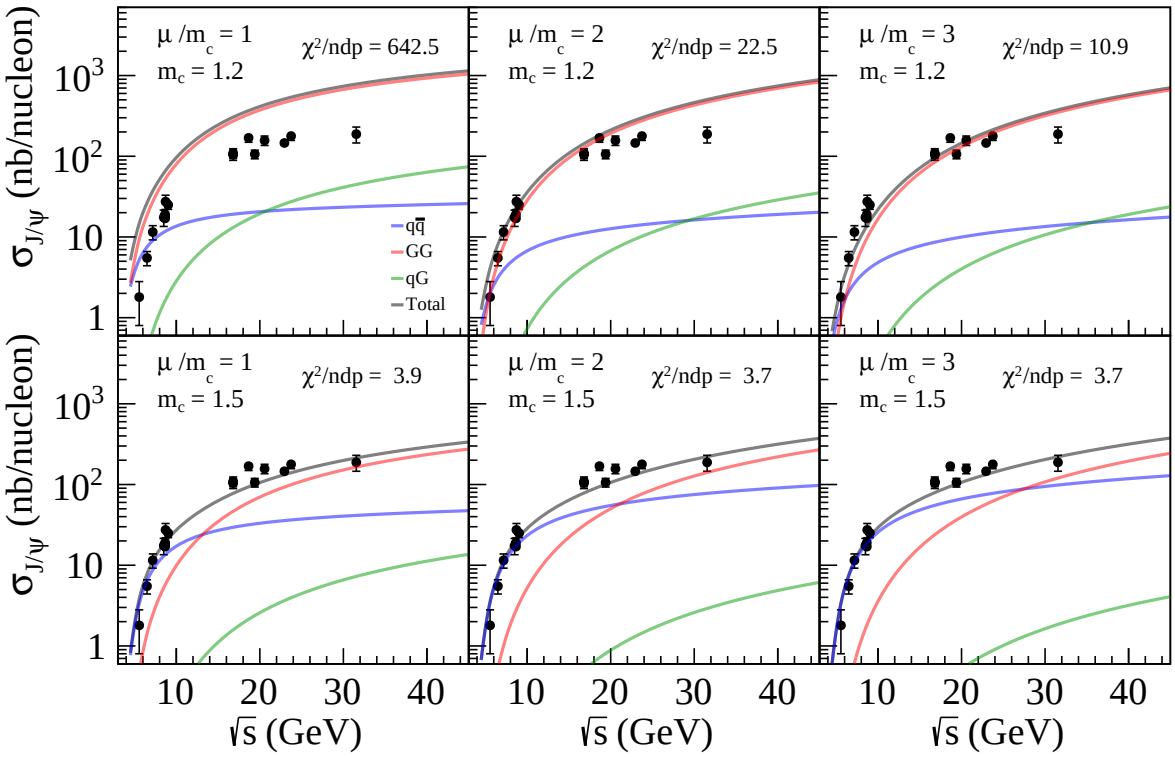

Figure 4.4: *The NRQCD results from an analysis of both proton-induced and pion-induced data sets under variation of charm quark mass m_c, renormalization scale μ_R and factorization scale μ_F, compared with the pion-induced data of J/ψ production as a function of $\sqrt{s}$. The total cross sections and $q\bar{q}$, GG, and qG contributions are denoted as black, blue, red and green lines, respectively. The values of m_c, $\mu = \mu_R = \mu_F$ in the NRQCD calculation as well as the best-fit χ^2/ndp are displayed in each plot.*

- **$q\bar{q}$, GG, and qG subprocesses**

The decomposition of J/ψ production cross sections for proton and pion beams into the $q\bar{q}$, GG and qG processes is shown in Fig. 4.5. We note that the qG contributions remain unchanged in the new analysis since the qG process only contributes to the formation of the χ_{c1} states and the LDMEs for χ_{cJ} are identical for "Fit-R" and "Fit-2". Fig. 4.5 also shows that the GG contribution is dominant in the J/ψ production with proton beam at all energies, except near the threshold. In contrast, the $q\bar{q}$ contribution for pion-induced data is enhanced due to the antiquark content in pion's valence region. Therefore, the inclusion of the pion data in the global fit provides additional constraints on those LDMEs which are sensitive to the $q\bar{q}$ process. The low-energy fixed-target pion data are particularly important for the determination of the $\langle \mathcal{O}_8^H[^3S_1] \rangle$ LDMEs.

In comparison with "Fit-R" from Ref. [93], the $\langle \mathcal{O}_8^H[^3S_1] \rangle$ LDME is increased, whereas Δ_8^H is decreased. These changes lead to an enhancement of the CO $q\bar{q}$ contribution and a reduction of the CO GG contribution. The increase of the fraction of $q\bar{q}$ contribution, especially at low-energies, accounts for the improvement in describing the pion data. The opposite trend for the variations of the two CO LDMEs $\langle \mathcal{O}_8^H[^3S_1] \rangle$ and Δ_8^H leads to significant changes on the energy dependence of J/ψ production cross sections, as shown in Fig. 4.5.

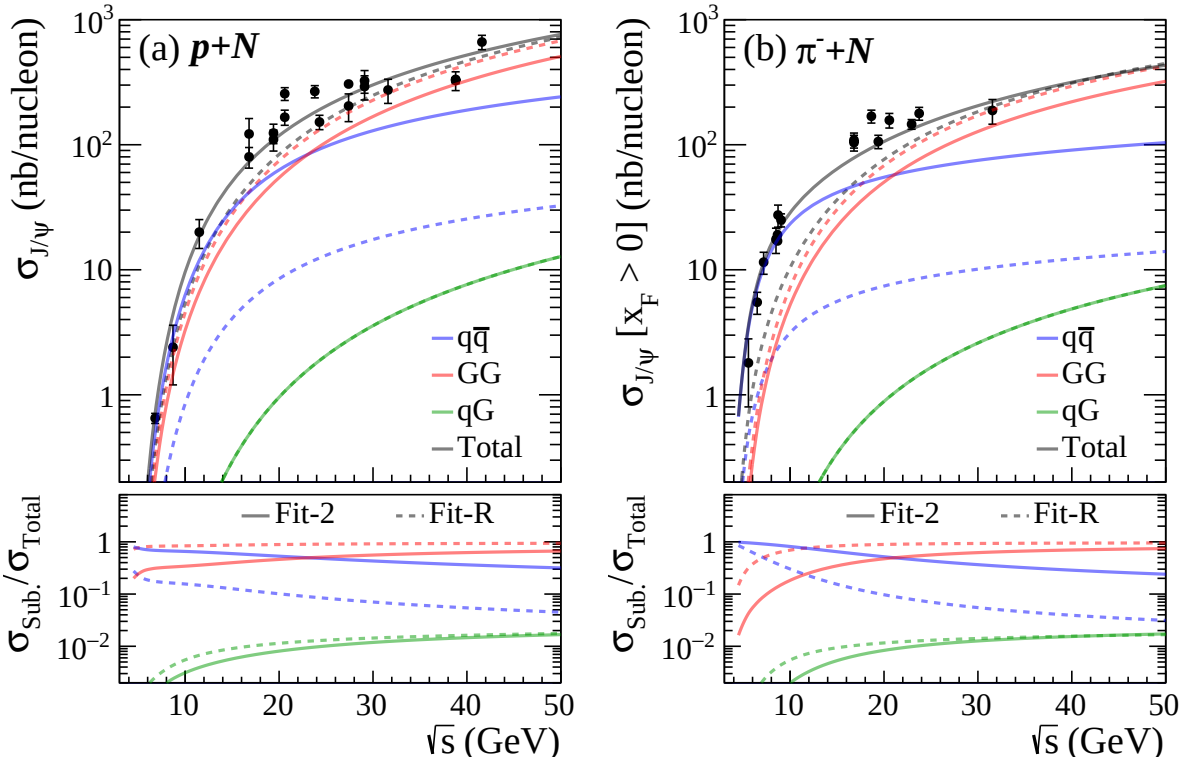

Figure 4.5: *Total cross sections (black) and contributions from $q\bar{q}$ (blue), GG (red) and qG (green) processes for J/ψ production as a function of $\sqrt{s}$ in (a) pN and (b) $\pi^- N$ interactions. The dashed and solid curves represent the "Fit-R" and "Fit-2" results. The fractions of each sub-process cross section are displayed at the bottom of each plot.*

- **color singlet versus color octet $c\bar{c}$ states**

Fig. 4.6 shows the decomposition of the J/ψ cross sections into contributions from the color octet and color singlet states. As the CS contribution (blue lines) in our study is fixed, the enlarged $\langle \mathcal{O}_8^H[^3S_1] \rangle$ LDMEs significantly enhance the CO contribution (red lines) at low energies, while in "Fit-2" the reduced Δ_8^H results in a reduction of CO contribution at high energies. Through the interplay of these two CO LDMEs, the CO contribution remains similar at high energies but is enhanced near threshold for the proton-induced production. In the case of pion-induced production, the CO contribution is slightly suppressed at high energies.

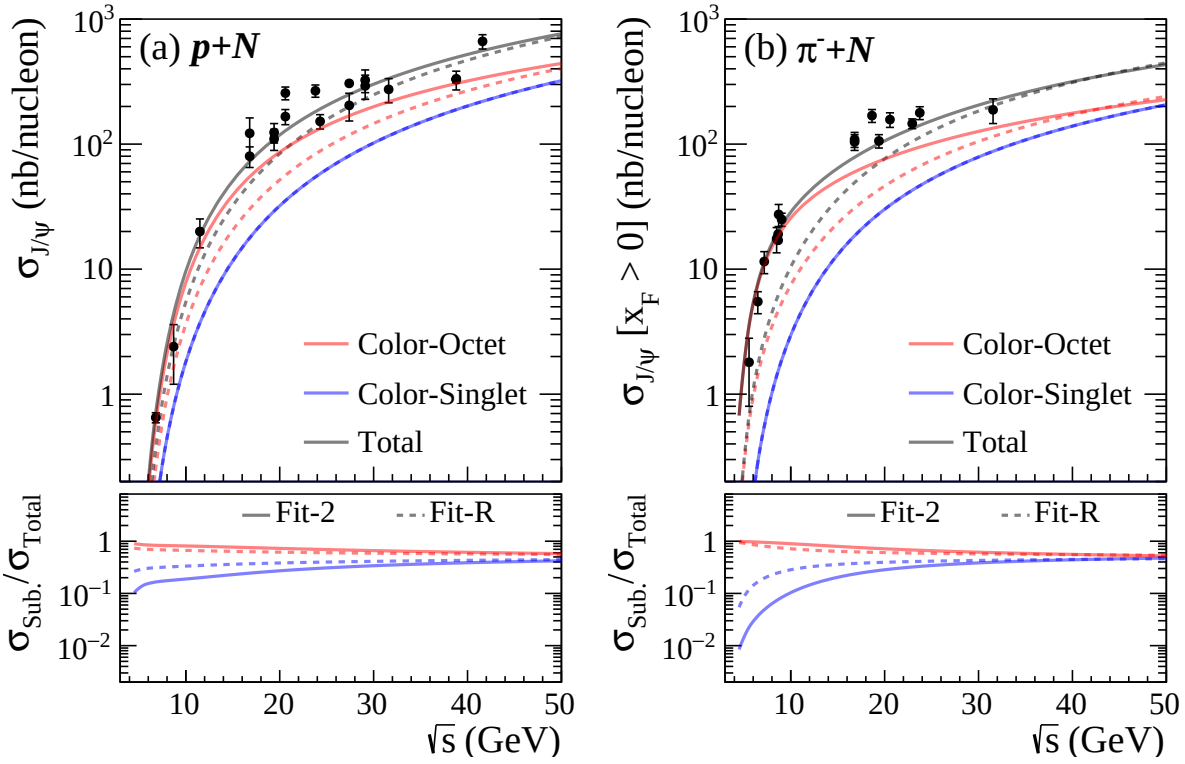

Figure 4.6: *Same as Fig. 4.5 for the decomposition of contributions from CS (blue) and CO (red) processes.*

- **direct production of J/ψ versus feed-down from $\psi(2S)$ and χ_c**

  Fig. 4.7 shows the J/ψ cross sections decomposed into the contributions from direct production (red lines) and the feed-down from heavier charmonium states of $\psi(2S)$ (blue lines) and χ_c (green lines). We note that the LDMEs for the three χ_c states kept unchanged for "Fit-R" and "Fit-2". The most notable change between the calculations with "Fit-2" and the "Fit-R" is the enhancement of the direct J/ψ production at low energies, as a consequence of an enlarged $\langle \mathcal{O}_8^H[^3S_1] \rangle$. Taking into account the decay branching ratios, the contributions to the J/ψ production in descending order of importance are direct production, χ_c, then $\psi(2S)$.

To summarize the main findings at this point, we note that the inclusion of the low-energy pion-induced total cross section data of J/ψ and $\psi(2S)$ production to the analysis of NRQCD provides an important constraint of the $\langle \mathcal{O}_8^H[^3S_1] \rangle$ LDMEs via the $q\bar{q}$ contributions. A good description of both proton- and pion-induced data by NRQCD can

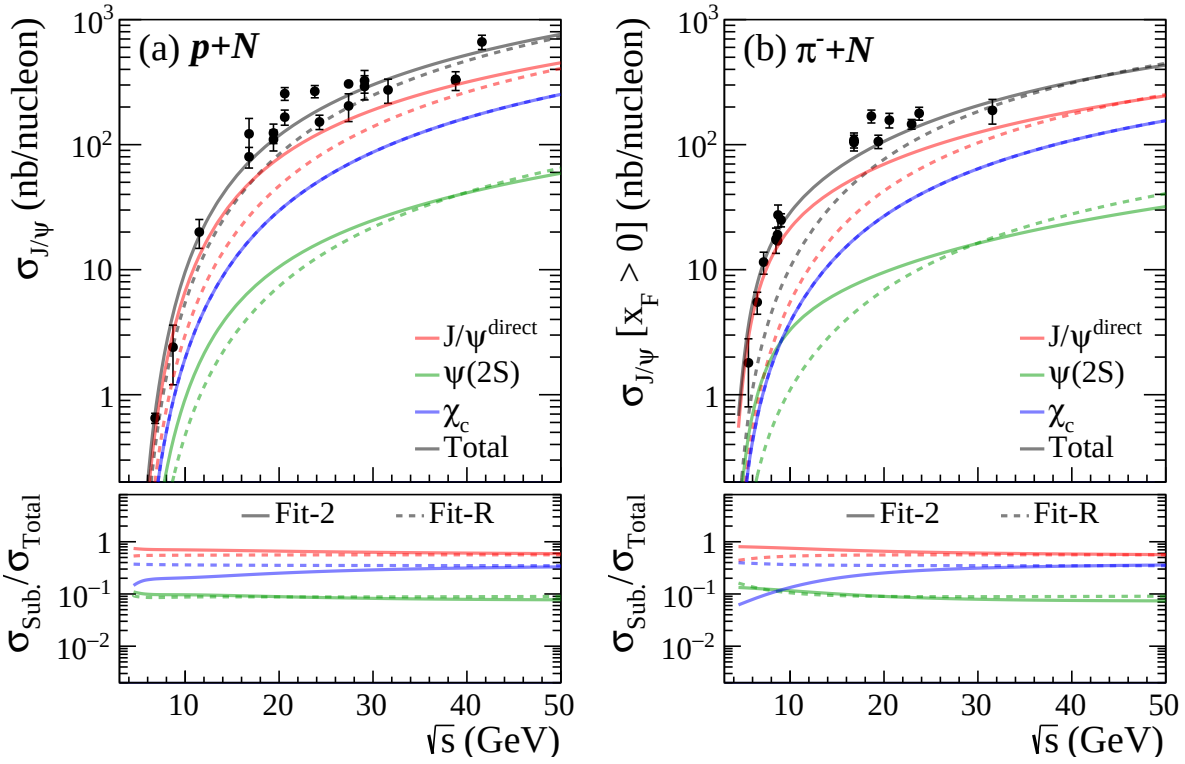

Figure 4.7: *Same as Fig. 4.5 for the decomposition of contributions of J/ψ production from direct production of J/ψ (red) and feed-down from $\psi(2S)$ (green) and all χ_c states (blue).*

be achieved. The $q\bar{q}$ and CO contributions from the NRQCD calculations with the new LDMEs are greatly enhanced at low energies with proton and pion beams, compared with results found in the earlier studies [93, 96].

4.3 Test the sensitivity of gluon distribution inside pion

The new set of LDMEs is now used to study the sensitivity of the J/ψ data to the various pion PDFs. We have considered four pion PDFs, namely, SMRS [15] and GRV [13], representative of the most widely used pion PDFs so far, as well as JAM [16] and xFitter [18], obtained from very recent global analyses. For SMRS, we select the default one in which the sea quarks carry 15% of the pion momentum at $Q^2 = 4$ GeV^2. As illustrated in Sec. 1.2.3, SMRS, JAM, and xFitter have similar valence-quark distributions, while the magnitude of the GRV distribution is smaller by about 20% to 30%. For the gluon distributions, SMRS and GRV have similar shapes and magnitudes, while xFitter and JAM have significantly smaller magnitudes by a factor of 2 to 4.

The NRQCD calculation with each of the four pion PDFs is compared with the data in Fig. 4.8. Overall, the total cross sections (black lines) using four pion PDFs exhibit similar $\sqrt{s}$ dependencies. However, the individual terms differ strongly. The $q\bar{q}$ contribution dominates near thresholds and the GG contribution increases rapidly at higher energies, while the qG component is relatively negligible over the whole energy range. The relative fractions of $q\bar{q}$ and GG contributions as a function of $\sqrt{s}$ vary for each pion PDFs, reflecting the differences among their parton distributions. For SMRS and GRV the GG contribution starts to dominate the cross section around $\sqrt{s} = 20$ GeV. For xFitter and JAM the corresponding values are larger at $\sim \sqrt{s} = 35$ GeV because of their relatively reduced

gluon strength in the valence region.

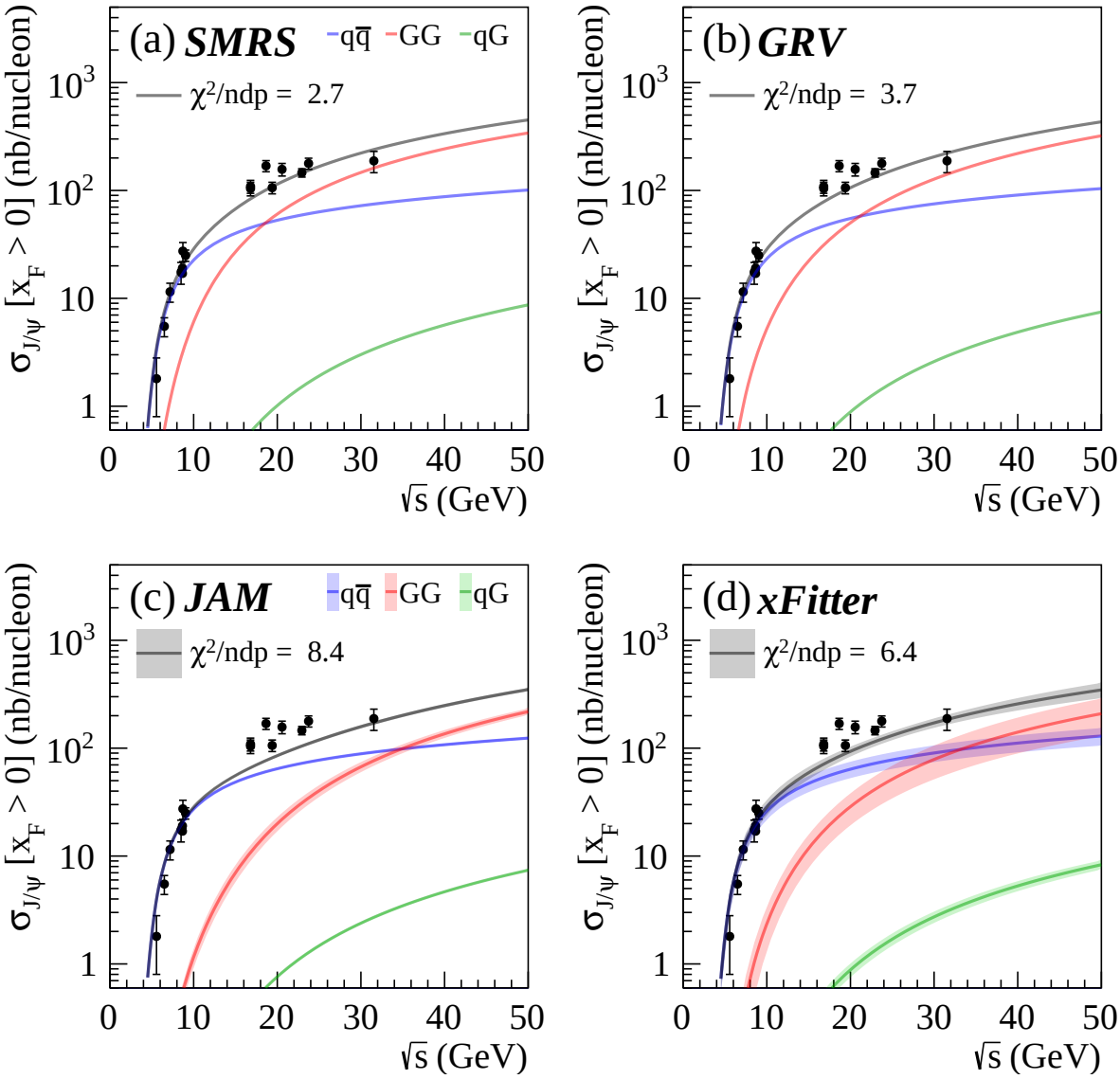

Figure 4.8: *The NRQCD J/ψ production cross sections at $x_F > 0$ for the $\pi^- N$ reactions, calculated for four pion PDFs (SMRS, GRV, JAM and xFitter) using LDMEs of "Fit-2". The black, blue, red, and green curves represent the calculated total cross sections, and the $q\bar{q}$, GG, and qG contributions, respectively. The shaded bands on the xFitter and JAM calculations come from the uncertainties of the corresponding PDF sets. The SMRS and GRV PDFs contain no information on uncertainties.*

Table. 4.4 lists the χ^2 values of NRQCD calculations for various data sets and best-fit CO LDMEs for each pion PDF. We find that the χ^2 of the pion-induced J/ψ data strongly correlates with the gluon density of pions over the valence quark regions [20]. The GG contributions are similar for GRV and SMRS, while those for xFitter and JAM are 50%-80% smaller due to their weaker gluon strength at $x = M(J/\psi)/\sqrt{s} = 0.1 - 0.6$, relative to GRV and SMRS [20]. The lower GG contribution of xFitter and JAM leads to an underestimation of the NRQCD calculations against the data over $\sqrt{s} = 15 - 25$ GeV , as shown in Fig. 4.8.

Table. 4.4 shows that the dependence of the best-fit LDMEs of J/ψ and $\psi(2S)$ to the

	SMRS	GRV	JAM	xFitter
χ^2_{total}/ndf	3.1	3.4	4.8	4.3
$\chi^2/ndp\vert^{\pi^-}_{\sigma(J/\psi)}$	2.7	3.7	8.4	6.4
$\chi^2/ndp\vert^{\pi^-}_{\sigma(\psi(2S))}$	0.4	0.7	0.4	0.2
$\langle \mathscr{O}_8^{J/\psi}[^3S_1]\rangle$	$(6.9 \pm 0.3) \times 10^{-2}$	$(9.5 \pm 0.4) \times 10^{-2}$	$(8.3 \pm 0.3) \times 10^{-2}$	$(7.4 \pm 0.9) \times 10^{-2}$
$\Delta_8^{J/\psi}$	$(2.5 \pm 0.2) \times 10^{-2}$	$(1.8 \pm 0.2) \times 10^{-2}$	$(2.0 \pm 0.2) \times 10^{-2}$	$(2.2 \pm 0.2) \times 10^{-2}$
$\langle \mathscr{O}_8^{\psi(2S)}[^3S_1]\rangle$	$(2.1 \pm 0.4) \times 10^{-2}$	$(2.6 \pm 0.2) \times 10^{-2}$	$(2.6 \pm 0.1) \times 10^{-2}$	$(2.3 \pm 0.4) \times 10^{-2}$
$\Delta_8^{\psi(2S)}$	$(1.7 \pm 1.0) \times 10^{-3}$	$(4.0 \pm 6.2) \times 10^{-4}$	$(3.7 \pm 3.4) \times 10^{-4}$	$(0.9 \pm 6.0) \times 10^{-3}$

Table 4.4: *The χ^2 values for the entire data sets and the individual J/ψ and $\psi(2S)$ data set from the NRQCD calculations. The best-fit LDMEs for each pion PDF are in units of* GeV^3.

pion PDFs is rather mild. We also checked that the overall reduced χ^2/ndf of data for each pion PDF has a very small variation when the calculations are done with the best-fit LDMEs obtained using a different set of pion PDFs.

Summary and Outlook

The internal parton distribution of pion - pion PDF, has been studied since 1980s, however the understand of it is still poorly known after 30 years due to the lack of the rest pion target. The pion-induced Drell-Yan data and the pion-induced J/ψ data serves as tools to probe valance distribution and gluon distribution of pion, respectively. There are three main topics in this thesis including (1) the data analysis of Drell-Yan cross section with 2018 COMPASS data, (2) hardware service of drift chamber in COMPASS, and (3) the phenomenology study of J/ψ production mechanism:

- **Data analysis**

  The fixed-target experiment, COMPASS experiment at CERN, performed the pion-induced Drell-Yan measurement with $190 GeV$ π^- beam collides the polarized ammonia target, alumina target, and tungsten target in 2015 and 2018. In this analysis, only 2018 data is used. The Drell-Yan cross-section as a function of x_F in various $\sqrt{\tau}$ regions help to constrain pion PDF. The COMPASS results are compared with pQCD calculation in NLO, E615 results with 252 GeV π^- beam [21], and NA10 results with 194 GeV π^- beams [22]. COMPASS results shows less than 20% inconsistency compared to the pQCD calculations done with pion PDFs, JAM and xFitter. In the compariosn with NA10 results, COMPASS data shows a consistent result with NA10 data in various $\sqrt{\tau}$ bins. However COMPASS results is larger than E615 results around 10% to 50% in the low $\sqrt{\tau}$ region. The normalization issue between NA10 and E615 was noticed in Ref. [30]. COMPASS data is more in favor of NA10 results. The systematic uncertainties of COMPASS result is around 5%.

  The study of the Drell-Yan cross section as a function of transverse momentum p_T serves as input of pion TMD. The COMPASS Drell-Yan cross-section as a function of p_T in various p_T and $M\mu\mu$ regions. The mean square transverse momentum $< p_T^2 >$ is evaluated and shows the expected outcomes, decreases with x_F and slightly increases $M_{\mu\mu}$. The intrinsic mean square transversed momentum of pion is extracted $< p_T^2 > [(MeV/c)^2] = 0.731 \pm 0.066[(GeV/c)^2]$ from the global pion-induced data. Furthermore, the p_T broadening effect is observed when comparing the $< p_T^2 >$ between PT cells(light target) and W cells(heavy target).

  With the current analysis framework, the J/ψ cross section with is COMPASS 2018 data is expected soon. Furthermore, the nuclear effect with both COMPASS Drell-Yan and J/ψ data will be further studied with the consideration of isoscaler effect of nucleon targets.

- **Hardware service**

  Drift Chamber 05(DC05) is a large-area planar chamber built as an upgrading project of COMPASS II to replace an old Straw Tube chamber. It is a crucial

detector for the track reconstruction in the large angle. In MC study, the reconstruction efficiency in large angle could drop 30% without it. It is a joint project done by University of Illinois in US and Acadamia Sinica in Taiwan responsible for the construction of detector and electronics, respectively.

The active area of DC05 is $249 \times 209 cm^2$. There are 8 planes with 4 kinds of wire orientations. The space between sense wire is around 8mm called one cell. In total, DC05 includes 2304 sense wires and 2312 field wires. There are three kinds of electronics built for DC05, FEM, DCM, and GANDALF modules. FEM is the front-end electronics includes amplifier, discriminator and FPGA-based TDC to digitize the analog signal from chamber to readable signal. DCM is the first-stage multiplexer to collect TDC data from all the FEMs of one layer and sent them to the COMPASS-data-collection module, GANDALF. DCM serves not just as an data collection module for DC05 but also a trigger, clock, and control distributor sent from GANDALF and distributes them to all the FEMs. In total, there are 144 FEMs, 8 DCMs , and 1 GANDALF used for DC05 with 8 planes.

During the developments, there are many issues occurred, such as noise problem, magnetic problem, event scrambling problem, etc. They were solved in the end. After 4 years of the development, from 2012 to 2016, DC05 was built and serves in COMPASS starting from 2016. The performance of DC05 at working condition, high voltage = -1675V and threshold at 6fC, gives the efficiency 86.7±0.09% and position resolution around $373.54 \mu m$.

- **Phenomenology study**

  In the past LDMEs extraction [93] [96], only the proton-induced data were used. The past LDME data set can't well described the pion-induced J/ψ data. To improve the LDMEs adopted to the pion-induced data, the study of the J/ψ and $\psi(2S)$ hadronic production data in fixed-target experiments within the framework of NLO NRQCD are performed with a simultaneous fit to both proton- and pion-induced data in this analysis to obtained a new set of LDMEs. The advantage of using pion-induced data, especially at low energies, is to have a great $q\bar{q}$ contribution and thus provide a strong constraint on one of the element $\langle \mathcal{O}_8^H[^3S_1] \rangle$ of LDMEs. The sensitivity is much reduced if the analysis is restricted to the proton-induced data alone.

  A new set of LDMEs for J/ψ and $\psi(2S)$ production at fixed-target energies has been obtained in an analysis of data with proton and pion beams in the range of $\sqrt{s} = [5, 50](GeV)$. In the comparison with the LDMEs of Ref. [93], the element $\langle \mathcal{O}_8^H[^3S_1] \rangle$ values of LDMEs for both J/ψ and $\psi(2S)$ are found to be about ∼10 times larger. In contrast, the element Δ_8^H of LDMEs, partly responsible for the GG contribution, are compatible for J/ψ but more than 10 times smaller for $\psi(2S)$.

  SMRS [15], GRV [13], JAM [16], xFitter [18] are the mostly used pion PDF sets, however a sizable difference are found in the gluon distribution between them - the gluon composition inside pion is higher for SMRS and GRV compare to JAM and xFitter. Since the J/ψ is sensitive to the gluon distribution of pion, the new LDMEs combined with four different pion PDFs were used to compare with the NRQCD calculation with the pion-induced J/ψ production cross-sections. It is found that a pronounced differences between the predicted individual quark-antiquark annihilation and gluon-gluon fusion terms of the J/ψ productions result from the different

shapes and magnitudes of the corresponding PDF parametrizations. When compared to the total cross section, the SMRS or GRV PDFs still provide a slightly better description of the data than JAM or xFitter, suggesting that the pion-induced data favor those PDFs with larger gluon contents at medium and large Bjorken-x_π. All these results are in line with the earlier findings [20] obtained with the CEM model.

Appendix

Numerical values of 1D cross-section

Table 4.5: *Numerical values of 1D cross-section :* $d\sigma/dM_{\mu\mu}$

$d\sigma/dM_{\mu\mu}$ **: mean ± statistic ± systematic (nb/GeV/nucleon)**			
Kinematics $M_{\mu\mu}(GeV)$	PT 2 cells	Al cell	W 2 cells
$M_{\mu\mu}$ = [4.300, 4.700]	0.1442 ± 0.0014 ± 0.0021	0.1453 ± 0.0036 ± 0.0043	-
$M_{\mu\mu}$ = [4.700, 5.100]	0.0936 ± 0.0011 ± 0.0014	0.0895 ± 0.0027 ± 0.0000	0.0828 ± 0.0009 ± 0.0017
$M_{\mu\mu}$ = [5.100, 5.500]	0.0636 ± 0.0009 ± 0.0010	0.0628 ± 0.0022 ± 0.0000	0.0524 ± 0.0007 ± 0.0013
$M_{\mu\mu}$ = [5.500, 5.900]	0.0441 ± 0.0008 ± 0.0008	0.0368 ± 0.0016 ± 0.0022	0.0359 ± 0.0006 ± 0.0011
$M_{\mu\mu}$ = [5.900, 6.300]	0.0311 ± 0.0006 ± 0.0000	0.0264 ± 0.0014 ± 0.0000	0.0249 ± 0.0005 ± 0.0008
$M_{\mu\mu}$ = [6.300, 6.700]	0.0217 ± 0.0005 ± 0.0006	0.0189 ± 0.0011 ± 0.0014	0.0172 ± 0.0004 ± 0.0005
$M_{\mu\mu}$ = [6.700, 7.100]	0.0164 ± 0.0005 ± 0.0000	0.0140 ± 0.0010 ± 0.0000	0.0118 ± 0.0003 ± 0.0005
$M_{\mu\mu}$ = [7.100, 7.500]	0.0108 ± 0.0004 ± 0.0004	0.0082 ± 0.0007 ± 0.0010	0.0090 ± 0.0003 ± 0.0004
$M_{\mu\mu}$ = [7.500, 7.900]	0.0079 ± 0.0003 ± 0.0000	0.0064 ± 0.0007 ± 0.0000	0.0062 ± 0.0003 ± 0.0003
$M_{\mu\mu}$ = [7.900, 8.500]	0.0058 ± 0.0002 ± 0.0000	0.0046 ± 0.0005 ± 0.0000	0.0043 ± 0.0002 ± 0.0002

Table 4.6: *Numerical values of 1D cross-section :* $d\sigma/d\sqrt{\tau}$

$d\sigma/d\sqrt{\tau}$ **: mean ± statistic ± systematic (nb/nucleon)**			
Kinematics $\sqrt{\tau}$	PT 2 cells	Al cell	W 2 cells
$\sqrt{\tau}$ = [0.228, 0.249]	2.6206 ± 0.0259 ± 0.0373	2.6362 ± 0.0650 ± 0.0784	-
$\sqrt{\tau}$ = [0.249, 0.270]	1.7498 ± 0.0212 ± 0.0263	1.6766 ± 0.0510 ± 0.0000	1.4917 ± 0.0171 ± 0.0300
$\sqrt{\tau}$ = [0.270, 0.291]	1.1904 ± 0.0173 ± 0.0190	1.1808 ± 0.0415 ± 0.0000	0.9851 ± 0.0138 ± 0.0241
$\sqrt{\tau}$ = [0.291, 0.312]	0.8261 ± 0.0143 ± 0.0158	0.6876 ± 0.0306 ± 0.0405	0.6791 ± 0.0114 ± 0.0207
$\sqrt{\tau}$ = [0.312, 0.333]	0.5813 ± 0.0120 ± 0.0000	0.4954 ± 0.0256 ± 0.0000	0.4675 ± 0.0094 ± 0.0152
$\sqrt{\tau}$ = [0.333, 0.354]	0.4045 ± 0.0100 ± 0.0121	0.3533 ± 0.0213 ± 0.0257	0.3245 ± 0.0078 ± 0.0094
$\sqrt{\tau}$ = [0.354, 0.376]	0.3050 ± 0.0088 ± 0.0000	0.2617 ± 0.0185 ± 0.0000	0.2250 ± 0.0065 ± 0.0089
$\sqrt{\tau}$ = [0.376, 0.397]	0.2022 ± 0.0071 ± 0.0073	0.1518 ± 0.0137 ± 0.0187	0.1653 ± 0.0056 ± 0.0070
$\sqrt{\tau}$ = [0.397, 0.418]	0.1473 ± 0.0061 ± 0.0000	0.1209 ± 0.0124 ± 0.0000	0.1176 ± 0.0047 ± 0.0054
$\sqrt{\tau}$ = [0.418, 0.450]	0.1014 ± 0.0040 ± 0.0000	0.0818 ± 0.0081 ± 0.0000	0.0783 ± 0.0031 ± 0.0032

Table 4.7: *Numerical values of 1D cross-section : $d\sigma/dp_T$*

$d\sigma/dp_T$: **mean ± statistic ± systematic (nb/GeV/nucleon)**			
Kinematics p_T	PT 2 cells	Al cell	W 2 cells
p_T = [0.000, 0.300]	0.0364 ± 0.0008 ± 0.0000	0.0330 ± 0.0019 ± 0.0023	0.0179 ± 0.0005 ± 0.0008
p_T = [0.300, 0.600]	0.0969 ± 0.0013 ± 0.0018	0.0858 ± 0.0031 ± 0.0035	0.0494 ± 0.0009 ± 0.0014
p_T = [0.600, 0.900]	0.1194 ± 0.0015 ± 0.0017	0.1176 ± 0.0036 ± 0.0000	0.0650 ± 0.0010 ± 0.0019
p_T = [0.900, 1.200]	0.1124 ± 0.0014 ± 0.0018	0.1050 ± 0.0034 ± 0.0000	0.0617 ± 0.0009 ± 0.0017
p_T = [1.200, 1.500]	0.0886 ± 0.0013 ± 0.0000	0.0855 ± 0.0030 ± 0.0030	0.0502 ± 0.0008 ± 0.0010
p_T = [1.500, 1.800]	0.0600 ± 0.0011 ± 0.0011	0.0538 ± 0.0023 ± 0.0000	0.0352 ± 0.0007 ± 0.0008
p_T = [1.800, 2.100]	0.0344 ± 0.0008 ± 0.0000	0.0320 ± 0.0017 ± 0.0000	0.0227 ± 0.0005 ± 0.0000
p_T = [2.100, 2.400]	0.0193 ± 0.0006 ± 0.0000	0.0186 ± 0.0013 ± 0.0013	0.0131 ± 0.0004 ± 0.0000
p_T = [2.400, 2.700]	0.0107 ± 0.0004 ± 0.0000	0.0101 ± 0.0009 ± 0.0000	0.0068 ± 0.0003 ± 0.0003
p_T = [2.700, 3.000]	0.0062 ± 0.0003 ± 0.0000	0.0055 ± 0.0007 ± 0.0008	0.0034 ± 0.0002 ± 0.0000
p_T = [3.000, 3.600]	0.0023 ± 0.0001 ± 0.0002	0.0022 ± 0.0003 ± 0.0000	0.0014 ± 0.0001 ± 0.0001

Table 4.8: *Numerical values of 1D cross-section : $d\sigma/dx_\pi$*

$d\sigma/dx_\pi$: **mean ± statistic ± systematic (nb/nucleon)**			
Kinematics	PT 2 cells	Al cell	W 2 cells
x_π = [0.000, 0.100]	0.0000 ± 0.0000 ± 0.0000	0.0000 ± 0.0000 ± 0.0000	0.0000 ± 0.0000 ± 0.0000
x_π = [0.100, 0.200]	0.0164 ± 0.0026 ± 0.0000	0.0191 ± 0.0060 ± 0.0000	0.0000 ± 0.0000 ± 0.0000
x_π = [0.200, 0.300]	0.3612 ± 0.0068 ± 0.0079	0.3169 ± 0.0136 ± 0.0150	0.1657 ± 0.0041 ± 0.0048
x_π = [0.300, 0.400]	0.4207 ± 0.0055 ± 0.0078	0.3919 ± 0.0123 ± 0.0126	0.2541 ± 0.0041 ± 0.0055
x_π = [0.400, 0.500]	0.3328 ± 0.0040 ± 0.0049	0.3224 ± 0.0094 ± 0.0000	0.2092 ± 0.0029 ± 0.0056
x_π = [0.500, 0.600]	0.2541 ± 0.0032 ± 0.0044	0.2401 ± 0.0075 ± 0.0000	0.1513 ± 0.0022 ± 0.0039
x_π = [0.600, 0.700]	0.1855 ± 0.0026 ± 0.0028	0.1721 ± 0.0064 ± 0.0088	0.1104 ± 0.0018 ± 0.0025
x_π = [0.700, 0.800]	0.1180 ± 0.0021 ± 0.0025	0.1059 ± 0.0051 ± 0.0073	0.0732 ± 0.0014 ± 0.0020
x_π = [0.800, 1.000]	0.0438 ± 0.0010 ± 0.0000	0.0483 ± 0.0026 ± 0.0000	0.0253 ± 0.0006 ± 0.0008

Table 4.9: *Numerical values of 1D cross-section : $d\sigma/dx_N$*

$d\sigma/dx_N$: **mean ± statistic ± systematic (nb/nucleon)**			
Kinematics x_N	PT 2 cells	Al cell	W 2 cells
x_N = [0.000, 0.050]	0.0000 ± 0.0000 ± 0.0000	0.0000 ± 0.0000 ± 0.0000	0.0000 ± 0.0000 ± 0.0000
x_N = [0.050, 0.100]	0.3803 ± 0.0057 ± 0.0000	0.4076 ± 0.0160 ± 0.0198	0.1129 ± 0.0027 ± 0.0032
x_N = [0.100, 0.150]	0.8131 ± 0.0079 ± 0.0097	0.7940 ± 0.0198 ± 0.0224	0.3860 ± 0.0047 ± 0.0076
x_N = [0.150, 0.200]	0.8051 ± 0.0089 ± 0.0132	0.7546 ± 0.0206 ± 0.0241	0.4607 ± 0.0056 ± 0.0113
x_N = [0.200, 0.250]	0.6761 ± 0.0096 ± 0.0112	0.6166 ± 0.0207 ± 0.0209	0.4164 ± 0.0062 ± 0.0109
x_N = [0.250, 0.300]	0.5206 ± 0.0102 ± 0.0130	0.4574 ± 0.0207 ± 0.0243	0.3419 ± 0.0067 ± 0.0107
x_N = [0.300, 0.350]	0.2368 ± 0.0074 ± 0.0000	0.1856 ± 0.0139 ± 0.0000	0.2033 ± 0.0059 ± 0.0060
x_N = [0.350, 0.400]	0.0850 ± 0.0045 ± 0.0000	0.0755 ± 0.0089 ± 0.0000	0.0719 ± 0.0037 ± 0.0000
x_N = [0.400, 0.450]	0.0315 ± 0.0030 ± 0.0000	0.0208 ± 0.0052 ± 0.0000	0.0220 ± 0.0022 ± 0.0000
x_N = [0.450, 0.600]	0.0038 ± 0.0010 ± 0.0000	0.0000 ± 0.0000 ± 0.0000	0.0019 ± 0.0005 ± 0.0000

Table 4.10: *Numerical values of 1D cross-section : $d\sigma/dx_F$*

$d\sigma/dx_F$ **: mean ± statistic ± systematic (nb/nucleon)**			
Kinematics x_F	PT 2 cells	Al cell	W 2 cells
x_F = [-0.100, 0.000]	0.2459 ± 0.0066 ± 0.0070	0.2163 ± 0.0124 ± 0.0151	0.1353 ± 0.0040 ± 0.0041
x_F = [0.000, 0.100]	0.2770 ± 0.0051 ± 0.0053	0.2396 ± 0.0106 ± 0.0000	0.1686 ± 0.0036 ± 0.0045
x_F = [0.100, 0.200]	0.2829 ± 0.0044 ± 0.0062	0.2488 ± 0.0099 ± 0.0104	0.1686 ± 0.0032 ± 0.0000
x_F = [0.200, 0.300]	0.2512 ± 0.0035 ± 0.0050	0.2527 ± 0.0081 ± 0.0083	0.1461 ± 0.0023 ± 0.0043
x_F = [0.300, 0.400]	0.2209 ± 0.0030 ± 0.0033	0.2100 ± 0.0071 ± 0.0081	0.1248 ± 0.0020 ± 0.0033
x_F = [0.400, 0.500]	0.1807 ± 0.0026 ± 0.0034	0.1703 ± 0.0063 ± 0.0077	0.1006 ± 0.0017 ± 0.0028
x_F = [0.500, 0.600]	0.1416 ± 0.0023 ± 0.0000	0.1318 ± 0.0057 ± 0.0061	0.0794 ± 0.0015 ± 0.0019
x_F = [0.600, 0.700]	0.0964 ± 0.0019 ± 0.0024	0.0916 ± 0.0048 ± 0.0049	0.0539 ± 0.0012 ± 0.0016
x_F = [0.700, 0.900]	0.0418 ± 0.0010 ± 0.0010	0.0478 ± 0.0027 ± 0.0000	0.0213 ± 0.0006 ± 0.0008

Numerical values of 2D cross-section in x_F and $\sqrt{\tau}$

Table 4.11: *Numerical values of 2D cross-section : $d^2\sigma/d\sqrt{\tau}dx_F$(1)*

$d^2\sigma/d\sqrt{\tau}dx_F$: **mean ± statistic ± systematic (nb/nucleon)**			
Kinematics in $\sqrt{\tau}$ and x_F	PT 2 cells	Al cell	W 2 cells
$\sqrt{\tau}$ = [0.231, 0.254] , x_F = [-0.1, 0.0]	3.5386 ± 0.1706 ± 0.1930	2.6489 ± 0.2888 ± 0.4346	-
$\sqrt{\tau}$ = [0.231, 0.254] , x_F = [0.0, 0.1]	3.8853 ± 0.1258 ± 0.0000	3.6830 ± 0.2745 ± 0.0000	-
$\sqrt{\tau}$ = [0.231, 0.254] , x_F = [0.1, 0.2]	3.9488 ± 0.1087 ± 0.0000	3.6911 ± 0.2542 ± 0.0000	-
$\sqrt{\tau}$ = [0.231, 0.254] , x_F = [0.2, 0.3]	3.4543 ± 0.0830 ± 0.0874	3.5573 ± 0.2010 ± 0.0000	-
$\sqrt{\tau}$ = [0.231, 0.254] , x_F = [0.3, 0.4]	2.9171 ± 0.0705 ± 0.0000	2.8048 ± 0.1755 ± 0.1969	-
$\sqrt{\tau}$ = [0.231, 0.254] , x_F = [0.4, 0.5]	2.3063 ± 0.0604 ± 0.0722	2.2878 ± 0.1622 ± 0.0000	-
$\sqrt{\tau}$ = [0.231, 0.254] , x_F = [0.5, 0.6]	1.8343 ± 0.0548 ± 0.0000	1.5914 ± 0.1451 ± 0.2444	-
$\sqrt{\tau}$ = [0.231, 0.254] , x_F = [0.6, 0.7]	1.2448 ± 0.0469 ± 0.0000	1.5198 ± 0.1413 ± 0.0000	-
$\sqrt{\tau}$ = [0.231, 0.254] , x_F = [0.7, 0.8]	0.7905 ± 0.0409 ± 0.0000	0.6925 ± 0.1064 ± 0.1352	-
$\sqrt{\tau}$ = [0.231, 0.254] , x_F = [0.8, 0.9]	0.3890 ± 0.0294 ± 0.0000	0.5609 ± 0.1098 ± 0.0000	-
$\sqrt{\tau}$ = [0.254, 0.277] , x_F = [-0.1, 0.0]	2.2841 ± 0.1344 ± 0.1412	2.1764 ± 0.2684 ± 0.0000	1.9512 ± 0.0983 ± 0.0000
$\sqrt{\tau}$ = [0.254, 0.277] , x_F = [0.0, 0.1]	2.4011 ± 0.0986 ± 0.0000	2.1931 ± 0.2146 ± 0.0000	2.2408 ± 0.0836 ± 0.0991
$\sqrt{\tau}$ = [0.254, 0.277] , x_F = [0.1, 0.2]	2.5996 ± 0.0882 ± 0.1029	2.0288 ± 0.1838 ± 0.1950	2.3524 ± 0.0781 ± 0.0000
$\sqrt{\tau}$ = [0.254, 0.277] , x_F = [0.2, 0.3]	2.0568 ± 0.0643 ± 0.0789	2.2168 ± 0.1590 ± 0.1655	1.9285 ± 0.0543 ± 0.0666
$\sqrt{\tau}$ = [0.254, 0.277] , x_F = [0.3, 0.4]	1.8888 ± 0.0568 ± 0.0000	1.7105 ± 0.1337 ± 0.1360	1.6117 ± 0.0459 ± 0.0484
$\sqrt{\tau}$ = [0.254, 0.277] , x_F = [0.4, 0.5]	1.5374 ± 0.0493 ± 0.0000	1.5224 ± 0.1282 ± 0.0000	1.2121 ± 0.0393 ± 0.0481
$\sqrt{\tau}$ = [0.254, 0.277] , x_F = [0.5, 0.6]	1.1752 ± 0.0425 ± 0.0438	1.0277 ± 0.1035 ± 0.0000	1.0167 ± 0.0359 ± 0.0000
$\sqrt{\tau}$ = [0.254, 0.277] , x_F = [0.6, 0.7]	0.8362 ± 0.0368 ± 0.0371	0.6980 ± 0.0927 ± 0.0000	0.7512 ± 0.0309 ± 0.0000
$\sqrt{\tau}$ = [0.254, 0.277] , x_F = [0.7, 0.8]	0.4839 ± 0.0309 ± 0.0000	0.4200 ± 0.0740 ± 0.0802	0.4516 ± 0.0243 ± 0.0000
$\sqrt{\tau}$ = [0.254, 0.277] , x_F = [0.8, 0.9]	0.2323 ± 0.0215 ± 0.0000	0.2976 ± 0.0635 ± 0.0000	0.2050 ± 0.0170 ± 0.0000
$\sqrt{\tau}$ = [0.277, 0.300] , x_F = [-0.1, 0.0]	1.2674 ± 0.0963 ± 0.0000	1.0677 ± 0.1734 ± 0.0000	1.1500 ± 0.0742 ± 0.0000
$\sqrt{\tau}$ = [0.277, 0.300] , x_F = [0.0, 0.1]	1.5015 ± 0.0779 ± 0.0000	1.3798 ± 0.1668 ± 0.0000	1.4649 ± 0.0687 ± 0.0000
$\sqrt{\tau}$ = [0.277, 0.300] , x_F = [0.1, 0.2]	1.4707 ± 0.0659 ± 0.0688	1.5276 ± 0.1594 ± 0.1797	1.3923 ± 0.0599 ± 0.0000
$\sqrt{\tau}$ = [0.277, 0.300] , x_F = [0.2, 0.3]	1.3102 ± 0.0519 ± 0.0602	1.4146 ± 0.1247 ± 0.0000	1.1793 ± 0.0421 ± 0.0585
$\sqrt{\tau}$ = [0.277, 0.300] , x_F = [0.3, 0.4]	1.2757 ± 0.0469 ± 0.0469	1.0070 ± 0.0996 ± 0.1267	1.0595 ± 0.0376 ± 0.0413
$\sqrt{\tau}$ = [0.277, 0.300] , x_F = [0.4, 0.5]	1.0384 ± 0.0405 ± 0.0462	0.8771 ± 0.0920 ± 0.1137	0.8485 ± 0.0323 ± 0.0374
$\sqrt{\tau}$ = [0.277, 0.300] , x_F = [0.5, 0.6]	0.8230 ± 0.0351 ± 0.0000	0.7601 ± 0.0914 ± 0.0000	0.6210 ± 0.0276 ± 0.0000
$\sqrt{\tau}$ = [0.277, 0.300] , x_F = [0.6, 0.7]	0.5516 ± 0.0288 ± 0.0289	0.4330 ± 0.0716 ± 0.0000	0.4057 ± 0.0220 ± 0.0230
$\sqrt{\tau}$ = [0.277, 0.300] , x_F = [0.7, 0.8]	0.3571 ± 0.0265 ± 0.0000	0.4355 ± 0.0753 ± 0.0000	0.2599 ± 0.0178 ± 0.0226
$\sqrt{\tau}$ = [0.277, 0.300] , x_F = [0.8, 0.9]	0.1197 ± 0.0150 ± 0.0181	0.1401 ± 0.0379 ± 0.0000	0.0942 ± 0.0106 ± 0.0000
$\sqrt{\tau}$ = [0.323, 0.346] , x_F = [-0.1, 0.0]	0.4751 ± 0.0578 ± 0.0000	0.7132 ± 0.1598 ± 0.0000	0.4117 ± 0.0467 ± 0.0000
$\sqrt{\tau}$ = [0.323, 0.346] , x_F = [0.0, 0.1]	0.7041 ± 0.0538 ± 0.0552	0.5282 ± 0.1178 ± 0.0000	0.6073 ± 0.0448 ± 0.0000
$\sqrt{\tau}$ = [0.323, 0.346] , x_F = [0.1, 0.2]	0.6779 ± 0.0452 ± 0.0547	0.4430 ± 0.0852 ± 0.0000	0.6330 ± 0.0408 ± 0.0000
$\sqrt{\tau}$ = [0.323, 0.346] , x_F = [0.2, 0.3]	0.6610 ± 0.0374 ± 0.0413	0.5830 ± 0.0810 ± 0.0000	0.5290 ± 0.0292 ± 0.0000
$\sqrt{\tau}$ = [0.323, 0.346] , x_F = [0.3, 0.4]	0.6000 ± 0.0330 ± 0.0354	0.4333 ± 0.0634 ± 0.0662	0.4489 ± 0.0242 ± 0.0298
$\sqrt{\tau}$ = [0.323, 0.346] , x_F = [0.4, 0.5]	0.5078 ± 0.0283 ± 0.0000	0.4187 ± 0.0627 ± 0.0631	0.4020 ± 0.0219 ± 0.0000
$\sqrt{\tau}$ = [0.323, 0.346] , x_F = [0.5, 0.6]	0.3358 ± 0.0221 ± 0.0000	0.3384 ± 0.0556 ± 0.0597	0.2896 ± 0.0184 ± 0.0190
$\sqrt{\tau}$ = [0.323, 0.346] , x_F = [0.6, 0.7]	0.2478 ± 0.0192 ± 0.0000	0.2355 ± 0.0507 ± 0.0000	0.2204 ± 0.0165 ± 0.0000
$\sqrt{\tau}$ = [0.323, 0.346] , x_F = [0.7, 0.8]	0.1158 ± 0.0150 ± 0.0185	0.1730 ± 0.0509 ± 0.0000	0.1104 ± 0.0117 ± 0.0000
$\sqrt{\tau}$ = [0.323, 0.346] , x_F = [0.8, 0.9]	0.0545 ± 0.0114 ± 0.0000	0.0982 ± 0.0484 ± 0.0000	0.0289 ± 0.0056 ± 0.0000

Table 4.12: *Numerical values of 2D cross-section : $d^2\sigma/d\sqrt{\tau}dx_F$(2)*

$d^2\sigma/d\sqrt{\tau}dx_F$: **mean ± statistic ± systematic (nb/nucleon)**			
Kinematics in $\sqrt{\tau}$ and x_F	PT 2 cells	Al cell	W 2 cells
$\sqrt{\tau}$ = [0.346, 0.369] , x_F = [-0.1, 0.0]	0.2497 ± 0.0426 ± 0.0000	0.4020 ± 0.1209 ± 0.0000	0.2607 ± 0.0369 ± 0.0000
$\sqrt{\tau}$ = [0.346, 0.369] , x_F = [0.0, 0.1]	0.4260 ± 0.0426 ± 0.0432	0.3599 ± 0.0915 ± 0.0000	0.4011 ± 0.0375 ± 0.0000
$\sqrt{\tau}$ = [0.346, 0.369] , x_F = [0.1, 0.2]	0.5196 ± 0.0397 ± 0.0419	0.3740 ± 0.0789 ± 0.0000	0.4006 ± 0.0317 ± 0.0000
$\sqrt{\tau}$ = [0.346, 0.369] , x_F = [0.2, 0.3]	0.4780 ± 0.0332 ± 0.0366	0.4388 ± 0.0753 ± 0.0000	0.3749 ± 0.0251 ± 0.0290
$\sqrt{\tau}$ = [0.346, 0.369] , x_F = [0.3, 0.4]	0.3949 ± 0.0273 ± 0.0000	0.4558 ± 0.0726 ± 0.0778	0.3400 ± 0.0218 ± 0.0000
$\sqrt{\tau}$ = [0.346, 0.369] , x_F = [0.4, 0.5]	0.3519 ± 0.0239 ± 0.0000	0.3365 ± 0.0553 ± 0.0000	0.2580 ± 0.0174 ± 0.0000
$\sqrt{\tau}$ = [0.346, 0.369] , x_F = [0.5, 0.6]	0.2651 ± 0.0199 ± 0.0000	0.2618 ± 0.0502 ± 0.0000	0.2228 ± 0.0162 ± 0.0000
$\sqrt{\tau}$ = [0.346, 0.369] , x_F = [0.6, 0.7]	0.1703 ± 0.0157 ± 0.0176	0.2254 ± 0.0607 ± 0.0000	0.1572 ± 0.0136 ± 0.0000
$\sqrt{\tau}$ = [0.346, 0.369] , x_F = [0.7, 0.8]	0.1202 ± 0.0165 ± 0.0000	0.0987 ± 0.0354 ± 0.0000	0.0562 ± 0.0085 ± 0.0000
$\sqrt{\tau}$ = [0.346, 0.369] , x_F = [0.8, 0.9]	0.0440 ± 0.0132 ± 0.0000	0.0000 ± 0.0000 ± 0.0000	0.0272 ± 0.0065 ± 0.0000
$\sqrt{\tau}$ = [0.369, 0.392] , x_F = [-0.1, 0.0]	0.2772 ± 0.0453 ± 0.0000	0.3593 ± 0.1455 ± 0.0000	0.1704 ± 0.0300 ± 0.0000
$\sqrt{\tau}$ = [0.369, 0.392] , x_F = [0.0, 0.1]	0.3366 ± 0.0381 ± 0.0404	0.3723 ± 0.0863 ± 0.0000	0.2959 ± 0.0329 ± 0.0340
$\sqrt{\tau}$ = [0.369, 0.392] , x_F = [0.1, 0.2]	0.2767 ± 0.0293 ± 0.0331	0.3423 ± 0.0968 ± 0.0000	0.2622 ± 0.0264 ± 0.0295
$\sqrt{\tau}$ = [0.369, 0.392] , x_F = [0.2, 0.3]	0.3316 ± 0.0283 ± 0.0000	0.4275 ± 0.0772 ± 0.0000	0.2433 ± 0.0212 ± 0.0000
$\sqrt{\tau}$ = [0.369, 0.392] , x_F = [0.3, 0.4]	0.2729 ± 0.0223 ± 0.0000	0.2786 ± 0.0609 ± 0.0000	0.2138 ± 0.0177 ± 0.0000
$\sqrt{\tau}$ = [0.369, 0.392] , x_F = [0.4, 0.5]	0.2309 ± 0.0192 ± 0.0000	0.2356 ± 0.0555 ± 0.0000	0.1716 ± 0.0149 ± 0.0162
$\sqrt{\tau}$ = [0.369, 0.392] , x_F = [0.5, 0.6]	0.1747 ± 0.0166 ± 0.0000	0.2247 ± 0.0616 ± 0.0000	0.1675 ± 0.0141 ± 0.0000
$\sqrt{\tau}$ = [0.369, 0.392] , x_F = [0.6, 0.7]	0.1378 ± 0.0154 ± 0.0000	0.1802 ± 0.0554 ± 0.0000	0.0915 ± 0.0108 ± 0.0000
$\sqrt{\tau}$ = [0.369, 0.392] , x_F = [0.7, 0.8]	0.0795 ± 0.0136 ± 0.0000	0.1326 ± 0.0472 ± 0.0000	0.0545 ± 0.0083 ± 0.0000
$\sqrt{\tau}$ = [0.369, 0.392] , x_F = [0.8, 0.9]	0.0239 ± 0.0110 ± 0.0000	0.0000 ± 0.0000 ± 0.0000	0.0135 ± 0.0071 ± 0.0000
$\sqrt{\tau}$ = [0.392, 0.415] , x_F = [-0.1, 0.0]	0.2315 ± 0.0484 ± 0.0000	0.3762 ± 0.1623 ± 0.0000	0.1356 ± 0.0327 ± 0.0000
$\sqrt{\tau}$ = [0.392, 0.415] , x_F = [0.0, 0.1]	0.1832 ± 0.0281 ± 0.0283	0.2144 ± 0.1055 ± 0.0000	0.1913 ± 0.0272 ± 0.0000
$\sqrt{\tau}$ = [0.392, 0.415] , x_F = [0.1, 0.2]	0.2321 ± 0.0285 ± 0.0298	0.2499 ± 0.0872 ± 0.0000	0.2110 ± 0.0243 ± 0.0000
$\sqrt{\tau}$ = [0.392, 0.415] , x_F = [0.2, 0.3]	0.2385 ± 0.0243 ± 0.0283	0.3054 ± 0.0771 ± 0.0000	0.1690 ± 0.0178 ± 0.0000
$\sqrt{\tau}$ = [0.392, 0.415] , x_F = [0.3, 0.4]	0.2287 ± 0.0230 ± 0.0000	0.2696 ± 0.0684 ± 0.0000	0.1701 ± 0.0161 ± 0.0000
$\sqrt{\tau}$ = [0.392, 0.415] , x_F = [0.4, 0.5]	0.1640 ± 0.0168 ± 0.0000	0.2662 ± 0.0731 ± 0.0000	0.1335 ± 0.0134 ± 0.0000
$\sqrt{\tau}$ = [0.392, 0.415] , x_F = [0.5, 0.6]	0.1260 ± 0.0152 ± 0.0000	0.1146 ± 0.0491 ± 0.0000	0.0909 ± 0.0107 ± 0.0112
$\sqrt{\tau}$ = [0.392, 0.415] , x_F = [0.6, 0.7]	0.0941 ± 0.0123 ± 0.0000	0.1639 ± 0.0517 ± 0.0000	0.0667 ± 0.0096 ± 0.0000
$\sqrt{\tau}$ = [0.392, 0.415] , x_F = [0.7, 0.8]	0.0667 ± 0.0142 ± 0.0000	0.1218 ± 0.0566 ± 0.0669	0.0496 ± 0.0100 ± 0.0000
$\sqrt{\tau}$ = [0.392, 0.415] , x_F = [0.8, 0.9]	0.0000 ± 0.0000 ± 0.0000	0.0000 ± 0.0000 ± 0.0000	0.0246 ± 0.0246 ± 0.0000
$\sqrt{\tau}$ = [0.415, 0.438] , x_F = [-0.1, 0.0]	0.1842 ± 0.0413 ± 0.0000	0.5685 ± 0.2847 ± 0.0000	0.1224 ± 0.0321 ± 0.0000
$\sqrt{\tau}$ = [0.415, 0.438] , x_F = [0.0, 0.1]	0.1819 ± 0.0297 ± 0.0000	0.2325 ± 0.1646 ± 0.0000	0.1291 ± 0.0215 ± 0.0000
$\sqrt{\tau}$ = [0.415, 0.438] , x_F = [0.1, 0.2]	0.1890 ± 0.0243 ± 0.0000	0.1974 ± 0.0683 ± 0.0000	0.1362 ± 0.0204 ± 0.0000
$\sqrt{\tau}$ = [0.415, 0.438] , x_F = [0.2, 0.3]	0.1374 ± 0.0191 ± 0.0000	0.1723 ± 0.0531 ± 0.0000	0.1416 ± 0.0176 ± 0.0000
$\sqrt{\tau}$ = [0.415, 0.438] , x_F = [0.3, 0.4]	0.1553 ± 0.0188 ± 0.0000	0.2645 ± 0.0602 ± 0.0000	0.1205 ± 0.0141 ± 0.0000
$\sqrt{\tau}$ = [0.415, 0.438] , x_F = [0.4, 0.5]	0.1423 ± 0.0169 ± 0.0000	0.1644 ± 0.0580 ± 0.0000	0.1185 ± 0.0131 ± 0.0000
$\sqrt{\tau}$ = [0.415, 0.438] , x_F = [0.5, 0.6]	0.0832 ± 0.0125 ± 0.0000	0.1572 ± 0.0883 ± 0.0000	0.0697 ± 0.0097 ± 0.0000
$\sqrt{\tau}$ = [0.415, 0.438] , x_F = [0.6, 0.7]	0.0706 ± 0.0138 ± 0.0000	0.1618 ± 0.1093 ± 0.0000	0.0710 ± 0.0102 ± 0.0000
$\sqrt{\tau}$ = [0.415, 0.438] , x_F = [0.7, 0.8]	0.0356 ± 0.0123 ± 0.0000	0.0000 ± 0.0000 ± 0.0000	0.0266 ± 0.0093 ± 0.0000
$\sqrt{\tau}$ = [0.415, 0.438] , x_F = [0.8, 0.9]	0.0000 ± 0.0000 ± 0.0000	0.0000 ± 0.0000 ± 0.0000	0.0000 ± 0.0000 ± 0.0000

Numerical values of 2D cross-section in x_F and p_T

Table 4.13: *Numerical values of 2D cross-section : $d^2\sigma/dp_T dx_F$(1).*

$d^2\sigma/dp_T dx_F$: **mean ± statistic ± systematic (nb/GeV/nucleon)**			
Kinematics in x_F and p_T	PT 2 cells	Al cell	W 2 cells
x_F = [-0.1, 0.0] ,p_T = [0.0, 0.2]	0.0407 ± 0.0058 ± 0.0000	0.0430 ± 0.0120 ± 0.0000	0.0176 ± 0.0032 ± 0.0000
x_F = [-0.1, 0.0] ,p_T = [0.2, 0.5]	0.1034 ± 0.0087 ± 0.0000	0.1008 ± 0.0185 ± 0.0000	0.0556 ± 0.0052 ± 0.0000
x_F = [-0.1, 0.0] ,p_T = [0.5, 0.8]	0.1586 ± 0.0108 ± 0.0119	0.1492 ± 0.0211 ± 0.0226	0.0818 ± 0.0063 ± 0.0066
x_F = [-0.1, 0.0] ,p_T = [0.8, 1.0]	0.1554 ± 0.0107 ± 0.0122	0.1110 ± 0.0179 ± 0.0244	0.0821 ± 0.0064 ± 0.0079
x_F = [-0.1, 0.0] ,p_T = [1.0, 1.2]	0.1212 ± 0.0095 ± 0.0112	0.1218 ± 0.0189 ± 0.0239	0.0819 ± 0.0063 ± 0.0000
x_F = [-0.1, 0.0] ,p_T = [1.2, 1.5]	0.1198 ± 0.0093 ± 0.0000	0.0669 ± 0.0137 ± 0.0000	0.0619 ± 0.0054 ± 0.0000
x_F = [-0.1, 0.0] ,p_T = [1.5, 1.8]	0.0884 ± 0.0079 ± 0.0000	0.0721 ± 0.0155 ± 0.0000	0.0441 ± 0.0045 ± 0.0000
x_F = [-0.1, 0.0] ,p_T = [1.8, 2.0]	0.0520 ± 0.0063 ± 0.0000	0.0540 ± 0.0133 ± 0.0000	0.0319 ± 0.0036 ± 0.0000
x_F = [-0.1, 0.0] ,p_T = [2.0, 2.2]	0.0284 ± 0.0048 ± 0.0000	0.0393 ± 0.0131 ± 0.0000	0.0196 ± 0.0031 ± 0.0000
x_F = [-0.1, 0.0] ,p_T = [2.2, 2.5]	0.0221 ± 0.0041 ± 0.0000	0.0355 ± 0.0132 ± 0.0000	0.0119 ± 0.0023 ± 0.0000
x_F = [-0.1, 0.0] ,p_T = [2.5, 2.8]	0.0169 ± 0.0054 ± 0.0000	0.0374 ± 0.0265 ± 0.0000	0.0105 ± 0.0041 ± 0.0041
x_F = [-0.1, 0.0] ,p_T = [2.8, 3.0]	0.0133 ± 0.0040 ± 0.0000	0.0000 ± 0.0000 ± 0.0000	0.0067 ± 0.0019 ± 0.0000
x_F = [-0.1, 0.0] ,p_T = [3.0, 3.2]	0.0122 ± 0.0070 ± 0.0000	0.0000 ± 0.0000 ± 0.0000	0.0076 ± 0.0035 ± 0.0000
x_F = [-0.1, 0.0] ,p_T = [3.2, 3.5]	0.0153 ± 0.0060 ± 0.0000	0.0000 ± 0.0000 ± 0.0000	0.0000 ± 0.0000 ± 0.0000
x_F = [0.0, 0.1] ,p_T = [0.0, 0.2]	0.0418 ± 0.0039 ± 0.0045	0.0344 ± 0.0085 ± 0.0000	0.0241 ± 0.0026 ± 0.0000
x_F = [0.0, 0.1] ,p_T = [0.2, 0.5]	0.1354 ± 0.0072 ± 0.0000	0.0863 ± 0.0134 ± 0.0188	0.0647 ± 0.0046 ± 0.0000
x_F = [0.0, 0.1] ,p_T = [0.5, 0.8]	0.1793 ± 0.0083 ± 0.0000	0.1742 ± 0.0186 ± 0.0000	0.0951 ± 0.0056 ± 0.0000
x_F = [0.0, 0.1] ,p_T = [0.8, 1.0]	0.1793 ± 0.0083 ± 0.0000	0.1406 ± 0.0164 ± 0.0205	0.1067 ± 0.0058 ± 0.0058
x_F = [0.0, 0.1] ,p_T = [1.0, 1.2]	0.1626 ± 0.0079 ± 0.0000	0.1263 ± 0.0152 ± 0.0000	0.1006 ± 0.0056 ± 0.0000
x_F = [0.0, 0.1] ,p_T = [1.2, 1.5]	0.1234 ± 0.0069 ± 0.0000	0.0979 ± 0.0135 ± 0.0000	0.0838 ± 0.0050 ± 0.0052
x_F = [0.0, 0.1] ,p_T = [1.5, 1.8]	0.0928 ± 0.0060 ± 0.0000	0.0715 ± 0.0115 ± 0.0000	0.0649 ± 0.0043 ± 0.0000
x_F = [0.0, 0.1] ,p_T = [1.8, 2.0]	0.0582 ± 0.0046 ± 0.0000	0.0642 ± 0.0111 ± 0.0000	0.0458 ± 0.0036 ± 0.0000
x_F = [0.0, 0.1] ,p_T = [2.0, 2.2]	0.0375 ± 0.0038 ± 0.0000	0.0360 ± 0.0081 ± 0.0000	0.0220 ± 0.0024 ± 0.0000
x_F = [0.0, 0.1] ,p_T = [2.2, 2.5]	0.0277 ± 0.0033 ± 0.0033	0.0298 ± 0.0074 ± 0.0000	0.0183 ± 0.0023 ± 0.0000
x_F = [0.0, 0.1] ,p_T = [2.5, 2.8]	0.0143 ± 0.0027 ± 0.0000	0.0190 ± 0.0093 ± 0.0000	0.0124 ± 0.0021 ± 0.0000
x_F = [0.0, 0.1] ,p_T = [2.8, 3.0]	0.0100 ± 0.0023 ± 0.0000	0.0147 ± 0.0073 ± 0.0000	0.0065 ± 0.0018 ± 0.0000
x_F = [0.0, 0.1] ,p_T = [3.0, 3.2]	0.0064 ± 0.0018 ± 0.0000	0.0211 ± 0.0150 ± 0.0000	0.0039 ± 0.0013 ± 0.0000
x_F = [0.0, 0.1] ,p_T = [3.2, 3.5]	0.0090 ± 0.0033 ± 0.0000	0.0270 ± 0.0191 ± 0.0000	0.0000 ± 0.0000 ± 0.0000

Table 4.14: *Numerical values of 2D cross-section : $d^2\sigma/dp_T dx_F$(2)*

$d^2\sigma/dp_T dx_F$: **mean ± statistic ± systematic (nb/GeV/nucleon)**			
Kinematics in x_F and p_T	PT 2 cells	Al cell	W 2 cells
$x_F = [0.1, 0.2]$,$p_T = [0.0, 0.2]$	0.0410 ± 0.0033 ± 0.0035	0.0326 ± 0.0080 ± 0.0000	0.0270 ± 0.0027 ± 0.0000
$x_F = [0.1, 0.2]$,$p_T = [0.2, 0.5]$	0.1196 ± 0.0058 ± 0.0065	0.1068 ± 0.0129 ± 0.0000	0.0650 ± 0.0041 ± 0.0056
$x_F = [0.1, 0.2]$,$p_T = [0.5, 0.8]$	0.1759 ± 0.0070 ± 0.0073	0.1535 ± 0.0157 ± 0.0000	0.1054 ± 0.0053 ± 0.0000
$x_F = [0.1, 0.2]$,$p_T = [0.8, 1.0]$	0.1910 ± 0.0073 ± 0.0079	0.1503 ± 0.0155 ± 0.0000	0.1139 ± 0.0054 ± 0.0000
$x_F = [0.1, 0.2]$,$p_T = [1.0, 1.2]$	0.1746 ± 0.0070 ± 0.0093	0.1712 ± 0.0164 ± 0.0000	0.0921 ± 0.0047 ± 0.0000
$x_F = [0.1, 0.2]$,$p_T = [1.2, 1.5]$	0.1329 ± 0.0061 ± 0.0000	0.1276 ± 0.0143 ± 0.0171	0.0690 ± 0.0040 ± 0.0049
$x_F = [0.1, 0.2]$,$p_T = [1.5, 1.8]$	0.0974 ± 0.0052 ± 0.0054	0.0755 ± 0.0109 ± 0.0000	0.0590 ± 0.0037 ± 0.0039
$x_F = [0.1, 0.2]$,$p_T = [1.8, 2.0]$	0.0638 ± 0.0043 ± 0.0000	0.0482 ± 0.0086 ± 0.0000	0.0380 ± 0.0029 ± 0.0029
$x_F = [0.1, 0.2]$,$p_T = [2.0, 2.2]$	0.0404 ± 0.0033 ± 0.0000	0.0409 ± 0.0090 ± 0.0000	0.0324 ± 0.0027 ± 0.0000
$x_F = [0.1, 0.2]$,$p_T = [2.2, 2.5]$	0.0194 ± 0.0024 ± 0.0000	0.0304 ± 0.0092 ± 0.0000	0.0166 ± 0.0019 ± 0.0000
$x_F = [0.1, 0.2]$,$p_T = [2.5, 2.8]$	0.0126 ± 0.0018 ± 0.0020	0.0163 ± 0.0054 ± 0.0000	0.0111 ± 0.0015 ± 0.0000
$x_F = [0.1, 0.2]$,$p_T = [2.8, 3.0]$	0.0094 ± 0.0017 ± 0.0000	0.0253 ± 0.0139 ± 0.0000	0.0067 ± 0.0012 ± 0.0000
$x_F = [0.1, 0.2]$,$p_T = [3.0, 3.2]$	0.0054 ± 0.0013 ± 0.0000	0.0079 ± 0.0079 ± 0.0000	0.0040 ± 0.0011 ± 0.0000
$x_F = [0.1, 0.2]$,$p_T = [3.2, 3.5]$	0.0058 ± 0.0015 ± 0.0000	0.0134 ± 0.0095 ± 0.0000	0.0036 ± 0.0018 ± 0.0000
$x_F = [0.2, 0.3]$,$p_T = [0.0, 0.2]$	0.0350 ± 0.0026 ± 0.0031	0.0339 ± 0.0063 ± 0.0000	0.0214 ± 0.0019 ± 0.0000
$x_F = [0.2, 0.3]$,$p_T = [0.2, 0.5]$	0.1062 ± 0.0045 ± 0.0063	0.1019 ± 0.0112 ± 0.0000	0.0599 ± 0.0031 ± 0.0033
$x_F = [0.2, 0.3]$,$p_T = [0.5, 0.8]$	0.1529 ± 0.0054 ± 0.0000	0.1426 ± 0.0128 ± 0.0134	0.0856 ± 0.0037 ± 0.0040
$x_F = [0.2, 0.3]$,$p_T = [0.8, 1.0]$	0.1689 ± 0.0057 ± 0.0060	0.1578 ± 0.0131 ± 0.0000	0.0967 ± 0.0039 ± 0.0000
$x_F = [0.2, 0.3]$,$p_T = [1.0, 1.2]$	0.1440 ± 0.0052 ± 0.0059	0.1275 ± 0.0116 ± 0.0000	0.0811 ± 0.0035 ± 0.0044
$x_F = [0.2, 0.3]$,$p_T = [1.2, 1.5]$	0.1198 ± 0.0048 ± 0.0000	0.1422 ± 0.0124 ± 0.0000	0.0773 ± 0.0033 ± 0.0000
$x_F = [0.2, 0.3]$,$p_T = [1.5, 1.8]$	0.0821 ± 0.0040 ± 0.0041	0.0724 ± 0.0087 ± 0.0000	0.0456 ± 0.0025 ± 0.0028
$x_F = [0.2, 0.3]$,$p_T = [1.8, 2.0]$	0.0580 ± 0.0033 ± 0.0000	0.0610 ± 0.0076 ± 0.0000	0.0346 ± 0.0022 ± 0.0024
$x_F = [0.2, 0.3]$,$p_T = [2.0, 2.2]$	0.0379 ± 0.0027 ± 0.0000	0.0399 ± 0.0063 ± 0.0000	0.0210 ± 0.0017 ± 0.0017
$x_F = [0.2, 0.3]$,$p_T = [2.2, 2.5]$	0.0195 ± 0.0019 ± 0.0000	0.0199 ± 0.0048 ± 0.0000	0.0175 ± 0.0015 ± 0.0000
$x_F = [0.2, 0.3]$,$p_T = [2.5, 2.8]$	0.0149 ± 0.0018 ± 0.0000	0.0132 ± 0.0050 ± 0.0000	0.0084 ± 0.0010 ± 0.0000
$x_F = [0.2, 0.3]$,$p_T = [2.8, 3.0]$	0.0109 ± 0.0016 ± 0.0000	0.0292 ± 0.0146 ± 0.0000	0.0069 ± 0.0012 ± 0.0000
$x_F = [0.2, 0.3]$,$p_T = [3.0, 3.2]$	0.0062 ± 0.0015 ± 0.0000	0.0178 ± 0.0075 ± 0.0000	0.0036 ± 0.0008 ± 0.0000
$x_F = [0.2, 0.3]$,$p_T = [3.2, 3.5]$	0.0038 ± 0.0014 ± 0.0000	0.0047 ± 0.0040 ± 0.0042	0.0022 ± 0.0010 ± 0.0000
$x_F = [0.3, 0.4]$,$p_T = [0.0, 0.2]$	0.0328 ± 0.0023 ± 0.0025	0.0378 ± 0.0076 ± 0.0000	0.0159 ± 0.0015 ± 0.0000
$x_F = [0.3, 0.4]$,$p_T = [0.2, 0.5]$	0.1036 ± 0.0041 ± 0.0000	0.0770 ± 0.0088 ± 0.0000	0.0473 ± 0.0026 ± 0.0032
$x_F = [0.3, 0.4]$,$p_T = [0.5, 0.8]$	0.1416 ± 0.0048 ± 0.0000	0.1490 ± 0.0127 ± 0.0000	0.0745 ± 0.0032 ± 0.0036
$x_F = [0.3, 0.4]$,$p_T = [0.8, 1.0]$	0.1386 ± 0.0047 ± 0.0052	0.1337 ± 0.0117 ± 0.0000	0.0757 ± 0.0032 ± 0.0037
$x_F = [0.3, 0.4]$,$p_T = [1.0, 1.2]$	0.1336 ± 0.0046 ± 0.0000	0.1296 ± 0.0111 ± 0.0000	0.0701 ± 0.0030 ± 0.0038
$x_F = [0.3, 0.4]$,$p_T = [1.2, 1.5]$	0.1115 ± 0.0042 ± 0.0000	0.0942 ± 0.0093 ± 0.0000	0.0639 ± 0.0028 ± 0.0000
$x_F = [0.3, 0.4]$,$p_T = [1.5, 1.8]$	0.0729 ± 0.0034 ± 0.0040	0.0622 ± 0.0074 ± 0.0000	0.0397 ± 0.0022 ± 0.0027
$x_F = [0.3, 0.4]$,$p_T = [1.8, 2.0]$	0.0439 ± 0.0026 ± 0.0000	0.0380 ± 0.0060 ± 0.0063	0.0290 ± 0.0018 ± 0.0022
$x_F = [0.3, 0.4]$,$p_T = [2.0, 2.2]$	0.0273 ± 0.0021 ± 0.0000	0.0238 ± 0.0055 ± 0.0000	0.0199 ± 0.0014 ± 0.0000
$x_F = [0.3, 0.4]$,$p_T = [2.2, 2.5]$	0.0184 ± 0.0018 ± 0.0000	0.0255 ± 0.0057 ± 0.0000	0.0132 ± 0.0012 ± 0.0000
$x_F = [0.3, 0.4]$,$p_T = [2.5, 2.8]$	0.0119 ± 0.0015 ± 0.0000	0.0167 ± 0.0052 ± 0.0000	0.0082 ± 0.0010 ± 0.0000
$x_F = [0.3, 0.4]$,$p_T = [2.8, 3.0]$	0.0086 ± 0.0014 ± 0.0000	0.0109 ± 0.0047 ± 0.0000	0.0047 ± 0.0008 ± 0.0000
$x_F = [0.3, 0.4]$,$p_T = [3.0, 3.2]$	0.0075 ± 0.0015 ± 0.0000	0.0091 ± 0.0065 ± 0.0000	0.0041 ± 0.0010 ± 0.0000
$x_F = [0.3, 0.4]$,$p_T = [3.2, 3.5]$	0.0050 ± 0.0016 ± 0.0000	0.0263 ± 0.0152 ± 0.0000	0.0017 ± 0.0006 ± 0.0000

Table 4.15: *Numerical values of 2D cross-section : $d^2\sigma/dp_T dx_F$ (3)*

$d^2\sigma/dp_T dx_F$: **mean ± statistic ± systematic (nb/GeV/nucleon)**			
Kinematics in x_F and p_T	PT 2 cells	Al cell	W 2 cells
$x_F = [0.4, 0.5]$,$p_T = [0.0, 0.2]$	0.0254 ± 0.0019 ± 0.0000	0.0297 ± 0.0070 ± 0.0000	0.0157 ± 0.0015 ± 0.0000
$x_F = [0.4, 0.5]$,$p_T = [0.2, 0.5]$	0.0868 ± 0.0036 ± 0.0038	0.0713 ± 0.0085 ± 0.0000	0.0401 ± 0.0023 ± 0.0023
$x_F = [0.4, 0.5]$,$p_T = [0.5, 0.8]$	0.1166 ± 0.0042 ± 0.0042	0.1028 ± 0.0106 ± 0.0000	0.0586 ± 0.0027 ± 0.0028
$x_F = [0.4, 0.5]$,$p_T = [0.8, 1.0]$	0.1243 ± 0.0043 ± 0.0000	0.1220 ± 0.0110 ± 0.0112	0.0637 ± 0.0028 ± 0.0030
$x_F = [0.4, 0.5]$,$p_T = [1.0, 1.2]$	0.1022 ± 0.0039 ± 0.0043	0.0985 ± 0.0098 ± 0.0000	0.0577 ± 0.0026 ± 0.0031
$x_F = [0.4, 0.5]$,$p_T = [1.2, 1.5]$	0.0858 ± 0.0036 ± 0.0000	0.0560 ± 0.0071 ± 0.0084	0.0473 ± 0.0023 ± 0.0000
$x_F = [0.4, 0.5]$,$p_T = [1.5, 1.8]$	0.0615 ± 0.0030 ± 0.0000	0.0545 ± 0.0069 ± 0.0000	0.0314 ± 0.0018 ± 0.0000
$x_F = [0.4, 0.5]$,$p_T = [1.8, 2.0]$	0.0355 ± 0.0023 ± 0.0000	0.0354 ± 0.0055 ± 0.0000	0.0247 ± 0.0016 ± 0.0000
$x_F = [0.4, 0.5]$,$p_T = [2.0, 2.2]$	0.0216 ± 0.0018 ± 0.0000	0.0225 ± 0.0044 ± 0.0000	0.0143 ± 0.0012 ± 0.0000
$x_F = [0.4, 0.5]$,$p_T = [2.2, 2.5]$	0.0137 ± 0.0014 ± 0.0000	0.0260 ± 0.0065 ± 0.0000	0.0093 ± 0.0009 ± 0.0000
$x_F = [0.4, 0.5]$,$p_T = [2.5, 2.8]$	0.0112 ± 0.0015 ± 0.0000	0.0132 ± 0.0061 ± 0.0000	0.0050 ± 0.0007 ± 0.0000
$x_F = [0.4, 0.5]$,$p_T = [2.8, 3.0]$	0.0081 ± 0.0015 ± 0.0000	0.0126 ± 0.0055 ± 0.0055	0.0041 ± 0.0007 ± 0.0000
$x_F = [0.4, 0.5]$,$p_T = [3.0, 3.2]$	0.0055 ± 0.0015 ± 0.0000	0.0000 ± 0.0000 ± 0.0000	0.0026 ± 0.0008 ± 0.0000
$x_F = [0.4, 0.5]$,$p_T = [3.2, 3.5]$	0.0061 ± 0.0025 ± 0.0000	0.0000 ± 0.0000 ± 0.0000	0.0025 ± 0.0007 ± 0.0000
$x_F = [0.5, 0.6]$,$p_T = [0.0, 0.2]$	0.0264 ± 0.0020 ± 0.0000	0.0169 ± 0.0051 ± 0.0000	0.0107 ± 0.0013 ± 0.0000
$x_F = [0.5, 0.6]$,$p_T = [0.2, 0.5]$	0.0658 ± 0.0031 ± 0.0000	0.0733 ± 0.0093 ± 0.0000	0.0324 ± 0.0021 ± 0.0000
$x_F = [0.5, 0.6]$,$p_T = [0.5, 0.8]$	0.0903 ± 0.0036 ± 0.0039	0.0777 ± 0.0090 ± 0.0106	0.0501 ± 0.0025 ± 0.0031
$x_F = [0.5, 0.6]$,$p_T = [0.8, 1.0]$	0.0957 ± 0.0037 ± 0.0000	0.0901 ± 0.0097 ± 0.0000	0.0521 ± 0.0025 ± 0.0000
$x_F = [0.5, 0.6]$,$p_T = [1.0, 1.2]$	0.0825 ± 0.0035 ± 0.0000	0.0697 ± 0.0086 ± 0.0000	0.0437 ± 0.0022 ± 0.0026
$x_F = [0.5, 0.6]$,$p_T = [1.2, 1.5]$	0.0680 ± 0.0031 ± 0.0000	0.0644 ± 0.0080 ± 0.0000	0.0359 ± 0.0020 ± 0.0000
$x_F = [0.5, 0.6]$,$p_T = [1.5, 1.8]$	0.0450 ± 0.0025 ± 0.0000	0.0296 ± 0.0054 ± 0.0055	0.0258 ± 0.0016 ± 0.0000
$x_F = [0.5, 0.6]$,$p_T = [1.8, 2.0]$	0.0274 ± 0.0020 ± 0.0000	0.0217 ± 0.0048 ± 0.0000	0.0184 ± 0.0013 ± 0.0000
$x_F = [0.5, 0.6]$,$p_T = [2.0, 2.2]$	0.0182 ± 0.0016 ± 0.0000	0.0132 ± 0.0040 ± 0.0000	0.0105 ± 0.0010 ± 0.0010
$x_F = [0.5, 0.6]$,$p_T = [2.2, 2.5]$	0.0091 ± 0.0012 ± 0.0000	0.0119 ± 0.0041 ± 0.0000	0.0067 ± 0.0008 ± 0.0000
$x_F = [0.5, 0.6]$,$p_T = [2.5, 2.8]$	0.0066 ± 0.0013 ± 0.0000	0.0146 ± 0.0061 ± 0.0000	0.0044 ± 0.0007 ± 0.0000
$x_F = [0.5, 0.6]$,$p_T = [2.8, 3.0]$	0.0054 ± 0.0012 ± 0.0000	0.0000 ± 0.0000 ± 0.0000	0.0022 ± 0.0005 ± 0.0000
$x_F = [0.5, 0.6]$,$p_T = [3.0, 3.2]$	0.0029 ± 0.0015 ± 0.0000	0.0053 ± 0.0053 ± 0.0000	0.0018 ± 0.0006 ± 0.0000
$x_F = [0.5, 0.6]$,$p_T = [3.2, 3.5]$	0.0033 ± 0.0016 ± 0.0000	0.0383 ± 0.0271 ± 0.0000	0.0017 ± 0.0009 ± 0.0009
$x_F = [0.6, 0.7]$,$p_T = [0.0, 0.2]$	0.0197 ± 0.0018 ± 0.0000	0.0222 ± 0.0060 ± 0.0000	0.0100 ± 0.0013 ± 0.0000
$x_F = [0.6, 0.7]$,$p_T = [0.2, 0.5]$	0.0504 ± 0.0028 ± 0.0034	0.0391 ± 0.0069 ± 0.0000	0.0322 ± 0.0021 ± 0.0000
$x_F = [0.6, 0.7]$,$p_T = [0.5, 0.8]$	0.0653 ± 0.0032 ± 0.0036	0.0557 ± 0.0083 ± 0.0000	0.0329 ± 0.0021 ± 0.0025
$x_F = [0.6, 0.7]$,$p_T = [0.8, 1.0]$	0.0629 ± 0.0031 ± 0.0000	0.0636 ± 0.0086 ± 0.0000	0.0342 ± 0.0020 ± 0.0020
$x_F = [0.6, 0.7]$,$p_T = [1.0, 1.2]$	0.0535 ± 0.0028 ± 0.0030	0.0444 ± 0.0069 ± 0.0000	0.0314 ± 0.0019 ± 0.0000
$x_F = [0.6, 0.7]$,$p_T = [1.2, 1.5]$	0.0410 ± 0.0025 ± 0.0000	0.0427 ± 0.0065 ± 0.0000	0.0234 ± 0.0016 ± 0.0018
$x_F = [0.6, 0.7]$,$p_T = [1.5, 1.8]$	0.0284 ± 0.0021 ± 0.0021	0.0246 ± 0.0051 ± 0.0000	0.0183 ± 0.0014 ± 0.0000
$x_F = [0.6, 0.7]$,$p_T = [1.8, 2.0]$	0.0150 ± 0.0015 ± 0.0000	0.0214 ± 0.0050 ± 0.0000	0.0111 ± 0.0010 ± 0.0000
$x_F = [0.6, 0.7]$,$p_T = [2.0, 2.2]$	0.0119 ± 0.0013 ± 0.0000	0.0116 ± 0.0034 ± 0.0000	0.0059 ± 0.0008 ± 0.0000
$x_F = [0.6, 0.7]$,$p_T = [2.2, 2.5]$	0.0063 ± 0.0012 ± 0.0000	0.0128 ± 0.0051 ± 0.0000	0.0028 ± 0.0005 ± 0.0000
$x_F = [0.6, 0.7]$,$p_T = [2.5, 2.8]$	0.0029 ± 0.0009 ± 0.0000	0.0098 ± 0.0054 ± 0.0000	0.0027 ± 0.0007 ± 0.0000
$x_F = [0.6, 0.7]$,$p_T = [2.8, 3.0]$	0.0046 ± 0.0016 ± 0.0000	0.0298 ± 0.0172 ± 0.0000	0.0020 ± 0.0007 ± 0.0000
$x_F = [0.6, 0.7]$,$p_T = [3.0, 3.2]$	0.0052 ± 0.0030 ± 0.0000	0.0000 ± 0.0000 ± 0.0000	0.0012 ± 0.0004 ± 0.0000
$x_F = [0.6, 0.7]$,$p_T = [3.2, 3.5]$	0.0012 ± 0.0010 ± 0.0000	0.0000 ± 0.0000 ± 0.0000	0.0000 ± 0.0000 ± 0.0000

Table 4.16: *Numerical values of 2D cross-section : $d^2\sigma/dp_T dx_F(4)$*

$d^2\sigma/dp_T dx_F$: **mean ± statistic ± systematic (nb/GeV/nucleon)**			
Kinematics in x_F and p_T	PT 2 cells	Al cell	W 2 cells
$x_F = [0.7, 0.8]$,$p_T = [0.0, 0.2]$	0.0135 ± 0.0016 ± 0.0000	0.0194 ± 0.0065 ± 0.0068	0.0063 ± 0.0010 ± 0.0000
$x_F = [0.7, 0.8]$,$p_T = [0.2, 0.5]$	0.0322 ± 0.0025 ± 0.0027	0.0388 ± 0.0075 ± 0.0000	0.0137 ± 0.0014 ± 0.0000
$x_F = [0.7, 0.8]$,$p_T = [0.5, 0.8]$	0.0458 ± 0.0030 ± 0.0000	0.0419 ± 0.0087 ± 0.0000	0.0189 ± 0.0016 ± 0.0025
$x_F = [0.7, 0.8]$,$p_T = [0.8, 1.0]$	0.0387 ± 0.0027 ± 0.0035	0.0402 ± 0.0070 ± 0.0000	0.0253 ± 0.0018 ± 0.0000
$x_F = [0.7, 0.8]$,$p_T = [1.0, 1.2]$	0.0345 ± 0.0026 ± 0.0000	0.0353 ± 0.0068 ± 0.0000	0.0165 ± 0.0014 ± 0.0017
$x_F = [0.7, 0.8]$,$p_T = [1.2, 1.5]$	0.0202 ± 0.0020 ± 0.0022	0.0256 ± 0.0055 ± 0.0000	0.0097 ± 0.0010 ± 0.0000
$x_F = [0.7, 0.8]$,$p_T = [1.5, 1.8]$	0.0140 ± 0.0016 ± 0.0000	0.0230 ± 0.0054 ± 0.0000	0.0090 ± 0.0010 ± 0.0011
$x_F = [0.7, 0.8]$,$p_T = [1.8, 2.0]$	0.0088 ± 0.0013 ± 0.0000	0.0000 ± 0.0000 ± 0.0000	0.0053 ± 0.0007 ± 0.0000
$x_F = [0.7, 0.8]$,$p_T = [2.0, 2.2]$	0.0062 ± 0.0011 ± 0.0000	0.0171 ± 0.0054 ± 0.0000	0.0029 ± 0.0005 ± 0.0000
$x_F = [0.7, 0.8]$,$p_T = [2.2, 2.5]$	0.0027 ± 0.0008 ± 0.0000	0.0066 ± 0.0036 ± 0.0000	0.0031 ± 0.0007 ± 0.0000
$x_F = [0.7, 0.8]$,$p_T = [2.5, 2.8]$	0.0041 ± 0.0026 ± 0.0000	0.0044 ± 0.0031 ± 0.0000	0.0009 ± 0.0004 ± 0.0000
$x_F = [0.7, 0.8]$,$p_T = [2.8, 3.0]$	0.0017 ± 0.0017 ± 0.0000	0.0000 ± 0.0000 ± 0.0000	0.0005 ± 0.0005 ± 0.0000
$x_F = [0.7, 0.8]$,$p_T = [3.0, 3.2]$	0.0000 ± 0.0000 ± 0.0000	0.0000 ± 0.0000 ± 0.0000	0.0006 ± 0.0003 ± 0.0000
$x_F = [0.7, 0.8]$,$p_T = [3.2, 3.5]$	0.0000 ± 0.0000 ± 0.0000	0.0000 ± 0.0000 ± 0.0000	0.0002 ± 0.0001 ± 0.0000
$x_F = [0.8, 0.9]$,$p_T = [0.0, 0.2]$	0.0075 ± 0.0013 ± 0.0000	0.0000 ± 0.0000 ± 0.0000	0.0044 ± 0.0014 ± 0.0000
$x_F = [0.8, 0.9]$,$p_T = [0.2, 0.5]$	0.0158 ± 0.0018 ± 0.0019	0.0206 ± 0.0061 ± 0.0000	0.0080 ± 0.0011 ± 0.0000
$x_F = [0.8, 0.9]$,$p_T = [0.5, 0.8]$	0.0220 ± 0.0021 ± 0.0000	0.0416 ± 0.0094 ± 0.0000	0.0086 ± 0.0010 ± 0.0000
$x_F = [0.8, 0.9]$,$p_T = [0.8, 1.0]$	0.0160 ± 0.0018 ± 0.0000	0.0257 ± 0.0069 ± 0.0000	0.0088 ± 0.0011 ± 0.0000
$x_F = [0.8, 0.9]$,$p_T = [1.0, 1.2]$	0.0121 ± 0.0015 ± 0.0000	0.0129 ± 0.0043 ± 0.0000	0.0045 ± 0.0007 ± 0.0008
$x_F = [0.8, 0.9]$,$p_T = [1.2, 1.5]$	0.0085 ± 0.0013 ± 0.0000	0.0106 ± 0.0032 ± 0.0000	0.0044 ± 0.0007 ± 0.0000
$x_F = [0.8, 0.9]$,$p_T = [1.5, 1.8]$	0.0057 ± 0.0014 ± 0.0000	0.0127 ± 0.0059 ± 0.0000	0.0028 ± 0.0005 ± 0.0000
$x_F = [0.8, 0.9]$,$p_T = [1.8, 2.0]$	0.0034 ± 0.0012 ± 0.0000	0.0000 ± 0.0000 ± 0.0000	0.0028 ± 0.0008 ± 0.0000
$x_F = [0.8, 0.9]$,$p_T = [2.0, 2.2]$	0.0020 ± 0.0009 ± 0.0000	0.0036 ± 0.0026 ± 0.0000	0.0012 ± 0.0005 ± 0.0000
$x_F = [0.8, 0.9]$,$p_T = [2.2, 2.5]$	0.0025 ± 0.0009 ± 0.0000	0.0022 ± 0.0017 ± 0.0000	0.0009 ± 0.0009 ± 0.0000
$x_F = [0.8, 0.9]$,$p_T = [2.5, 2.8]$	0.0000 ± 0.0000 ± 0.0000	0.0000 ± 0.0000 ± 0.0000	0.0009 ± 0.0009 ± 0.0000
$x_F = [0.8, 0.9]$,$p_T = [2.8, 3.0]$	0.0000 ± 0.0000 ± 0.0000	0.0000 ± 0.0000 ± 0.0000	0.0010 ± 0.0010 ± 0.0000
$x_F = [0.8, 0.9]$,$p_T = [3.0, 3.2]$	0.0011 ± 0.0008 ± 0.0000	0.0000 ± 0.0000 ± 0.0000	0.0001 ± 0.0001 ± 0.0000
$x_F = [0.8, 0.9]$,$p_T = [3.2, 3.5]$	0.0000 ± 0.0000 ± 0.0000	0.0000 ± 0.0000 ± 0.0000	0.0000 ± 0.0000 ± 0.0000

Numerical values of 2D cross-section in p_T and $dM_{\mu\mu}$

Table 4.17: *Numerical values of 2D cross-section : $d^2\sigma/dp_T dM_{\mu\mu}$(1)*

$d^2\sigma/dp_T dM_{\mu\mu}$: **mean ± statistic ± systematic (nb/GeV^2/nucleon)**			
Kinematics in $M_{\mu\mu}(GeV)$ and p_T	PT 2 cells	Al cell	W 2 cells
$M_{\mu\mu}$ = [4.50, 4.95] , p_T = [0.0, 0.2]	0.0190 ± 0.0010 ± 0.0000	0.0162 ± 0.0023 ± 0.0000	-
$M_{\mu\mu}$ = [4.50, 4.95] , p_T = [0.2, 0.5]	0.0519 ± 0.0016 ± 0.0018	0.0449 ± 0.0038 ± 0.0000	-
$M_{\mu\mu}$ = [4.50, 4.95] , p_T = [0.5, 0.8]	0.0725 ± 0.0019 ± 0.0022	0.0736 ± 0.0049 ± 0.0000	-
$M_{\mu\mu}$ = [4.50, 4.95] , p_T = [0.8, 1.0]	0.0743 ± 0.0019 ± 0.0023	0.0744 ± 0.0048 ± 0.0000	-
$M_{\mu\mu}$ = [4.50, 4.95] , p_T = [1.0, 1.2]	0.0654 ± 0.0018 ± 0.0000	0.0613 ± 0.0043 ± 0.0044	-
$M_{\mu\mu}$ = [4.50, 4.95] , p_T = [1.2, 1.5]	0.0555 ± 0.0017 ± 0.0000	0.0552 ± 0.0040 ± 0.0000	-
$M_{\mu\mu}$ = [4.50, 4.95] , p_T = [1.5, 1.8]	0.0380 ± 0.0014 ± 0.0000	0.0330 ± 0.0031 ± 0.0000	-
$M_{\mu\mu}$ = [4.50, 4.95] , p_T = [1.8, 2.0]	0.0226 ± 0.0011 ± 0.0000	0.0238 ± 0.0026 ± 0.0000	-
$M_{\mu\mu}$ = [4.50, 4.95] , p_T = [2.0, 2.2]	0.0152 ± 0.0009 ± 0.0000	0.0154 ± 0.0021 ± 0.0000	-
$M_{\mu\mu}$ = [4.50, 4.95] , p_T = [2.2, 2.5]	0.0089 ± 0.0007 ± 0.0000	0.0089 ± 0.0017 ± 0.0000	-
$M_{\mu\mu}$ = [4.50, 4.95] , p_T = [2.5, 2.8]	0.0049 ± 0.0005 ± 0.0000	0.0057 ± 0.0016 ± 0.0000	-
$M_{\mu\mu}$ = [4.50, 4.95] , p_T = [2.8, 3.0]	0.0029 ± 0.0004 ± 0.0000	0.0043 ± 0.0017 ± 0.0000	-
$M_{\mu\mu}$ = [4.50, 4.95] , p_T = [3.0, 3.2]	0.0024 ± 0.0005 ± 0.0000	0.0030 ± 0.0015 ± 0.0000	-
$M_{\mu\mu}$ = [4.50, 4.95] , p_T = [3.2, 3.5]	0.0020 ± 0.0004 ± 0.0000	0.0030 ± 0.0030 ± 0.0000	-
$M_{\mu\mu}$ = [4.95, 5.40] , p_T = [0.0, 0.2]	0.0098 ± 0.0007 ± 0.0008	0.0110 ± 0.0022 ± 0.0000	0.0091 ± 0.0006 ± 0.0007
$M_{\mu\mu}$ = [4.95, 5.40] , p_T = [0.2, 0.5]	0.0339 ± 0.0013 ± 0.0013	0.0269 ± 0.0028 ± 0.0000	0.0256 ± 0.0010 ± 0.0000
$M_{\mu\mu}$ = [4.95, 5.40] , p_T = [0.5, 0.8]	0.0457 ± 0.0015 ± 0.0000	0.0469 ± 0.0038 ± 0.0000	0.0370 ± 0.0012 ± 0.0000
$M_{\mu\mu}$ = [4.95, 5.40] , p_T = [0.8, 1.0]	0.0480 ± 0.0015 ± 0.0000	0.0390 ± 0.0033 ± 0.0036	0.0398 ± 0.0012 ± 0.0014
$M_{\mu\mu}$ = [4.95, 5.40] , p_T = [1.0, 1.2]	0.0444 ± 0.0015 ± 0.0000	0.0398 ± 0.0034 ± 0.0034	0.0354 ± 0.0012 ± 0.0014
$M_{\mu\mu}$ = [4.95, 5.40] , p_T = [1.2, 1.5]	0.0337 ± 0.0013 ± 0.0000	0.0340 ± 0.0031 ± 0.0031	0.0285 ± 0.0010 ± 0.0011
$M_{\mu\mu}$ = [4.95, 5.40] , p_T = [1.5, 1.8]	0.0240 ± 0.0011 ± 0.0000	0.0218 ± 0.0024 ± 0.0000	0.0205 ± 0.0008 ± 0.0000
$M_{\mu\mu}$ = [4.95, 5.40] , p_T = [1.8, 2.0]	0.0153 ± 0.0009 ± 0.0000	0.0116 ± 0.0018 ± 0.0000	0.0153 ± 0.0007 ± 0.0008
$M_{\mu\mu}$ = [4.95, 5.40] , p_T = [2.0, 2.2]	0.0101 ± 0.0007 ± 0.0000	0.0101 ± 0.0018 ± 0.0000	0.0091 ± 0.0005 ± 0.0006
$M_{\mu\mu}$ = [4.95, 5.40] , p_T = [2.2, 2.5]	0.0051 ± 0.0005 ± 0.0000	0.0089 ± 0.0017 ± 0.0000	0.0060 ± 0.0004 ± 0.0000
$M_{\mu\mu}$ = [4.95, 5.40] , p_T = [2.5, 2.8]	0.0041 ± 0.0005 ± 0.0000	0.0028 ± 0.0010 ± 0.0000	0.0032 ± 0.0003 ± 0.0000
$M_{\mu\mu}$ = [4.95, 5.40] , p_T = [2.8, 3.0]	0.0030 ± 0.0005 ± 0.0000	0.0067 ± 0.0024 ± 0.0000	0.0016 ± 0.0002 ± 0.0000
$M_{\mu\mu}$ = [4.95, 5.40] , p_T = [3.0, 3.2]	0.0018 ± 0.0004 ± 0.0000	0.0000 ± 0.0000 ± 0.0000	0.0017 ± 0.0003 ± 0.0000
$M_{\mu\mu}$ = [4.95, 5.40] , p_T = [3.2, 3.5]	0.0013 ± 0.0004 ± 0.0000	0.0000 ± 0.0000 ± 0.0000	0.0011 ± 0.0002 ± 0.0000
$M_{\mu\mu}$ = [5.40, 5.85] , p_T = [0.0, 0.2]	0.0068 ± 0.0006 ± 0.0000	0.0070 ± 0.0017 ± 0.0000	0.0054 ± 0.0005 ± 0.0000
$M_{\mu\mu}$ = [5.40, 5.85] , p_T = [0.2, 0.5]	0.0196 ± 0.0010 ± 0.0010	0.0167 ± 0.0022 ± 0.0000	0.0159 ± 0.0008 ± 0.0009
$M_{\mu\mu}$ = [5.40, 5.85] , p_T = [0.5, 0.8]	0.0291 ± 0.0012 ± 0.0013	0.0266 ± 0.0028 ± 0.0000	0.0223 ± 0.0009 ± 0.0011
$M_{\mu\mu}$ = [5.40, 5.85] , p_T = [0.8, 1.0]	0.0301 ± 0.0012 ± 0.0000	0.0281 ± 0.0028 ± 0.0033	0.0247 ± 0.0010 ± 0.0013
$M_{\mu\mu}$ = [5.40, 5.85] , p_T = [1.0, 1.2]	0.0271 ± 0.0011 ± 0.0000	0.0202 ± 0.0023 ± 0.0024	0.0221 ± 0.0009 ± 0.0000
$M_{\mu\mu}$ = [5.40, 5.85] , p_T = [1.2, 1.5]	0.0213 ± 0.0010 ± 0.0012	0.0187 ± 0.0023 ± 0.0000	0.0188 ± 0.0008 ± 0.0010
$M_{\mu\mu}$ = [5.40, 5.85] , p_T = [1.5, 1.8]	0.0159 ± 0.0009 ± 0.0000	0.0104 ± 0.0017 ± 0.0000	0.0120 ± 0.0007 ± 0.0008
$M_{\mu\mu}$ = [5.40, 5.85] , p_T = [1.8, 2.0]	0.0100 ± 0.0007 ± 0.0000	0.0097 ± 0.0017 ± 0.0000	0.0090 ± 0.0005 ± 0.0000
$M_{\mu\mu}$ = [5.40, 5.85] , p_T = [2.0, 2.2]	0.0066 ± 0.0006 ± 0.0000	0.0060 ± 0.0013 ± 0.0000	0.0056 ± 0.0004 ± 0.0000
$M_{\mu\mu}$ = [5.40, 5.85] , p_T = [2.2, 2.5]	0.0040 ± 0.0005 ± 0.0000	0.0044 ± 0.0013 ± 0.0000	0.0039 ± 0.0004 ± 0.0000
$M_{\mu\mu}$ = [5.40, 5.85] , p_T = [2.5, 2.8]	0.0027 ± 0.0005 ± 0.0000	0.0038 ± 0.0027 ± 0.0000	0.0024 ± 0.0003 ± 0.0000
$M_{\mu\mu}$ = [5.40, 5.85] , p_T = [2.8, 3.0]	0.0023 ± 0.0005 ± 0.0000	0.0000 ± 0.0000 ± 0.0000	0.0014 ± 0.0002 ± 0.0000
$M_{\mu\mu}$ = [5.40, 5.85] , p_T = [3.0, 3.2]	0.0019 ± 0.0005 ± 0.0000	0.0000 ± 0.0000 ± 0.0000	0.0011 ± 0.0002 ± 0.0000
$M_{\mu\mu}$ = [5.40, 5.85] , p_T = [3.2, 3.5]	0.0018 ± 0.0007 ± 0.0000	0.0000 ± 0.0000 ± 0.0000	0.0007 ± 0.0002 ± 0.0000

Table 4.18: *Numerical values of 2D cross-section : $d^2\sigma/dp_T dM_{\mu\mu}$(2)*

$d^2\sigma/dp_T dM_{\mu\mu}$: **mean ± statistic ± systematic(nb/GeV^2/nucleon)**			
Kinematics in $M_{\mu\mu}(GeV)$ and p_T	PT 2 cells	Al cell	W 2 cells
$M_{\mu\mu}$ = [5.85, 6.30] , p_T = [0.0, 0.2]	0.0052 ± 0.0005 ± 0.0000	0.0085 ± 0.0023 ± 0.0000	0.0034 ± 0.0004 ± 0.0000
$M_{\mu\mu}$ = [5.85, 6.30] , p_T = [0.2, 0.5]	0.0129 ± 0.0008 ± 0.0008	0.0145 ± 0.0021 ± 0.0000	0.0106 ± 0.0006 ± 0.0000
$M_{\mu\mu}$ = [5.85, 6.30] , p_T = [0.5, 0.8]	0.0170 ± 0.0009 ± 0.0000	0.0157 ± 0.0021 ± 0.0000	0.0139 ± 0.0007 ± 0.0009
$M_{\mu\mu}$ = [5.85, 6.30] , p_T = [0.8, 1.0]	0.0216 ± 0.0010 ± 0.0000	0.0189 ± 0.0023 ± 0.0000	0.0146 ± 0.0007 ± 0.0000
$M_{\mu\mu}$ = [5.85, 6.30] , p_T = [1.0, 1.2]	0.0175 ± 0.0009 ± 0.0009	0.0121 ± 0.0017 ± 0.0000	0.0154 ± 0.0007 ± 0.0009
$M_{\mu\mu}$ = [5.85, 6.30] , p_T = [1.2, 1.5]	0.0151 ± 0.0009 ± 0.0010	0.0125 ± 0.0018 ± 0.0000	0.0119 ± 0.0007 ± 0.0007
$M_{\mu\mu}$ = [5.85, 6.30] , p_T = [1.5, 1.8]	0.0112 ± 0.0007 ± 0.0000	0.0099 ± 0.0019 ± 0.0024	0.0096 ± 0.0006 ± 0.0000
$M_{\mu\mu}$ = [5.85, 6.30] , p_T = [1.8, 2.0]	0.0053 ± 0.0005 ± 0.0006	0.0072 ± 0.0016 ± 0.0000	0.0068 ± 0.0005 ± 0.0000
$M_{\mu\mu}$ = [5.85, 6.30] , p_T = [2.0, 2.2]	0.0042 ± 0.0005 ± 0.0000	0.0053 ± 0.0015 ± 0.0000	0.0036 ± 0.0004 ± 0.0000
$M_{\mu\mu}$ = [5.85, 6.30] , p_T = [2.2, 2.5]	0.0025 ± 0.0004 ± 0.0004	0.0028 ± 0.0010 ± 0.0000	0.0028 ± 0.0003 ± 0.0000
$M_{\mu\mu}$ = [5.85, 6.30] , p_T = [2.5, 2.8]	0.0026 ± 0.0004 ± 0.0000	0.0139 ± 0.0077 ± 0.0000	0.0016 ± 0.0003 ± 0.0000
$M_{\mu\mu}$ = [5.85, 6.30] , p_T = [2.8, 3.0]	0.0011 ± 0.0004 ± 0.0000	0.0025 ± 0.0018 ± 0.0000	0.0016 ± 0.0003 ± 0.0000
$M_{\mu\mu}$ = [5.85, 6.30] , p_T = [3.0, 3.2]	0.0013 ± 0.0005 ± 0.0000	0.0027 ± 0.0027 ± 0.0000	0.0012 ± 0.0003 ± 0.0000
$M_{\mu\mu}$ = [5.85, 6.30] , p_T = [3.2, 3.5]	0.0006 ± 0.0004 ± 0.0000	0.0000 ± 0.0000 ± 0.0000	0.0007 ± 0.0004 ± 0.0000
$M_{\mu\mu}$ = [6.30, 6.75] , p_T = [0.0, 0.2]	0.0032 ± 0.0004 ± 0.0000	0.0074 ± 0.0022 ± 0.0000	0.0021 ± 0.0003 ± 0.0000
$M_{\mu\mu}$ = [6.30, 6.75] , p_T = [0.2, 0.5]	0.0085 ± 0.0006 ± 0.0000	0.0087 ± 0.0018 ± 0.0000	0.0062 ± 0.0005 ± 0.0000
$M_{\mu\mu}$ = [6.30, 6.75] , p_T = [0.5, 0.8]	0.0127 ± 0.0008 ± 0.0000	0.0130 ± 0.0021 ± 0.0000	0.0092 ± 0.0006 ± 0.0000
$M_{\mu\mu}$ = [6.30, 6.75] , p_T = [0.8, 1.0]	0.0131 ± 0.0008 ± 0.0000	0.0133 ± 0.0020 ± 0.0000	0.0109 ± 0.0006 ± 0.0000
$M_{\mu\mu}$ = [6.30, 6.75] , p_T = [1.0, 1.2]	0.0115 ± 0.0007 ± 0.0009	0.0119 ± 0.0019 ± 0.0020	0.0101 ± 0.0006 ± 0.0000
$M_{\mu\mu}$ = [6.30, 6.75] , p_T = [1.2, 1.5]	0.0100 ± 0.0007 ± 0.0000	0.0096 ± 0.0016 ± 0.0000	0.0074 ± 0.0005 ± 0.0000
$M_{\mu\mu}$ = [6.30, 6.75] , p_T = [1.5, 1.8]	0.0078 ± 0.0006 ± 0.0000	0.0076 ± 0.0015 ± 0.0000	0.0054 ± 0.0004 ± 0.0000
$M_{\mu\mu}$ = [6.30, 6.75] , p_T = [1.8, 2.0]	0.0054 ± 0.0006 ± 0.0000	0.0031 ± 0.0011 ± 0.0000	0.0036 ± 0.0003 ± 0.0000
$M_{\mu\mu}$ = [6.30, 6.75] , p_T = [2.0, 2.2]	0.0034 ± 0.0005 ± 0.0000	0.0072 ± 0.0022 ± 0.0000	0.0029 ± 0.0003 ± 0.0000
$M_{\mu\mu}$ = [6.30, 6.75] , p_T = [2.2, 2.5]	0.0025 ± 0.0004 ± 0.0000	0.0043 ± 0.0025 ± 0.0000	0.0023 ± 0.0003 ± 0.0000
$M_{\mu\mu}$ = [6.30, 6.75] , p_T = [2.5, 2.8]	0.0015 ± 0.0004 ± 0.0000	0.0060 ± 0.0043 ± 0.0000	0.0019 ± 0.0003 ± 0.0000
$M_{\mu\mu}$ = [6.30, 6.75] , p_T = [2.8, 3.0]	0.0023 ± 0.0005 ± 0.0000	0.0091 ± 0.0064 ± 0.0000	0.0012 ± 0.0003 ± 0.0000
$M_{\mu\mu}$ = [6.30, 6.75] , p_T = [3.0, 3.2]	0.0010 ± 0.0004 ± 0.0000	0.0000 ± 0.0000 ± 0.0000	0.0009 ± 0.0004 ± 0.0000
$M_{\mu\mu}$ = [6.30, 6.75] , p_T = [3.2, 3.5]	0.0009 ± 0.0006 ± 0.0000	0.0000 ± 0.0000 ± 0.0000	0.0006 ± 0.0003 ± 0.0000
$M_{\mu\mu}$ = [6.75, 7.20] , p_T = [0.0, 0.2]	0.0025 ± 0.0005 ± 0.0000	0.0057 ± 0.0033 ± 0.0000	0.0025 ± 0.0004 ± 0.0000
$M_{\mu\mu}$ = [6.75, 7.20] , p_T = [0.2, 0.5]	0.0057 ± 0.0005 ± 0.0000	0.0075 ± 0.0017 ± 0.0000	0.0054 ± 0.0005 ± 0.0000
$M_{\mu\mu}$ = [6.75, 7.20] , p_T = [0.5, 0.8]	0.0105 ± 0.0007 ± 0.0000	0.0096 ± 0.0018 ± 0.0000	0.0067 ± 0.0005 ± 0.0005
$M_{\mu\mu}$ = [6.75, 7.20] , p_T = [0.8, 1.0]	0.0086 ± 0.0006 ± 0.0000	0.0081 ± 0.0015 ± 0.0000	0.0067 ± 0.0005 ± 0.0000
$M_{\mu\mu}$ = [6.75, 7.20] , p_T = [1.0, 1.2]	0.0082 ± 0.0007 ± 0.0007	0.0067 ± 0.0017 ± 0.0000	0.0054 ± 0.0004 ± 0.0005
$M_{\mu\mu}$ = [6.75, 7.20] , p_T = [1.2, 1.5]	0.0073 ± 0.0006 ± 0.0000	0.0065 ± 0.0014 ± 0.0000	0.0057 ± 0.0005 ± 0.0000
$M_{\mu\mu}$ = [6.75, 7.20] , p_T = [1.5, 1.8]	0.0048 ± 0.0005 ± 0.0000	0.0054 ± 0.0015 ± 0.0000	0.0044 ± 0.0004 ± 0.0000
$M_{\mu\mu}$ = [6.75, 7.20] , p_T = [1.8, 2.0]	0.0037 ± 0.0005 ± 0.0000	0.0058 ± 0.0021 ± 0.0000	0.0030 ± 0.0004 ± 0.0000
$M_{\mu\mu}$ = [6.75, 7.20] , p_T = [2.0, 2.2]	0.0019 ± 0.0003 ± 0.0000	0.0040 ± 0.0016 ± 0.0000	0.0021 ± 0.0003 ± 0.0000
$M_{\mu\mu}$ = [6.75, 7.20] , p_T = [2.2, 2.5]	0.0011 ± 0.0003 ± 0.0000	0.0051 ± 0.0029 ± 0.0000	0.0018 ± 0.0003 ± 0.0000
$M_{\mu\mu}$ = [6.75, 7.20] , p_T = [2.5, 2.8]	0.0027 ± 0.0011 ± 0.0000	0.0041 ± 0.0024 ± 0.0000	0.0011 ± 0.0003 ± 0.0000
$M_{\mu\mu}$ = [6.75, 7.20] , p_T = [2.8, 3.0]	0.0009 ± 0.0004 ± 0.0000	0.0029 ± 0.0020 ± 0.0000	0.0008 ± 0.0003 ± 0.0000
$M_{\mu\mu}$ = [6.75, 7.20] , p_T = [3.0, 3.2]	0.0003 ± 0.0003 ± 0.0003	0.0000 ± 0.0000 ± 0.0000	0.0007 ± 0.0005 ± 0.0000
$M_{\mu\mu}$ = [6.75, 7.20] , p_T = [3.2, 3.5]	0.0007 ± 0.0004 ± 0.0000	0.0000 ± 0.0000 ± 0.0000	0.0000 ± 0.0000 ± 0.0000

Table 4.19: *Numerical values of 2D cross-section : $d^2\sigma/dp_T dM_{\mu\mu}(3)$*

$d^2\sigma/dp_T dM_{\mu\mu}$: **mean ± statistic ± systematic(nb/GeV^2/nucleon)**			
Kinematics in $M_{\mu\mu}(GeV)$ and p_T	PT 2 cells	Al cell	W 2 cells
$M_{\mu\mu}$ = [7.20, 7.65] , p_T = [0.0, 0.2]	0.0022 ± 0.0005 ± 0.0000	0.0080 ± 0.0040 ± 0.0000	0.0016 ± 0.0003 ± 0.0000
$M_{\mu\mu}$ = [7.20, 7.65] , p_T = [0.2, 0.5]	0.0055 ± 0.0006 ± 0.0000	0.0044 ± 0.0013 ± 0.0000	0.0030 ± 0.0004 ± 0.0000
$M_{\mu\mu}$ = [7.20, 7.65] , p_T = [0.5, 0.8]	0.0053 ± 0.0005 ± 0.0000	0.0056 ± 0.0016 ± 0.0000	0.0050 ± 0.0005 ± 0.0005
$M_{\mu\mu}$ = [7.20, 7.65] , p_T = [0.8, 1.0]	0.0072 ± 0.0006 ± 0.0000	0.0058 ± 0.0016 ± 0.0000	0.0046 ± 0.0004 ± 0.0000
$M_{\mu\mu}$ = [7.20, 7.65] , p_T = [1.0, 1.2]	0.0060 ± 0.0005 ± 0.0000	0.0066 ± 0.0015 ± 0.0000	0.0042 ± 0.0004 ± 0.0000
$M_{\mu\mu}$ = [7.20, 7.65] , p_T = [1.2, 1.5]	0.0047 ± 0.0005 ± 0.0000	0.0045 ± 0.0016 ± 0.0000	0.0034 ± 0.0004 ± 0.0000
$M_{\mu\mu}$ = [7.20, 7.65] , p_T = [1.5, 1.8]	0.0038 ± 0.0004 ± 0.0000	0.0032 ± 0.0019 ± 0.0000	0.0032 ± 0.0004 ± 0.0000
$M_{\mu\mu}$ = [7.20, 7.65] , p_T = [1.8, 2.0]	0.0034 ± 0.0005 ± 0.0000	0.0049 ± 0.0020 ± 0.0000	0.0025 ± 0.0003 ± 0.0000
$M_{\mu\mu}$ = [7.20, 7.65] , p_T = [2.0, 2.2]	0.0014 ± 0.0004 ± 0.0000	0.0059 ± 0.0030 ± 0.0000	0.0017 ± 0.0003 ± 0.0000
$M_{\mu\mu}$ = [7.20, 7.65] , p_T = [2.2, 2.5]	0.0016 ± 0.0004 ± 0.0000	0.0000 ± 0.0000 ± 0.0000	0.0012 ± 0.0003 ± 0.0000
$M_{\mu\mu}$ = [7.20, 7.65] , p_T = [2.5, 2.8]	0.0015 ± 0.0005 ± 0.0000	0.0000 ± 0.0000 ± 0.0000	0.0013 ± 0.0004 ± 0.0000
$M_{\mu\mu}$ = [7.20, 7.65] , p_T = [2.8, 3.0]	0.0010 ± 0.0005 ± 0.0000	0.0000 ± 0.0000 ± 0.0000	0.0006 ± 0.0006 ± 0.0000
$M_{\mu\mu}$ = [7.20, 7.65] , p_T = [3.0, 3.2]	0.0005 ± 0.0005 ± 0.0000	0.0000 ± 0.0000 ± 0.0000	0.0008 ± 0.0004 ± 0.0000
$M_{\mu\mu}$ = [7.20, 7.65] , p_T = [3.2, 3.5]	0.0013 ± 0.0008 ± 0.0000	0.0000 ± 0.0000 ± 0.0000	0.0008 ± 0.0006 ± 0.0000
$M_{\mu\mu}$ = [7.65, 8.10] , p_T = [0.0, 0.2]	0.0018 ± 0.0005 ± 0.0000	0.0000 ± 0.0000 ± 0.0000	0.0017 ± 0.0006 ± 0.0000
$M_{\mu\mu}$ = [7.65, 8.10] , p_T = [0.2, 0.5]	0.0032 ± 0.0004 ± 0.0000	0.0054 ± 0.0025 ± 0.0000	0.0024 ± 0.0004 ± 0.0000
$M_{\mu\mu}$ = [7.65, 8.10] , p_T = [0.5, 0.8]	0.0048 ± 0.0006 ± 0.0000	0.0061 ± 0.0017 ± 0.0000	0.0035 ± 0.0004 ± 0.0000
$M_{\mu\mu}$ = [7.65, 8.10] , p_T = [0.8, 1.0]	0.0037 ± 0.0005 ± 0.0000	0.0037 ± 0.0014 ± 0.0000	0.0042 ± 0.0004 ± 0.0000
$M_{\mu\mu}$ = [7.65, 8.10] , p_T = [1.0, 1.2]	0.0040 ± 0.0005 ± 0.0000	0.0055 ± 0.0018 ± 0.0000	0.0038 ± 0.0004 ± 0.0000
$M_{\mu\mu}$ = [7.65, 8.10] , p_T = [1.2, 1.5]	0.0038 ± 0.0005 ± 0.0000	0.0047 ± 0.0017 ± 0.0000	0.0025 ± 0.0003 ± 0.0000
$M_{\mu\mu}$ = [7.65, 8.10] , p_T = [1.5, 1.8]	0.0028 ± 0.0004 ± 0.0004	0.0050 ± 0.0023 ± 0.0000	0.0025 ± 0.0004 ± 0.0000
$M_{\mu\mu}$ = [7.65, 8.10] , p_T = [1.8, 2.0]	0.0021 ± 0.0005 ± 0.0000	0.0066 ± 0.0030 ± 0.0000	0.0019 ± 0.0003 ± 0.0000
$M_{\mu\mu}$ = [7.65, 8.10] , p_T = [2.0, 2.2]	0.0014 ± 0.0004 ± 0.0000	0.0071 ± 0.0050 ± 0.0000	0.0015 ± 0.0003 ± 0.0000
$M_{\mu\mu}$ = [7.65, 8.10] , p_T = [2.2, 2.5]	0.0012 ± 0.0004 ± 0.0000	0.0085 ± 0.0060 ± 0.0000	0.0020 ± 0.0005 ± 0.0000
$M_{\mu\mu}$ = [7.65, 8.10] , p_T = [2.5, 2.8]	0.0009 ± 0.0006 ± 0.0000	0.0000 ± 0.0000 ± 0.0000	0.0021 ± 0.0011 ± 0.0000
$M_{\mu\mu}$ = [7.65, 8.10] , p_T = [2.8, 3.0]	0.0000 ± 0.0000 ± 0.0000	0.0000 ± 0.0000 ± 0.0000	0.0004 ± 0.0002 ± 0.0000
$M_{\mu\mu}$ = [7.65, 8.10] , p_T = [3.0, 3.2]	0.0007 ± 0.0004 ± 0.0000	0.0016 ± 0.0016 ± 0.0000	0.0010 ± 0.0005 ± 0.0000
$M_{\mu\mu}$ = [7.65, 8.10] , p_T = [3.2, 3.5]	0.0000 ± 0.0000 ± 0.0000	0.0000 ± 0.0000 ± 0.0000	0.0000 ± 0.0000 ± 0.0000

Numerical values of 3D cross-section

Table 4.20: *Numerical values of 3D cross-section : $d^3\sigma/dM_{\mu\mu}dp_Tdx_F$(1)*

$d^3\sigma/dM_{\mu\mu}dp_Tdx_F$: **mean ± statistic ± systematic (nb/GeV^2/nucleon)**					
Kinematics in $M_{\mu\mu}(GeV)$, $p_T(GeV)$ and x_F			PT cells	Al cell	W cells
$M_{\mu\mu}$ = [4.3, 4.7]	p_T = [0.0, 0.7]	x_F = [-0.1, 0.0]	0.0786 ± 0.0074 ± 0.0077	0.1047 ± 0.0173 ±0.0000	-
$M_{\mu\mu}$ = [4.3, 4.7]	p_T = [0.0, 0.7]	x_F = [0.0, 0.1]	0.0961 ± 0.0057 ± 0.0060	0.0901 ± 0.0123 ±0.0000	-
$M_{\mu\mu}$ = [4.3, 4.7]	p_T = [0.0, 0.7]	x_F = [0.1, 0.2]	0.0869 ± 0.0046 ± 0.0061	0.0846 ± 0.0113 ±0.0000	-
$M_{\mu\mu}$ = [4.3, 4.7]	p_T = [0.0, 0.7]	x_F = [0.2, 0.3]	0.0841 ± 0.0037 ± 0.0000	0.0686 ± 0.0085 ±0.0000	-
$M_{\mu\mu}$ = [4.3, 4.7]	p_T = [0.0, 0.7]	x_F = [0.3, 0.4]	0.0674 ± 0.0031 ± 0.0035	0.0517 ± 0.0074 ± 0.0082	-
$M_{\mu\mu}$ = [4.3, 4.7]	p_T = [0.0, 0.7]	x_F = [0.4, 0.5]	0.0584 ± 0.0028 ± 0.0031	0.0686 ± 0.0095 ± 0.0000	-
$M_{\mu\mu}$ = [4.3, 4.7]	p_T = [0.0, 0.7]	x_F = [0.5, 0.6]	0.0540 ± 0.0028 ± 0.0000	0.0517 ± 0.0084 ± 0.0000	-
$M_{\mu\mu}$ = [4.3, 4.7]	p_T = [0.0, 0.7]	x_F = [0.6, 0.7]	0.0366 ± 0.0024 ± 0.0000	0.0362 ± 0.0068 ± 0.0000	-
$M_{\mu\mu}$ = [4.3, 4.7]	p_T = [0.0, 0.7]	x_F = [0.7, 0.8]	0.0216 ± 0.0020 ± 0.0021	0.0305 ± 0.0094 ± 0.0000	-
$M_{\mu\mu}$ = [4.3, 4.7]	p_T = [0.0, 0.7]	x_F = [0.8, 0.9]	0.0105 ± 0.0015 ± 0.0016	0.0302 ± 0.0101 ± 0.0000	-
$M_{\mu\mu}$ = [4.3, 4.7]	p_T = [0.7, 1.1]	x_F = [-0.1, 0.0]	0.1292 ± 0.0127 ± 0.0000	0.0724 ± 0.0191 ± 0.0288	-
$M_{\mu\mu}$ = [4.3, 4.7]	p_T = [0.7, 1.1]	x_F = [0.0, 0.1]	0.1458 ± 0.0094 ± 0.0000	0.1250 ± 0.0201 ± 0.0000	-
$M_{\mu\mu}$ = [4.3, 4.7]	p_T = [0.7, 1.1]	x_F = [0.1, 0.2]	0.1650 ± 0.0084 ± 0.0086	0.1176 ± 0.0174 ± 0.0194	-
$M_{\mu\mu}$ = [4.3, 4.7]	p_T = [0.7, 1.1]	x_F = [0.2, 0.3]	0.1312 ± 0.0062 ± 0.0065	0.0883 ± 0.0123 ± 0.0171	-
$M_{\mu\mu}$ = [4.3, 4.7]	p_T = [0.7, 1.1]	x_F = [0.3, 0.4]	0.1111 ± 0.0052 ± 0.0000	0.1071 ± 0.0135 ± 0.0000	-
$M_{\mu\mu}$ = [4.3, 4.7]	p_T = [0.7, 1.1]	x_F = [0.4, 0.5]	0.0863 ± 0.0045 ± 0.0052	0.0815 ± 0.0123 ± 0.0000	-
$M_{\mu\mu}$ = [4.3, 4.7]	p_T = [0.7, 1.1]	x_F = [0.5, 0.6]	0.0692 ± 0.0041 ± 0.0000	0.0925 ± 0.0143 ± 0.0000	-
$M_{\mu\mu}$ = [4.3, 4.7]	p_T = [0.7, 1.1]	x_F = [0.6, 0.7]	0.0458 ± 0.0035 ± 0.0000	0.0526 ± 0.0107 ± 0.0000	-
$M_{\mu\mu}$ = [4.3, 4.7]	p_T = [0.7, 1.1]	x_F = [0.7, 0.8]	0.0374 ± 0.0035 ± 0.0000	0.0425 ± 0.0125 ± 0.0000	-
$M_{\mu\mu}$ = [4.3, 4.7]	p_T = [0.7, 1.1]	x_F = [0.8, 0.9]	0.0179 ± 0.0025 ± 0.0000	0.0451 ± 0.0177 ± 0.0000	-
$M_{\mu\mu}$ = [4.3, 4.7]	p_T = [1.1, 1.6]	x_F = [-0.1, 0.0]	0.0945 ± 0.0099 ± 0.0101	0.0507 ± 0.0157 ± 0.0000	-
$M_{\mu\mu}$ = [4.3, 4.7]	p_T = [1.1, 1.6]	x_F = [0.0, 0.1]	0.1079 ± 0.0072 ± 0.0000	0.0697 ± 0.0128 ± 0.0000	-
$M_{\mu\mu}$ = [4.3, 4.7]	p_T = [1.1, 1.6]	x_F = [0.1, 0.2]	0.1083 ± 0.0062 ± 0.0000	0.1066 ± 0.0153 ± 0.0000	-
$M_{\mu\mu}$ = [4.3, 4.7]	p_T = [1.1, 1.6]	x_F = [0.2, 0.3]	0.0928 ± 0.0046 ± 0.0000	0.1018 ± 0.0112 ± 0.0000	-
$M_{\mu\mu}$ = [4.3, 4.7]	p_T = [1.1, 1.6]	x_F = [0.3, 0.4]	0.0810 ± 0.0040 ± 0.0000	0.0779 ± 0.0101 ± 0.0000	-
$M_{\mu\mu}$ = [4.3, 4.7]	p_T = [1.1, 1.6]	x_F = [0.4, 0.5]	0.0585 ± 0.0033 ± 0.0036	0.0619 ± 0.0096 ± 0.0000	-
$M_{\mu\mu}$ = [4.3, 4.7]	p_T = [1.1, 1.6]	x_F = [0.5, 0.6]	0.0448 ± 0.0029 ± 0.0000	0.0510 ± 0.0096 ± 0.0000	-
$M_{\mu\mu}$ = [4.3, 4.7]	p_T = [1.1, 1.6]	x_F = [0.6, 0.7]	0.0317 ± 0.0026 ± 0.0000	0.0304 ± 0.0064 ± 0.0000	-
$M_{\mu\mu}$ = [4.3, 4.7]	p_T = [1.1, 1.6]	x_F = [0.7, 0.8]	0.0206 ± 0.0023 ± 0.0000	0.0358 ± 0.0116 ± 0.0000	-
$M_{\mu\mu}$ = [4.3, 4.7]	p_T = [1.1, 1.6]	x_F = [0.8, 0.9]	0.0087 ± 0.0017 ± 0.0000	0.0143 ± 0.0071 ± 0.0000	-
$M_{\mu\mu}$ = [4.3, 4.7]	p_T = [1.6, 3.6]	x_F = [-0.1, 0.0]	0.0162 ± 0.0019 ± 0.0000	0.0167 ± 0.0043 ± 0.0000	-
$M_{\mu\mu}$ = [4.3, 4.7]	p_T = [1.6, 3.6]	x_F = [0.0, 0.1]	0.0178 ± 0.0014 ± 0.0020	0.0192 ± 0.0033 ± 0.0000	-
$M_{\mu\mu}$ = [4.3, 4.7]	p_T = [1.6, 3.6]	x_F = [0.1, 0.2]	0.0209 ± 0.0013 ± 0.0017	0.0180 ± 0.0030 ± 0.0000	-
$M_{\mu\mu}$ = [4.3, 4.7]	p_T = [1.6, 3.6]	x_F = [0.2, 0.3]	0.0185 ± 0.0010 ± 0.0000	0.0225 ± 0.0026 ± 0.0000	-
$M_{\mu\mu}$ = [4.3, 4.7]	p_T = [1.6, 3.6]	x_F = [0.3, 0.4]	0.0124 ± 0.0008 ± 0.0011	0.0141 ± 0.0020 ± 0.0000	-
$M_{\mu\mu}$ = [4.3, 4.7]	p_T = [1.6, 3.6]	x_F = [0.4, 0.5]	0.0114 ± 0.0007 ± 0.0000	0.0087 ± 0.0015 ± 0.0000	-
$M_{\mu\mu}$ = [4.3, 4.7]	p_T = [1.6, 3.6]	x_F = [0.5, 0.6]	0.0081 ± 0.0006 ± 0.0007	0.0083 ± 0.0017 ± 0.0018	-
$M_{\mu\mu}$ = [4.3, 4.7]	p_T = [1.6, 3.6]	x_F = [0.6, 0.7]	0.0039 ± 0.0004 ± 0.0000	0.0071 ± 0.0016 ± 0.0019	-
$M_{\mu\mu}$ = [4.3, 4.7]	p_T = [1.6, 3.6]	x_F = [0.7, 0.8]	0.0024 ± 0.0004 ± 0.0004	0.0070 ± 0.0021 ± 0.0000	-
$M_{\mu\mu}$ = [4.3, 4.7]	p_T = [1.6, 3.6]	x_F = [0.8, 0.9]	0.0012 ± 0.0003 ± 0.0000	0.0037 ± 0.0026 ± 0.0000	-

Table 4.21: *Numerical values of 3D cross-section : $d^3\sigma/dM_{\mu\mu}dp_Tdx_F$ (2)*

$d^3\sigma/dM_{\mu\mu}dp_Tdx_F$: **mean ± statistic ± systematic (nb/GeV^2/nucleon)**					
Kinematics in $M_{\mu\mu}(GeV)$, $p_T(GeV)$ and x_F			PT cells	Al cell	W cells
$M_{\mu\mu}$ = [4.7, 5.4]	p_T = [0.0, 0.7]	x_F = [-0.1, 0.0]	0.0450 ± 0.0041 ± 0.0000	0.0397 ± 0.0083 ± 0.0000	0.0384 ± 0.0031 ± 0.0000
$M_{\mu\mu}$ = [4.7, 5.4]	p_T = [0.0, 0.7]	x_F = [0.0, 0.1]	0.0571 ± 0.0033 ± 0.0000	0.0380 ± 0.0063 ± 0.0000	0.0413 ± 0.0025 ± 0.0000
$M_{\mu\mu}$ = [4.7, 5.4]	p_T = [0.0, 0.7]	x_F = [0.1, 0.2]	0.0534 ± 0.0028 ± 0.0000	0.0437 ± 0.0060 ± 0.0069	0.0458 ± 0.0025 ± 0.0026
$M_{\mu\mu}$ = [4.7, 5.4]	p_T = [0.0, 0.7]	x_F = [0.2, 0.3]	0.0409 ± 0.0020 ± 0.0023	0.0496 ± 0.0054 ± 0.0000	0.0378 ± 0.0017 ± 0.0021
$M_{\mu\mu}$ = [4.7, 5.4]	p_T = [0.0, 0.7]	x_F = [0.3, 0.4]	0.0404 ± 0.0018 ± 0.0020	0.0367 ± 0.0046 ± 0.0000	0.0311 ± 0.0015 ± 0.0015
$M_{\mu\mu}$ = [4.7, 5.4]	p_T = [0.0, 0.7]	x_F = [0.4, 0.5]	0.0318 ± 0.0016 ± 0.0000	0.0262 ± 0.0039 ± 0.0000	0.0225 ± 0.0012 ± 0.0015
$M_{\mu\mu}$ = [4.7, 5.4]	p_T = [0.0, 0.7]	x_F = [0.5, 0.6]	0.0263 ± 0.0014 ± 0.0015	0.0262 ± 0.0039 ± 0.0000	0.0218 ± 0.0013 ± 0.0000
$M_{\mu\mu}$ = [4.7, 5.4]	p_T = [0.0, 0.7]	x_F = [0.6, 0.7]	0.0208 ± 0.0013 ± 0.0000	0.0164 ± 0.0035 ± 0.0000	0.0163 ± 0.0011 ± 0.0012
$M_{\mu\mu}$ = [4.7, 5.4]	p_T = [0.0, 0.7]	x_F = [0.7, 0.8]	0.0145 ± 0.0012 ± 0.0000	0.0162 ± 0.0037 ± 0.0000	0.0096 ± 0.0008 ± 0.0010
$M_{\mu\mu}$ = [4.7, 5.4]	p_T = [0.0, 0.7]	x_F = [0.8, 0.9]	0.0076 ± 0.0009 ± 0.0000	0.0163 ± 0.0061 ± 0.0000	0.0061 ± 0.0007 ± 0.0000
$M_{\mu\mu}$ = [4.7, 5.4]	p_T = [0.7, 1.1]	x_F = [-0.1, 0.0]	0.0765 ± 0.0075 ± 0.0000	0.0619 ± 0.0128 ± 0.0149	0.0665 ± 0.0054 ± 0.0060
$M_{\mu\mu}$ = [4.7, 5.4]	p_T = [0.7, 1.1]	x_F = [0.0, 0.1]	0.0823 ± 0.0053 ± 0.0000	0.0702 ± 0.0110 ± 0.0000	0.0761 ± 0.0046 ± 0.0061
$M_{\mu\mu}$ = [4.7, 5.4]	p_T = [0.7, 1.1]	x_F = [0.1, 0.2]	0.0882 ± 0.0047 ± 0.0050	0.0542 ± 0.0088 ± 0.0156	0.0891 ± 0.0045 ± 0.0000
$M_{\mu\mu}$ = [4.7, 5.4]	p_T = [0.7, 1.1]	x_F = [0.2, 0.3]	0.0736 ± 0.0035 ± 0.0000	0.0584 ± 0.0078 ± 0.0000	0.0677 ± 0.0030 ± 0.0000
$M_{\mu\mu}$ = [4.7, 5.4]	p_T = [0.7, 1.1]	x_F = [0.3, 0.4]	0.0620 ± 0.0030 ± 0.0000	0.0646 ± 0.0082 ± 0.0000	0.0504 ± 0.0024 ± 0.0025
$M_{\mu\mu}$ = [4.7, 5.4]	p_T = [0.7, 1.1]	x_F = [0.4, 0.5]	0.0494 ± 0.0026 ± 0.0000	0.0555 ± 0.0072 ± 0.0000	0.0428 ± 0.0022 ± 0.0000
$M_{\mu\mu}$ = [4.7, 5.4]	p_T = [0.7, 1.1]	x_F = [0.5, 0.6]	0.0416 ± 0.0023 ± 0.0000	0.0279 ± 0.0055 ± 0.0056	0.0318 ± 0.0019 ± 0.0020
$M_{\mu\mu}$ = [4.7, 5.4]	p_T = [0.7, 1.1]	x_F = [0.6, 0.7]	0.0281 ± 0.0020 ± 0.0022	0.0243 ± 0.0053 ± 0.0000	0.0255 ± 0.0016 ± 0.0000
$M_{\mu\mu}$ = [4.7, 5.4]	p_T = [0.7, 1.1]	x_F = [0.7, 0.8]	0.0160 ± 0.0016 ± 0.0018	0.0197 ± 0.0054 ± 0.0000	0.0173 ± 0.0014 ± 0.0015
$M_{\mu\mu}$ = [4.7, 5.4]	p_T = [0.7, 1.1]	x_F = [0.8, 0.9]	0.0092 ± 0.0014 ± 0.0000	0.0093 ± 0.0041 ± 0.0000	0.0063 ± 0.0009 ± 0.0000
$M_{\mu\mu}$ = [4.7, 5.4]	p_T = [1.1, 1.6]	x_F = [-0.1, 0.0]	0.0579 ± 0.0056 ± 0.0000	0.0521 ± 0.0103 ± 0.0000	0.0475 ± 0.0040 ± 0.0000
$M_{\mu\mu}$ = [4.7, 5.4]	p_T = [1.1, 1.6]	x_F = [0.0, 0.1]	0.0545 ± 0.0038 ± 0.0000	0.0654 ± 0.0099 ± 0.0101	0.0621 ± 0.0036 ± 0.0038
$M_{\mu\mu}$ = [4.7, 5.4]	p_T = [1.1, 1.6]	x_F = [0.1, 0.2]	0.0635 ± 0.0035 ± 0.0000	0.0628 ± 0.0081 ± 0.0000	0.0547 ± 0.0031 ± 0.0000
$M_{\mu\mu}$ = [4.7, 5.4]	p_T = [1.1, 1.6]	x_F = [0.2, 0.3]	0.0553 ± 0.0027 ± 0.0000	0.0589 ± 0.0067 ± 0.0000	0.0519 ± 0.0023 ± 0.0000
$M_{\mu\mu}$ = [4.7, 5.4]	p_T = [1.1, 1.6]	x_F = [0.3, 0.4]	0.0505 ± 0.0024 ± 0.0024	0.0422 ± 0.0054 ± 0.0000	0.0426 ± 0.0019 ± 0.0000
$M_{\mu\mu}$ = [4.7, 5.4]	p_T = [1.1, 1.6]	x_F = [0.4, 0.5]	0.0398 ± 0.0020 ± 0.0000	0.0351 ± 0.0049 ± 0.0000	0.0299 ± 0.0016 ± 0.0017
$M_{\mu\mu}$ = [4.7, 5.4]	p_T = [1.1, 1.6]	x_F = [0.5, 0.6]	0.0295 ± 0.0017 ± 0.0000	0.0304 ± 0.0048 ± 0.0000	0.0244 ± 0.0014 ± 0.0000
$M_{\mu\mu}$ = [4.7, 5.4]	p_T = [1.1, 1.6]	x_F = [0.6, 0.7]	0.0183 ± 0.0014 ± 0.0015	0.0220 ± 0.0043 ± 0.0000	0.0161 ± 0.0012 ± 0.0016
$M_{\mu\mu}$ = [4.7, 5.4]	p_T = [1.1, 1.6]	x_F = [0.7, 0.8]	0.0099 ± 0.0012 ± 0.0000	0.0150 ± 0.0041 ± 0.0000	0.0081 ± 0.0008 ± 0.0012
$M_{\mu\mu}$ = [4.7, 5.4]	p_T = [1.1, 1.6]	x_F = [0.8, 0.9]	0.0056 ± 0.0009 ± 0.0000	0.0106 ± 0.0034 ± 0.0000	0.0034 ± 0.0006 ± 0.0000
$M_{\mu\mu}$ = [4.7, 5.4]	p_T = [1.6, 3.6]	x_F = [-0.1, 0.0]	0.0105 ± 0.0012 ± 0.0000	0.0088 ± 0.0024 ± 0.0000	0.0098 ± 0.0008 ± 0.0000
$M_{\mu\mu}$ = [4.7, 5.4]	p_T = [1.6, 3.6]	x_F = [0.0, 0.1]	0.0133 ± 0.0009 ± 0.0000	0.0118 ± 0.0020 ± 0.0000	0.0125 ± 0.0008 ± 0.0000
$M_{\mu\mu}$ = [4.7, 5.4]	p_T = [1.6, 3.6]	x_F = [0.1, 0.2]	0.0123 ± 0.0008 ± 0.0000	0.0083 ± 0.0015 ± 0.0000	0.0129 ± 0.0007 ± 0.0000
$M_{\mu\mu}$ = [4.7, 5.4]	p_T = [1.6, 3.6]	x_F = [0.2, 0.3]	0.0105 ± 0.0006 ± 0.0006	0.0111 ± 0.0014 ± 0.0015	0.0101 ± 0.0005 ± 0.0000
$M_{\mu\mu}$ = [4.7, 5.4]	p_T = [1.6, 3.6]	x_F = [0.3, 0.4]	0.0085 ± 0.0005 ± 0.0000	0.0075 ± 0.0011 ± 0.0012	0.0086 ± 0.0004 ± 0.0004
$M_{\mu\mu}$ = [4.7, 5.4]	p_T = [1.6, 3.6]	x_F = [0.4, 0.5]	0.0070 ± 0.0004 ± 0.0000	0.0083 ± 0.0012 ± 0.0000	0.0067 ± 0.0003 ± 0.0004
$M_{\mu\mu}$ = [4.7, 5.4]	p_T = [1.6, 3.6]	x_F = [0.5, 0.6]	0.0054 ± 0.0004 ± 0.0000	0.0046 ± 0.0009 ± 0.0000	0.0051 ± 0.0003 ± 0.0000
$M_{\mu\mu}$ = [4.7, 5.4]	p_T = [1.6, 3.6]	x_F = [0.6, 0.7]	0.0027 ± 0.0003 ± 0.0003	0.0039 ± 0.0010 ± 0.0000	0.0029 ± 0.0002 ± 0.0000
$M_{\mu\mu}$ = [4.7, 5.4]	p_T = [1.6, 3.6]	x_F = [0.7, 0.8]	0.0017 ± 0.0002 ± 0.0000	0.0027 ± 0.0009 ± 0.0000	0.0013 ± 0.0001 ± 0.0002
$M_{\mu\mu}$ = [4.7, 5.4]	p_T = [1.6, 3.6]	x_F = [0.8, 0.9]	0.0007 ± 0.0002 ± 0.0000	0.0011 ± 0.0005 ± 0.0000	0.0006 ± 0.0001 ± 0.0000

Table 4.22: *Numerical values of 3D cross-section : $d^3\sigma/dM_{\mu\mu}dp_Tdx_F(3)$*

$d^3\sigma/dM_{\mu\mu}dp_Tdx_F$: **mean ± statistic ± systematic (nb/GeV^2/nucleon)**					
Kinematics in $M_{\mu\mu}(GeV)$, $p_T(GeV)$ and x_F			PT cells	Al cell	W cells
$M_{\mu\mu}$ = [5.4, 8.5]	p_T = [0.0, 0.7]	x_F = [-0.1, 0.0]	0.0089 ± 0.0008 ± 0.0000	0.0089 ± 0.0016 ± 0.0000	0.0072 ± 0.0006 ± 0.0000
$M_{\mu\mu}$ = [5.4, 8.5]	p_T = [0.0, 0.7]	x_F = [0.0, 0.1]	0.0113 ± 0.0007 ± 0.0008	0.0067 ± 0.0012 ± 0.0012	0.0102 ± 0.0006 ± 0.0000
$M_{\mu\mu}$ = [5.4, 8.5]	p_T = [0.0, 0.7]	x_F = [0.1, 0.2]	0.0109 ± 0.0006 ± 0.0006	0.0078 ± 0.0012 ± 0.0016	0.0101 ± 0.0006 ± 0.0000
$M_{\mu\mu}$ = [5.4, 8.5]	p_T = [0.0, 0.7]	x_F = [0.2, 0.3]	0.0105 ± 0.0005 ± 0.0005	0.0086 ± 0.0010 ± 0.0000	0.0081 ± 0.0004 ± 0.0005
$M_{\mu\mu}$ = [5.4, 8.5]	p_T = [0.0, 0.7]	x_F = [0.3, 0.4]	0.0100 ± 0.0004 ± 0.0000	0.0091 ± 0.0010 ± 0.0011	0.0073 ± 0.0003 ± 0.0004
$M_{\mu\mu}$ = [5.4, 8.5]	p_T = [0.0, 0.7]	x_F = [0.4, 0.5]	0.0085 ± 0.0004 ± 0.0004	0.0062 ± 0.0008 ± 0.0000	0.0062 ± 0.0003 ± 0.0004
$M_{\mu\mu}$ = [5.4, 8.5]	p_T = [0.0, 0.7]	x_F = [0.5, 0.6]	0.0058 ± 0.0003 ± 0.0004	0.0052 ± 0.0008 ± 0.0008	0.0047 ± 0.0003 ± 0.0003
$M_{\mu\mu}$ = [5.4, 8.5]	p_T = [0.0, 0.7]	x_F = [0.6, 0.7]	0.0048 ± 0.0003 ± 0.0003	0.0040 ± 0.0007 ± 0.0000	0.0041 ± 0.0002 ± 0.0000
$M_{\mu\mu}$ = [5.4, 8.5]	p_T = [0.0, 0.7]	x_F = [0.7, 0.8]	0.0029 ± 0.0002 ± 0.0000	0.0039 ± 0.0007 ± 0.0000	0.0020 ± 0.0002 ± 0.0002
$M_{\mu\mu}$ = [5.4, 8.5]	p_T = [0.0, 0.7]	x_F = [0.8, 0.9]	0.0012 ± 0.0002 ± 0.0002	0.0019 ± 0.0006 ± 0.0000	0.0007 ± 0.0001 ± 0.0000
$M_{\mu\mu}$ = [5.4, 8.5]	p_T = [0.7, 1.1]	x_F = [-0.1, 0.0]	0.0146 ± 0.0014 ± 0.0000	0.0108 ± 0.0026 ± 0.0000	0.0131 ± 0.0012 ± 0.0000
$M_{\mu\mu}$ = [5.4, 8.5]	p_T = [0.7, 1.1]	x_F = [0.0, 0.1]	0.0184 ± 0.0012 ± 0.0000	0.0157 ± 0.0024 ± 0.0000	0.0150 ± 0.0010 ± 0.0010
$M_{\mu\mu}$ = [5.4, 8.5]	p_T = [0.7, 1.1]	x_F = [0.1, 0.2]	0.0195 ± 0.0011 ± 0.0000	0.0124 ± 0.0019 ± 0.0000	0.0160 ± 0.0009 ± 0.0000
$M_{\mu\mu}$ = [5.4, 8.5]	p_T = [0.7, 1.1]	x_F = [0.2, 0.3]	0.0187 ± 0.0009 ± 0.0000	0.0185 ± 0.0020 ± 0.0000	0.0146 ± 0.0007 ± 0.0008
$M_{\mu\mu}$ = [5.4, 8.5]	p_T = [0.7, 1.1]	x_F = [0.3, 0.4]	0.0158 ± 0.0007 ± 0.0000	0.0150 ± 0.0017 ± 0.0000	0.0128 ± 0.0006 ± 0.0007
$M_{\mu\mu}$ = [5.4, 8.5]	p_T = [0.7, 1.1]	x_F = [0.4, 0.5]	0.0145 ± 0.0007 ± 0.0000	0.0139 ± 0.0017 ± 0.0000	0.0110 ± 0.0005 ± 0.0006
$M_{\mu\mu}$ = [5.4, 8.5]	p_T = [0.7, 1.1]	x_F = [0.5, 0.6]	0.0107 ± 0.0005 ± 0.0006	0.0104 ± 0.0013 ± 0.0000	0.0088 ± 0.0005 ± 0.0005
$M_{\mu\mu}$ = [5.4, 8.5]	p_T = [0.7, 1.1]	x_F = [0.6, 0.7]	0.0073 ± 0.0005 ± 0.0000	0.0062 ± 0.0011 ± 0.0012	0.0047 ± 0.0003 ± 0.0004
$M_{\mu\mu}$ = [5.4, 8.5]	p_T = [0.7, 1.1]	x_F = [0.7, 0.8]	0.0047 ± 0.0004 ± 0.0004	0.0069 ± 0.0014 ± 0.0000	0.0030 ± 0.0003 ± 0.0000
$M_{\mu\mu}$ = [5.4, 8.5]	p_T = [0.7, 1.1]	x_F = [0.8, 0.9]	0.0012 ± 0.0002 ± 0.0000	0.0014 ± 0.0006 ± 0.0000	0.0009 ± 0.0001 ± 0.0000
$M_{\mu\mu}$ = [5.4, 8.5]	p_T = [1.1, 1.6]	x_F = [-0.1, 0.0]	0.0120 ± 0.0011 ± 0.0000	0.0114 ± 0.0023 ± 0.0000	0.0100 ± 0.0009 ± 0.0000
$M_{\mu\mu}$ = [5.4, 8.5]	p_T = [1.1, 1.6]	x_F = [0.0, 0.1]	0.0149 ± 0.0010 ± 0.0000	0.0096 ± 0.0018 ± 0.0000	0.0134 ± 0.0008 ± 0.0009
$M_{\mu\mu}$ = [5.4, 8.5]	p_T = [1.1, 1.6]	x_F = [0.1, 0.2]	0.0159 ± 0.0009 ± 0.0009	0.0135 ± 0.0018 ± 0.0000	0.0115 ± 0.0007 ± 0.0000
$M_{\mu\mu}$ = [5.4, 8.5]	p_T = [1.1, 1.6]	x_F = [0.2, 0.3]	0.0142 ± 0.0007 ± 0.0000	0.0140 ± 0.0016 ± 0.0000	0.0112 ± 0.0005 ± 0.0006
$M_{\mu\mu}$ = [5.4, 8.5]	p_T = [1.1, 1.6]	x_F = [0.3, 0.4]	0.0131 ± 0.0006 ± 0.0006	0.0124 ± 0.0013 ± 0.0000	0.0100 ± 0.0004 ± 0.0006
$M_{\mu\mu}$ = [5.4, 8.5]	p_T = [1.1, 1.6]	x_F = [0.4, 0.5]	0.0105 ± 0.0005 ± 0.0000	0.0076 ± 0.0011 ± 0.0012	0.0084 ± 0.0004 ± 0.0004
$M_{\mu\mu}$ = [5.4, 8.5]	p_T = [1.1, 1.6]	x_F = [0.5, 0.6]	0.0085 ± 0.0004 ± 0.0000	0.0069 ± 0.0010 ± 0.0000	0.0060 ± 0.0003 ± 0.0004
$M_{\mu\mu}$ = [5.4, 8.5]	p_T = [1.1, 1.6]	x_F = [0.6, 0.7]	0.0050 ± 0.0003 ± 0.0003	0.0040 ± 0.0008 ± 0.0000	0.0044 ± 0.0003 ± 0.0000
$M_{\mu\mu}$ = [5.4, 8.5]	p_T = [1.1, 1.6]	x_F = [0.7, 0.8]	0.0025 ± 0.0003 ± 0.0000	0.0025 ± 0.0006 ± 0.0000	0.0021 ± 0.0002 ± 0.0000
$M_{\mu\mu}$ = [5.4, 8.5]	p_T = [1.1, 1.6]	x_F = [0.8, 0.9]	0.0007 ± 0.0002 ± 0.0000	0.0020 ± 0.0010 ± 0.0000	0.0007 ± 0.0001 ± 0.0000
$M_{\mu\mu}$ = [5.4, 8.5]	p_T = [1.6, 3.6]	x_F = [-0.1, 0.0]	0.0026 ± 0.0003 ± 0.0000	0.0026 ± 0.0005 ± 0.0000	0.0020 ± 0.0002 ± 0.0000
$M_{\mu\mu}$ = [5.4, 8.5]	p_T = [1.6, 3.6]	x_F = [0.0, 0.1]	0.0030 ± 0.0002 ± 0.0000	0.0030 ± 0.0005 ± 0.0000	0.0031 ± 0.0002 ± 0.0000
$M_{\mu\mu}$ = [5.4, 8.5]	p_T = [1.6, 3.6]	x_F = [0.1, 0.2]	0.0032 ± 0.0002 ± 0.0002	0.0024 ± 0.0004 ± 0.0004	0.0032 ± 0.0002 ± 0.0002
$M_{\mu\mu}$ = [5.4, 8.5]	p_T = [1.6, 3.6]	x_F = [0.2, 0.3]	0.0030 ± 0.0002 ± 0.0002	0.0023 ± 0.0003 ± 0.0000	0.0026 ± 0.0001 ± 0.0002
$M_{\mu\mu}$ = [5.4, 8.5]	p_T = [1.6, 3.6]	x_F = [0.3, 0.4]	0.0026 ± 0.0001 ± 0.0000	0.0017 ± 0.0002 ± 0.0000	0.0023 ± 0.0001 ± 0.0000
$M_{\mu\mu}$ = [5.4, 8.5]	p_T = [1.6, 3.6]	x_F = [0.4, 0.5]	0.0020 ± 0.0001 ± 0.0000	0.0022 ± 0.0003 ± 0.0000	0.0018 ± 0.0001 ± 0.0000
$M_{\mu\mu}$ = [5.4, 8.5]	p_T = [1.6, 3.6]	x_F = [0.5, 0.6]	0.0014 ± 0.0001 ± 0.0000	0.0012 ± 0.0002 ± 0.0000	0.0013 ± 0.0001 ± 0.0000
$M_{\mu\mu}$ = [5.4, 8.5]	p_T = [1.6, 3.6]	x_F = [0.6, 0.7]	0.0008 ± 0.0001 ± 0.0001	0.0008 ± 0.0002 ± 0.0000	0.0007 ± 0.0000 ± 0.0001
$M_{\mu\mu}$ = [5.4, 8.5]	p_T = [1.6, 3.6]	x_F = [0.7, 0.8]	0.0004 ± 0.0001 ± 0.0000	0.0004 ± 0.0001 ± 0.0000	0.0002 ± 0.0000 ± 0.0000
$M_{\mu\mu}$ = [5.4, 8.5]	p_T = [1.6, 3.6]	x_F = [0.8, 0.9]	0.0001 ± 0.0000 ± 0.0000	0.0004 ± 0.0001 ± 0.0000	0.0001 ± 0.0000 ± 0.0000

Data selection of beam flux Estimation

The data selection of the beam flux estimation are listed below. The data used in this analysis was collected between May to November in 2018 is divided into 9 periods (P00-P08). For each period, it is further divided into sub-periods with opposite polarization of the PT cells. Details on the data-periods, as the polarization states and run-number intervals defining each sub-period, are are listed in Table. 4.3.

Table 4.23: *2018 Periods.*

Period-sub(Polarization)	First run	Last run	Start date	End date	Nspill
P00-SP1 (−+)	283117	283285	2018-05-16	2018-05-23	23600
P00-SP2 (+−)	283338	283464	2018-05-25	2018-05-30	14263
P00-SP3 (+−)	283588	283705	2018-06-08	2018-06-13	13560
P01-SP1 (−+)	283849	284003	2018-06-21	2018-06-26	15462
P01-SP2 (+−)	284022	284233	2018-06-27	2018-07-03	15695
P02-SP1 (+−)	284348	284469	2018-07-06	2018-07-11	12069
P02-SP2 (+−)	284471	284623	2018-07-11	2018-07-17	17569
P02-SP3 (−+)	284642	284802	2018-07-18	2018-07-25	18690
P02-SP4 (−+)	284815	284935	2018-07-26	2018-07-31	13871
P03-SP1 (−+)	284941	285141	2018-08-01	2018-08-08	27344
P03-SP2 (+−)	285149	285333	2018-08-09	2018-08-15	19195
P04-SP1 (+−)	285359	285512	2018-08-16	2018-08-21	13143
P04-SP2 (+−)	285517	285646	2018-08-22	2018-08-27	12796
P04-SP3 (−+)	285707	285844	2018-08-31	2018-09-05	19614
P05-SP1 (−+)	285865	285994	2018-09-05	2018-09-11	15376
P05-SP2 (+−)	286019	286103	2018-09-12	2018-09-17	12529
P06-SP1 (+−)	286170	286324	2018-09-20	2018-09-26	16734
P06-SP2 (−+)	286330	286462	2018-09-26	2018-10-01	16924
P07-SP1 (−+)	286481	286742	2018-10-03	2018-10-10	11496
P07-SP2 (−+)	286749	286929	2018-10-11	2018-10-17	21428
P07-SP3 (+−)	286941	287096	2018-10-17	2018-10-24	13732
P07-SP4 (+−)	287107	287256	2018-10-25	2018-10-30	13212
P08-SP1 (−+)	287296	287404	2018-11-01	2018-11-06	14686
P08-SP2 (+−)	287458	287537	2018-11-09	2018-11-12	7435

- Random triggers uesd.
  PHAST::PaEvent::MasterTriggerMask() is used to chose random trigger to avoid the ambiguous when firing both random trigger and physics trigger at the same time even though the chance of such case is rare.

- Good periods

  In this analysis, P00 is not used due to the unstable beam condition.

- Good spills selected

The quality of the data was checked on spill-by-spill and run-by-run basis. Basic quantities like number of tracks, number of verities, rate of triggers, etc. The spills or runs gives the unstable values from neighboring channels are removed from analysis. The quantities checked are listed below :

- number of beam particles divided by number of events.
- number of beam particles divided by number of primary vertices
- number of hits per beam track divided by number of beam particles
- number of primary vertices divided by number of events
- number of outgoing tracks divided by number of events
- number of outgoing tracks divided by number of events
- number of outgoing particles from primary vertex divided by number of primary vertices
- number of outgoing particles from primary vertex divided by number of events
- number of hits in outgoing particles divided by number of outgoing particles
- number of $\mu^{\pm}$ tracks divided by number of events
- number of $\mu^{\pm}$ tracks from primary vertex divided by number of events
- $\sum \chi^2$ of outgoing particles divided by number of outgoing particles
- $\sum \chi^2$ of all vertices divided by number of all vertices
- Trigger rates (LAS×MT, LAS×OT, LAS×LAS)

- Good spill time selected

The beam delivered from SPS has strong gradient in the beginning of the spill and the end of the spill. This could affect the perfomance of the detector and DAQ system. Therefore spill time is selected only within the period of stable beam extraction As show in Fig. 4.9, the beam extraction is distributed in $1.0s < t_{spill} < 5.6s$, Δt_{spill} = 4.6s. The good spill list is a shared documents used in every 2018 COMPASS data analysis. It can be found under COMPASS Twiki (password protected).

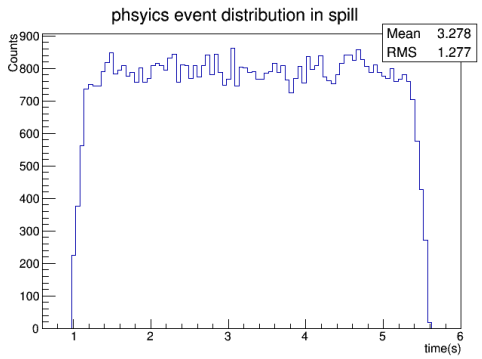

Figure 4.9: *The physics event distribution in spill time is same as the beam time = [1.0, 5.6] second in spill time.*

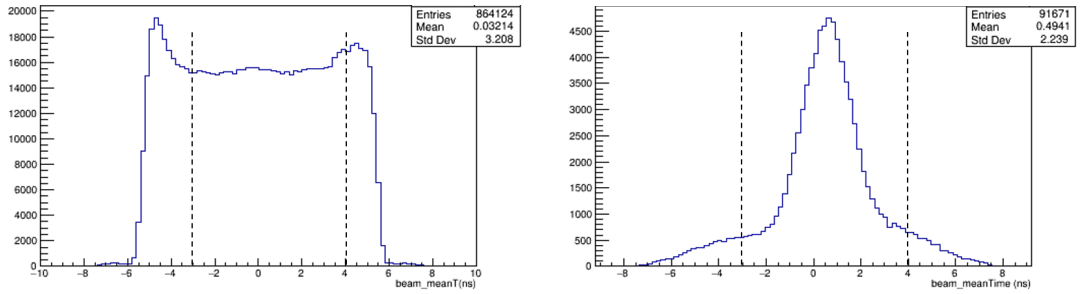

(a) **(b)**

Figure 4.10: *Beam time distribution of (a) random trigger (b) physics trigger. The dot lines shows the cut regions which are in the safe regions for both trigger types.*

- Beam time selected

  In flux calculation, we ask for beam time, $-3.0ns < t_{beam} < 4.0ns$ ($\Delta t_{beam} = 7\ ns$). Fig. 4.10 shows the beam time distribution from random triggers(left) and physics triggers(right). The chosen $-3.0ns < t_{beam} < 4.0ns$ is in the range of the correlated time peak of the dimuon event for physics triggers and the flat part of the beam time distribution for random trigger. The same cut must be applied in the selection of physics events to ensure the correction normalization of the cross section.

- Beam track pass through target

  In flux calculation, we ask for the beam tracks pass through target region after the extrapolation. Beam tracks are extrapolated to the upstream surface of NH_3 target($Z = -294.5\ cm$) and downstream surface of selected W target ($Z = -10\ cm$). The extrapolation is within the transverse ellipsoid same as selected-vertex region in X and Y directions, $\frac{x^2_{extra}}{(1.9cm)^2} + \frac{(y_{extra}-0.15cm)^2}{(1.3cm)^2} < 1.0$. Fig. 4.11 shows the vertex distribution of physics events of P04 period. The cut region is drawn with the dot line.

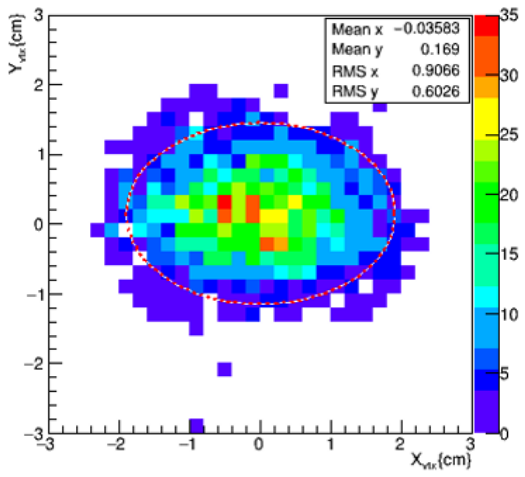

Figure 4.11: *The vertex distribution of physics events. The cut region is drawn with the dot line.*

Data selection of DAQ and VETO lifetime estimation

In the estimation of DAQ lifetime, there are two cuts need to be applied :

- Channels of Misc scaler used.

  The channels of Misc scaler used in DAQ lifetime analysis are $ch2 = N_{att}^{RT}$ and $ch13 = N_{att}^{FLT}$.

Table 4.24: *Misc Scaler channels with* $N_{TrigAtt}$.

Ch	Name
2	Random
13	FLT
16	LASTxMT
18	LASTxLAST
20	LASTxOT

- Good spills selected.

  The quality of the data was checked on spill-by-spill and run-by-run basis. Basic quantities like number of tracks, number of verities, rate of triggers, etc. The spills or runs gives the unstable values from neighboring channels are removed from analysis. The good spill list is a shared documents used in every 2018 COMPASS data analysis. It can be found under COMPASS Twiki (password protected).

- Good spill time selected, $1.0s < t_{spill} < 5.6s$, $\Delta t_{spill} = 4.6$s.

  The beam delivered from SPS has strong gradient in the beginning of the spill and the end of the spill. This could affect the perfomance of the detector and DAQ system. Therefore spill time is selected only within the period of stable beam extraction As show in Fig. 4.9, the beam extraction is distributed in $1.0s < t_{spill} < 5.6s$, $\Delta t_{spill} = 4.6$s.

- Good periods, P01-P08 (cut P00).

  Run number of each periods are described in Table. . P00 is not used because of the unstable beam condition.

Real data selection of the dimuon events

The following cuts are applied in the selection of Drell-Yan dimuon events :

- Select good dimuon events from the best primary vertex
  All the combinations of the opposite charged particles crossing more than 30 radiation length ($X/X0 \geq 30$) are considered and emerging from a common vertex are identified as Drell-Yan pairs. The best primary vertex (BPV) of the dimuon pairs are chosen by PHAST function (PaEvent::iBestCoralPrimaryVertex()). If there is no BPV identified by CORAL, the primary vertex has the smallest fitting χ^2_{vertex} is considered.

- Dimuon mass region
  DY mass region is selected. However different target cover different mass region due to the mass resolution along Z_{vtx}. The background of the selected mass region expected to be below 5%. For NH_3 and Al targets : $4.3 < M_{\mu\mu} < 8.5$ GeV/c^2 ; For W targets : $4.7 < M_{\mu\mu} < 8.5$ GeV/c^2 .

- Dimuon triggers
  LAS⊗LAS and LAS⊗OT triggers given by trigger mask are used. LAS⊗MT is ignored due to the high beam-decay muon contamination. Dimuon-trigger used are validated by extrapolation of muon tracks to the active area of respective hodoscopes fired. If there is events satisfy more than one di-muon trigger, the priority is given first to LAS⊗LAS and then to LAS⊗OT.

- Cut 2.5cm on the edges of Hodoscope deadzone
  The boarder of the hodoscope deadzones are difficult to be measured. Trigger experts in COMPASS suggests to remove the muon tracks passing the area on the edge of deadzone by 2.5cm for the hodoscopes of LAS(HGO1Y1, HGO2Y1, HGO2Y2) and Out(HO03Y1, HO04Y1, HO04Y2) triggers.

- Long muon tracks
  To ensure muon track pass the first Muon Wall A (at Z around 300cm) and last Muon Wall B (at Z around 1500cm). We ask PaTrack::ZLast$_\mu$ $>$ 1500 cm and PaTrack::ZFirst$_\mu$ $<$ 300 cm

- Good reconstruction quality in space
  To ensure the muon tracks are reconstructed in a good condition, we ask the reduced χ^2 of muons in space is $\chi^2/ndf < 10$.

- Good time correlation between tracks
  Good time correlation between muons and beams can help us to remove fake muon pairs. We ask the time of muons defined and $|t_{\mu^+} - t_{\mu^-}| < 3$ ns and $|t_{beam} - t_{\mu^\pm}| < 3$ ns. The time distributions of t_{beam}, $|t_{beam} - t_{\mu^\pm}|$, $|t_{\mu^+} - t_{\mu^-}|$ of LAS×LAS and LAS×OT are shown in Fig. 4.13. The cut limitations are chosen in the safe regions.

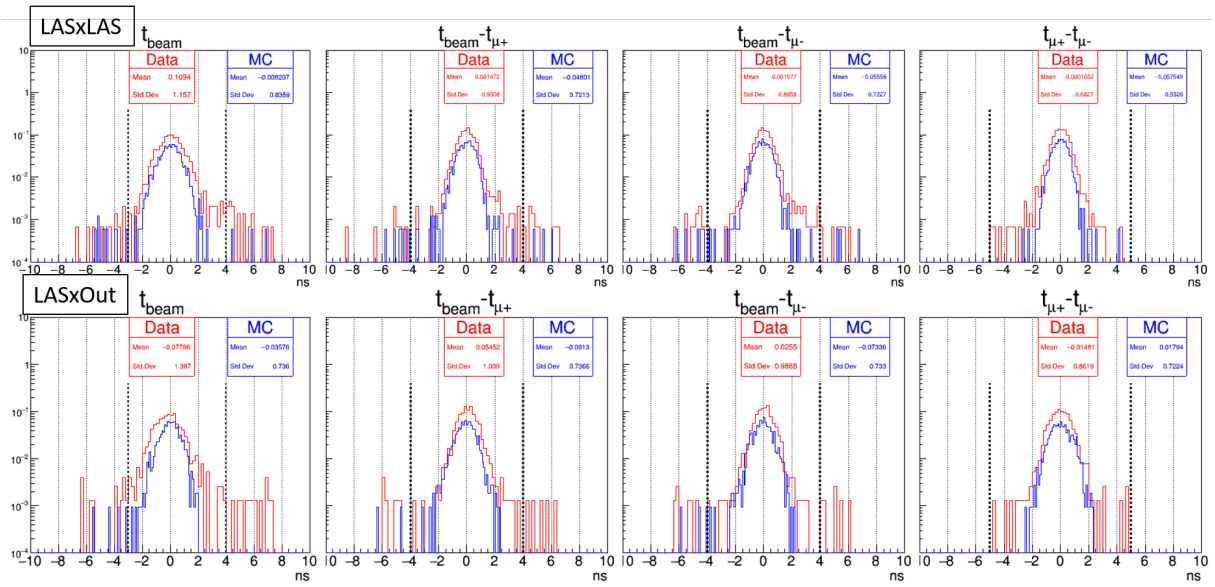

Figure 4.12: *The time distributions of t_{beam}, $|t_{beam} - t_{\mu^{\pm}}|$, $|t_{\mu^+} - t_{\mu^-}|$ of LAS×LAS and LAS×OT. the black dash lines are the cut limitation used in this analysis. Distribution is red is from real data. Distribution in blue is from MC data.*

- Dimuon kinematics in p_T, x_F, x_π, x_N
  The cuts on kinematics of p_T and x_F are decided by the 1D acceptance. Within the chosen p_T and x_F regions, the 1D acceptance is larger than 1% and the relative statistical error of it is less than 10 %. The discussion of acceptance will be further liberated in Sec.3.4. For x_π and x_N, full ranges are used.

  (1) $0.0 < p_T < 3.6$ GeV/c

  (2) $-0.10 < x_F < 0.70$ for LAST⊗LAST

  (3) $0.20 < x_F < 0.9$ for OUT⊗LAST

  (4) $0.0 < x_\pi < 1.0$

  (5) $0.0 < x_N < 1.0$

- Good spills selected
  This cut is the same as the one applied in the calculation of beam flux (Sec. 3.1). One can find more details there.

- Good spill time selected
  The spill time is selected only within the period of stable beam extraction, $1.0s < t_{spill} < 5.6s$. This cut is the same as the one applied in the calculation of beam flux in Sec. 3.1 . One can find more details there.

- Good periods selected
  There are 9 period in 2018 data-taking , P00-P08. However P00 is not used due to unstable of the beam condition. This cut is the same as the one applied in the calculation of beam flux (Sec. 3.1). One can find more details there.

- Beam time selected
  In flux calculation, we ask for beam time, $-3.0ns < t_{beam} < 4.0ns$, therefore the

same cut must be applied in the selection of dimuon events to ensure the correction normalization of the cross section. One can find more details in Sec. 3.1.

- Beam track pass through targets
  In flux calculation, we ask for the beam tracks pass through target region after the extrapolation : $\frac{x_{extra}^2}{(1.9cm)^2} + \frac{(y_{extra}-0.15cm)^2}{(1.3cm)^2} < 1.0$ at the upstream surface of NH_3 target($Z = -294.5\ cm$) and downstream surface of selected W target ($Z = -10\ cm$), therefore the same cut apply in the selection of dimuon events to ensure the correction normalization of the cross section. One can find more details in Sec. 3.1.

- Target region in X_{vtx} and Y_{vtx}
  The selected vertex is within the transverse ellipsoid, $\frac{X_{vtx}^2}{(1.9cm)^2} + \frac{(Y_{vtx}-0.15cm)^2}{(1.3cm)^2} < 1.0$

- Target region in Z_{vtx}
  We separate the them into 5 regions: NH_3 1^{st} cell, NH_3 2^{nd} cell, Al, W 1^{st} cell, and W $2^{nd}cell$.

  - PT 1^{st} cell : Z_{vtx} = [-294.5, -239.4] cm
  - PT 1^{nd} cell : Z_{vtx} = [-219.1, -163.9] cm
  - Al cell : Z_{vtx} = [-80.0, -60.0] cm (reality in [-73.5, -66.5] cm)
  - W 1^{st} cell : Z_{vtx} = [-40.0, -20.0] cm (reality in [-30.0, -10.0] cm)
  - W 2^{nd} cell : Z_{vtx} = [-20.0, -10.0] cm

  For NH_3 targets and W_{2nd} cell, the selected Z_{vtx} positions are same as the real position given by survey. However it is not the case for Al and W_{1st} targets. In order to increase the statistics, we try to include the migrated events due to the position resolution. The selected Z_{vtx} positions are larger than the real range. **plots**

Table. 4.25 gives the statistics of cut flow of the whole 2018 data. There are only $5 \sim 10\%$ dimuon events left after all the selections.

Table 4.25: *Data Flow of all 2018 data.*

Selected good dimuon pairs and $4.3 < M_{\mu\mu}/(\mathbf{GeV}/c^2) < 8.5$			
	Selections	**LAST⊗LAST**	**LAST⊗OT**
1	Trigger validation	117136 (100.00%)	104686 (100.00%)
2	Cut 2.5cm in Hodoscope deadzone	103246 (88.14%)	98618 (94.20%)
3	Long muon tracks : $ZFirst_{mu^{\pm}}$(cm)>300 and $ZLast_{mu^{\pm}}$(cm)< 1500	102944 (87.88%)	97913 (93.53%)
4	Good time correlation between muon tracks : $\lvert t_{mu^+}$-$t_{mu^-}\rvert$(ns)<3	101494 (86.65%)	92708 (88.56%)
5	Good reconstruction quality in space : mu^{pm} $chi2/ndf$<10.0	101041 (86.26%)	92381 (88.25%)
6	Dimuon kinematics in p_T selected	100160 (85.51%)	91930 (87.81%)
7	Dimuon kinematics in x_{pi}, x_N, x_F selected	95983 (81.94%)	84960 (81.16%)
8	Good spill selected	86564 (73.90%)	76872 (73.43%)
9	Xvtx and Yvtx selected : $[(X_{vtx} - 0.00)/1.9]^2 + [(Y_{vtx} - 0.15)/1.3]^2(cm) < 1$	76990 (65.73%)	67569 (64.54%)
10	Good spill time selected : 1.0<t_{spill}(s)<5.6	76910 (65.66%)	67515 (64.49%)
11	Beam time selected : -3<$t_{beam}(ns)$<4	74768 (63.83%)	65457 (62.53%)
12	Beam track pass through targets	72858 (62.20%)	63687 (60.84%)
13	Good time correlation between beam and muon : $\lvert t_{beam} - t_{mu^{\pm}}\rvert(ns) < 3$	72308 (61.73%)	62855 (60.04%)
$4.3 < M_{\mu\mu}/(\mathrm{GeV}/c^2) < 8.5$			
14	PT 1^{st} cell : Z_{vtx} = [-294.5, -239.4] cm	14409 (12.30%)	8375 (8.00%)
15	PT 2^{nd} cell : Z_{vtx} = [-219.1, -163.9] cm	11454 (9.78%)	7219 (6.90%)
16	Al cell : Z_{vtx} = [-80.0, -60.0] cm	3895 (3.33%)	2895 (2.77%)
$4.7 < M_{\mu\mu}/(\mathrm{GeV}/c^2) < 8.5$			
17	W 1^{st} cell : Z_{vtx} = [-40.0, -20.0] cm	10393 (8.87%)	8283 (7.91%)
18	W 2^{nd} cell : Z_{vtx} = [-20.0, -10.0] cm	6421 (5.48%)	5800 (5.54%)

MC selection of the dimuon events

For N_i^{gen} :

- Dimuon pairs selected
  Primary vertex with 2 reconstructed muons (PID=5 for μ^+ and PID=6 for μ^-).

- Dimuon mass region in mass
  For NH_3 and Al targets : $4.3 < M_{\mu\mu} < 8.5$ GeV/c^2 ; For W target : $4.7 < M_{\mu\mu} < 8.5$ GeV/c^2.

- Dimuon kinematics in p_T, x_F, x_π, x_N
  $0.0 < p_T < 3.6$ GeV/c, $-0.1 < x_F < 0.9$, $0.0 < x_\pi < 1.0$, $0.0 < x_N < 1.0$.

- Cuts on beams
  The reconstruction efficiency of the beam telescope is already taken into account in the beam flux extraction. Thus, in order to avoid double counting of this efficiency, its effect needs to be "canceled", by considering only events with at least one reconstructed beam track that crosses the two extreme targets within the limits of the transverse ellipsoid, in the time interval defined, for both the generated and the reconstructed MC samples.

  (1) $-3.0ns < t_{beam} < 4.0ns$

  (2) Beam tracks are extrapolated to the upstream surface of NH_3 target($Z = -294.5\ cm$) and downstream surface of selected W target ($Z = -10\ cm$). And they are satisfied $\frac{x_{extra}^2}{(1.9cm)^2} + \frac{(y_{extra}-0.15cm)^2}{(1.3cm)^2} < 1.0$.

- Selected target region in X_{vtx} and Y_{vtx} : $\frac{X_{vtx}^2}{(1.9cm)^2} + \frac{(Y_{vtx}-0.15cm)^2}{(1.3cm)^2} < 1.0$

- Selected target region in Z_{vtx}
  One has to pay attention the position of Al cell and W 1^{st} cell are in the real position. In MC generated level, there is no migration effect to be considered.

  - PT 1^{st} cell : [-294.5, -239.4] cm
  - PT 1^{nd} cell : [-219.1, -163.9] cm
  - Al cell : [-73.5, -66.5] cm (real length)
  - W 1^{st} cell : [-30.0, -20.0] cm (real length)
  - W 2^{nd} cell : [-20.0, -10.0] cm

For N_i^{rec} : They are almost the same as the selections of real data except for the spill time selections, the bad spill selection, and bad run exclusion. There is no simulation of spills in MC.

- Select good dimuon events from the best primary vertex
  All the combinations of the opposite charged particles crossing more than 30 radiation length ($X/X0 \geq 30$) are considered and emerging from a common vertex are identified as Drell-Yan pairs. The best primary vertex (BPV) of the dimuon pairs are chosen by PHAST function (PaEvent::iBestCoralPrimaryVertex()). If there is no BPV identified by CORAL, the primary vertex has the smallest fitting χ^2_{vertex} is considered.

- Dimuon mass region
  DY mass region is selected. However different target cover different mass region due to the mass resolution along Z_{vtx}. The background of the selected mass region expected to be below 5%. For NH_3 and Al targets : $4.3 < M_{\mu\mu} < 8.5$ GeV/c^2 ; For W targets : $4.7 < M_{\mu\mu} < 8.5$ GeV/c^2.

- Dimuon triggers
  LAS⊗LAS and LAS⊗OT triggers given by trigger mask are used. LAS⊗MT is ignored due to the high beam-decay muon contamination. Dimuon-trigger used are validated by extrapolation of muon tracks to the active area of respective hodoscopes fired. If there is events satisfy more than one di-muon trigger, the priority is given first to LAS⊗LAS and then to LAS⊗OT.

- Cut 2.5cm on the edges of Hodoscope deadzone
  The boarder of the hodoscope deadzones are difficult to be measured. Trigger experts in COMPASS suggests to remove the muon tracks passing the area on the edge of deadzone by 2.5cm for the hodoscopes of LAS(HGO1Y1, HGO2Y1, HGO2Y2) and Out(HO03Y1, HO04Y1, HO04Y2) triggers.

- Long muon tracks
  To ensure muon track pass the first Muon Wall A (at Z around 300cm) and last Muon Wall B (at Z around 1500cm). We ask PaTrack::ZLast$_\mu$ $>$ 1500 cm and PaTrack::ZFirst$_\mu$ $<$ 300 cm

- Good reconstruction quality in space
  To ensure the muon tracks are reconstructed in a good condition, we ask the reduced χ^2 of muons in space is $\chi^2/ndf < 10$.

- Good time correlation between tracks
  Good time correlation between muons and beams can help us to remove fake muon pairs. We ask the time of muons defined and $|t_{\mu^+} - t_{\mu^-}| < 3$ ns and $|t_{beam} - t_{\mu^\pm}| < 3$ ns. The time distributions of t_{beam}, $|t_{beam} - t_{\mu^\pm}|$, $|t_{\mu^+} - t_{\mu^-}|$ of LAS×LAS and LAS×OT are shown in Fig. 4.13. The cut limitations are chosen in the safe regions.

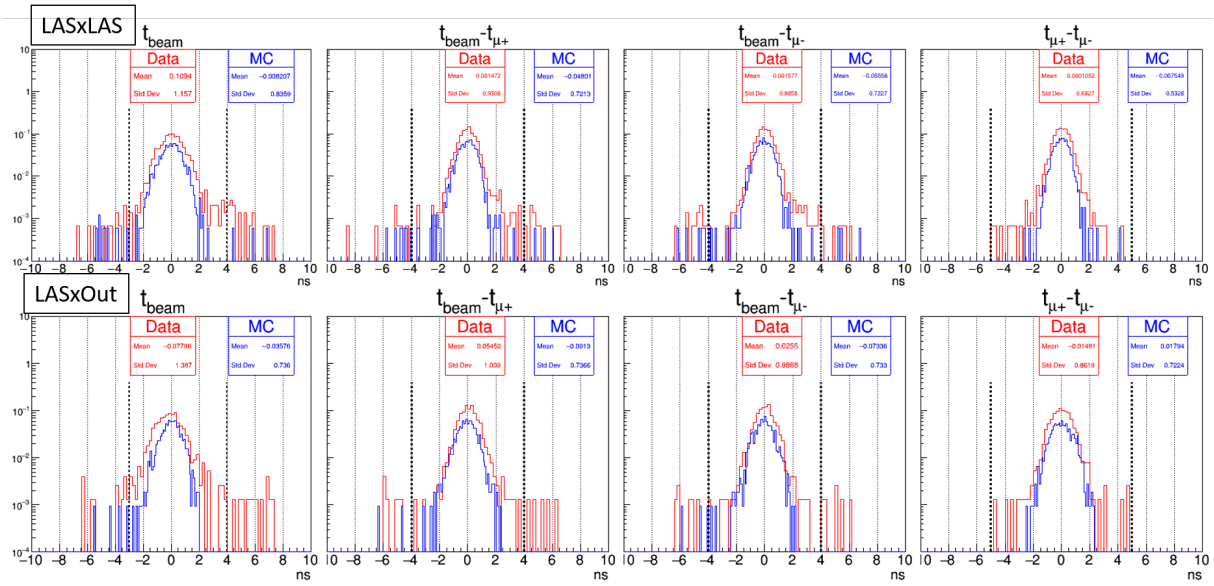

Figure 4.13: *The time distributions of t_{beam}, $|t_{beam} - t_{\mu^\pm}|$, $|t_{\mu^+} - t_{\mu^-}|$ of LAS×LAS and LAS×OT. the black dash lines are the cut limitation used in this analysis. Distribution is red is from real data. Distribution in blue is from MC data.*

- Dimuon kinematics in p_T, x_F, x_π, x_N
  The cuts on kinematics of p_T and x_F are decided by the 1D acceptance. Within the chosen p_T and x_F regions, the 1D acceptance is larger than 1% and the relative statistical error of it is less than 10 %. The discussion of acceptance will be further liberated in Sec.3.4. For x_π and x_N, full ranges are used.

  (1) $0.0 < p_T < 3.6$ GeV/c

  (2) $-0.10 < x_F < 0.70$ for LAST⊗LAST

  (3) $0.20 < x_F < 0.9$ for OUT⊗LAST

  (4) $0.0 < x_\pi < 1.0$

  (5) $0.0 < x_N < 1.0$

- Beam time selected
  In flux calculation, we ask for beam time, $-3.0ns < t_{beam} < 4.0ns$, therefore the same cut must be applied in the selection of dimuon events to ensure the correction normalization of the cross section. One can find more details in Sec. 3.1.

- Beam track pass through targets
  In flux calculation, we ask for the beam tracks pass through target region after the extrapolation : $\frac{x_{extra}^2}{(1.9cm)^2} + \frac{(y_{extra}-0.15cm)^2}{(1.3cm)^2} < 1.0$ at the upstream surface of NH_3 target($Z = -294.5\ cm$) and downstream surface of selected W target ($Z = -10\ cm$), therefore the same cut apply in the selection of dimuon events to ensure the correction normalization of the cross section. One can find more details in Sec. 3.1.

- Target region in X_{vtx} and Y_{vtx}
  The selected vertex is within the transverse ellipsoid, $\frac{X_{vtx}^2}{(1.9cm)^2} + \frac{(Y_{vtx}-0.15cm)^2}{(1.3cm)^2} < 1.0$

- Target region in Z_{vtx}
  We separate the them into 5 regions: NH_3 1^{st} cell, NH_3 2^{nd} cell, Al, W 1^{st} cell, and W $2^{nd}cell$.

  - PT 1^{st} cell : Z_{vtx} = [-294.5, -239.4] cm
  - PT 1^{nd} cell : Z_{vtx} = [-219.1, -163.9] cm
  - Al cell : Z_{vtx} = [-80.0, -60.0] cm (reality in [-73.5, -66.5] cm)
  - W 1^{st} cell : Z_{vtx} = [-40.0, -20.0] cm (reality in [-30.0, -10.0] cm)
  - W 2^{nd} cell : Z_{vtx} = [-20.0, -10.0] cm

  For NH_3 targets and W_{2nd} cell, the selected Z_{vtx} positions are same as the real position given by survey. However it is not the case for Al and W_{1st} targets. In order to increase the statistics, we try to include the migrated events due to the position resolution. The selected Z_{vtx} positions are larger than the real range. **plots**

Pythia setting

For Drell-Yan process setting :

```
WeakSingleBoson:ffbar2gmZ = on
WeakZ0:gmZmode = 1
23:mMin =  3.5
23:mMin = 11.0
23:onMode = off
23:onIfAll = 13  -13
```

p_T **tunning** :

```
BeamRemnants:primordialKT = on
BeamRemnants:primordialKTsoft = 1.1
BeamRemnants:primordialKThard = 1.8
BeamRemnants:halfScaleForKT = 2.0
BeamRemnants:halfMassForKT = 4.0
BeamRemnants:reducedKTatHighY = 0.7
BeamRemnants:primordialKTremnant = 0.4
```

p-n mixture of PT cells

```
$ISACTIVATED = YES
$PROCESS = DYHM
$RATIO = 1.83
```

Bibliography

[1] C. Patrignani, *et al*. Chin. Phys. C, 40, 100001 (2016)

[2] H1 and ZEUS Collaboration, Eur. Phys. J. C75, 580 (2015)

[3] S. Dulat, *et al*., Phys. Rev. D 93, 033006 (2016)

[4] NNPDF Collaboration, NNPDF Website

[5] L. A. Harland-Lang, *et al*., Eur. Phys. J. C75, 204 (2015)

[6] T. Horn and C. D. Roberts, J. Phys. G 43, 073001 (2016)

[7] C. D. Roberts, Symmetry 12, 1468 (2020)

[8] Parada T. P. Hutauruk, *et al*., Phys. Rev. C 94, 035201 (2016)

[9] Z. F. Cui *et al*., Eur. Phys. J. C 80, no. 11, 1064 (2020)

[10] X. Ji, *et al*., Phys. Rev. Lett. 110, 262002 (2013)

[11] J. F. Owens, Phys. Rev. D 30, 943 (1984)

[12] P. Aurenche, *et al*., Phys. Lett. B 233, 517 (1989).

[13] M. Glfick, *et al*., Z. Phys. C 53, 651-655 (1992)

[14] M. Gl¨uck, *et al*., Eur. Phys. J. C 10, 313(1999)

[15] P. J. Sutton, *et al*., Phys. Rev. D 45, 2349(1992)

[16] P. C. Barry, *et al*., Phys. Rev. Lett. 121, 152001 (2018)

[17] ZEUS Collaboration, Nuclear Phys. B 776, 1-37 (2007)

[18] I. Novikov, *et al*., Phys. Rev. Lett. 102, 014040 (2020)

[19] S. D. Drell and Tung-Mow Yan, Phys. Rev. Lett. 25, 316 (1970)

[20] W.-C. Chang, *et al*., Phys. Rev. D 102, 054024 (2020)

[21] J. S. Conway, *et al*., Phys. Rev. D 39, 92 (1989)

[22] B. Betev, *et al*., Z. Phys. C 28, 9-14 (1985)

[23] J. Badier, *et al*., Conf. C790823 (1979)

[24] R. J. Holt and C. D. Roberts, Rev. Mod. Phys. 82, 2991(2010)

[25] K. D. Bednar, *et al.*, Phys. Rev. Lett. 124, 042002 (2020)

[26] M. Aicher, *et al.*, Phys. Rev. Lett. 105, 252003 (2010)

[27] J. T. Londergan, *et al.*, Phys. Lett. B 361, 110 (1995)

[28] J. H. Christenson, *et al.*, Phys. Rev. Lett. 25, 1523 (1970)

[29] I. R. Kenyon, Rep. Prog. Phys. 45, 1261 (1982)

[30] W. J. Stirling and M. R. Whalley, J. Phys. G 19, D 1 (1993)

[31] A. L. S. Angelis, *et al.*, Phys. Lett. 87B, 398 (1979)

[32] C. Kourkoumelis, *et al.*, Phys. Lett. 91B, 475 (1979)

[33] J. Alitti, *et al.*, Phys. Lett. 275B, 202 (1992)

[34] D. Antreasyan, *et al.*, Phys. Rev. Lett. 48, 302 (1981)

[35] E. Anassontzis, *et al.*, Phys. Rev. D38, 1377 (1988)

[36] M. J. Corden, *et al.*, Phys. Lett. 96B (1980)

[37] A. S. Ito, *et al.*, Phys. Rev. D 23, 604-633 (1981)

[38] D. Antreasyan, *et al.*, Phys.Rev.Lett. 39, 906 (1979)

[39] K. J. Anderson, *et al.*, Phys. Rev. Lett. 42, 944-947 (1979)

[40] S. R. Smith, *et al.*, Phys. Rev. Lett. 46, 1607-1610 (1981)

[41] D. M. Alde, *et al.*, Phys. Rev. D 43, 2815-2835 (1991)

[42] D. M. Alde, *et al.*, Phys. Rev. Lett. 64, 2479-2482 (1990)

[43] M. A. Vasiliev, *et al.*, Phys. Rev. Lett. 83, 2304-2307 (1999)

[44] H. B. Greenlee, *et al.*, Phys. Rev. Lett. 55, 1555 (1985)

[45] R. Barate, *et al.*, Phys. Rev. Lett. 43, 1541 (1979)

[46] R. Aghasyan, *et al.*, Phys. Rev. Lett. 119, 112002 (2017)

[47] P.L. McGaughey, *et al.*, Annu. Rev. Nucl. Part. Sci. 49, 217–53 (1999)

[48] J.-C. Peng, *et al.*, Phys. Rev. Lett. B 789, 10, 356-359 (2019)

[49] D. M. Alde, *et al.*, Phys. Rev. Lett. 66, 2, 133–136 (1990)

[50] J. Badier, *et al.*, Phys. Rev. Lett. B 104, 4, 335-359(1981)

[51] S. Falciano, *et al.*, Preprint CERN-EP/81-52

[52] A.V. Lipatov, *et al.*, JHEP 2011, 117 (2011)

[53] M. Tanabashi, *et al.* Phys. Rev. D 98, 030001 (2018)

[54] D. Cassel, J. Rosner, CERN Courier

[55] P. Nason, *et al.*, Nucl. Phys. B303, 607 (1988)

[56] H. Fritzsch, Phys. Lett. 67, 217 (1977)

[57] E. L. Berger, D. L. Jones, Phys. Rev. D 23, 1521 (1981)

[58] K.-T. Chao, PoS ConfinementX, 003 (2012)

[59] Geoffrey T. Bodwin, *et al.*, Phys. Rev. D 51 , 1125 (1995); 55, 5853 (1997).

[60] COMPASS Collaboration, COMPASS Website

[61] COMPASS Collaboration, COMPASS Wikipedia

[62] G. Baum, *et al.*, Tech. rep. CERN (1996)

[63] G. Baum, *et al.*, Tech. rep. CERN (1996)

[64] F. Gautheron, *et al.*, Tech. rep. CERN-SPSC-2010-014 (2010)

[65] D. R. Longo, *et al.*, PhD Thesis of D. R. Longo (2018)

[66] L. Gatignon, M. Leberig, Slides for Villars Meeting at CERN (2004)

[67] NA62 Collaboration, Document from NA62 Experiment

[68] A. Abragam, *et al.*, The Clarendon Press Oxford (1961)

[69] P. Abbon, *et al.*, Nucl. Instr. and Meth. A Vol. 577, 455-518 (2007)

[70] P. Wintz, *et al.*, COSY Experiment

[71] M. Bodlak, *et al.*, J. Phys.: Conf. Ser. 513, 012029 (2014)

[72] COMPASS Collaboration, COMPASS Experiment

[73] COMPASS Collaboration, COMPASS Experiment

[74] COMPASS Collaboration, COMPASS Experiment

[75] C. Quintans , *et al.*, COMPASS Internal Note, March, 28 (2014)

[76] C.-J. Naïm, *et al.*, PhD Thesis of C.-J. Naïm (2020)

[77] R. S. Heitz, *et al.*, PhD thesis of R. S. Heitz (2019)

[78] M. Chiossoa, *et al.*, Document of CMAD chip

[79] S. Tavernier, Interactions of Particles in Matter

[80] Particle Data Group, Particle Data Group

[81] B. Adeva, *et al.*, Nucl.Instrum.Meth.A 419, 60-82 (1998)

[82] F., Springer, ISBN : 978-3-540-46356-6

[83] T. Sjostrand, *et al.*, Comput. Phys. Commun., 178, 852–867 (2008)

[84] M. Glück, *et al.*, Eur. Phys. J., C5, 461–470, (1998)

[85] M. R. Whalley, *et al.*, HEP-PH/0508110

[86] S. Catani, *et al.*, Phys. Rev. Lett. 103, 082001 (2019)

[87] S. Catani, *et al.*, Phys. Rev. D 103, 114014 (2021)

[88] M. Donnat, *et al.*, Z.Phys. C 38, 371 (1988)

[89] A. Vladimirov, JHEP 2019, 90 (2019)

[90] Xiaofeng Guo, Phys. Rev. D 58, 036001(1998)

[91] E. Anassontzis, *et al.*, Phys. Rev. D 38, 1377 (1988)

[92] Particle Data Group, PDG 2020

[93] M. Beneke and I. Z. Rothstein, Phys. Rev. D 54, 2005 (1996)

[94] E. J. Eichten and C. Quigg, Phys. Rev. D 52, 1762 (1995)

[95] P. L. Cho and A. K. Leibovich, Phys. Rev. D 53, 6203 (1996)

[96] F. Maltoni, *et al.*, Phys. Lett. B 638, 202 (2006)

[97] R. Vogt, Phys. Rept.310, 197 (1999)

[98] G. A. Schuler, arXiv:hep-ph/9403387

[99] I. Abt, *et al.* Eur. Phys. J. C 49, 545 (2007)

[100] C. Baglin, *et al.*, Phys. Lett. B 345, 617 (1995)

[101] M. J. Corden, *et al.*, Phys. Lett. 96B, 411 (1980)

[102] M. Butenschoen and B. A. Kniehl, Phys. Rev. Lett. 106, 022003 (2011)

[103] Y. Q. Ma, *et al.*, Phys. Rev. Lett. 106, 042002 (2011)

[104] M. Butenschoen and B. A. Kniehl, Phys. Rev. D 84, 051501 (2011)

[105] Y. Q. Ma, *et al.*, Phys. Rev. D 84, 114001 (2011)